Tunable Cation Release and Surface Oxides on Cu-Based Alloys: Investigating the Roles of Al and Sn in FCC Cu Solid Solutions with Implications Towards Anti-Tarnishing combined with Antimicrobial Functionality

---

A Dissertation

Presented to

the faculty of the School of Engineering and Applied Science

University of Virginia

---

in partial fulfillment

of the requirements for the degree

Doctor of Philosophy

by

Michael J. Hutchison

August

2018

APPROVAL SHEET

The dissertation
is submitted in partial fulfillment of the requirements
for the degree of
Doctor of Philosophy

AUTHOR

The dissertation has been read and approved by the examining committee:

Prof. John R. Scully
Advisor

Prof. Robert G. Kelly

Prof. Petra Reinke

Prof. Kevin Ogle

Prof. James A. Smith

Accepted for the School of Engineering and Applied Science:

Craig H. Benson, Dean, School of Engineering and Applied Science

August
2018

Tunable Cation Release and Surface Oxides on Cu-Based Alloys: Investigating the Roles of Al and Sn in FCC Cu Solid Solutions with Implications Towards Anti-Tarnishing combined with Antimicrobial Functionality

Abstract

Copper alloys have received renewed interest in functional and structural materials and pathogenic microbiological communities due to recent studies which demonstrate its ability to kill/inactivate even antibiotic-resistant so-called 'superbugs', such as methicillin-resistant Staphylococcus aureus (MRSA), via soluble Cu ion release. A general rule is that copper alloys with >65% copper exhibit antimicrobial efficacy. However, not all alloy systems are equally effective, and many different alloys behave without clear dose-response relationships traceable to alloying content. The copper alloy surface itself is not antimicrobial, but the soluble Cu ions that it releases into the local environment through the corrosion process are responsible for the antimicrobial efficacy of the alloy. Corrosion is the essential link between alloying and antimicrobial performance, yet we still do not understand how alloying affects corrosion, oxide formation (tarnishing), and ion release for antimicrobial function. Moreover, the critical copper ion concentration necessary for timely reduction in bacteria colony population (i.e., dose-response relationship) is not clear. Fundamental understanding of how alloying affects corrosion and ion release as well as the dose-response relationship is crucial to the effective use and deployment of tunable Cu-based systems as antimicrobial alloys.

A critical balance is needed between corrosion, oxide formation, and ion release; corrosion rates must be sufficient to release enough Cu for desired antimicrobial function with simultaneous adequate suppression of undesired tarnish-forming or passivating oxides.

The objective of this dissertation is to explore two selected alloying elements. Al and Sn were specifically chosen to investigate the effects on corrosion and antimicrobial response as a function of alloy content in binary and ternary alloy systems designed with attributes favorable for Cu ion release (Sn) and corrosion/tarnish resistance (Al). This was accomplished by determining the fate of the elements by measuring corrosion rates, Cu ion release and quantitatively comparing the composition, structure, and molecular identities of all corrosion products including oxides and precipitated compounds. This data was utilized to understand pertinent phenomena, i.e. enhanced release and passivation, as regulated by Sn and Al.

Sn was shown to enhance Cu dissolution by affecting the anodic dissolution kinetics of Cu in Cu-Sn systems, but this could be mediated by formation of a protective inner layer of SnO_2 under a Cu_2O surface film. The minimum alloying amount of Sn needed for complete layer coverage of SnO2 was determined through a new theoretical framework for specifying the critical alloying content for passivation in duplex films based on solute enrichment theory and wetting phenomena governed by the interphase surface energies of insoluble oxides. This framework could not be applied to Al_2O_3 as this oxide was not found as a phase-separated oxide co-existing with Cu_2O nor a Cu-Al-O phase as predicted from high temperature phase equilibria. Instead, Al^{3+} was observed to dope the Cu_2O oxide as evidenced by structural, chemical, and electronic modifications to the Cu_2O oxide indicating a metastable oxide. This dopant effect led to a formation of a thinner more tarnish-resistant oxide than seen in Al-free alloys. These doped Cu_2O oxides, while tarnish-resistant, did not impede copper ion release. Investigations of ternary Cu-Al-Sn alloys over a range of compositions in the single-phase region demonstrated that the function of Sn-enhanced Cu dissolution operated concurrently and possibly synergistically with Al-doping of Cu_2O and high tarnish-resistance. This combination of properties applied to the copper alloying system permitted both antimicrobial yet tarnish-resistant functions. A certain compositional range of solid solution Cu-Al-Sn alloys were found to be both antimicrobial and tarnish-resistant, able to kill all planktonic E. Coli under 24 hours in using a custom disinfection test.

The key engineering achievement of this thesis is the design of a specific alloy composition tuned to serve a very important societal function that avoids alloying elements which cause preferential solute release (dealloying), allergic responses, toxicity, or unaesthetic tarnishing.

The scientific achievements herein advance the science of alloy design moving away from trial and error alloy approaches towards integrated computation – experimental design where the dose-response behavior is established, and mechanistic understanding is developed regarding the role(s) of each element from phase equilibria, defect chemistry, electrochemical as well as surface science viewpoints.

List of Tables

List of Figures

1 Introduction

1.1 Antimicrobial Copper Surfaces

1.1.1 Historical and Safe Usage of Antimicrobial Copper

Cu is a safe, reliable, and long-lasting antimicrobial surface. Humans have been making and using tools with copper and copper alloys since before the beginning of recorded history [1]. Cu is actually a micronutrient necessary to support human life and furthermore, the human body has the ability to easily filter out excess copper (with exceptions to those afflicted with the very rare Wilson's disease [2]). The antimicrobial function of Cu surfaces has only recently been 'rediscovered' in the early 1980's [1,3]. However, ancient civilizations used Cu and its alloys for drinking, handwashing, water purification, treatment of open wounds, and as surgical instruments [1]. British naval vessels relied on Cu sheathing of their submerged hulls to prevent marine growth (biofouling) [4]. Indeed, Royal Navy scientists (*circa 1750*) historically attempted an empirical approach to find the optimal Cu alloy composition for this purpose, endeavoring to balance specific weight, biofouling resistance (Cu ion release), and 'wastage' (corrosion rate) [4]. They recognized, even then, that alloys needed sufficient corrosion to prevent excess marine growth [4]; suggesting that soluble Cu ions from corrosion, not the Cu surface itself, is responsible for biofouling resistance [5] and antimicrobial function. With the advent of multi-antibiotic-resistant pathogens, more modern approaches aim to understand essentially the same phenomenon (biofouling/antimicrobial), albeit with more sophisticated tools, theories, and targeted methods.

1.1.2 Microorganisms and 'Superbugs' Susceptible to High-Purity Cu

Copper surfaces have demonstrated the ability to rapidly kill/inactivate a wide variety of bacteria, fungi, and viruses. Multiple microorganisms which have demonstrated susceptibility to the antimicrobial function of Cu and are summarized from the literature in Table 1-1. The US Environmental Protection Agency (EPA) has developed a standard testing methodology for antimicrobial surfaces and has currently approved over 300 Cu-based alloys as sanitizing surfaces: 99.9% (3 log) reduction under two (2) hours [6]. This EPA standard tests commercial Cu and Cu-alloys for antimicrobial performance using 'dry' (laboratory ambient RH) inoculum testing where a high concentration (>10^7 CFU/coupon) of a microorganism is deposited in a small droplet spread across the surface. (Table 1-1). However, not all Cu surfaces are equally effective at removing these bacteria and at present there are no clear dose-response relationships between alloy copper content and antimicrobial performance.

1.1.3 Cu Surfaces Can Reduce Hospital Infection Rates Including Antibiotic-Resistant Pathogens

Hospital-acquired and healthcare-associated infections are becoming an increasingly prevalent and difficult to treat. Antibiotic-resistant infectious microorganisms are entirely to blame. These so-called 'superbugs' are approaching a limit of pan-resistance at which they cannot be treated with antibiotics even in a hospital setting with multiple drugs [7,8]. High-touch surfaces are the most common transmission vector for bacteria, passing from hand to surface then back to hand again [9–11]. Instead of treating these pathogens after the patient becomes infected, another method could be to reduce the risk of infection altogether.

One possible remedy to this growing epidemic is replacement of high-touch surfaces with Cu alloys [12]. Cu and many Cu-alloy surfaces have demonstrated the ability to kill a wide range on microorganisms including many drug-resistant strains (Table 1-1) [1,6]. Hand-washing, and active sanitation procedures are indeed effective methods to prevent the spread of bacteria and viruses yet, these procedures require constant active and vigilant attention and have not been effective enough to reduce the spread of these pathogens [7,10,13].

Clinical trials have revealed that high-touch surfaces such as bed and chair rails, door handles, and nurse call buttons replaced with copper alloys showed significantly reduced bacterial loads. The risk of infection from commonly-touched equipment with Cu alloys surfaces compared against non-copper surfaces for a given microbial surface loading is given in Figure 1.1. The measurable decrease in microbial surface loading (CFU/100 cm^2) on Cu-based alloys directly led to fewer hospital-acquired infections (HAI) in a hospital intensive care unit (ICU) compared to non-Cu-based surfaces such as stainless steel or plastics [1]. Consequently, infection rates decreased by over 50% in wards where commonly touched surfaces were replaced with antimicrobial copper alloys [14–16]. A significant result considering less than 10% of the total surface area, representing high-touch locations, were replaced with various copper alloys [13,14]. These clinical results show that copper and Cu-alloy surfaces can reduce the spread of infection due to its innate ability to kill a wide range of pathogenic microorganisms (Table 1-1).

Replacement of a common infection transmission vector such as high-touch surfaces with a passively antimicrobial surface could be a reliable and continuously active second line of defense against proliferation of these harmful bacteria. Cu and many Cu-based alloys have demonstrated the ability to kill a wide range of microorganisms, making this alloy system an ideal antimicrobial surface as a second line of defense against pandemic infection.

1.1.4 Antimicrobial Effectiveness of Several Cu-Based Alloy Systems

Many Cu-based alloys are also antimicrobial as well. There is one caveat however: not all alloy systems are equally antimicrobial, and many different alloys behave in a non-predicable manner because specific effects of major and minor alloying elements must be considered. While no clear alloying relationships exist, Cu alloys with at least 65 wt% Cu are considered antimicrobial as a typical rule-of-thumb [17]. Generally, higher Cu content [18], temperature

[19,20] and relative humidity [19,20] increase antimicrobial killing rates on copper surfaces. Killing times (> 4 log reductions of inoculum) on selected alloy systems with three example disease-causing bacteria: *Escherichia coli* (*E. Coli*), *Clostridium difficile* (*C. difficile*), and Methicillin-resistant *Staphylococcus aureus* (MRSA) are presented in Table 1-2 and ranked by descending Cu content. During so-called 'dry' tests (thin electrolyte films), copper and many alloys can kill pathogenic bacteria within minutes [20]. Yet, these studies have not been able to produce quantifiable dose-response relationship between Cu-based alloy solvent/solute contents and antimicrobial efficacy.

As demonstrated in Table 1-2, Cu content in the alloy is somewhat related to the antimicrobial response. However, the nuances of the metallurgy, corrosion potential, dealloying phenomena can change the surface state and corrosion of the alloy. The specific mechanisms of how Cu-facilitated bacteria killing are under debate [9,21,22]. However, soluble Cu ions have been shown to be the most important factor for antimicrobial efficacy [1,9,17,23–25]. Generally, Cu content in the alloy does increase the killing rate of these alloys but, the variability in antimicrobial performance of Cu-based alloy are directly related to *the differences in Cu ion release* from dissimilar corrosion modes and dissolution rates i.e. corrosion.

1.1.5 Soluble Cu Release: The Link Between Antimicrobial Function and Corrosion

The copper alloy surface itself is not antimicrobial, but the soluble ions that it releases into the local environment are responsible for the antimicrobial efficacy of the alloy. Soluble cations enter the aqueous environment through the corrosion process. But, not all oxidized copper is dissolved and alloying elements as well as their oxides have differing solubility. Many alloy systems corrode at different rates with varying preference to soluble release or oxide formation which in turn affects their antimicrobial efficacy. Corrosion and soluble Cu release are influenced by alloying independently through effects such as passivity and dealloying. Cu and its alloying elements may terminate in one of several ‘fates’ following corrosion, some of which are illustrated schematically with Figure 1.2. Consequently, not all alloys are equally antimicrobial even with the same corrosion rates, and the variability of killing efficacy between alloys types is demonstrably evident from Table 1-2.

Cu ion release from the corroding alloy surface is the determining factor for antimicrobial performance [1,9,17,23,24,26] and is illustrated with a test of planktonic *Legionella pneumophila* in Figure 1.3, [24] and *Escherichia. coli* in Figure 1.4, [26] viabilities in deionized water and simulated artificial perspiration, respectively. These tests do not use a metal contact surface, Cu or otherwise. Increasing soluble [Cu^{2+}] (as dissolved $CuCl_2$) unambiguously demonstrates increased kill rates (see Figure 1.3 and Figure 1.4). Despite this recent knowledge, Cu alloys system are still evaluated individually (Table 1-2) for antimicrobial response without essential ties to corrosion in more appropriately-simulative chemistries such as artificial perspiration. Critically, antimicrobial testing (e.g., Table 1-2) does not investigate corrosion rates of the alloys tested, the released soluble Cu ion concentration required to kill bacteria (see Figure 1.4), or quantitatively tie these data to alloying contents. Antimicrobial tests directly evaluate the killing ability of Cu alloys. Moreover, this Edisonian approach is limited to only current commercially available alloys and offers minimal insight to specific alloying influences for improved antimicrobial alloy design.

Corrosion is the essential link between alloying and antimicrobial performance, yet we still do not understand how alloying affects: corrosion, oxide formation (tarnishing), and ion release for antimicrobial function. Fundamental understanding of how alloying affects corrosion and ion release is crucial to the effective use and deployment of tunable Cu-based alloys as antimicrobial surfaces.

1.2 Present Challenges of Antimicrobial Cu Alloys

1.2.1 Disparate Knowledge Bases and Intersectional Knowledge Gaps of Scientific Communities

Deployment of antimicrobial Cu alloys is restricted by key gaps in scientific understanding in the present literature. The current body of knowledge surrounding antimicrobial Cu alloys is, to a certain extent, restricted to two communities: (1) corrosion of Cu and its alloys in service environments e.g., seawater, potable waters, and atmospheric exposure, and (2) antimicrobial performance of Cu alloys against various bacteria flora. The disparate knowledge base of these two different scientific communities have made significant and impressive strides in scientific understanding individually, but their intersection is left with many unaddressed gaps and unknowns.

Investigations on the corrosion of copper and its alloys are primarily concerned with evaluating corrosion rates (metal loss) in various environments and do not typically quantitatively measure soluble ions needed for antimicrobial function. A survey of Cu alloy corrosion literature reveals most major classes of Cu alloys studied have no statements on release, cation flux, or account for alloy surface to electrolyte volume ratio. Out of over 5000 recent papers on the subject, fewer than 50 mention cation release. However, studies which do monitor soluble Cu emphasize rainfall-induced runoff, which is related to the relative chemical dissolution of pre-formed corrosion products from impinging rainwater, rather than the electrochemical corrosion process or direct ion release from the alloy [27]. Seawater and marine atmospheric environments are the most common media for corrosion studies of Cu and its alloys. Due in no small part to its excellent corrosion resistance and resistance to biofouling (marine organism accumulation) in these settings compared with other metals.

Antimicrobial tests are evaluated with a pass or fail criterion (99.9% reduction in under two hours [6]) which does not aid in determination of specific mechanisms, or parse individual effects of alloying elements. The methodology is optimized for rapid practical assessment of disinfectant efficacy and as such use environments targeted for this objective. The physiological buffers or bacteria growth media solution chemistries used in evaluating antimicrobial performance, e.g., agar, saline, and soy broth [18–22,24], are often selected to feed and accelerate particular bacterial culture growth for optimal sanitation testing conditions but consequently cannot address their effect on corrosion despite the fact that corrosion is required for antimicrobial function [1,9,21,28,29]. These media are not representative of more simulative high-touch environments which are known to be more aggressive towards corrosion [30] and may cause thicker oxides and/or greater corrosion rates potentially altering observed trends of alloying effects seen in other environments. Antimicrobial testing is also not designed to test Cu ion concentration and this parameter is left unevaluated [1,6,9,18–21,31]. In other words, while Cu ions are responsible for killing the alloy's killing efficacy, the relative antimicrobial function of alloys is not yet linked to release of Cu cations from corrosion.

1.2.2 Empirical Approaches: Cu Contents and Seawater Corrosion Rates

Alloying elements in Cu-based alloys have been empirically selected for aesthetic, mechanical, or corrosion-resistant properties. Consequently, alloying influences on corrosion in the context of antimicrobial performance, i.e. soluble Cu release, remains poorly understood. Commonly stated, 65 wt% Cu is the currently accepted minimum value for antimicrobial performance [17] (see Table 1-2). Increased Cu in the alloy generally corresponds to greater antimicrobial functionality [18]. However, several alloys, do not subscribe to this minimum 65 wt% Cu 'litmus-test' criterion. This suggested threshold does not work for two main reasons, passivity and dealloying: passivity shuts down the corrosion rate through the formation of a thin film of the alloying solute element (e.g., Cr), and dealloying selectively corrodes one element over another such as Zn dealloying from brass. Both phenomena can have threshold limits for these negative effects which limit Cu ion release, violating this Cu-content rule-of-thumb. For example: passive elements such as Ni, Ti, and Cr form thin (nm thick) passive oxides on the alloy surface at concentrations below 35 wt%, thereby suppressing the corrosion process almost entirely at 65 wt% Cu and thus preventing release of soluble ions needed for antimicrobial activity despite satisfying the 65 wt% Cu criterion.

Moreover, several other elements, including Mn, Al, and Zn, when added to Cu, dealloy [32–42]. Because certain elements tarnish (Sn, Zn), passivate (Cr, Ti, Al), or dealloy (Mn, Al, Zn) in Cu-based alloys, Cu content or corrosion rates alone are poor metrics of ranking Cu alloys for antimicrobial performance because these corrosion rates of these alloys do not directly correlate to soluble Cu release.

1.2.3 Elemental Effects on Cu-Alloy Corrosion in an Antimicrobial Context

The effects of alloying elements on corrosion, dealloying, and passivity are still poorly understood and we still cannot predict performance from alloying content and/or structure – *a fundamental challenge* to the intersection of corrosion and materials sciences [43,44]. Most corrosion studies characterize corrosion product films and corrosion rates but have not yet established quantitative relationships between alloy solute content and observed corrosion response. Elemental effects also can vary between environments. Furthermore, net corrosion rates do not directly correlate with released *Cu* ions into solution, especially when considering oxide formation or incongruent dissolution i.e. dealloying (see Figure 1.2). Thus, a complete assessment of the 'fates' of the elements following corrosion is needed to identify and understand the key mechanisms responsible for corrosion product formation and cation release as influenced by alloy content.

Some elements when alloyed with Cu can promote oxide formation, whereas others promote dissolution [45]. The interplay between the Cu-M and M-O bonding character with respect to copper is presented for several elements in Figure 1.5. Elements such as Ni and Al both promote oxide formation and inhibit dissolution, whereas elements such as Sn and Mn may make dissolution easier due to their lower bonding energies.

Addressing the greater challenge of tunable Cu-based alloys with stable film-mitigated corrosion and enhanced Cu ion release moderated by alloying requires an interdisciplinary approach. Some of the relevant work and remaining knowledge gaps and challenges faced by these communities are highlighted herein.

1.3 Modern Understanding of How Alloying Elements Affect Antimicrobial Function of Cu-Based Alloys

1.3.1 Marine Biofouling Resistance and Copper Alloys in Seawater

Copper is most commonly alloyed with Sn (bronze), Zn (brass), Ni (cupronickel), and Al (aluminum bronze). A summary of some basic general trends as to the effect of the most common solute elements on corrosion of Cu alloys in given in Table 1-3. A copper corrosion rate of at least 1 mpy is provide copper ions to the adjacent environment to be toxic to marine life and prevent biofouling [5]. Biofouling resistance can lend insight to a predicted antimicrobial response albeit in a marine exposure setting rather than high-touch and biological simulants which may yield quite different corrosion and antimicrobial efficacy. These survey studies are inherently limited in their ability to determine mechanistic insight as to alloying without comparison between alloy content or systematic controls. However, biofouling studies are useful for evaluating potential antimicrobial function. Furthermore, while some general trends of binary and a few ternary elements are well documented [5,46,47] (e.g., Table 1-3); binary, ternary, and minor solute effects on antimicrobial efficacy (Cu ion release) remain unexplored.

The various effects of alloying content on seawater corrosion rates and antimicrobial efficacy is illustrated by Figure 1.6. This schematic figure shows the landscape of copper alloys and demonstrates the complicating effects of alloying and how corrosion rates alone cannot accurately predict antimicrobial alloys due to phenomena such as oxide formation, passivity and dealloying. The only alloys which approach an ideal zone, i.e. low corrosion rates with fast antimicrobial killing kinetics, contain Ni which is an increasingly common allergen to skin contact and thus would be unwelcome as an element in a high-touch alloy [9]; especially as Ni has demonstrates preferential release in artificial perspiration [30] grossly exceeding (30x) minimum allergy trigger levels: 0.5 μg cm^{-2} $week^{-1}$ Ni [48]. However, the rankings of alloy behavior in seawater are not always preserved in perspiration of high touch surfaces, and solution chemistries can strongly influence the relative corrosion of Cu alloys.

1.3.2 Effects of Environment Chemistry on Corrosion of Cu-Based Alloys

Copper is a popular alloy for use in marine and outdoor environments and applications for its excellent resistance to both corrosion and biofouling in seawater and atmospheric exposures. Corrosion studies therefore, are most commonly conducted in seawater (or 3.5 wt% NaCl) or unsheltered atmospheric environments. Aside from rainfall-induced runoff for environmental concerns [49–51], however, soluble Cu is not determined or distinguished from corrosion rates or scale formation in most corrosion studies of Cu alloys! Furthermore, these studies acknowledge corrosion as necessary to facilitate biofouling resistance (via soluble Cu), yet do not correlate their efficacy to corrosion rate and Cu ion release. Moreover, corrosion studies fail to correlate fundamental relationships between a given corrosion response to alloying composition.

The chemical stability of corrosion products as a function of soluble Cu ion concentration and pH is given for some common corrosion products of copper in Figure 1.7. Oxide and corrosion product chemical stability can be a strong function of environment as illustrated by this figure. The extrapolated killing times from Figure 1.4 are indicated for several chemical equilibria points. Equilibrium of soluble Cu with one or more corrosion products will yield antimicrobial function with killing kinetics on the order of days rather than the desired hours or minutes (99.9% disinfection within two hours). Therefore, an actively corroding alloy surface is needed to maintain effective antimicrobial function. Alloying element corrosion products formed do not contribute to, and indeed may hinder, antimicrobial function. Corrosion products sequester anodic charge and oxidized Cu ions which could otherwise be soluble and contribute to antimicrobial function. The variable solubility of Cu corrosion products (Figure 1.7) leads to different ion concentrations in solutions, and appropriate solution chemistry therefore is critical.

Biological solutions are more appropriate electrolytes for studying the corrosion of copper in the context of antimicrobial function as they simulate the media which these pathogenic bacteria proliferate. Attempting to predict behavior in biological solutions compared with those established literature data obtained in seawater or atmospheric conditions is challenging as biological solution chemistries have various complexing and chelating compounds [52]. Halide and sulfate concentrations normally dominate definitions of environmental severity for Cu [5,46] and differ significantly between a seawater environment and biological solutions as would be encountered in a high-touch environment. Complexation and chelation of Cu due to organic and inorganic species have strong influences on the chemical stability of corrosion product films [52]. Consequently, the antimicrobial response from a Cu alloy cannot be predicted directly from the corrosion rates or biofouling efficacy in seawater, atmosphere and other environments alone. Oxide formation and composition, ion valence state, corrosion response, electrolyte specificity, and solution complexing effects are critical to understanding antimicrobial function of Cu-based alloys. Antimicrobial studies acknowledge that corrosion is necessary to provide Cu(I)/Cu(II) ions to the surrounding environment but fail to monitor either overall corrosion rates or soluble Cu ions in these studies. However, soluble Cu cations may not be enough to be antimicrobial in all environment chemistries. Strong complexing or chelating agents may inhibit free Cu^{+}/Cu^{2+} required for antimicrobial function [27].

Bioavailability

Cu alloy panels showed that bioavailable Cu able to participated in antimicrobial function was shown be significantly lower than the total soluble Cu content [27]. Soluble Cu measured via graphite furnace atomic absorption spectroscopy (GF-AAS), or inductively-coupled plasma optical emission spectroscopy (ICP-OES), do not provide information on bioavailability and do not differentiate between free, complexed, or chelated ions. The difference between bioavailable Cu and soluble Cu investigated by bioluminescent staining of *E. Coli* in rainfall-induced runoff of atmospherically exposed Bioavailability is strongly affected by the solution chemistry through important factors such as complexation and chelation.

These observations highlight the need to critically evaluate the entire fate of the elements, looking at specifics such as corrosion rate, oxide and corrosion product identity, soluble ligand state, environment chemistry, temperature, relative humidity, alloy surface condition, minor and micro alloying elements in appropriately simulative environments.

Artificial Perspiration

Simulated human perspiration [48], contains known complexing and Cu-chelating[1] compounds [30] and offers a more representative electrolyte for high-touch surfaces subjected to hand contact. Perspiration is a highly corrosive environment to Cu directly due to these complexing and chelating compounds (Cl^-, ammonia) [30] and there stands a risk that corrosivity and tarnishing behavior in Cl^- solutions is not the same for other electrolytes as in perspiration. By simulating artificial perspiration as an analogue to a high-touch environment in both full immersion [26] and wetting and drying cycles [23], prior passivation in air or furnace oxidation had negligible effect on cation release for both pure copper and a tarnish-resistant Cu alloy (Cu-5Zn-5Al-1Sn). Nordic Gold demonstrated comparable cuprous ion release as Cu in both full-immersion and cyclic wet/dry exposures to artificial perspiration with limited corrosion [23,26]. This result is likely due to the aggressiveness of this solution and its Cu-complexing effects. This outcome highlights another shortcoming in current practices, as an alloy system may perform unsatisfactorily in an antimicrobial test in a bacteria-growth media, yet *in operando* conditions would be an excellent candidate alloy in high touch wet/dry environmental conditions (e.g., Nordic Gold). Furthermore, the passivation behavior of alloys cannot be tied directly to alloy content, particularly for ternary systems. However, the passive layer may further be tunable in a specific solution chemistry to partial coverage through strict control of solid solution alloying below minimum thresholds.

1.3.3 Copper Alloy Corrosion and Soluble Cation Release in Biological Solutions

Biological simulants such as artificial perspiration and Ringer's solution have been employed when investigating the fate of Cu alloys following corrosion. Ringer's solution was far less aggressive (10x) to a Cu-Ni alloy (Cu-18Ni-20Zn) than artificial perspiration [30]. Ni released

---

[1] Bioavailable Cu and chelation effects [6,18,27,30], are specifically related to the chemistry of the solution where corrosion trends of an alloy system should be grossly unaffected.

from these alloys was problematic, amounts release in 30 days were far in excess of those required to trigger an allergic response [30]. In biological solutions where urea and lactic acid are common, Cu-lactic acid and Cu-urea complexes were shown to have accelerated Cu alloy corrosion [30,53].

Survey studies using commercial alloy systems can provide utility by revealing some alloying trends [17,54–56]. Several common alloys (Cu, Cu-Zn, Cu-Sn, Cu-Ni, and Cu-Zn-Ni) subjected to intermittent hand contact revealed different tarnishing behavior dependent on alloying elements [57]. Zn and Sn containing alloys as well as pure Cu heavily tarnished (via oxide charge) after 2 years of discontinuous hand contact whereas, Ni containing alloys remained relatively tarnish-free. Though it was concluded that the tarnish resistance was not due to a lack of corrosion, but surface roughness. Cu-Ni alloys corroded in artificial perspiration more uniformly leaving behind a relatively smooth surface morphology compared to other alloys (Sn, Zn, pure Cu) which had rougher surface morphologies [57].

Cu alloying content alone is insufficient to predict the propensity for the alloy to release Cu through corrosion [17]. Horton *et al.* demonstrated that there was no correlation between alloying content of several common Cu-based alloys, their corrosion rates, Cu ion release, or tarnishing behavior in artificial perspiration [17]. The lack of correlation between alloying content and any of these parameters is illustrated by Figure 1.8.

Survey studies reveal that ranking alloys for antimicrobial activity by corrosion rate or biofouling in seawater is an ineffective screening metric to predict antimicrobial performance due to several probable circumstances: incongruent or preferential dissolution of the solute elements (i.e. dealloying), differing corrosion rankings for other chemical environments, and formation of insoluble corrosion products including protective passive films which impede Cu release.

1.3.4 Dealloying and Incongruent Dissolution

Cu is a semi-noble element and its alloying elements may dealloy [32–42], a process by which the less noble element preferentially corrodes leaving the more noble element behind. Several notable examples of dealloying are found in Cu-based alloys systems, particularly Cu-Zn, Cu-Al, and Cu-Mn [36–42]. The Cu-Mn system is highlighted in Figure 1.6, where dealloying in seawater causes high corrosion but poor antimicrobial performance due to the lack of Cu ion release. The Cu-rich surface-reconstructed [32,39–42,57] metallic phase is protected from anodic dissolution; deactivating any antimicrobial function despite a corrosion rate suggesting otherwise. Zhou *et al.*[58] were able to show dealloying of Cu-Zn alloys in real-time with atomic emission spectroelectrochemistry. A Cu-42Zn alloy left at open circuit in simulated tap water preferentially released Zn, inhibiting Cu dissolution as shown in Figure 1.9. This example illustrates how corrosion rates alone do not directly correlate to element release.

Effects of ternary and minor alloying elements on Cu-alloy corrosion are usually neglected but can mitigate dealloying. A notable example: Sn added to Cu-Zn (brass) can inhibit dealloying [59]. *Only a 1 wt%* addition of Sn to cartridge brass (Cu-30Zn) is enough to *significantly improve* the corrosion and dealloying resistance of the solid solution Cu-Zn system (admiralty brass: Cu-19Zn-1Sn). The Sn effect is also operative on the duplex (alpha + beta) brasses such as Muntz/yellow metal (Cu-40Zn) to form a dealloying-resistant Naval brass alloy (Cu-39Zn-1Sn) [60]. Sn has a comparable synergistic effect on aluminum bronzes as well. Al bronzes are susceptible to dealloying of Al [37,40–42]. However, Cu-Al alloys with minor amounts of Sn (1 wt%) significantly increased the resistance to corrosion by over two orders of magnitude [61,62]. Similar dealloying-resistant effects are observed with ternary arsenic (Cu-Zn-As) and are referred to as arsenical brasses [60,63]. These effects are listed in the literature as interesting nuances, though, fundamental knowledge of how these synergisms of minor alloying arise and operate however, is lacking [64].

1.3.5 Tarnishing or Passivating Solute Oxides

A passive Cu-alloy, protected from corrosion by a thin adherent and self-healing oxide layer such as Cr_2O_3 on stainless steel, would remain tarnish-free and maintain a high luster and shiny appearance in a high-touch environment. However, the reduction in corrosion rate prevents sufficient soluble Cu release for continuous antimicrobial function as demonstrated in Figure 1.6. Foster *et al*. illustrates this point (see Figure 1.10) in a study of MRSA survivability on Nordic Gold (Cu-5Zn-5Al-1Sn, a European coinage metal) both freshly polished and left exposed to lab air [26]. The freshly polished alloy actively corroded, releasing Cu ions, and was able to completely kill MRSA within six (6) hours, but the same alloy formed a protective passive oxide layer after seven (7) days in lab air which impeded antimicrobial function.

Understanding which factors influence solute-endued passivation is critical for a tunable tarnish-resistant alloy which is also antimicrobial. For example, complete passivation shuts off antimicrobial function by disabling Cu cation release from corrosion while highly antimicrobial alloys that corrode at high rates tend to form unaesthetic tarnishing layers [17]. The mechanisms of solute-endued passivation of metals are still vehemently debated; several proposed theories attempt to explain the influences of solutes on these binary systems [45,65–73], critical solute contents [65,69,72,74–79], and stability [68,70,80–84].

Biological solutions are more appropriate electrolytes for studying the corrosion of copper in the context of antimicrobial function as they simulate the media which these pathogenic bacteria proliferate. Attempting to predict behavior in biological solutions compared with those established literature data obtained in seawater or atmospheric conditions is challenging as biological solution chemistries have various complexing and chelating compounds [52]. Foster *et al.* also demonstrated that Nordic gold had similar ion release (and implicitly had similar antimicrobial function as Cu) in artificial perspiration solutions despite this alloy having tested to not have antimicrobial function when passivated by lab air (see Table 1-2) [26]. Complexation and chelation of Cu due to organic and inorganic species have strong influences on the chemical stability of corrosion product films [52]. Consequently, the passivity and potential antimicrobial response from a Cu alloy cannot be predicted directly from the corrosion rates or biofouling efficacy in seawater, atmosphere and other environments alone.

1.4 Critical Unresolved Issues

Copper-based alloy surfaces have a proven ability to be antimicrobial. However, not all alloying systems are equally effective as the antimicrobial performance is directly related to Cu ion release from corrosion. Copper as a soluble ion can kill a wide range of microorganisms, including antibiotic-resistant strains which cannot be killed by antibiotics. Corrosion of copper alloys transforms the elements to their oxidized state in one of several 'fates'. Alloying elements can drastically affect element fates following corrosion, especially in the cases of dealloying or passivation which may shut down soluble Cu release and/or corrosion entirely. Oxidized alloy elements can be directly formed into surface oxides or dissolved in the electrolyte as a soluble ion which then may be precipitated to form a metal salt or -hydro/oxychlorides. For an antimicrobial system: passivity, allergy triggers (e.g., Ni), and preferential solute ion release (dealloying) would be undesirable traits.

Trial and error disinfection studies are both effective and necessary to prove the effectiveness of alloys as antimicrobial surfaces. However, generating a tunable alloy system for an antimicrobial function requires the use of new tools, scientific theory, and the collective effort of researchers from the fields of microbiology, epidemiology, materials and metallurgical sciences, electrochemistry, and corrosion science as well as other biological and physical fields of science.

The effects of alloying need to be understood to generate a tunable alloy system which is tarnish-resistant for public acceptance and aesthetics yet remain actively corroding to provide continuous soluble Cu release required for antimicrobial function. There are several critical unresolved issues in antimicrobial Cu alloy surfaces and gaps in scientific understanding of Cu-based alloy corrosion which inhibit the development of tunable antimicrobial Cu-based alloys.

- Not all corrosion products from Cu-based alloys form soluble ions and may form insoluble corrosion products. Knowledge of the fate of copper and its alloying elements as an ion or oxide is required. Alloying elements can strongly influence the 'fate' of elements (Figure 1.8) and the knowledge of specific effects is lacking.
- Minimum Cu content (e.g., ≥65 wt% Cu) is not an effective criterion for predicting antimicrobial function. Cu alloy content does not track to soluble ion release due to alloying influences such as preferential element ion release (e.g., dealloying) and surface corrosion product films (e.g., passivity).
- Evaluating corrosion rates of Cu-based alloys in seawater is not an effective metric to screen for potential antimicrobial function as corrosion rates do not directly track to antimicrobial function (Figure 1.6). The direct release of soluble Cu from corroding Cu-based alloys must be investigated in the context of antimicrobial function.
- Environment chemistry, especially biological solutions, strongly affects corrosion, cation release, and ion/oxide solubility. Antimicrobial function and alloy corrosion rates are not evaluated in simulative biological environments such as artificial perspiration, where harmful bacteria are likely to proliferate and spread.

- Cu release from chemical dissolution of copper oxides does not provide sufficient [Cu^+] to the local environment to kill bacteria within an acceptable timeframe (99.9% killing in under 2 hours [6]). Furthermore, reduction of the corrosion rate for tarnish-resistance below chemical precipitation thresholds also inhibit Cu release to below desirable kill rates (Figure 1.7). A continuously corroding Cu-based alloy is required to facilitate antimicrobial function.
- Cupronickel (Cu-Ni) alloys have both desirable tarnish-resistance and antimicrobial function (Figure 1.6) through Ni-doped copper oxides [85,86] and could be promising antimicrobial alloys. However, Ni is becoming an increasingly common metal allergen [9] and therefore, Cu-Ni alloys may not be suitable as an antimicrobial alloy system and alternative hypoallergenic systems should be investigated.

1.5 Research Overview

1.5.1 Approach

The primary aim of this dissertation is to advance the theoretical understanding of Cu-alloy dissolution as influenced by alloying at the intersection of electrochemical (corrosion) sciences with metallurgical understanding (solid solution alloying) for the purposes of generating a tunable system for potential future antimicrobial surface applications (microbiology / public health). Two (2) primary alloying effects and their combination/synergisms on corrosion will be interrogated: soluble cation release, and insoluble surface films (patina / oxides) with additional attention on the minimum alloying content required for passivation. Based on previous studies of Cu alloys [17,23,26,87], Sn has been identified as useful regarding Cu release, and Al for passivity. For these reasons, Sn and Al have been selected for study.

This approach is targeted to address previously mentioned background issues:

1. Explore notable alloy systems (Cu-Sn, Cu-Al, Cu-Al-Sn) and investigate the effects on corrosion and antimicrobial response as a function of alloy content using elements selected with attributes favorable for Cu ion release (Sn) and corrosion resistance (Al).
2. Select specific amounts of alloying elements within binary and ternary solid solubility limits to avoid precipitation of secondary intermetallic phases and below literature-identified passivity thresholds.
3. Fabricate high-purity model binary and ternary alloys to eliminate potential effects of minor or micro elements used in commercial systems that are impurities or added for mechanical performance and/or corrosion resistance considerations.
4. Employ artificial perspiration as simulative environment for high-touch surfaces as a choice of a relevant environment in lieu of seawater or 3.5 wt% NaCl.
5. Determine the fate of the elements by measuring corrosion rates and quantitatively compare all corrosion products including oxides, soluble ions, and precipitated compounds; using this data to investigate pertinent phenomena (i.e. enhanced release, passivation) as influenced by alloying additions.
6. Develop mechanistic understanding of the influence of alloying Cu with Sn and Al using both novel and standard methodologies such as AESEC, CV, and other diagnostic electrochemical methods.
7. Understand rate-limiting processes and solute-endued passivation of thin and thick films utilizing contemporary passivity theories such as graph theory [74–76], high field model [88,89], the point defect model [90,91], and thick films through Wagner [66] or other rate laws [65,69,72,73,78,79].

8. Use existing literature [45] and high-purity custom alloys to advance knowledge on how M-M and Me-O bonding characteristics affect corrosion and cation release of Cu-based alloys in aqueous environments.
9. Advance theoretical development [65,69,72,74–76,79] regarding alloying passivity, the role of alloying elements in oxide films, and minimum alloying thresholds for passivity.

In this aim, the fate of the solvent and solute alloying elements will be tracked to elucidate relevant operative mechanisms of film composition and morphology and Cu ion release during corrosion in a simulative high-touch environment (artificial perspiration). Cu-based binary and ternary solid solution alloys will be studied as influenced by selected compositions of alloying elements: Sn and Al.

The fate of the elements following corrosion in artificial perspiration is identified in each alloy system. Open circuit corrosion exposures conducted up to 96 and 130 hours determined the fate of Cu, Sn, and/or Al. Corrosion rates were monitored, and individual corrosion products were identified and quantitatively measured. The effects of the individual oxides formed during corrosion were assessed with potentiodynamic and galvanostatic testing in various chemical environments. Released aqueous ion concentrations were measured via inductively-coupled plasma – optical emission spectrometry (ICP-OES) from solution aliquots. Atomic emission spectroelectrochemistry (AESEC) analysis was also utilized to elucidate the fate of Cu in oxides/compounds vs. solution, relevant corrosion mechanisms, and deduce the dominant valence states of soluble Cu in artificial perspiration. Furthermore, mechanistic insight was obtained using simulated Cu and solute-doped surfaces using *ab initio* density functional theory (DFT) methods.

1.5.2 Objectives

The overarching goal is to further scientific understanding of alloying effects and responsible mechanisms pertinent to Cu-based alloy corrosion and cation release in an antimicrobial context. Elements were selected from two classes identified in the literature with opposing effects of promoting dissolution (Sn) and oxide formation (Al). Systematic compositions were selected

at subcritical levels of passivity and solid solution solubility limits. These alloying elements have the potential to form a tunable system balancing Cu release (via Sn) and tarnish resistance (via Al) through strict metallurgical control. The principles of which should be then applicable to any alloy system. In this aim, this dissertation is organized into five main chapters, each with individual objectives:

- Improve our understanding of the effect of Sn for enhanced Cu release, assign responsible mechanisms, and define critical contents of Sn in commercial Cu-Sn-Zn alloys (Chapter 2).
- Interrogate the role of Sn regarding surface films (patina), identify the critical content for complete surface coverage of protective films (passivity), and assign responsible mechanisms of Sn in high-purity model solid solution Cu-Sn alloys isolated from minor and micro-alloying elements of commercial systems (Chapter 3).
- Develop a theoretical framework to determine critical alloying thresholds for alloys with insoluble oxides based on interphase surface energetics to address gaps in knowledge of alloying thresholds for passivity (Chapter 4).
- Investigate critical factors and responsible mechanisms of Al in forming protective layers on aluminum bronze using high-purity binary alloys (Chapter 5).

- Evaluate alloying element interactions for a ternary system (Cu-Al-Sn) as they relate in conflict, concert, or synergy with the individual binary systems (Cu-Sn, Cu-Al) for soluble cation release, surface corrosion products, and corrosion (Chapter 6).

1.5.3 Thesis Organization

The problem statement, introduction to present understanding, unresolved critical issues, and research overview are presented in Chapter 1. Chapter 2 investigates the enhanced dissolution of Cu due to the addition of Sn to the alloy in commercial Cu-Sn-Zn gunmetal alloys. In this chapter, the valence of the soluble Cu ion in artificial perspiration was determined through atomic emission spectroelectrochemistry and the validity of the fate of the elements analysis testing was evaluated and confirmed. Chapter 3 removes the complications of minor and impurity elements in commercial alloy to investigate the role of SnO_2 on the surface corrosion products (patinas) and passivation of high-purity Cu-Sn alloys. The minimum amount of solute element (Sn) in an alloy (Cu-Sn) needed to passivate was found using a new model. This new theoretical framework regarding the passivity thresholds of alloy systems is based on solute enrichment theory and interphase boundary energies of alloys with oxides with no solute cation solubility and is derived fully in Chapter 4. The effect of Al on surface oxides that increased the corrosion resistance of high-purity Cu-Al alloys was investigated in Chapter 5. Finally, the combination and synergies of Sn with Al in FCC Cu on cation release and oxide formation was investigated in Chapter 6. In this chapter, custom-designed antimicrobial testing of high-purity Cu-Al-Sn alloys was carried out and compared against tarnishing behavior in artificial perspiration. Conclusions and suggested future work are presented in the final chapter (Chapter 7).

Tables

Table 1-1. Microorganisms susceptible to the antimicrobial function of high-purity copper surfaces. Greatest reported time to achieve > 99.99% reduction (> 4 log) of inoculated species is reported. Secondary sources: [1,6].

Microorganism	**> 4 log Reduction**	**Comments**	**Reference**
<u>Bacteria</u>			
Acinetobacter species	3 h	Antibiotic resistant, Gram-negative	[92–95]
Bacillus subtilis	30 min	Non-spore, vegetative cells	[96,97]
Brachybacterium conglomernatum	5 min		[21]
Burkholderia species	8 h	Antibiotic resistant	[98,99]
Campylobacter jejuni	8 h	Food poisoning	[100]
Clostridium difficile	30 min	Spores - 48h	[18,101]
Deinococcus radiodurans	1 h	Radiation resistant, DNA repair	[21]
Enterobacter species	24 h	Gram-negative	[93]
Enterococci species	1.5 h	Antibiotic resistant	[25,102–105]
Escherichia coli	2 h	Gram-negative	[102,106–108]
Klebsiella pneumonia	1 h	Gram-negative	[10,92,93]
Legionella pneumophila	1 h	Gram-negative	[24,109,110]
Listeria monocytogenes	1 h		[111]
Mycobacterium tuberculosis	5 d		[92]
Pantoea stewartii	1 min	A disease affecting corn crops	[95]
Pseudomonas species	3 h	Gram-negative	[31,93–95,102]
Salmonella enterica	4 h	Gram-negative	[10,100,112]
Staphylococcus aureus	1 h – 3 h	MRSA, Antibiotic resistant	[19,20,94,102,113]
<u>Fungi</u>			
Aspergillus species	120 h	Spores	[109]
Candida albicans	24 h	Spores	[21,92,109]
Fusarium species	24 h		[109]
Penicillium chrysogenum	24 h		[109]
Saccharomyces cerevisiae	30 s	Brewer's yeast	[21]
<u>Viruses</u>			
Coronavirus	30 min		[11]
Influenza A	6 h		[20,114]
Norovirus	2 h		[115–117]
Bacteriophage	3 h		[118]

Table 1-2. Differences in killing rates (> 99.99% reduction) between Cu-based alloy and stainless steel control specimens for three test organisms: *Escherichia coli*, *Clostridium difficile* and Methicillin-resistant *Staphylococcus aureus* (MRSA).

Min. Cu Content	Alloy	UNS Designation	Killing Time	Species	Ref.
100	Cu	C11000	60 min	*C. difficile*, MRSA	[18,119]
98	Cu-1Fe	C19700	90 min	MRSA	[20,119]
95	Cu-5Sn	C51000	180 min, 24 h	*C. difficile*, MRSA	[18,19]
94	Cu-4Si-1Mn	C87300	180 min	*E. Coli*	[119]
92	Cu-2Zn-1Sn-1Pb	C83300	180 min	*E. Coli*	[119]
90	Cu-10Zn	C22000	60 min	*E. Coli*	[119]
89	Cu-10Ni-1Fe	C70600	60 min	*C. difficile*, MRSA	[18,19]
88	Cu-5Zn-4Si	C83600	180 min	*E. Coli*	[119]
80	Cu-20Zn	C24000	360 min	MRSA	[114,119]
70	Cu-30Zn	C26000	24 h	*C. difficile*, MRSA	[18,19]
65	Cu-18Ni-17Zn	C75200	60 min, 24 h	*C. difficile*, MRSA	[18,19]
58	Cu-32Zn-1Sn-1Pb	C85700	360 min	*E. Coli*	[119]
55	Cu-27Sn-18Ni	C77000	Did not kill	*E. Coli*, MRSA	[119]
89	Cu-5Zn-5Al-1Sn		Did not kill*	MRSA	[26]
0	Fe-18Cr-8Ni	S30400	Did not kill	*E. Coli*, *C. difficile*, MRSA	[18–20,119]

*Alloy did not kill bacteria in the passive state

Table 1-3. *General* common effects of alloying solute elements on Cu-based alloys in seawater relative to pure copper. Biofouling resistance used here as a proxy for antimicrobial function. For details see references: [5,46,47].

			Effect of the Element on:	
Alloying Element	**Cu Alloy**	**Preferentially Released Ion by Corrosion**	**Corrosion Rate**	**Biofouling Resistance (Antimicrobial Efficacy)**
Sn	Tin Bronze	Cu	Increased	Increased
Zn	Brass	Zn	Decreased*	Decreased
Al	Aluminum Bronze	Al	Decreased	Decreased
Ni	Cupronickels	Ni	Decreased	Decreased with flow

* up to 15 wt% Zn

Table 1-4. Selected Standard Gibbs Free Energies of Cu, Sn, and Al Corrosion Products [120–123].

Compound Name		**ΔG^0_{298} (kJ/mol)**
Cu_2O	Cuprite	-147.9
CuO	Tenorite	-127.9
$CuCl$	Nantokite	-119.7
$CuCl_2{\bullet}2H_2O$	Eriochalcite	-655.9
$Cu_2(OH)_3Cl$	Atacamite	-1339.2
$Cu_2(OH)_3Cl$	Botallackite	-1322.6
$Cu_2(OH)_3Cl$	Clinoatacamite	-1341.8
$CuSO_4{\bullet}2Cu(OH)_2$	Langite	-2044.1
$Cu_4(OH)_6SO_4$	Brochantite	-1817.1
$Cu_3(CO_3)_2(OH)_2$	Azurite	-111.2
$Cu_2CO_3(OH)_2$	Malachite	-123.2
SnO_2	Cassiterite	-520.4
Al_2O_3	Alumina	-1581.4
$CuAlO_2$	Copper Aluminate	-868.6
$CuAl_2O_4$	Copper Aluminate	-1695.1

Figures

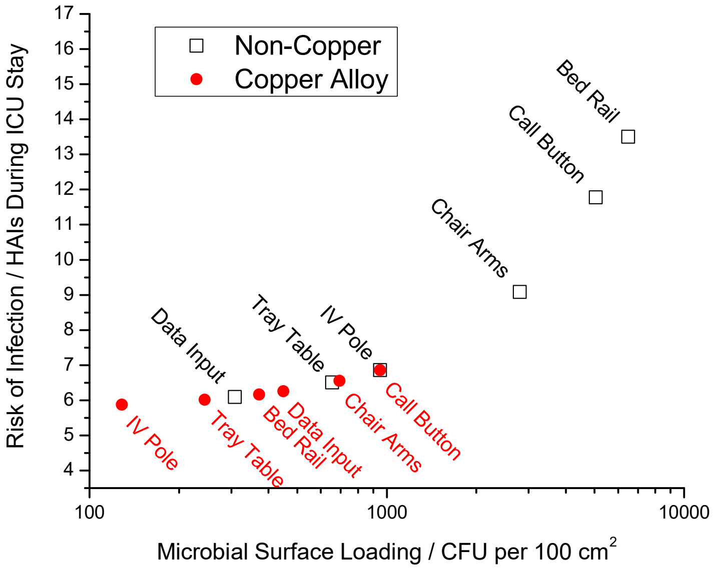

Figure 1.1. Surface loading of microorganisms of various Cu-based and non-Cu-based high-touch hospital surfaces and associated risk of hospital-acquired infection (HAI). Risk of infection taken directly from the number of measured HAI acquired during patient stays in an ICU study. Data from Michels and Michels [1].

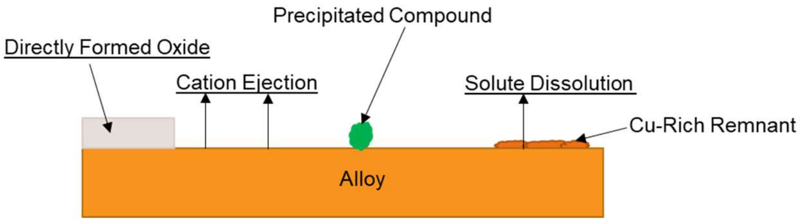

Figure 1.2. Schematic of possible fates of the elements following corrosion of a copper alloy. Possible fates include: oxide formation, direct cation ejection, metal salt precipitation, and preferential solute dissolution, i.e. dealloying or incongruent dissolution.

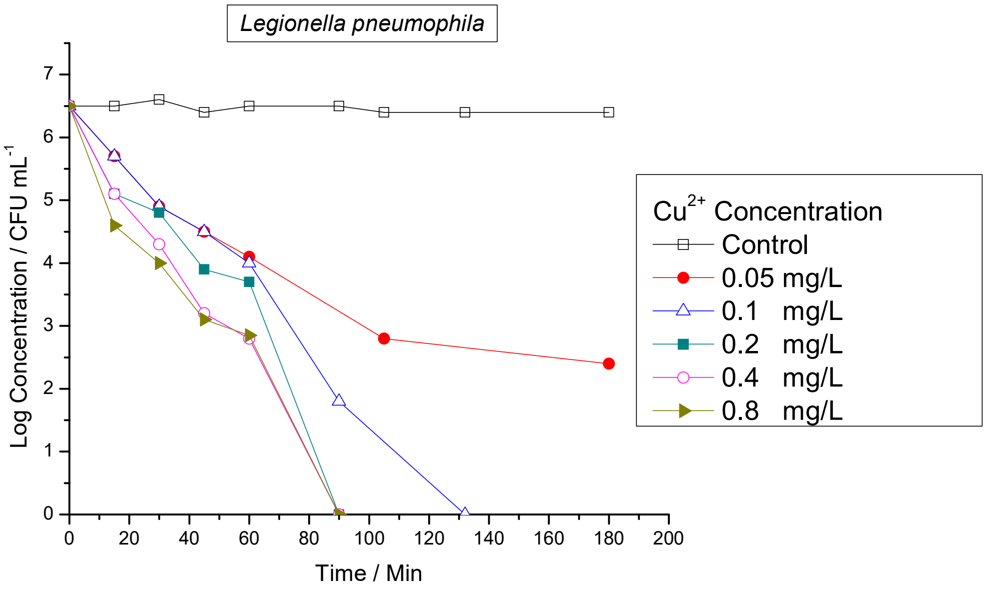

Figure 1.3. Inactivation of *L. Pneumophila* in deionized water with increasing [Cu^{2+}] from $CuCl_2$. Plot reproduced from [24].

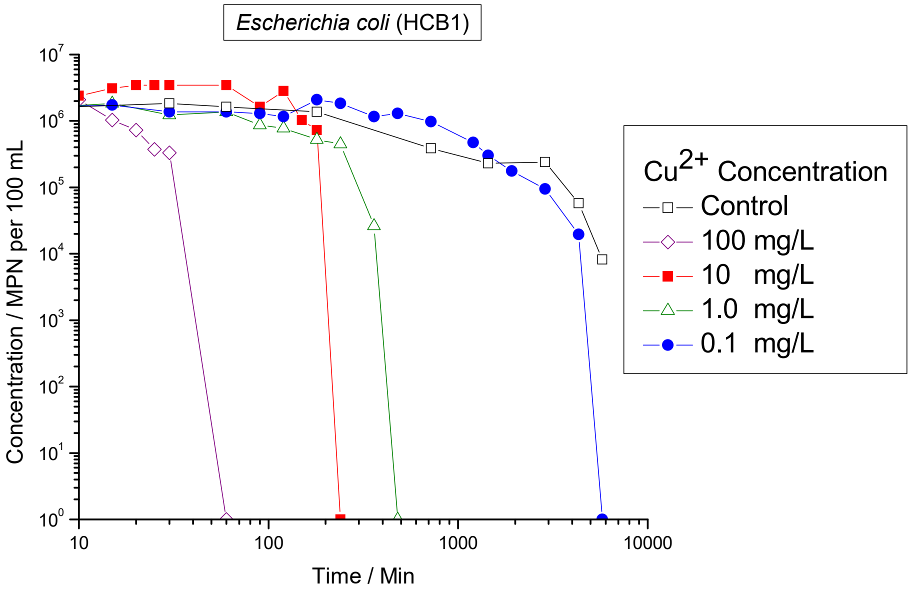

Figure 1.4. The viability of *E. coli* (HCB1) in artificial perspiration solution with increasing [Cu^{2+}] from $CuCl_2$. Reproduced from [26]. MPN – Most Probable Number enumeration method.

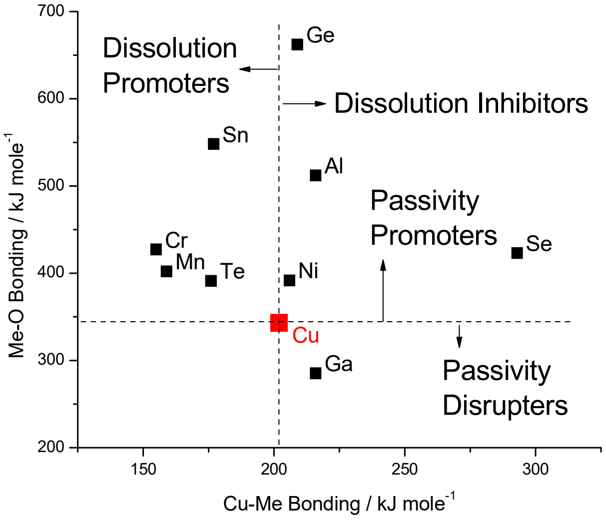

Figure 1.5. Passivity promoting and dissolution moderating alloying elements according to the synergy between the metal-oxygen (Me-O) and Cu-metal (Cu-Me) bond dissociation energies Bond dissociation energy values from reference [124].

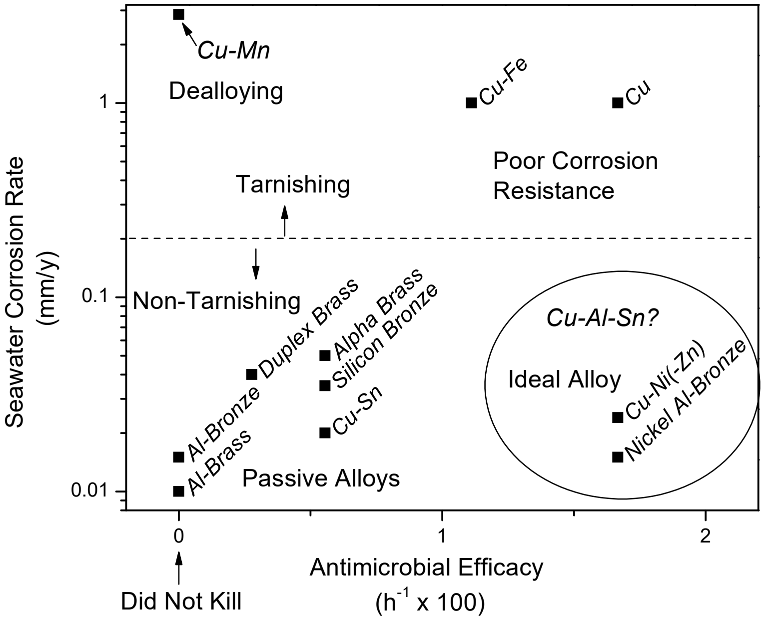

Figure 1.6. Corrosion rate in seawater compared with antimicrobial efficacy (inverse of killing time). Killing time defined as the time (in hours) required to destroy/inactivate 99.99% of bacteria. Ni-containing alloys may cause contact dermatitis from Ni release [9]. Data obtained from Table 1-2 and corrosion rates from [5,46,60].

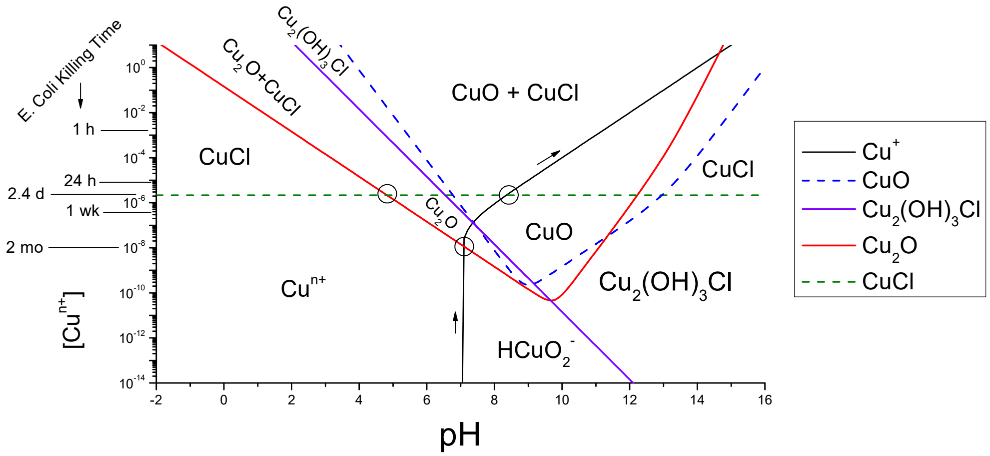

Figure 1.7. Chemical stability diagram [125–127] of copper oxides and chlorides. CuCl [Cl-] estimated from composition of artificial perspiration [48]. *E. Coli* killing times taken from Figure 1.4.

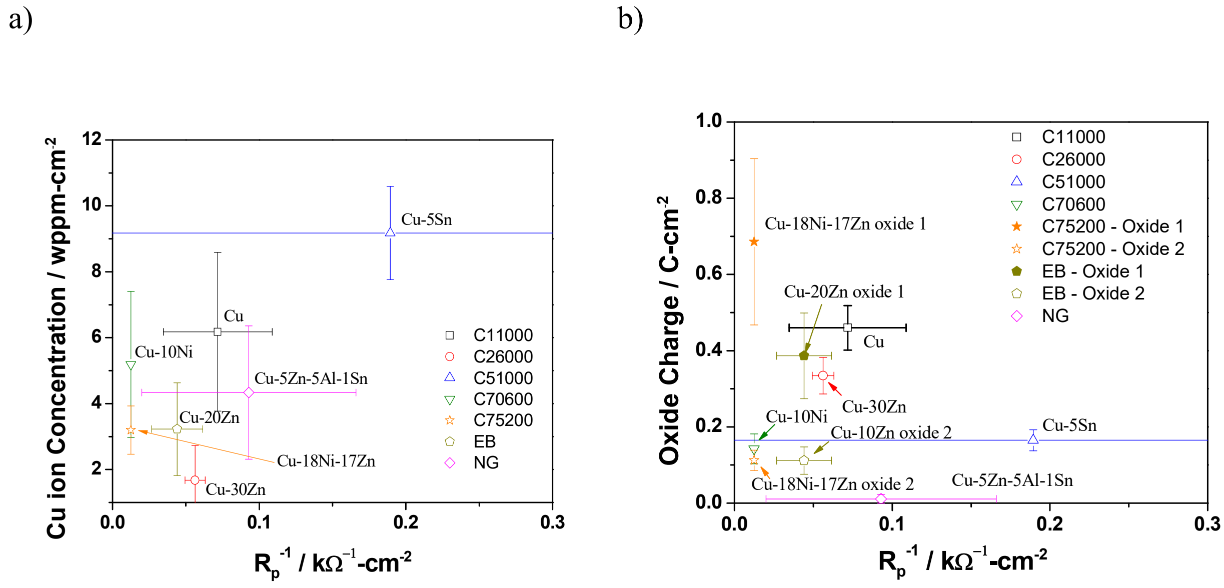

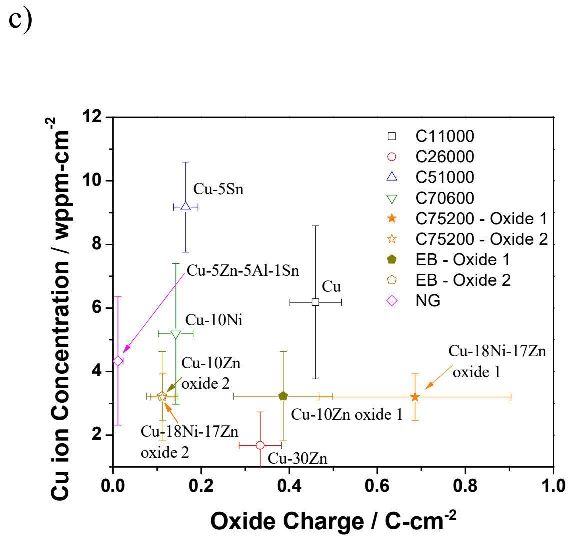

Label	Alloy Composition
C11000	Cu
C26000	Cu-30Zn
C51000	Cu-5Sn
C70600	Cu-10Ni-1.5Fe-1Zn
C75200	Cu-17Zn-18Ni-1Mn
EB	Cu-20Zn-3Si
NG	Cu-5Zn-5Al-1Sn

Figure 1.8. Survey study of Cu alloys following 130 h at open circuit in naturally-aerated artificial perspiration solution demonstrating the relation between a) corrosion rate ($1/R_p$) and Cu ion concentration, b) corrosion rate ($1/R_p$) and charge associated with oxide tarnish, and c) charge associated with oxide tarnish and total Cu ion concentration. Labels are UNS alloy designations, EB and NG are Eco Brass® and Nordic Gold, respectively. Data from Horton *et al.*[17].

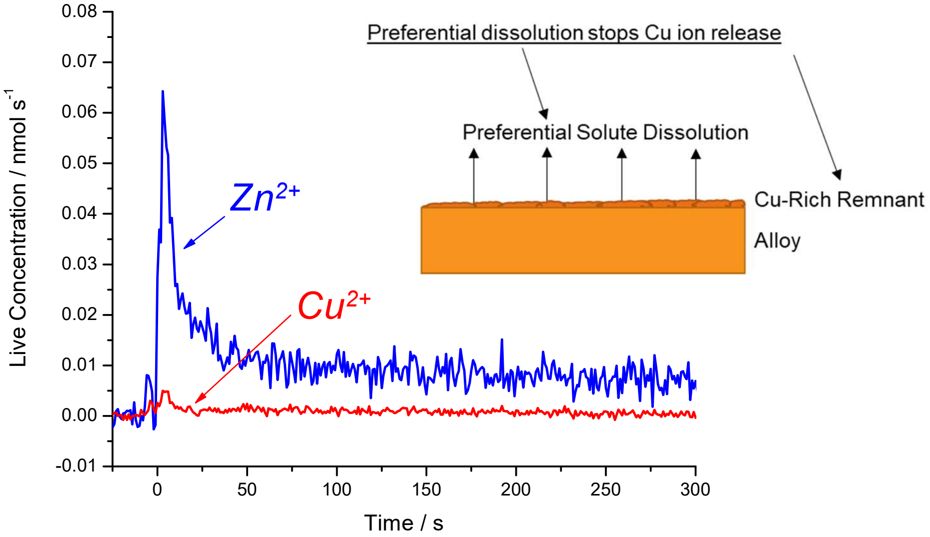

Figure 1.9. Live element-resolved open circuit dissolution of Zn and Cu from Cu-42Zn in laminar flowing simulated tap water measured *in operando* using atomic emission spectroelectrochemistry. Modified and reproduced from [58].

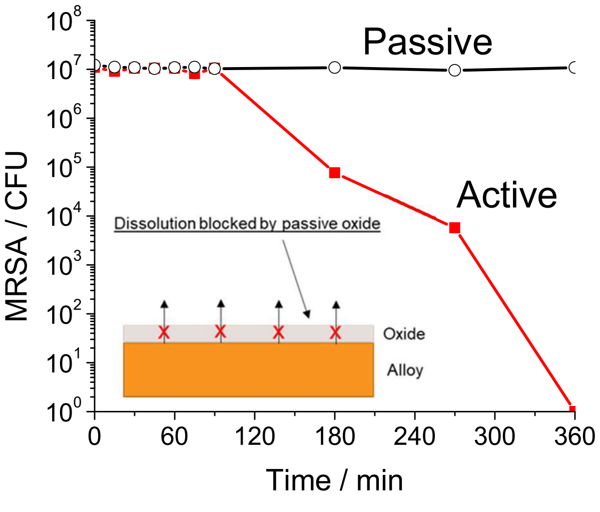

Figure 1.10. MRSA viability on Cu-5Zn-5Al-1Sn alloy in both the passive (7 days in lab air) and active state (freshly polished). Data from Foster *et al* [26].

2 Enhanced Electrochemical Cu Release from Commercial Cu-Sn Alloys: Fate of the Alloying Elements in Artificial Perspiration

Abstract

Commercially pure Cu (Cu), Cu-4.5Sn-0.1Zn, and Cu-9.7Sn-0.1Zn (wt%) were evaluated for corrosion and cation release in modified artificial human perspiration solution. Open circuit corrosion exposures were conducted for up to 130 hours to determine corrosion rate and the fate of Cu and Sn. Released aqueous ion concentrations were monitored via inductively-coupled plasma – optical emission spectroscopy (ICP-OES). *Operando* atomic emission spectroelectrochemistry (AESEC) analysis was utilized to elucidate the fate of Cu, whether in oxides or solution and deduce the dominant valence states, Cu(I)/Cu(II), of soluble Cu in artificial perspiration. Sn was not observed as a soluble ionic species within ICP-OES or AESEC limits of detection (LOD). Corrosion products were characterized using grazing incidence X-ray diffraction (GIXRD), Raman spectroscopy, and X-ray photoelectron spectroscopy (XPS), and quantified with coulometric reduction (CR). Cu-4.5Sn-0.1Zn displayed the highest corrosion rates in artificial perspiration, followed by Cu-9.7Sn-0.1Zn, and then Cu. Primary corrosion products were Cu_2O, with CuCl as an outer solid product, and an inner layer of SnO_2 for Sn-containing alloys. Cu was dissolved as cuprous (Cu^+) ions. Minor Sn alloying in solid solution catalyzed Cu dissolution which is counteracted at higher Sn contents by a passivating layer of SnO_2, achieving complete passivity at 10.3 wt% Sn according to graph theory. Cu-9.7Sn-0.1Zn indicated semi-passive behavior, speculated to be due a SnO_2 layer and close proximity (9.7 wt%) to this critical value for passivation (10.3 wt%). The effect of alloyed Sn as a dissolution promoter for electrochemical Cu ion release, critical Sn contents for passivity, and subsequent implications of antimicrobial function are discussed. Oxidized Zn was not detected above LOD nor demonstrated any measurable effect on corrosion in artificial perspiration.

2.1 Background

2.1.1 Copper as a Functional Antimicrobial Surface

Copper has received renewed interest in corrosion and pathogenic microbiological communities due to recent works which demonstrate its ability to kill/inactivate even antibiotic-resistant so-called ‘superbugs’, such as methicillin-resistant *Staphylococcus aureus* (MRSA), via soluble Cu ion release [6,19,20]. Probable bacteria transmission sites such as high-touch surfaces containing perspiration droplets utilizing Cu alloys showed significantly reduced bacterial counts and nosocomial infections [16,119]. Despite this effect, Cu alloys remain undesirable for use in these high-touch applications due to tarnishing (surface discoloration from an oxide) from hand contact. Soluble ion release is required to maintain antimicrobial function and hence, metallic corrosion is compulsory. A critical balance is needed between corrosion, oxide formation, and ion release: corrosion rates must be sufficient to release enough Cu for desired antimicrobial function with simultaneous adequate suppression of undesired tarnish-forming and/or passivating oxides. Sufficiently thick or ‘passive’ oxides can also reduce bactericidal/fungicidal efficacy [18,21,22]. Alloy content-induced variations of oxide structure, porosity, and composition, while acknowledged, have not been addressed [18,21,22]. These variations play crucial roles as they can potentially completely deactivate antimicrobial action by suppressing copper release rates.

Stainless steel was revealed to be ineffective even with a bactericidal silver ion-containing coating [119]. An ideally-engineered Cu-based alloy would tune passivation and copper ion release as regulated by major and minor alloying. Recently explored [17], the solid-solution Cu-Sn system exhibited enhanced Cu release and concomitant increase in antimicrobial efficacy compared to Cu alone despite a lower bulk Cu content. This system is of particular interest to elucidate the mechanism by which such beneficial alloying elements function.

2.1.2 Antimicrobial Copper Testing

Generally, higher Cu content [18], temperature [19,20], and relative humidity [19,20] increase antimicrobial killing rates on copper surfaces. During so-called ‘dry’ tests (thin electrolyte films), copper can kill pathogenic bacteria within minutes [20]. Bronze (Cu-5Sn) and pure copper had identical kill rates for multiple types of pathogenic bacteria: *S. aureus, E. aerogenes, MRSA, P. aeruginosa,* and *E. coli* [119]. Kill rate testing of MRSA indicated that pure copper and bronze (Cu-5Sn) performed identically (>6 log reduction in 24 h [19]) despite lower bulk Cu content in the bronze. Critically, these studies do not provide a quantifiable dose-response relationship nor establish the mechanism which connects Cu alloy content with antimicrobial efficacy.

The solution chemistries of microbial studies’, e.g., agar, saline, and soy broth [18–22,24], are often selected based on bacterial culture growth and consequently do not address Cu corrosion under realistic high-touch situations despite acknowledging that corrosion is necessary for antimicrobial function. Bacteria growth media are merely physiological buffers that are not representative of simulative and more aggressive high-touch environments and may cause thicker oxides and/or higher corrosion rates. Indeed, environmental specificity potentially alters the observed trends with respect to copper alloying. Therefore, oxide formation and composition, ion valence state, corrosion response, electrolyte specificity, and solution complexing effects are critical to understanding antimicrobial function of Cu-based alloys. Moreover, simulated human perspiration [48] contains known complexing and Cu-chelating[2] compounds [30] and offer a more representative electrolyte for high-touch environments.

2.1.3 Corrosion and Ion Release of Copper Alloys in Simulated Human Perspiration Solution

---

[2] Bioavailable Cu and chelation effects [6,18,27,30], are specifically related to the chemistry of the solution where corrosion trends of an alloy system should be grossly unaffected.

In a recent survey [17], several commercial copper-base alloys were investigated in artificial perspiration solution for corrosion response, soluble cation release, and oxide tarnish behavior. The results of this study established that Cu-Sn alloys possessed enhanced Cu cation release relative to Cu despite having reduced Cu solvent content [17]. Furthermore, by simulating artificial perspiration as an analogue to a high-touch environment in both full immersion [26] and in wetting and drying cycles [23], prior passivation in air or furnace oxidation had a negligible effect on cation release for both pure copper and a tarnish-resistant Cu alloy (Cu-5Zn-5Al-1Sn). This result is likely due to the aggressiveness of the artificial perspiration solution and its Cu-complexing effects [30]. Cu-Sn bronze was also shown to have similar rainfall-induced runoff release as Cu despite having reduced bulk Cu content [55]. This would suggest that Sn alloying would be of interest for potential functional/tunable antimicrobial alloys. Yet, little is known about corrosion of Cu-Sn alloys in perspiration solutions while atmospheric and full-immersion studies on Cu alloys in marine environments are well-established [5,46]. Moreover, systematic effects of Sn alloying content on Cu-Sn alloy dissolution or passivity remain unexplored. Given these findings, this study investigates the Cu-Sn system for its unusual corrosion behavior and enhanced soluble Cu release.

2.1.4 Archeological Bronze Corrosion

Bronze alloys exposed to atmospheric urban and industrial conditions (e.g., statues) usually exhibit protective power law oxide growth in the Wagner regime [128] and are often comprised of three layers: An inner layer of cuprite (Cu_2O), an outer or middle layer of precipitated copper salts, and inner embedded tin oxide residues [128]. These patinas have high proportions of tin in the patina compared to their alloy content [129].

Sn enrichment in the corrosion product layer is a main characteristic of outdoor bronze corrosion [130]. Some copper remains in the patina, but most oxidized Cu is released in soluble form. Sn oxidation products in protective patinas are characterized as insoluble and amorphous or poorly-crystallized [130]. *In vacuo* Raman measurements suggested poorly or non-crystallized compounds with ambiguous attribution of cuprite and/or Sn(IV) oxide vibration modes that display similar characteristic peaks (190-220 cm^{-1}, and 620 cm^{-1}) [129]. Dendritic Cu-13Sn (wt%) demonstrated (in Na_2SO_4, pH 5.8) greater protective patinas covering dendrites of higher Sn content compared to the interdendritic regions (EDS determined Sn/Cu: 0.30 *vs*. 0.16 overall) [131]. Archeological studies of bronze provide critical insight into the factors governing the behavior of Cu-Sn alloys. However, because of their forensic nature, these studies lack quantification of copper release rates or the fate of the elements.

2.1.5 Rainfall-Induced Runoff of Cu: Bronze Alloys Undergoing Atmospheric Corrosion

Bronze panels (Cu-6Sn) exposed to unsheltered atmospheric environments release comparable amounts of soluble Cu in rainfall-induced runoff[3] compared to Cu sheets despite lower bulk Cu content [55,56]. Tin was not found in the form of soluble products when exposed in these conditions as evidenced by a lack of measurable tin content in captured rainwater runoff [55]. In marine atmospheric conditions bronze (Cu-4Sn) forms loosely adherent product films which were observed to flake and spall from the surface [132]. Sn was found in these studies to be retained at the inner oxide/alloy interface via EDS measurements. Atacamite ($Cu_2(OH)_3Cl$) compounds were all found to be on the external oxide/fluid surface. The mechanism of flaking of bronze corrosion product is attributed to voluminous transformation of nantokite (CuCl) to atacamite ($Cu_2(OH)_3Cl$)

---

[3] Rainfall-induced runoff, measured by collecting the rainwater (artificial or outdoor atmospheric exposure), are related mostly to the chemical dissolution of the previously formed oxide in the outdoor environment, rather than electrochemical corrosion processes [27].

[54]. Studies on the influence of chloride deposition rates as an environmental severity indicator on bronze found Sn retained as an internal layer at the alloy/patina interface [54]. Tin enrichment at the oxide/alloy interface was confirmed but oxidized versus metallic tin could not be differentiated [54]. Increased corrosion damage severity was shown with increased Cl^- loading. However, Cu-4Sn showed significantly greater corrosion rates (38 g m^{-2} y^{-1}) when compared to pure copper (24 g m^{-2} y^{-1}) during the first year. Bronze and pure copper showed comparable rainfall-induced runoff release of soluble Cu(I)/Cu(II), 1.0 and 1.4 g m^{-2} y^{-1}, respectively. For comparison, runoff values of Cu(I)/Cu(II) from Cu sheet, both freshly exposed and 200-year pre-patinated Cu, showed runoff rates of 1.5 and 1.3 g m^{-2} y^{-1}, respectively [27]. These runoff rates remained fairly stable over time and were related to the chemical dissolution of the oxide in the dilute rainwater environment, given high Cu_2O solubility ($K_{sp} = 2.6 \times 10^{-2}$ [17]) [27]. The current body of work surrounding Cu-Sn corrosion characterizes product films and corrosion rates but does not investigate direct cation release by oxidative processes. Cation release monitored from atmospheric exposure studies, however, is mostly due to chemical dissolution from pre-patinated surfaces rather than direct cation ejection during electrochemical dissolution. The effect of Cu-Sn solid solution and its role of Cu(I)/Cu(II) release remains unaddressed. Additionally, most published corrosion studies investigate corrosion on time-scales (years) not directly relevant to those of interest for antimicrobial function (hours/days).

The objective of the work presented herein is to monitor the corrosion response, the fate of cations, and oxide growth, as they relate to Sn alloying content. The opposing roles of Sn as a passive film former and as a dissolution promoter is investigated. Three commercial alloys: Cu, Cu-4.5Sn-0.1Zn, Cu-9.7Sn-0.1Zn (wt%), and Sn were evaluated in modified simulated human perspiration solution [48] for up to 130 hours to determine the complete fate of the elements in a simulative high-touch environment.

2.2 Experimental Procedures

2.2.1 Materials

Commercially pure Cu (99.9 wt%, UNS C11000), Cu-4.5Sn-0.1Zn (UNS C51000), Cu-9.7Sn-0.1Zn (UNS C52480), and commercially pure Sn were evaluated. The wrought alloy sheets were obtained from commercial suppliers and sectioned into roughly 2.5 cm x 2.5 cm pieces. Alloy compositions are given in Table 2-1. The compositions of each commercial alloy were evaluated using ASTM E478 [133]. For comparison of alloy behavior without impurities (Zn or otherwise), a high-purity model binary alloy Cu-10Sn (wt%) was fabricated via arc-melting. Alloy constituents were of 99.99% elemental purity by weight. Solid solution was facilitated by heat treatments and verified with X-ray diffraction (not shown). Selected data is presented in figures to highlight the effect of Sn, discussed later, rather than impurities and other minor alloying in the commercial Cu-Sn system. Simulated human perspiration solution (Table 2-2) was used as an appropriate analogue to a high-touch environment where copper alloys may be of interest. This solution is based on the BS EN 1811:2011 standard [48]. In addition, complexing and non-complexing buffers at the same pH (6.5) were prepared. Quantitative cation content in oxides (for AESEC) was facilitated by citrate buffer solutions (CBS), which were prepared from mixed 0.1 M solutions of citric acid ($C_6H_8O_7$) and trisodium citrate ($Na_3C_6H_5O_7$) solutions to achieve a pH of 5.00 ±0.1. Non-complexing boric acid buffer at the same pH as artificial perspiration was prepared from mixing solutions of 0.1 M boric acid (H_3BO_3) and 0.1 M sodium tetraborate ($Na_2B_4O_7$), to achieve a target pH of 6.50 ±0.05. A borate buffer (pH 8.40 ±0.05) was prepared from 0.11 M boric acid (H_3BO_3) and 21 mM sodium tetraborate ($Na_2B_4O_7$) for coulometric reductions at a pH where existing Cu oxides are stable before reduction [126]. Buffer solutions of citric/citrate or boric/borate were deaerated for a minimum of one hour by grade-5 pure N_2 gas bubbling prior to each test. Electrochemical cells were also purged with grade-5 nitrogen gas for at least 10 min prior to deaerated experiments with continuous bubbling throughout the duration of the test.

2.2.2 Methods

Cyclic Voltammetry

Cyclic voltammetry scans were conducted at sweep rates of 10 mV/s in deaerated boric acid buffer (pH 6.5) as well as borate buffer (pH 8.4) from -1.145 to +0.350 V_{MMSE}. Prior to the first sweep, samples were polarized to $^{-}1.4$ V_{MMSE} for 10 min to reduce any air-formed oxide on the surface.

On-line Operando AESEC Measurements

A schematic description of this experimental methodology is given in Figure 2.1. *Operando* Atomic Emission Spectroelectrochemical (AESEC) measurements were conducted in a custom-designed 3-electrode 2-compartment flow cell using a Pt counter (5 cm^2) and Ag/AgCl (sat. KCl) reference electrode. The flow cell working electrode area was $A = 1.0$ cm^2, and a flow rate $f = 3.0$ mL min^{-1} was used. Convolution calculations of the applied current compensating for the flow condition are provided in detail by the authors in a previous publication [134]. The details and capabilities of this technique are outlined elsewhere [135–138]. Briefly, an electrochemical flow cell's effluent stream is connected to an ICP-AES (Horiba Jobin Yvon, Ultima 2™). A Gamry Reference 600™ potentiostat was used to control applied current and monitor the potential. Simultaneous measurements of applied current and downstream ion concentration are obtained under open circuit and galvanostatic control. Cu, Cu-4.5Sn-0.1Zn, and Cu-9.7Sn-0.1Zn samples were subjected to 10 min of open circuit in synthetic perspiration solution, followed by a 20-min anodic pulse of 0, 5, 20, or 80 µA/cm^2 during which Cu, and Sn ion release, and potential, were recorded. These time-frames and currents were selected to optimize the downstream signal for this experimental setup. After release of galvanostatic control, samples were allowed to stabilize for 10 min before switching the influent electrolyte to a deaerated CBS to chemically dissolve and therefore quantitatively assess corrosion product films. CBS was used due to its low corrosion rate of Cu and proven ability to chemically dissolve Cu oxides [134] without dissolving oxidized Sn. Oxidation of Sn comprised only a small portion of total current. Cu signal was detected by monochromator at the wavelength of 324.75 nm; Sn and Zn signals were detected by polychromator at 235.49 nm and 213.68 nm, respectively. Cu ion calibration standards were 20, 40, and 60 ppb in artificial perspiration solution and 20, 40, and 100 ppb in citrate buffer solution (CBS, pH 5.0 ±0.1). The three-standard calibration was finished with correlation coefficient $R^2 \geq 0.99$. The detection limit was defined as three times the standard deviation of the blank measured over 100 s, with a 1 s integration time per point.

Artificial Perspiration Exposure Conditions

Alloy samples were polished with successive grades of abrasive SiC grit paper up to 1200 grit, during the final stage samples were polished under ethanol. Samples were then rinsed and stored in ethanol until placed into 3-electrode electrochemical full-immersion exposure cells. Sample exposure area was 0.8 cm^2. Cells were cleaned with 0.1 M HCl prior to each experiment and thoroughly rinsed with deionized water. For soluble ion concentration analysis: 300 ml (± 2.5 mL) of artificial perspiration were added to cells. Exposures were monitored and extracted where appropriate at specified time-points up to 130 hours. Electrochemical potentials in halide-containing solutions were measured using saturated calomel electrodes (SCE) fitted with Luggin capillary tips. Reproducibility of experiments was determined to be satisfactory as most experiments were replicated at least once and good agreement of trends was observed among multiple separate methodologies using independent samples. Corrosion rates were measured with mass loss and impedance circuit fits. The total anodic charge density from these results was then compared to the amount of corrosion products formed and soluble ions released, and all forms of metal cations were converted to charge density. Corrosion products were identified using grazing incidence X-ray diffraction (GIXRD), Raman spectroscopy, and X-ray photoelectron spectroscopy (XPS).

Corrosion Rate: Mass Loss and Electrochemical Impedance Spectroscopy (EIS)

Mass loss measurements were conducted according to ASTM G1 [139]. Mass loss (M_1-M_3) values were obtained by measuring mass of samples before (M_1) and after exposure (M_2) and again following a 2-3 min 6 M HCl cleaning step to remove both Cu, Zn, and Sn corrosion products (M_3). Base metal removal rates were determined to be negligible during cleaning as evaluated with a freshly polished sample. For charge analysis, congruent dissolution was assumed with equivalent weights of 63.6 g/equiv., 60.1 g/equiv., and 57.0 g/equiv. for Cu, Cu-4.5Sn-0.1Zn, and Cu-9.7Sn-0.1Zn, respectively.

Electrochemical impedance spectroscopy (EIS) measurements were performed on Gamry® Instruments REF600 potentiostats. Impedance was measured at 8 points per decade from 100 kHz to 1 mHz. EIS analysis and model circuit fit was performed using ZView® and Gamry® software. An equivalent DC circuit (Figure 2.2) was simulated to determine the zero frequency (DC) limit of the impedance spectra which can then be related to the polarization resistance of the electrochemical system. Values were assigned to the circuit parameters which best fit the experimental data. A representative example fit of this circuit is given in Figure 2.2. Constant phase elements (CPE) were used in place of ideal capacitors in this circuit. The Warburg diffusional impedance (Z_D) is defined as:

$$Z_D = R_D \frac{\tanh\left(B_D\sqrt{j\omega}\right)}{B_D\sqrt{j\omega}}$$ Equation 2.1

where j is the imaginary unit, ω is the angular frequency, and R_D is the zero-frequency response of the Warburg element (under AC conditions) and is defined as follows:

$$R_D = \frac{B_D}{Y_D}$$ Equation 2.2

Y_D is the admittance, and the definition of the parameter B_D:

$$B_D = \frac{\delta}{D^{½}}$$ Equation 2.3

where δ is the Nernst boundary layer or rate-limiting product layer thickness and D is the average value of diffusion coefficients of the rate-determining diffusing species. The polarization resistance (Rp) defined for this system was as such:

$$R_P = R_{ox} + R_{ct} + R_D$$ Equation 2.4

R_{ox} and R_{ct} are the oxide resistance and charge transfer resistance of the system, respectively. The polarization resistance is inversely related to the instantaneous corrosion rate through a well-known Stern-Geary expression [140]. Based on inspection of potentiodynamic polarization data (not presented), an assumed Stern-Geary constant value of B = 0.025 V was used for charge analysis which also provided a best fit for comparison with mass loss results. The total oxidation charge (Q_{EIS}), as estimated from EIS, expressed as charge, was calculated:

$$Q_{EIS} = \int \frac{B}{R_P} dt$$ Equation 2.5

where dt is the time interval of interest. A total integration from all EIS-derived instantaneous corrosion rates was considered for the total anodic charge. An electrical equivalent circuit sensitivity study was performed to evaluate the relative influence of various circuit element values on the impedance response. Selected parameters were ranged independently while holding others constant surrounding a best fit as determined by fitting software.

Solid Corrosion Products – Quantification

Coulometric (galvanostatic) reductions (CR) were performed on Princeton Applied Research PAR273A potentiostats. Samples were removed from exposure cells and repositioned to chloride-free cells where constant current of -20 µA was applied to an exposed electrode area of 0.8 cm² (-25 µA/cm²). Reductions were performed in a deaerated chloride-free borate buffer (pH 8.4) with mercury/mercurous sulfate reference electrodes also fitted with Luggin capillary tips. The amount of corrosion product expressed as charge (Q_{CR}) was calculated from CR by the expression:

$$Q_{CR} = i_{app} \times t_{red}$$

Equation 2.6

where i_{app} is the applied cathodic current density, and t_{red} is the reduction time evaluated from first-derivative analysis. Reduction times of individual corrosion products were evaluated based intervals of the maxima of the first derivate (w.r.t. time) of the CR plots for each reduction wave.

Solid Corrosion Products - Molecular Identity

Crystalline products were identified using grazing incidence X-ray diffraction (GIXRD) using a PANalytical X'Pert diffractometer with copper Kα radiation. Incident grazing angle gave optimal signal/noise at ω=0.5° with a 10 mm width limiting mask. 2Θ ranged from 20 to 100°. Compounds were identified by comparison to powder diffraction database (ICDD® PDF-4+). Detection limits of crystalline compounds for this instrument and methodology are approximately 5 vol%.

Raman spectroscopy measurements performed post-exposure were acquired using a Renishaw InVia Raman microscope, utilizing a 514 nm line of an argon laser with 180° back scattering geometry and a 3000 l/mm grating. For compound identification, Raman spectra were compared with prepared in-house cold-pressed powder samples of known molecular identity and structure. To avoid thermal heating and conversion of sample corrosion products by laser illumination, low laser intensities with long (~minutes) acquisition times were used.

X-ray Photoelectron Spectroscopy (XPS) was also employed to investigate the corrosion products formed. A Thermo-Scientific K-Alpha™ XPS system was equipped with an Al Kα monochromatic X-ray source and an Ar ion gun (3 KeV) for sputtering. Sputter rates were 0.3 nm/s using a SiO_2 sample of known thickness. High-resolution scans were taken with a pass energy of 20 eV and a spot size of ~0.5 mm^2. Au $4f_{7/2}$ was used as an energy reference assigned to 84.0 eV. Peak fits were made using a Shirley background and a Gaussian-Lorenzian shape. Spin orbit energy splits were set as the only constraint with all other parameters unconstrained for the best software fit.

Release of Cu and Sn - Ions in solution

A Thermo Scientific™ iCAP 6000 inductively-coupled plasma optical emission spectrometer (ICP-OES) was used for solution ion concentration determination. Aliquot samples taken from exposure cells at specified time points were stored and later directly nebulized into the plasma. Acidification was not performed on solution samples[4]. Data points are averaged values of three measurements per aliquot with appropriate statistical variances applied to combine values of all measured wavelengths. Measured Cu lines were 2043, 2178, 2247 Å. Measured Sn lines: 1899

---

[4] Acidification did not produce any measurable differences in detected solution concentrations of Cu. More information of ICP methodologies employed, including comments on acidification, can be found in [17].

and 2243 Å. Limits of detection (LOD) were defined as the measured value of a blank sample of artificial perspiration (no Cu metal exposure) with three times the standard deviation added to this value. Zn was not measured as the maximum anticipated amount was below instrument limits (<1 ppb). LOD for Cu was 15 ppb, and 40 ppb for Sn. Measured soluble Cu and Sn was also converted to charge (Q_{ICP}), and evaluated as follows:

$$Q_{ICP} = \sum \frac{\rho n F V}{A.W.} \quad \text{Equation 2.7}$$

where rho is the measured mg/L (ppm) value measured from photoemission intensity correlated to a calibration curve of serial-diluted prepared concentrations, n is the soluble ion valence. F is Faraday's constant (coul/equiv.), V is the solution cell volume (L), A.W. is atomic weight of the element (mg/equiv). Soluble ion concentration measured via ICP-OES were reported as charge using a Faradaic conversion with a Cu ion valence state assumed to be cuprous (Cu^+, n=1). This assumption was validated by *operando* AESEC studies, the results of which are presented below.

2.3 Results

2.3.1 Cyclic Voltammetry in Non-Complexing Buffer

Cyclic voltammograms in deaerated boric acid buffers at pH 6.5 and pH 8.4 are shown in Figure 2.3. The first sweep (Figure 2.3a) and the third sweep (Figure 2.3b) are presented. This buffer is at the same pH as the artificial perspiration solution: pH = 6.5. An initial anodic peak was present on all alloys followed by an increasing current with increasing potentials indicating limited film induced mitigation. This E-I behavior was likely due to direct ion ejection during oxidation since all alloys demonstrate only one cathodic peak ($E = {}^{-}0.4\ V_{SCE}$) attributed to cuprous reduction (Figure 2.3). Cu-Sn alloys had greater anodic current densities compared to either Cu or Sn. Anodic current densities were highest for Cu-4.5Sn-0.1Zn for all cycles when compared to the other alloys. In the first cycle (Figure 2.3a) the lowest current density for the anodic peak was found on Cu-

9.7Sn-0.1Zn. In the third cycle (Figure 2.3b) Cu-9.7Sn-0.1Zn had higher current densities in the first anodic peak compared to Cu. Commercial-purity Sn sheet showed initially high anodic activity in the first cycle (Figure 2.3a) but by the third, it became relatively insensitive to potential (Figure 2.3b), suggesting a passive film.

In contrast, at pH 8.4 (Figure 2.3c) all alloys indicated clear oxidation and reduction of both CuO and Cu_2O with substantial 'thick-film' passivation. Cu-4.5Sn-0.1Zn again exhibited the greatest anodic current densities at both pH 6.5 and 8.4. Cu-9.7Sn-0.1Zn displayed lowered anodic reaction rates and a broad reduction peak. Cupric reduction was observed ($E= {}^{-}1.0\ V_{SCE}$) at pH 8.4 for all alloys (Figure 2.3c). The high purity Cu-10Sn alloy demonstrated nearly identical behavior to Cu-9.7Sn-0.1Zn.

2.3.2 Atomic Emission Spectroelectrochemistry – AESEC

AESEC-measured downstream soluble Cu for all samples at an applied current of 80 $\mu A/cm^2$ is presented in Figure 2.4a. AESEC results for all applied currents are shown for the Cu-9.7Sn-0.1Zn alloy in Figure 2.4b. Solid lines correspond to the measured mol/s of Cu while dashed lines are calculated ideal mol/s assuming 1:1 release (i.e. applied e^- mol/s = Cu mol/s) and accounting for the flow-cell condition [134]. This calculation accounts for the baseline open circuit corrosion rates which are determined from the control ($i_{app} = 0\ \mu A/cm^2$). Chemical dissolution in flowing deaerated CBS of mol/s of oxides pre-formed in perspiration were integrated over time to provide a quantitative measure of total Cu corrosion products and are indicated in mass balance calculations in Figure 2.5.

Nearly all of the applied anodic current led directly to soluble Cu release. Cu and Cu-Sn alloys indicated significant direct release of cuprous ions in comparison to corrosion product formation in artificial perspiration (Figure 2.4). Notably, Cu-9.7Sn-0.1Zn demonstrated the greatest release of Cu for the same applied currents than both Cu or Cu-4.5Sn-0.1Zn (Figure 2.4a). Greater moles of cuprite formed on Cu compared to Cu-4.5Sn-0.1Zn and Cu-9.7Sn-0.1Zn (see Figure 2.5) for the same imposed current densities. Though, all samples displayed increased moles of corrosion product with applied current which was about 5-10% of the total at all applied currents. As demonstrated in Figure 2.5, mass balance revealed that soluble cuprous ions (Cu^+) and insoluble cuprous oxide (Cu_2O) were the dominant forms of cations produced in artificial perspiration due to the close correlation between applied charge (e^-) converted to moles (mol/s) compared to total moles of measured ions (i.e. 1:1 correlation of applied moles of e^- vs. sensed moles of Cu, assuming Cu(I) oxidation). SnO_2 is insoluble in both artificial perspiration CBS and thus was not detectable with AESEC.

Applied currents yielded corresponding anodic potentials which followed Tafel behavior with a slope of ~76 mV/dec as shown in Figure 2.6. Cu required greater polarization compared to Cu-Sn samples (ΔE~25 mV) at identical applied anodic currents suggesting that Sn promotes anodic dissolution.

2.3.3 Interfacial Impedance and Corrosion Rate at Open Circuit

Alloys with tin exhibited more noble open circuit potentials (~+50 mV after 48 h) than Cu in artificial perspiration as conveyed in Figure 2.7. Cu decreased its open circuit potential after 24 hours in solution by ~80 mV while those alloys with tin retained higher OCPs which remained fairly constant after 12 hours of exposure. An identical elevation in potential was observed for the high-purity sample as well (Figure 2.7).

Visual appearance and secondary electron images of the outer surface of alloys after 130 h in artificial perspiration are presented in Figure 2.8. Uniform dark brown corrosion products were present for both commercially Cu (Figure 2.8a) and Cu-9.7Sn-0.1Zn (Figure 2.8c). Darker brown corrosion products were observed on Cu-4.5Sn-0.1Zn (Figure 2.8b). Broken areas on product films were observed on Cu (Figure 2.8a) as well as Cu-4.5Sn-0.1Zn (Figure 2.8b) with greater deterioration of surface layers compared to Cu-9.7Sn-0.1Zn. Cu-9.7Sn-0.1Zn, did not demonstrate corrosion product film breakage which correlated with lower corrosion rates compared to Cu-4.5Sn-0.1Zn (Figure 2). All alloys displayed evenly distributed particles (~100 nm) containing Cu and Cl (EDS, not shown) as shown in Figure 2.8c. Disruptions in the continuous layer (ascribed as Cu_2O via EDS), were accompanied by greater Cl-containing precipitates (Figure 2.8a and b), likely atacamite ($Cu_2(OH)_3Cl$, or a structural polymorph) formed during sample drying. A cracked inner layer was observable in Figure 2.8b and the edge of Figure 2.8c is rich in Sn and O (EDS not shown), which was ascribed to an inner layer of SnO_2. This inner layer is strongly suggestive of mud-cracking of a hydrated compound upon drying following sample extraction and exposure to SEM chamber vacuum.

All impedance data showed evidence of at least two time-constants with diffusional impedance behavior at lower frequencies (see Figure 2.9). An evaluation of the sensitivity of the equivalent circuit employed (Figure 2.10) demonstrates that a diffusion process was controlling near or approaching the zero-frequency-limit (under AC conditions) as those parameters (B, and Y_{diff}) which relate to the Warburg diffusional impedance element (Eq. 2.1-3) entirely govern the sensitivity of the low frequency response and consequently, the corrosion rate. The dominant mechanism is implied to be diffusion controlled. Figure 2.11 demonstrates that inverse polarization resistances obtained from impedance fits and using Eq. 2.4 showed two regimes. Cu and Cu-9.7Sn-0.1Zn showed an initial higher corrosion rate ($B/R_p = \sim 4$ $\mu A/cm^2$) followed by gradual decline over time to 1 and 2.5 $\mu A/cm^2$, respectively. Cu-4.5Sn-0.1Zn exhibited higher corrosion rates (9 $\mu A/cm^2$) than other alloys with gradual decline which stabilized after 48 hours (~4.5 $\mu A/cm^2$). All alloys' corrosion rates remained relatively constant after 48 hours (Figure 2.11). Cu-4.5Sn-0.1Zn showed the highest corrosion rate as measured by both mass loss and EIS circuit fits (Figure 2.11). In AESEC experiments, open circuit corrosion rates of Cu-4.5Sn-0.1Zn in perspiration were also higher than commercially pure copper (Figure 2.4a).

2.3.4 Corrosion Product Quantification after Open Circuit Exposure

Coulometric reduction curves following exposure to artificial perspiration are shown in Figure 2.12. Several reduction waves were observed indicative of multiple corrosion products followed by a final plateau associated with electrolyte reduction (i.e., hydrogen evolution reaction - HER). The reduction times and plateau potentials for corrosion products' reductions on each alloy are shown in Figure 2.13. Reduction waves generally had increased reduction time with increasing exposure times. Cu (Figure 2.12a) in these time scales showed the greatest product thickness (i.e. greatest reduction charge) at 48 hours. Product thickness increased monotonically on Cu-Sn alloys as a function of increased exposure time (Figure 2.12b and c). Cu-4.5Sn-0.1Zn indicated relatively large (2.2 Coul/cm² at 130 h) total product thickness as a function of increasing exposure time. The anodic charge densities of individual corrosion products are given in Table 2-5. Assignments are justified in the next section. Considering analysis of the third wave ($E_{red} < {}^{-}1.1$ V_{MMSE}, as SnO_2 reduction), the Sn content in the product layer of Cu-4.5Sn-0.1Zn was negligible until 24 hours; after which Sn accounted for approximately 40% of the total charge of the product layer (Table 2-5). The greatest amounts of each corrosion product were found on Cu-4.5Sn-0.1Zn. In contrast, Cu-9.7Sn-0.1Zn displayed far less corrosion product formation after 130 hours (0.4 Coul/cm²) compared to Cu-4.5Sn-0.1Zn (2.2 Coul/cm²).

Cu-9.7Sn-0.1Zn exhibited parabolic growth of corrosion products ($Q=0.0324\bullet t^{1/2}$, Figure 2.19d). The first reduction wave ($E_{red} > {}^{-}0.8$ $V_{MMSE,}$ CuCl) was far less pronounced (Figure 2.12c) for Cu-9.7Sn-0.1Zn. The relative amounts of Sn in all corrosion product layers remained fairly stable over time: the product charge was ~60% Sn (Table 2-5). It is worth noting that the higher ratio of Sn in the product layer correlated with the higher Sn content of the alloy. The total analysis of all reduction times (t_{red}) indicated markedly less corrosion products on Cu-9.7Sn-0.1Zn.

2.3.5 Corrosion Product Molecular Identity

A summary of the compounds identified as solid corrosion products and methods used is given in Table 2-3. A list of the measured photoelectron peaks and X-ray generated Auger peaks and their assignments based on literature-obtained values [30,141–146] can be found in Table 2-4. The three solid corrosion products identified herein were nantokite (CuCl), cuprite (Cu_2O), and oxidized Sn (SnO_x) assumed to be cassiterite (SnO_2). The identified corrosion products with their decreasing thermodynamic reduction potential order (E_{red}: CuCl > Cu_2O > SnO_2) were completely consistent with these three assignments when considering potential reduction plateaus in coulometric reduction (Figure 2.12).

Nantokite – CuCl

Evidence of CuCl was indicated on Cu-4.5Sn-0.1Zn by one peak at ($2\Theta = 28.5°$, Cu K_α) utilizing GIXRD and is shown in Figure 2.14. This line is the most intense diffraction peak for nantokite [PDF: 00-006-0344, (111) plane]. XPS also revealed Cl (2p orbital) on the as-introduced surface and lightly sputtered (~20 nm) surface (not shown). From this evidence the product is assumed to be nantokite (CuCl). The potential plateau feature above -0.8 V_{MMSE} (Figure 2.12) assumed to be CuCl was present on all alloys. However, this product may not have been strongly observable with GIXRD due to its small amount (<5 vol%). CuCl cannot be confirmed by Raman spectroscopy (Figure 2.15) as CuCl easily degrades through thermal heating even with low laser intensity approaching instrument noise levels [147].

Cuprite – Cu_2O

The primary solid corrosion product for all three alloys was cuprous oxide (Cu_2O). This product was observed with all techniques employed (Table 2-3). Raman spectroscopy (Figure 2.15) revealed only Cu_2O the peak centered at 535 cm^{-1} is due to a Cu-OH vibration in defective Cu_2O [148] and therefore was not present in the prepared powder reference. GIXRD (Figure 2.14) verified cuprite formation for all alloys. Cuprite formation was greatest for Cu-4.5Sn-0.1Zn (Figure 2.13). X-Ray excited Auger Cu LMM transition photoelectric lines (Table 2-4) validated that oxidized Cu is in the cuprous state [30,141–146], together with the absence of the characteristic cupric 2p shift and shake-up satellite peaks in XPS which further confirmed the presence of cuprous oxide.

Cassiterite – SnO_2

Direct evidence of oxidized Sn was only observed using XPS (Figure 2.16) measured on a sample of Cu-4.5Sn-0.1Zn corroded for 24 hours in artificial perspiration at open circuit. The sample was stored with desiccant during transport and tested within 24 hours of extraction to avoid conversion of corrosion products in ambient air (e.g., $CuCl \rightarrow Cu_2(OH)_3Cl$). A pair of energy-shifted 3d photoelectron peaks assigned to oxidized Sn was observable on the corroded sample and following sputtering (~250 nm). Metallic Sn was also detected after sputtering indicating close proximity to the oxide/alloy interface. Signal intensity from oxidized tin greatly increased when near the oxide/alloy interface as illustrated in Figure 2.16. $SnCl_x$ species were excluded from consideration due to the lack of Cl 2p photoelectron peaks (198.4 eV, not shown) at the sputter depth near the oxide/alloy interface.

2.3.6 Released Ions in Artificial Perspiration Solution

Released Cu cations (Figure 2.17a) showed the greatest concentrations in solution at all exposure times from Cu-4.5Sn-0.1Zn followed by Cu-9.7Sn-0.1Zn and lastly Cu. Sn was not observed above the LOD for any alloy (Figure 2.17b). Cation release from high purity Cu-10Sn is plotted alongside these results show comparable release to the Cu-9.7Sn-0.1Zn alloy as expected. Both Cu-Sn alloys showed nearly constant rates of release while Cu indicated a decreased rate of cation release after 96 hours. Replicate sample exposures of Cu after 130 hours, given by open symbols (Figure 2.17a), demonstrate the reproducibility and data scatter of these measurements.

2.3.7 Comparative Analysis of Total Charge

To demonstrate the correlation between techniques, the data for Cu-9.7Sn-0.1Zn are presented in Figure 2.18. Good correlation of charge density as a function of time is observed between multiple independent methods (Figure 2.18).

The total charge density as evaluated from multiple methods is presented in Figure 2.19. EIS-determined anodic charge density is presented in Figure 2.19a, mass loss in Figure 2.19b, released ions as measured by ICP-OES in Figure 2.19c, and corrosion product charge density from CR in Figure 2.19d. Copper had similar corrosion rates (evaluated by EIS and mass loss, Figure 2.19) as Cu-9.7Sn-0.1Zn while Cu-4.5Sn-0.1Zn clearly had higher corrosion rates. Both Cu-Sn alloys had similar charge associated with soluble release which was linear with time. In contrast, Cu released progressively less soluble Cu in solution over time (Figures 2a and 2c). Cu had a decreasing trend of corrosion product formation with time whereas Cu-4.5Sn-0.1Zn indicated increased corrosion product formation with time (Figure 2.19d). Finally, Cu-9.7Sn-0.1Zn had corrosion product growth rates which correlated well with parabolic growth law kinetics, as shown in Figure 2.19d. Cu and Cu-9.7Sn-0.1Zn indicated the largest proportion of total anodic charge density contributing to ion release (Figure 2.18a and e). Though, the total corrosion product charge was greatest for the Cu-4.5Sn-0.1Zn alloy due to its higher corrosion rate (Figure 2.19).

2.4 Discussion

2.4.1 Summary of Findings – Corrosion Behavior and Ion Release

A schematic description of corrosion product morphology for each alloy and Cu is given in Figure 2.20. Corrosion product layers formed on Cu and Cu-Sn alloys in artificial perspiration (Figure 2.20) in a manner consistent with the literature within Cl^- containing environments [54,132]: an outer distribution of copper salts (e.g., CuCl), a middle layer of defective cuprite (Cu_2O), and an inner layer of hydrated cassiterite (SnO_2) for Sn-containing alloys. Retention of oxidized Sn at the alloy-corrosion product interface was also observed on corroded bronze evaluated via other methods such as cross-sectional metallography, glow discharge optical emission spectroscopy (GD-OES), XPS, EDS, and Raman mapping [53,54,132,142,144,146,148,149]. This layering was also evidenced by high-resolution XPS measurements taken at the sputter depth (Figure 2.16) near the corrosion product / Cu-Sn alloy interface and furthermore supported by the literature in atmospheric, seawater, and archaeological studies [54,130,132,142,144,146,149,150].

Oxidized Zn was not detected with any measurement due to its low amount and furthermore was not observed to have any measurable influence on corrosion in this system. The two Cu-Sn alloys also possess other minor elements (see Table 2-1) but were also not measurable with methods employed. It is reasonable to ascribe these effects to Sn rather than the minor elements as the high-purity Cu-10Sn sample demonstrates the same behavior as Cu-9.7Sn-0.1Zn in Figures 2c, 3, and 2a.

Notwithstanding the lack of a protective product layer (i.e. indicated by a decreasing rate of formation upon thickening), Cu had modest corrosion rates after 130 h in artificial perspiration (i_{corr}~1 ±1 µA/cm^2). The corrosion rate and OCP of Cu-4.5Sn-0.1Zn were highest among the alloys tested (i_{corr} = 5 ±1 µA/cm^2, E_{OCP} = $^-$30 mV_{SCE}), also without protective corrosion products for all investigated times (Figure 2.19). Cu-4.5Sn-0.1Zn had greater anodic current density for a given potential as revealed by both cyclic voltammetry and AESEC (Figures 2 and 3, respectively). The greatest release of ionic Cu in solution (1.2 mg/cm^2 after 130 h) was observed on this alloy (Cu-4.5Sn-0.1Zn), interpreted to be commensurate with its elevated corrosion rate. Cu-4.5Sn-0.1Zn had the greatest anodic current density as a function of applied potentials compared to Cu-9.7Sn-0.1Zn and Cu (CV, Figure 2.3). AESEC galvanostatic tests mirrored this result, as lower potentials were observed on Cu-4.5Sn-0.1Zn as a function of applied current density when compared to Cu (Figure 2.6) demonstrating that Cu-Sn is more anodically active than Cu. Diminution of this effect on Cu-9.7Sn-0.1Zn can be ascribed to its protective corrosion product formation. Based on the more positive potential observed and higher Sn content, the corrosion rate of Cu-9.7Sn-0.1Zn would be anticipated to be as high as or worse than Cu-4.5Sn-0.1Zn. However, the corrosion rate of Cu-9.7Sn-0.1Zn was significantly lower than Cu-4.5Sn-0.1Zn (2.5 vs 4.5 µA/cm^2 at 130 hours, respectively, see Figure 2.11). Corrosion product production on this alloy (Cu-9.7Sn-0.1Zn) was lowest among all alloys (Figure 2.19d) and a pseudo-passive or protective product layer formation behavior substantiated by parabolic growth of corrosion products was observed with EIS, mass loss (Figure 2.11), and CR (Figure 2.12). Yet, Cu ion release (Figure 2.17) from Cu-9.7Sn-0.1Zn was nearly identical to Cu-4.5Sn-0.1Zn despite lower bulk Cu, protective corrosion product growth (Figure 2.19d), and reduced corrosion rates (Figure 2.19a, and b). This suggests a high residual rate of direct Cu cation ejection through semi-protective SnO_2 layer. From these observations, one can infer that Cu-9.7Sn-0.1Zn forms a corrosion product layer which is more uniform with fewer disruptions in coverage in solution. Predictably, Cu-9.7Sn-0.1Zn corrosion products as observed under SEM (Figure 2.8c) were more uniform than the corrosion products on other alloys (Figure 2.8a and b). CV results (Figure 2.3) corroborate this assumption. For this alloy (Cu-9.7Sn-0.1Zn), overall corrosion product amounts were lower with a higher proportion of Sn charge in the product layer (Table 2-5). The implication for Cu-9.7Sn-0.1Zn (Figure 2.8c) is that there is sufficient Sn oxidized near the surface to form a continuous or nearly continuous SnO_2 layer which is semi-passivating in that it does not restrict direct release of ionic Cu into solution (Figure 2.20). Graph theory [76] considers the 'connectivity' (a mathematical abstraction) of the passivating solute oxide (SnO_2) interrupted by solvent cations (Cu^+ in this case), and the critical solute (Sn) content to produce a continuous 'connected' or passive layer is 10.3 wt% Sn. Cu-9.7Sn-0.1Zn closely approaches this value, and hence its semi-passive behavior may be explained by a nearly continuous or 'connected' layer of SnO_2 while permitting cuprous ion transmission through this layer.

2.4.2 Rate Limiting Step and Corrosion Mechanisms

From the impedance data, referring to Equation 2.3, and taking the effective diffusion distance δ as the corrosion product layer estimated from multiple methods, effective diffusion coefficient values calculated for all samples (0→10 wt% Sn) and times (0→130 hours) range from $10^{-10} \leftrightarrow 10^{-17}$ cm²/s. This result would imply that Cu cation diffusion outward from the surface (through SnO_2/Cu_2O) is controlling as is consistent with other bronze corrosion findings [129–131]. Typically, the diffusion coefficient of oxygen in aqueous solution is on the order of 10^{-5} cm²/s [151], far too fast to be the rate-controlling factor in this case.

Cu was simultaneously released as both cuprite (Cu_2O) and soluble cuprous ions in artificial perspiration for both Cu and Cu-Sn alloys as determined from AESEC testing (Figure 2.5) and confirmed with cyclic voltammetry (Figure 2.3) in non-complexing buffer of the same pH (6.5). Cu and Cu-Sn alloys favored cuprous ion release over corrosion product formation in artificial perspiration (Figure 2.5). Kinetic information of copper corrosion probed by AESEC in a previous publication [134] also proposed a simultaneous mechanism of both ion release and oxide formation. Modifications here include cuprous ion release, reflective of the solution chemistry employed and the role of Sn [134]. Cuprous ion release from the alloy occurs directly from the metal and is increased by Sn in solid solution:

$$Cu[Sn] \rightarrow Cu^+(aq) + e^- \qquad \text{Equation 2.8}$$

Simultaneously, cuprous oxide (cuprite) formation occurs also directly from the metallic state:

$$2Cu[Sn] + H_2O \rightarrow Cu_2O + 2e^- + 2H^+ \qquad \text{Equation 2.9}$$

Typically, CuCl is reported to form from a precipitation reaction:

$$Cu^+(aq) + Cl^-(aq) \rightarrow CuCl(s) \qquad \text{Equation 2.10}$$

Alternatively, CuCl can be chemically formed from cuprite:

$$Cu_2O + 2Cl^- + 2H^+ \rightarrow 2CuCl + H_2O \qquad \text{Equation 2.11}$$

Were CuCl formed via Eq. 2.10, the soluble ion concentration of the reacting species, $[Cu^+]$ and $[Cl^-]$, would dictate the nantokite (CuCl) product yield and therefore would be identical for Cu-4.5Sn-0.1Zn and Cu-9.7Sn-0.1Zn. However, CuCl formed via Eq. 2.11 would result in the greatest amounts of CuCl would increase with corrosion rate which was observed here (Cu-4.5Sn-0.1Zn, Table 2-5).

In both full immersion exposures and AESEC experiments, soluble Sn was not detected (Figure 2.17b) nor chemically and only slightly dissolved by CBS. Regardless, based on CR (Figure 2.12d), CV (Figure 2.3a), SEM (Figure 2.8), XPS (Figure 2.16), and a lower free energy of formation, Sn is likely oxidized first [131,150] and forms a hydrated SnO_2 layer at the metal /corrosion product interface:

$$Sn + 2H_2O \rightarrow SnO_2 + 4H^+ + 4e^- \qquad \text{Equation 2.12}$$

CV and CR results on pure Sn sheet (Figures 2 and 2d) demonstrate that a thin oxidized layer of Sn was readily formed initially at low potentials ($E = {}^-0.6\ V_{SCE}$) which then exhibits a low anodic dissolution rate at the pH (6.5) and potential ranges (${}^-0.8\ V_{SCE} < E < +0.8\ V_{SCE}$) consistent with open circuit corrosion of Cu-Sn alloys in artificial perspiration (Figure 2.7).

2.4.3 Effect of Sn: Enhanced Dissolution and Passivity

Two main observations as to the effect of Sn as a solute in FCC Cu were observed: an elevated open circuit potential typical of films obeying Wagner growth (Figure 2.7), and an enhanced dissolution fraction of Cu released which increases with Sn content rather than Cu content (Figures 2-2). Evaluation of the impedance results (Figure 2.10) and prior literature [129–131] suggest that outward cation diffusion through Cu_2O/SnO_2 controls the corrosion rate. Moreover, increased open circuit potentials on Cu-Sn is due to Wagner-regime oxide films formed on the surface. We speculate that anodic dissolution kinetics of alloys are governed by their chemical composition, reflected in atomic bonding [152]. The enhanced Cu release on Cu-Sn may be understood by considering atomic bonding of Cu and Sn in solid solution. Sn nearest neighbors in Cu functions as a dissolution promoter due to the weaker Cu-Sn bond ($\Delta H_{f,298} = 177$ kJ/mol

[124]), compared to Cu-Cu (202 kJ/mol [124]); this has an effect even in small solute concentrations of a few atomic percent as solute (Sn) affects its surrounding Cu neighbors. Yet, Sn remains on the surface due to both its insolubility in this electrolyte (Figure 2.17b) and strong affinity for oxide formation (SnO_2: $\Delta G_{f,298} = {}^{-}519$ kJ/mol [130]). Cu atoms surrounding the Sn solute consequently have increased anodic activity resulting in greater dissolution rates. Indeed, solute elements such as Cr are also dissolution promoters in Fe solvents (stainless steels) [45,152], though the stable passive Cr_2O_3 film typically conceals this effect at higher Cr alloying contents (e.g., 13 wt% Cr). Sn-enhanced cuprous ion release was observed for both Cu-Sn alloys but was functionally different for the two alloys. Cu-4.5Sn-0.1Zn released Cu preferentially, but this was accompanied by a higher overall corrosion rate. The tin composition of Cu-9.7Sn-0.1Zn was close to the critical Sn content for passivity (10.3 Sn [76]) calculated from graph theory, which yielded semi-passive behavior. This SnO_2 film limits the overall corrosion rate yet maintained enhanced Cu release originating from the dissolution promoter effect of metallic Sn as a solute in FCC Cu.

2.5 Conclusions

- Cu-Sn in artificial perspiration provided a continuous supply of soluble cuprous ions into the environment (and available for antimicrobial function) linearly with respect to exposure time up to 130 hours whereas Cu ion release from Cu plateaued approaching 96 hours of exposure.
- In solid solution FCC Cu, Sn was observed to enhanced Cu release in artificial perspiration from Cu-Sn alloys whereas oxidized Sn was retained on the surface as SnO_2 due to oxide insolubility.
- The enhanced soluble Cu release of Cu-4.5Sn-0.1Zn was due to an elevated corrosion rate with incomplete SnO_2 coverage.

- Alloying Cu with 10 wt% Sn (Cu-9.7Sn-0.1Zn) also demonstrated enhanced ionic Cu release offset by lower corrosion rates due to a more complete protective inner SnO_2 layer coverage in artificial perspiration.

Tables

Table 2-1. Commercial copper, tin and copper-tin alloy compositions (wt%). Commercial alloy composition testing performed via ICP analysis according to ASTM E478 [133].

Alloy	**UNS#**	**Cu**	**Sn**	**Zn**	**P**	**Fe**	**Pb**	**Other**
Cu	C11000	99.915	0.001	0.005	--	0.003	0.002	--
Cu-4.5Sn-0.1Zn	C51000	95.06	4.52	0.08	0.207	0.02	0.05	0.02Si
Cu-9.7Sn-0.1Zn	C52480	89.63	9.72	0.10	0.170	0.16	0.02	0.10Si, 0.05Ni
Cu-10Sn	--	99.00	10.00	--	--	--	--	--
Sn	--	0.06	99.85	0.001	-	0.004	0.03	--

Table 2-2. Artificial perspiration solution composition. Based on [48].

Chemical Name	**g/L**	**Molarity (mM)**
NaCl – Sodium Chloride	5.00	85.6
CH_4N_2O - Urea	1.00	16.7
$C_3H_6O_3$ - L(+) Lactic Acid (90%)	1.00	11.1
NH_4OH – Ammonium Hydroxide	pH Adjuster	~11

Table 2-3. Identified corrosion products on Cu and commercial Cu-Sn alloys exposed to artificial perspiration solution up to 130 h at open circuit. Italicized values are obtained from literature [142,144–146,150].

Alloy	**XPS** [142,144–146,150]	**GIXRD**	**Raman Spectroscopy**	**Coulometric Reduction Potential Wave**
Cu	*Cu_2O*	Cu_2O	Cu_2O	Cu_2O
Cu-4.5Sn-0.1Zn	Cu_2O, SnO_x	Cu_2O, CuCl	Cu_2O	Cu_2O, CuCl
Cu-9.7Sn-0.1Zn	*CuCl, Cu_2O, SnO_2*	Cu_2O	Cu_2O	Cu_2O
Sn	*SnO_2*	--	SnO_x	SnO_x

Table 2-4. XPS binding energies (eV), X-ray generated Auger electron energy (eV), and corrosion product assignment from fit of high-resolution photoelectron spectral data on Cu-4.5Sn-0.1Zn after 24 hours in artificial perspiration solution at open circuit. Literature values from: [30,141–146].

Chemical State	Orbital/Auger	Experiment (eV)	Literature (eV)	Assignment
Cu^0	$2p_{3/2}$	Not Detected	932.7	Cu, Cu_2O
Cu^+	$2p_{3/2}$	932.2	932.0, 932.5, 933.0	CuCl, Cu_2O
Cu^{2+}	$2p_{3/2}$	Not Detected	935.0, 934.9, 935.2	CuO, $Cu(OH)_2$, $CuCl_2$
Cu_{Auger}	LMM	569.8	569.8	CuCl, Cu_2O
Sn^0	$3d_{5/2}$	484.7	484.8, 485.4	Sn
Sn^{2+}	$3d_{5/2}$	486.4	486.0, 486.6, 486.9	SnO
Sn^{4+}	$3d_{5/2}$	486.4	486.6, 486.7, 487.1	SnO_2

Table 2-5. Anodic charge (Coul/cm²) of individual corrosion products as evaluated by coulometric reduction (CR) following 130 h at open circuit in artificial perspiration. N.D. – Not detected.

Alloy	CuCl	Cu_2O	SnO_2	Cu^+	Total
		Coulomb cm^{-2}			
Cu	*N.D.*	0.120	--	0.742	0.86
Cu-4.5Sn-0.1Zn	0.613	0.772	0.790	1.337	3.51
Cu-9.7Sn-0.1Zn	0.001	0.162	0.228	1.154	1.54
Sn	--	--	0.014	--	0.01

Figures

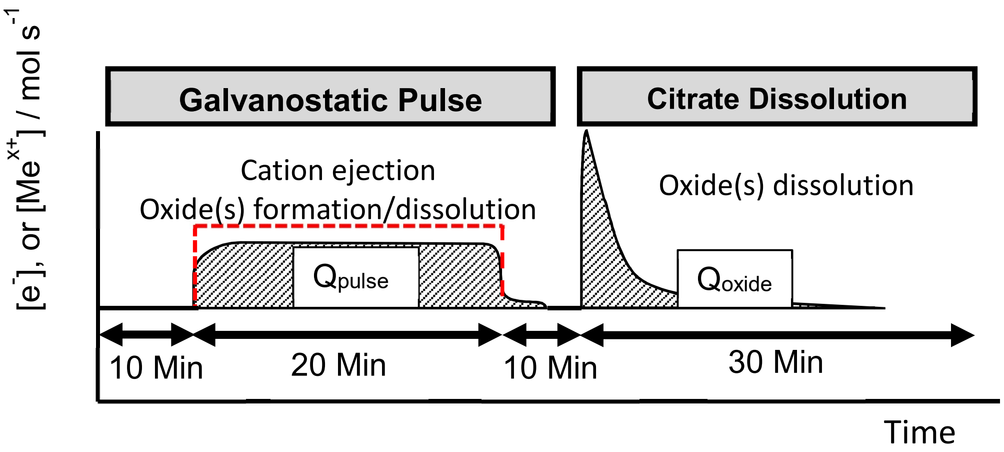

Figure 2.1. Schematic diagram of *operando* AESEC experimental method. Galvanostatic pulse conducting in artificial perspiration solution. Citrate dissolution stage was conducted in a deaerated citrate buffer solution (CBS, pH 5.0). Dashed red line indicates applied current [e^-], Solid black lines indicate AESEC measured release [Me^{x+}] expressed as nmol/s. Grey-shaded integrated areas under curves represent moles.

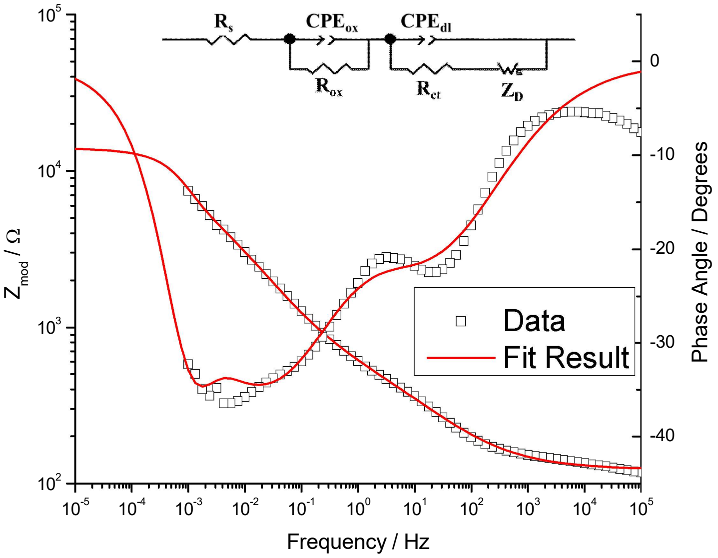

Figure 2.2. Equivalent DC Circuit, and representative example fit of Cu-4.5Sn-0.1Zn after 48 h in artificial perspiration solution (Area= 0.8 cm²). R_s - solution resistance (122.8 Ω), R_{ox} – oxide resistance (2350 Ω), R_{ct} – charge transfer resistance (502 Ω), Z_D – diffusional Warburg impedance (Y_{diff} = 2.12 x10^{-3} S•$s^{0.5}$, B = 23.8 $s^{0.5}$), CPE_{ox} - oxide constant phase element (Y_{ox} = 3.20 x10^{-3} S•s^a, a_{ox} = 0.603), CPE_{dl} – double layer capacitance (Y_{dl} = 3.89 x10^{-4} S•s^a, a_{dl} = 0.5).

a)

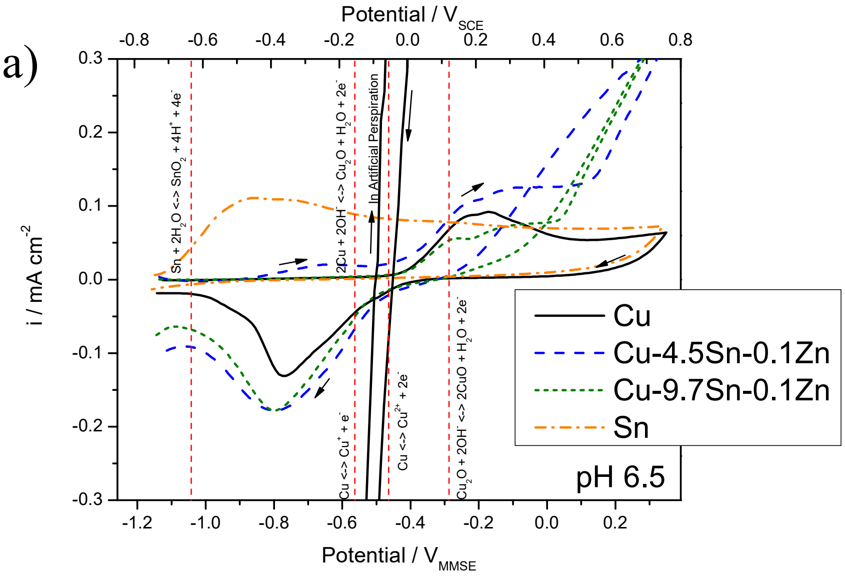
Potential / V_{SCE}
-0.8 -0.6 -0.4 -0.2 0.0 0.2 0.4 0.6 0.8
i / mA cm^{-2}
0.3 0.2 0.1 0.0 -0.1 -0.2 -0.3
-1.2 -1.0 -0.8 -0.6 -0.4 -0.2 0.0 0.2
Potential / V_{MMSE}
$Sn + 2H_2O <-> SnO_2 + 4H^+ + 4e^-$
$2Cu + 2OH^- <-> Cu_2O + H_2O + 2e^-$
In Artificial Perspiration
$Cu <-> Cu^+ + e^-$
$Cu <-> Cu^{2+} + 2e^-$
$Cu_2O + 2OH^- <-> 2CuO + H_2O + 2e^-$
Cu
Cu-4.5Sn-0.1Zn
Cu-9.7Sn-0.1Zn
Sn
pH 6.5

b)

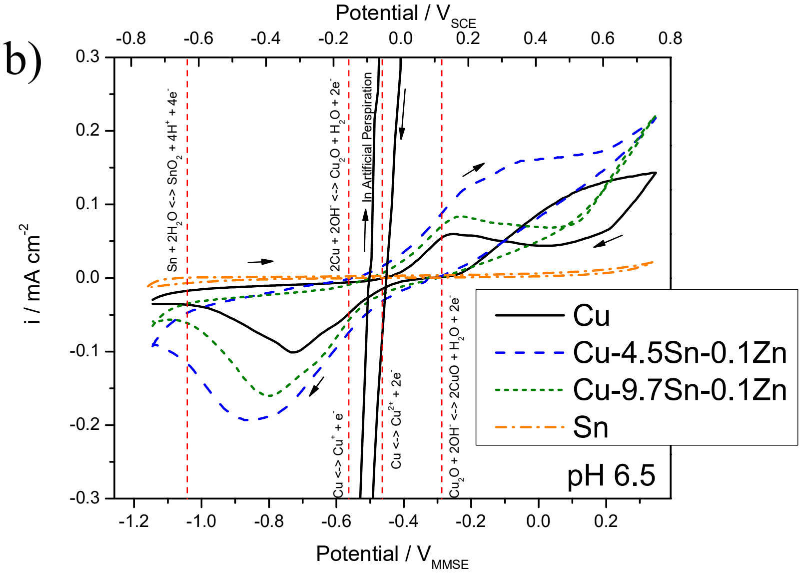
Potential / V_{SCE}
-0.8 -0.6 -0.4 -0.2 0.0 0.2 0.4 0.6 0.8
i / mA cm^{-2}
0.3 0.2 0.1 0.0 -0.1 -0.2 -0.3
-1.2 -1.0 -0.8 -0.6 -0.4 -0.2 0.0 0.2
Potential / V_{MMSE}
$Sn + 2H_2O <-> SnO_2 + 4H^+ + 4e^-$
$2Cu + 2OH^- <-> Cu_2O + H_2O + 2e^-$
In Artificial Perspiration
$Cu <-> Cu^+ + e^-$
$Cu <-> Cu^{2+} + 2e^-$
$Cu_2O + 2OH^- <-> 2CuO + H_2O + 2e^-$
Cu
Cu-4.5Sn-0.1Zn
Cu-9.7Sn-0.1Zn
Sn
pH 6.5

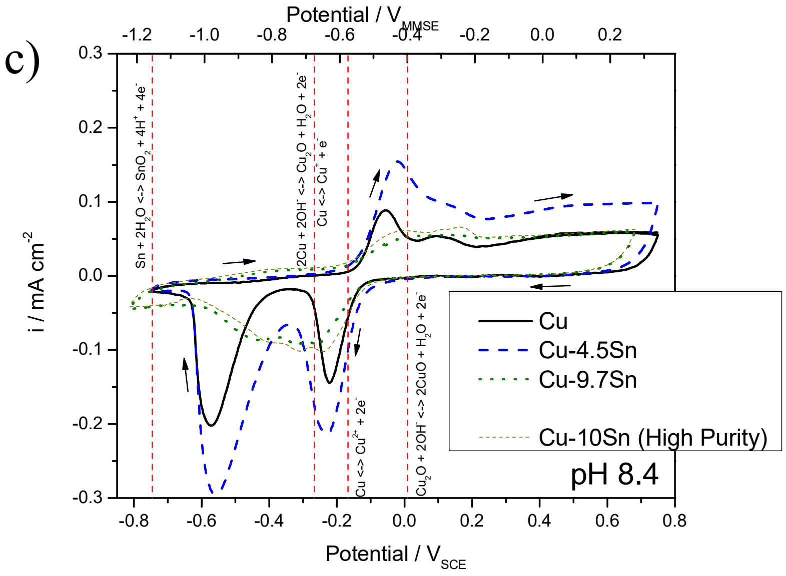

Figure 2.3. Cyclic voltammograms in deaerated boric acid buffer (pH 6.5) and borate buffer (pH 8.4). a) Boric acid buffer cycle 1, b) boric acid buffer cycle 3, c) borate buffer cycle 3. Scan rate 10 mV/s. Samples were held at -1.4 V$_{MMSE}$ for 10 min prior to initial scan.

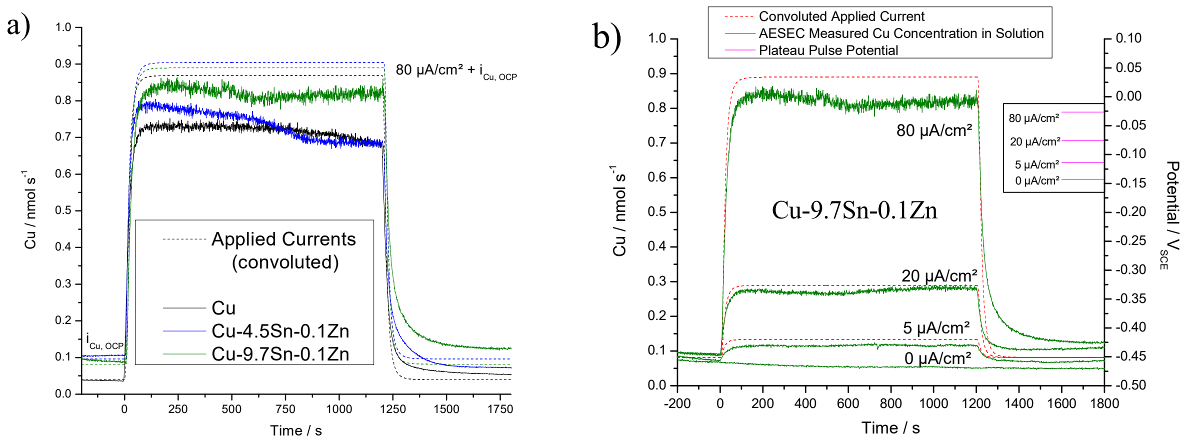

Figure 2.4. *Operando* AESEC galvanostatic pulse measurements of Cu-Sn samples in artificial perspiration solution at an applied current of 80 µA/cm² (a) and multiple applied currents of 0, 5, 20, and 80 µA/cm² on Cu-9.7Sn-0.1Zn (b). Exposed area = 1 cm². Convoluted applied current profiles are shown in dashed lines. Convolution of the current was used to account for residence time of the flow condition and cell geometry [134]. Applied current convolution includes addition of non-zero open circuit corrosion rate ($i_{Cu, OCP}$) measured during prior 10 min OCP (Time < 0). Measured steady-state potentials in the plateau region of the pulse are overlaid with magenta lines.

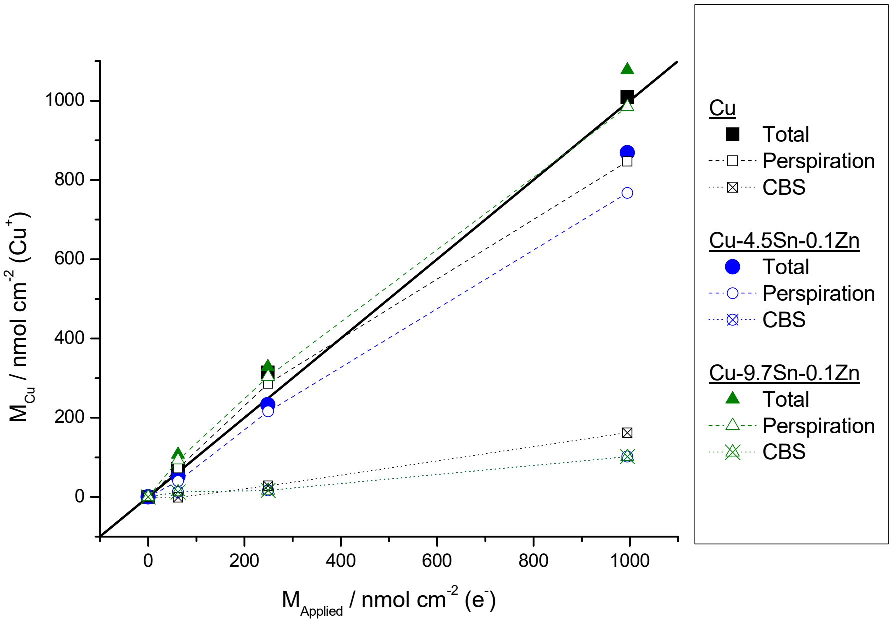

Figure 2.5. AESEC total amount of Cu from soluble release in artificial perspiration + oxide dissolution in CBS on Cu compared to Cu-4.5Sn-0.1Zn. Assumed Cu^+ valence state for both soluble release and oxide. Line indicates 1:1 correlation between applied current and total detected ion concentration. $M_{Applied}$: Applied anodic current. M_{Cu}: Cu ions detected via downstream ICP for both artificial perspiration and CBS stages. Compensated for OCP corrosion rate.

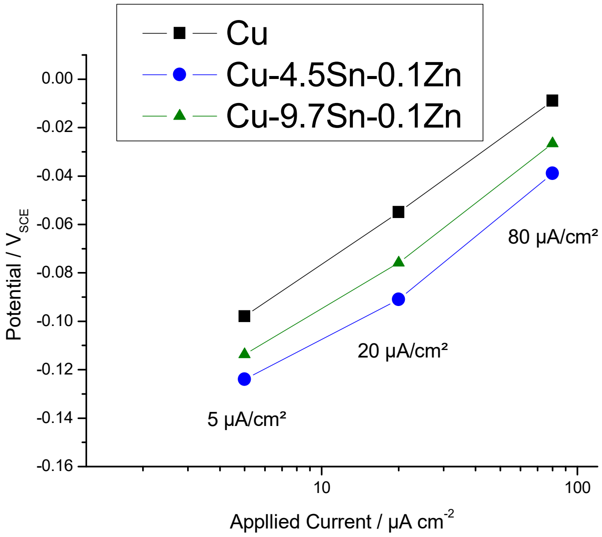

Figure 2.6. Measured potential plotted against applied current during anodic dissolution stage of AESEC measurements in artificial perspiration.

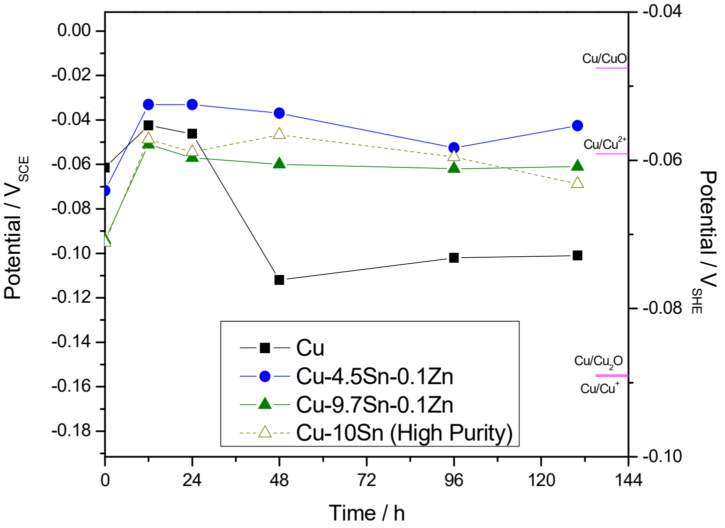

Figure 2.7. Open circuit potential of Cu compared to commercial Cu-Sn alloys fully immersed in naturally-aerated artificial perspiration solution (pH 6.5) up to 130 hours. Selected Nernst potentials for half-cell reactions of interest are overlaid on graph. (E_r: Sn/SnO_2 → -0.75 V_{SCE}, not shown)

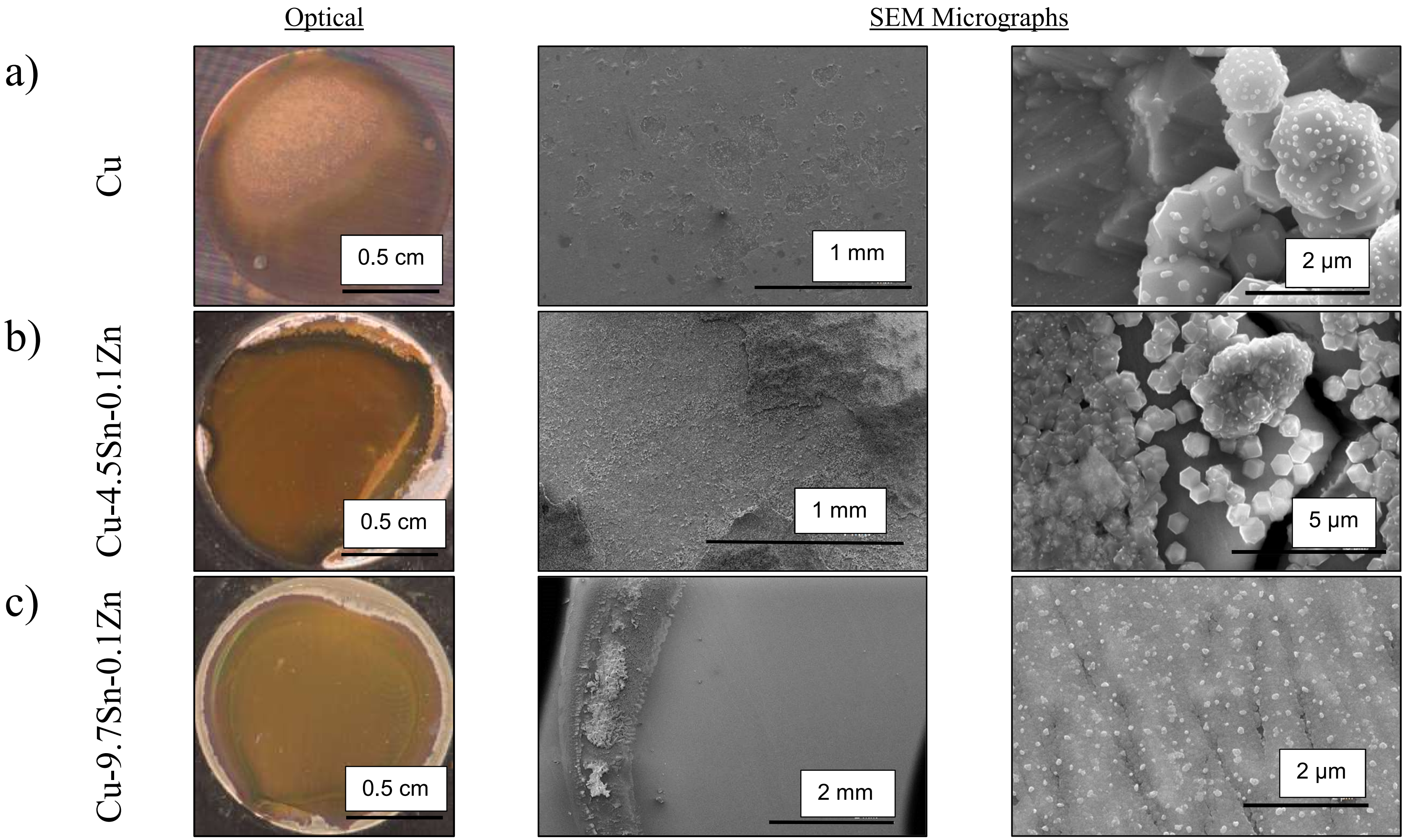

Figure 2.8. Visual condition and secondary electron images of Cu and Cu-Sn samples post-exposure following open circuit in artificial perspiration solution after 130 hours. a) Cu, b) Cu-4.5Sn-0.1Zn, and c) Cu-9.7Sn-0.1Zn.

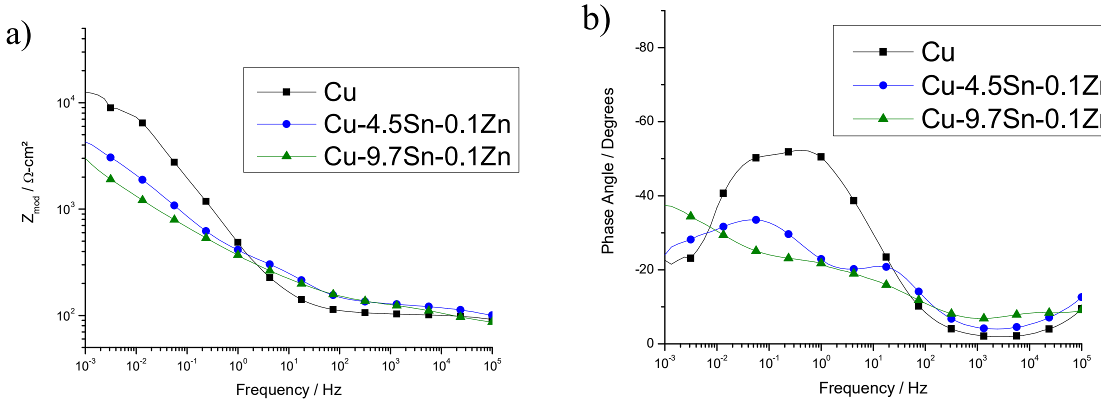

Figure 2.9. Comparison of electrochemical impedance behavior of Cu and commercial Cu-Sn alloys in artificial perspiration solution after 130 hours at open circuit.

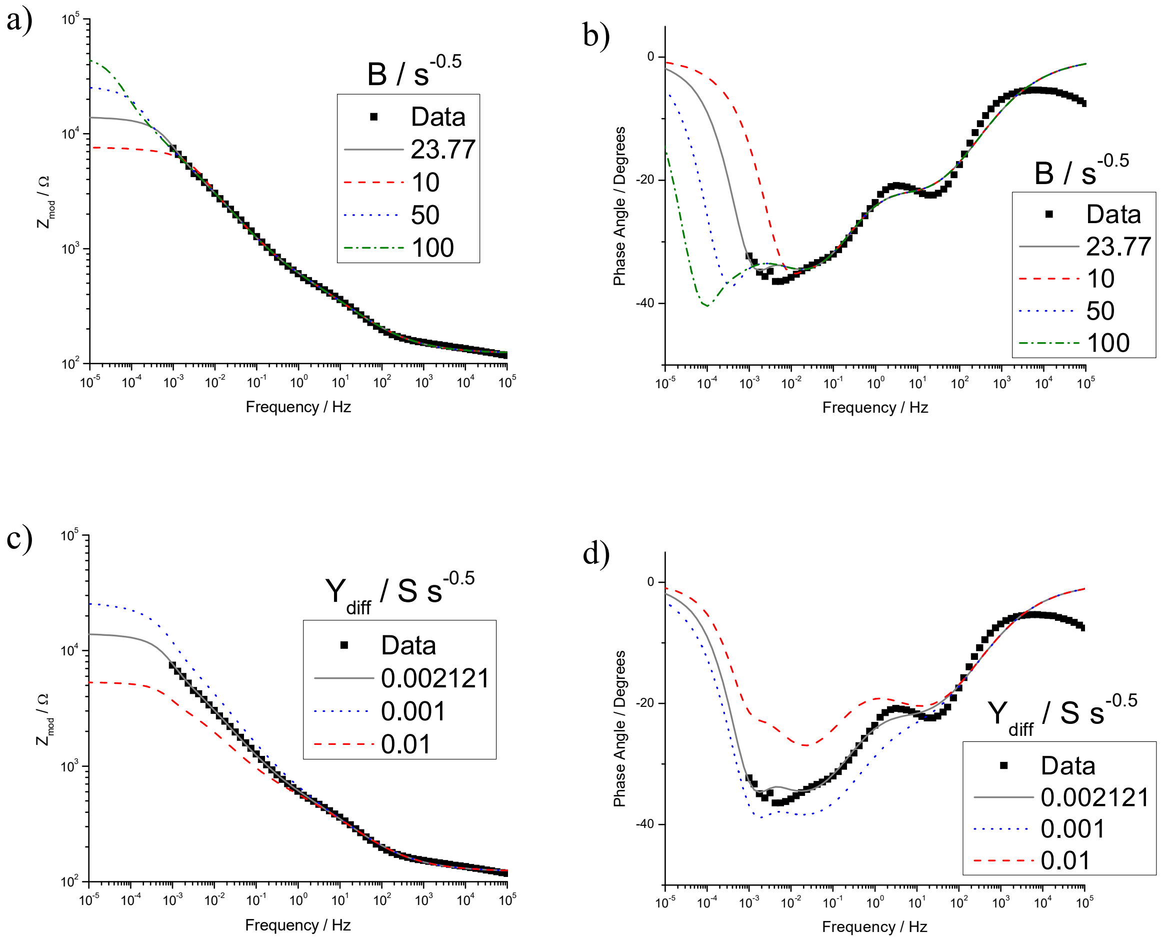

Figure 2.10. Equivalent circuit sensitivity study: Selected ranges for values of B (a and b), and Y_{diff} (c and d), about best fit (solid line) and relative effect of selected fit parameter range on the calculated impedance response of magnitude (a and c) and phase angle (b and d) for the simulated DC equivalent circuit (see Figure 2.2).

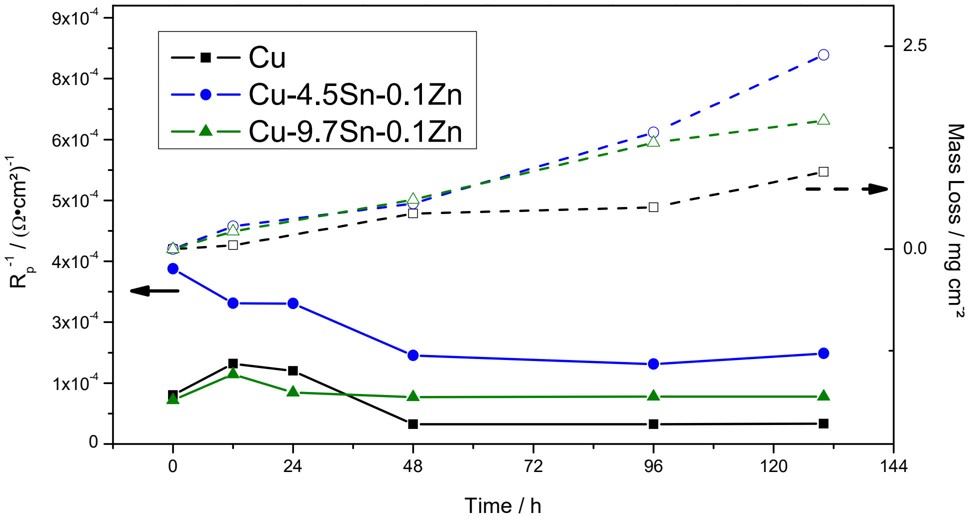

Figure 2.11. Inverse polarization resistance ($1/R_p$) values obtained from circuit fit of experimental impedance response data (Filled Symbols) and mass loss (Open Symbols) of Cu and commercial Cu-Sn alloys corroded at open circuit in artificial perspiration solution. Corrosion product removal for mass loss facilitated by 2-3 min exposure to 6 M HCl.

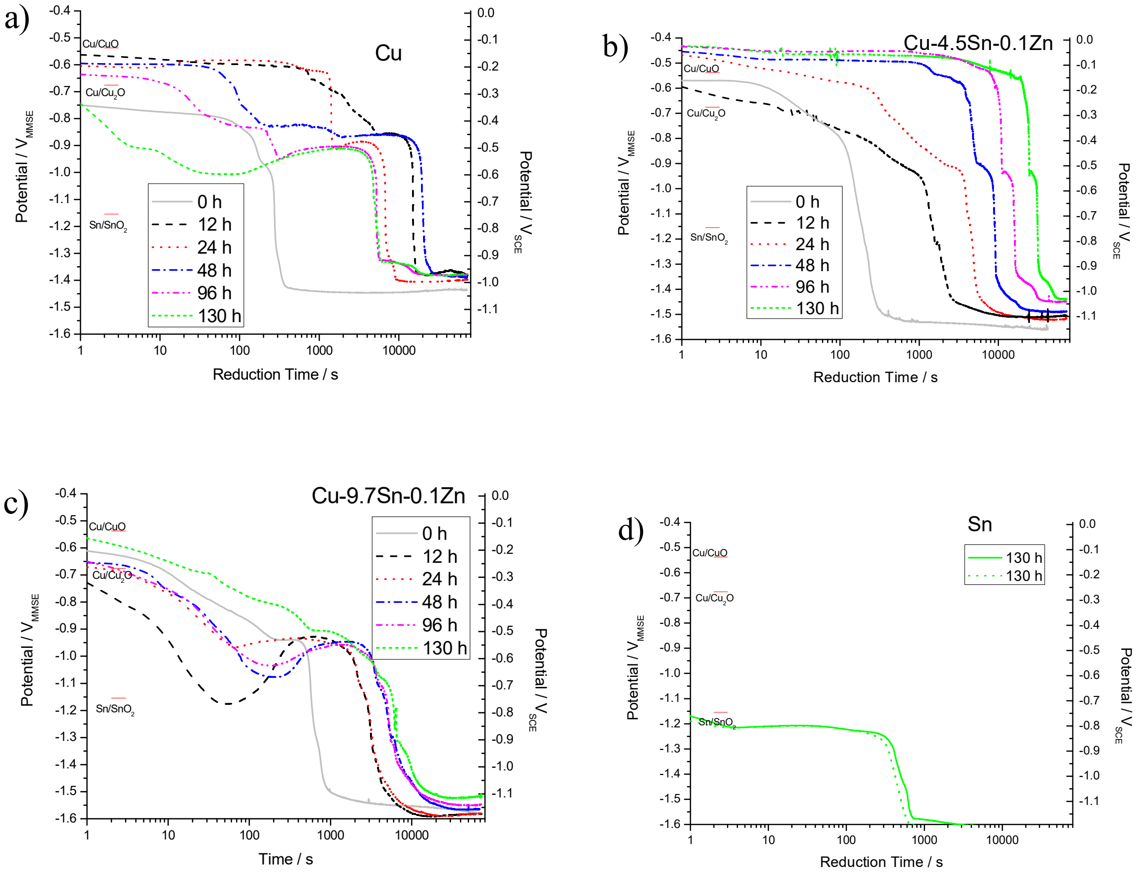

Figure 2.12. Coulometric cathodic reduction in deaerated borate buffer (pH 8.4) of commercial Cu-Sn alloys following exposures in artificial perspiration solution at open circuit up to 130 hours. Applied cathodic current of -20 µA over electrode area 0.8 cm² (-25 µA/cm²). (a) Cu, (b) Cu-4.5Sn-0.1Zn, (c) Cu-9.7Sn-0.1Zn, and (d) Sn.

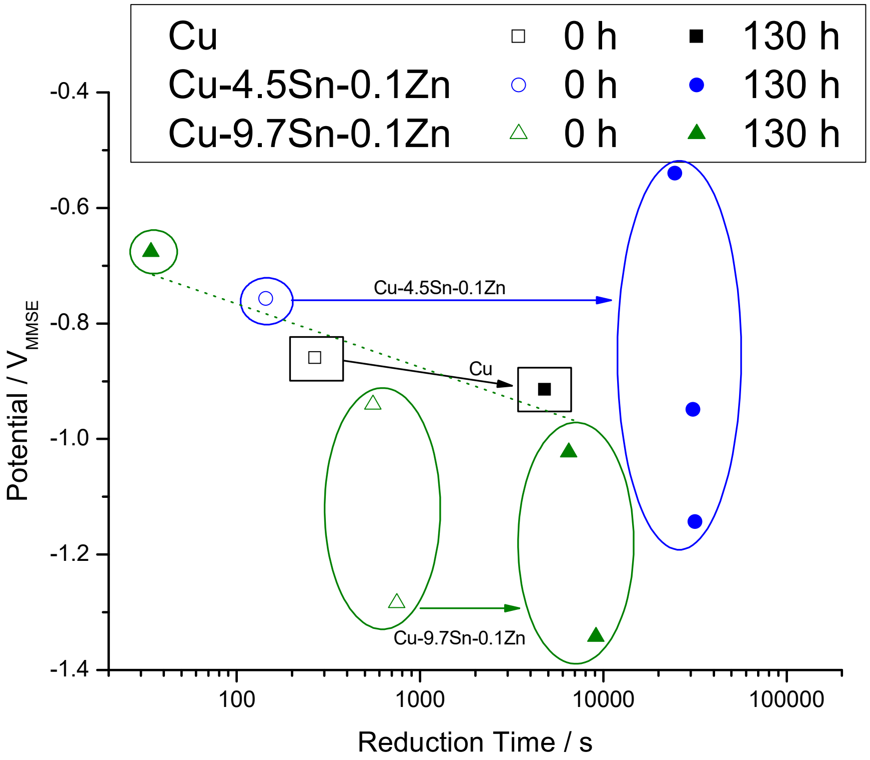

Figure 2.13. Corrosion product terminus reduction times and reduction plateau potentials of coulometric cathodic reduction on Cu and commercial Cu-Sn alloys freshly polished (Open Symbols) and exposed for 130 hours (Filled Symbols) in artificial perspiration solution at open circuit.

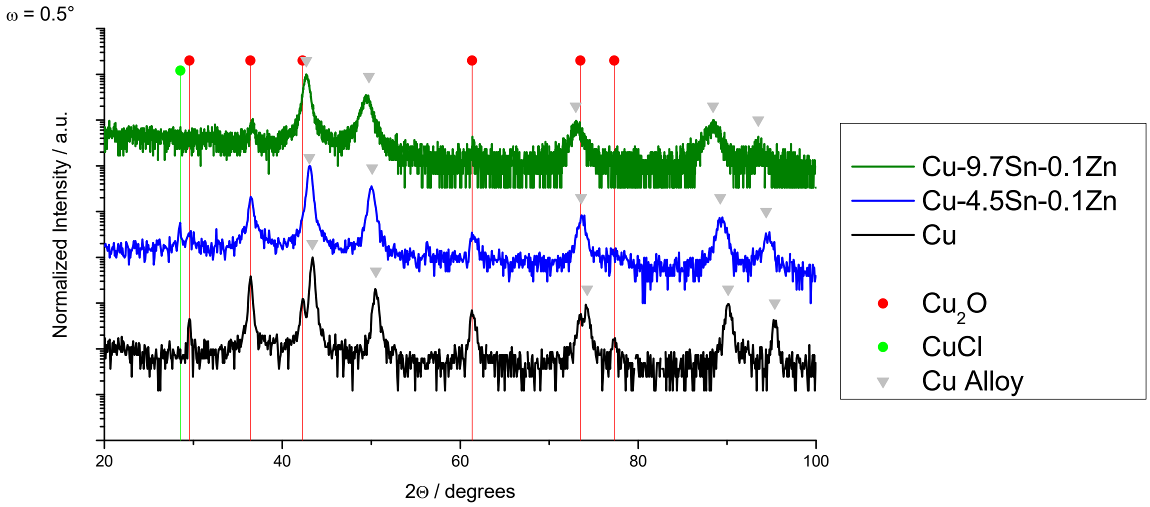

Figure 2.14. GIXRD of surface corrosion products on commercial Cu-Sn alloys compared to Cu following 130 h Exposure to artificial perspiration solution at open circuit. Gray triangles represent base alloy FCC Cu peaks calculated with stretched lattice parameter fit of a substitutional solid solution alloy. Corrosion product identification was facilitated using standard X-Ray PDF cards (ICDD® PDF-4+).

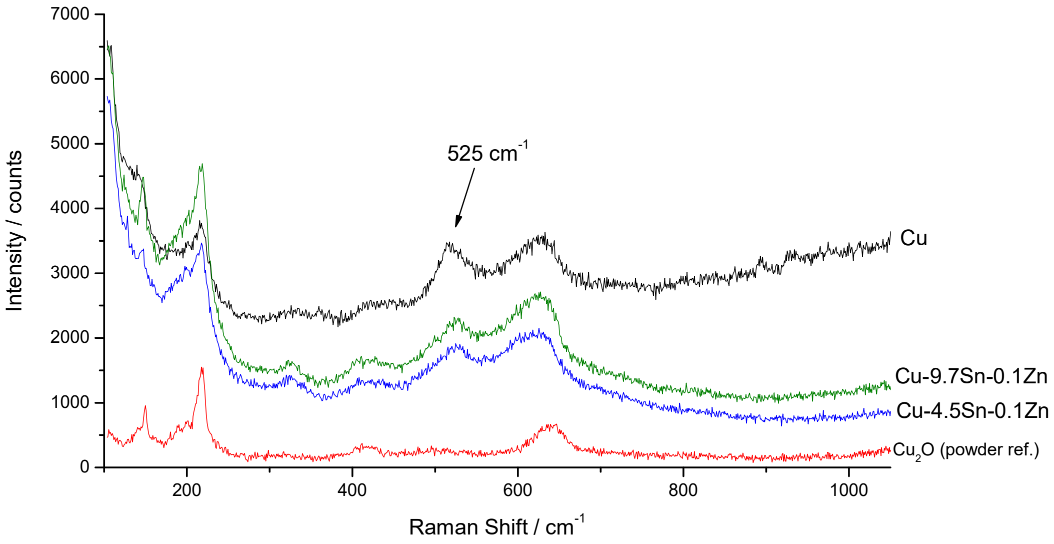

Figure 2.15. *Ex Situ* Raman spectroscopy of surface corrosion products on Cu and commercial Cu-Sn alloys following 130 h exposure to artificial perspiration solution at open circuit. Cuprite (Cu_2O) cold-pressed powder reference (red) displayed for comparison. Labeled peak at 525 cm^{-1} is discussed in text.

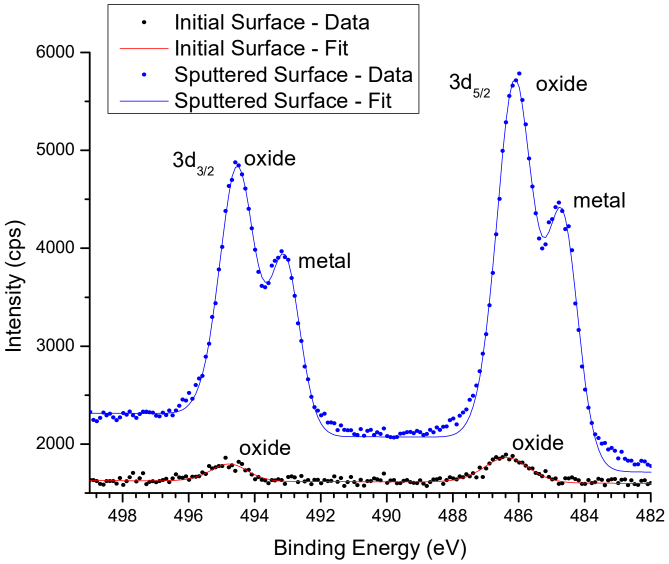

Figure 2.16. Initial and sputtered surface high-resolution XPS spectra of Cu-4.5Sn-0.1Zn sample exposed for 24 hours in artificial perspiration focused on Sn 3d range including $3d_{3/2}$ and $3d_{5/2}$ regions.

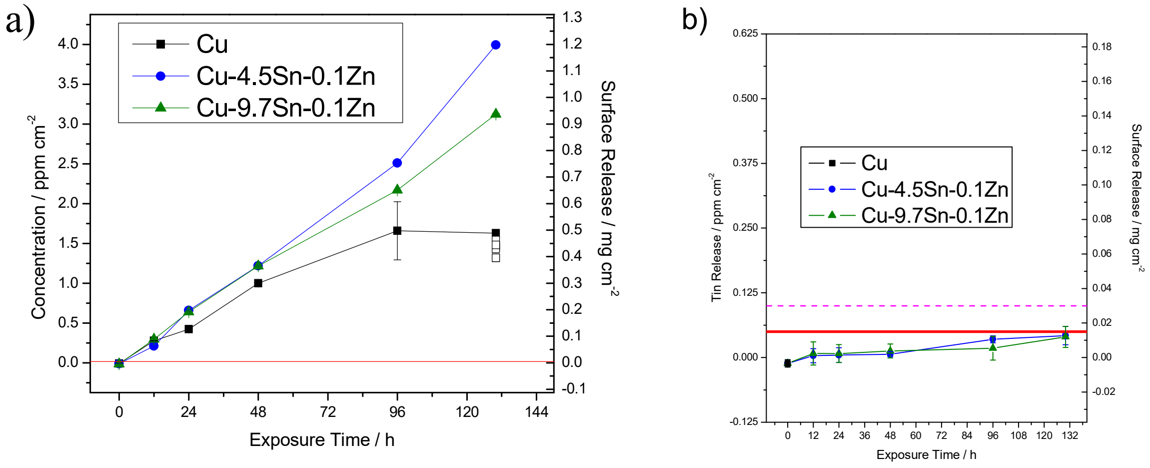

Figure 2.17. Copper release (a) available for antimicrobial function measured via ICP-OES (red line: Cu LOD) Open symbols are replicates. Tin release (b) was below LOD of ~40 ppb (red line). Magenta dashed line: expected soluble Sn assuming congruent dissolution (see text). Soluble ion concentration in artificial perspiration solution was measured from aliquots of solution taken from open circuit corrosion cells at specified time points. Exposed area 0.8 cm², solution volume 300 mL.

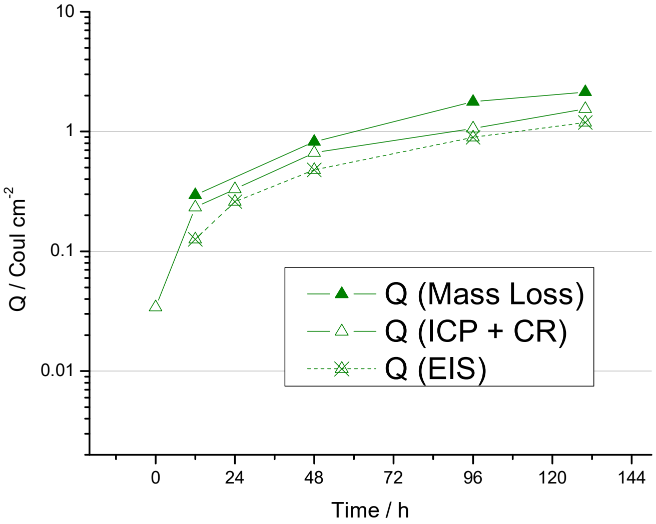

Figure 2.18. Example comparison of total anodic charge as a function of time for Cu-9.7Sn-0.1Zn alloy as measured by various techniques following open circuit exposure to artificial perspiration up to 130 hours. ICP + CR represents the anodic charge from both released ions (ICP) and corrosion products (CR).

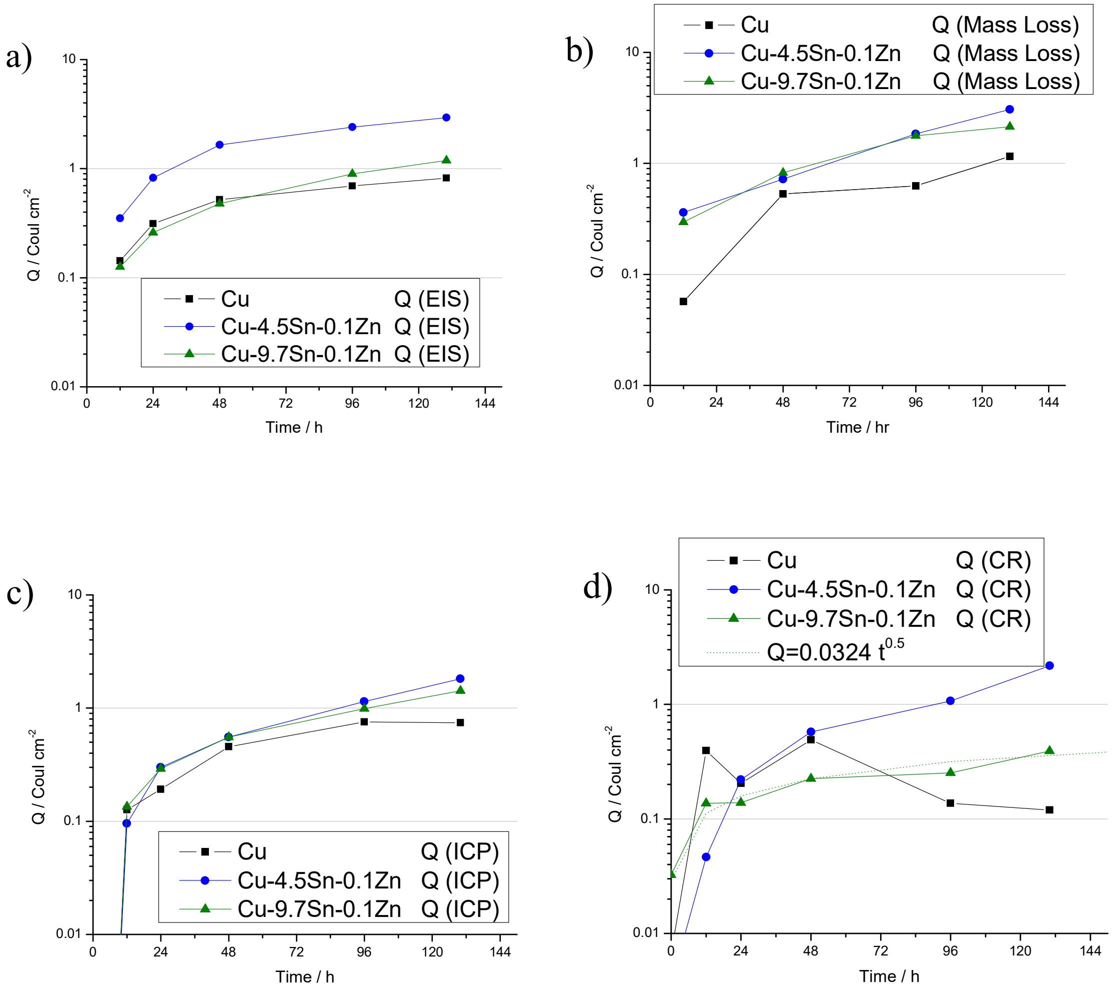

Figure 2.19. Comparison of anodic charge assessments by alloy composition as measured by various techniques: (a) Total anodic charge by EIS, (b) total anodic charge by mass loss, (c) released soluble Cu by ICP-OES, (d) corrosion product charge by coulometric reduction.

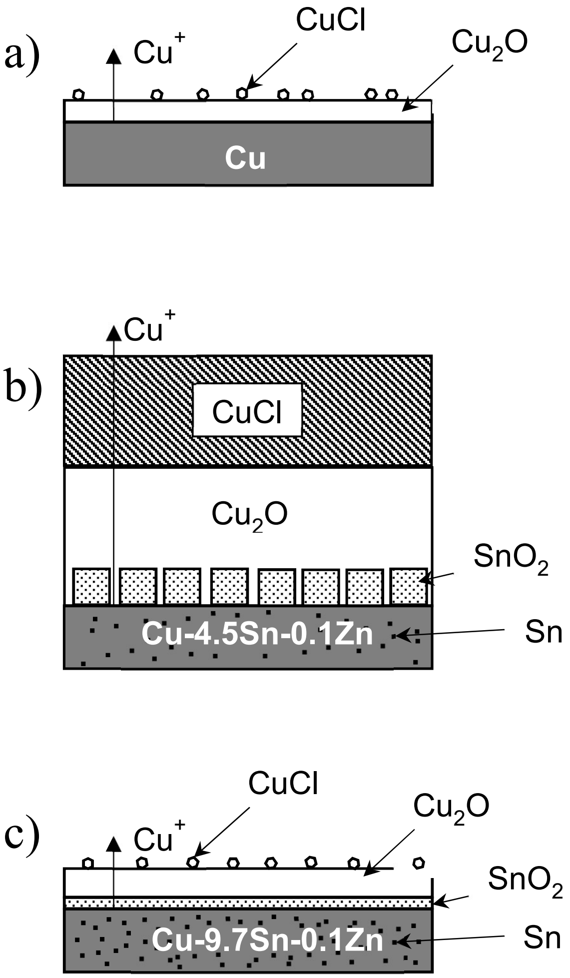

Figure 2.20. Schematic cross-sectional description of corrosion product morphology following open circuit exposure in artificial perspiration for a) Cu, b) Cu-4.5Sn-0.1Zn, and c) Cu-9.7Sn-0.1Zn. Relative dimensions of corrosion products are based on results in Table 2-5.

3 Patina Enrichment of SnO_2 and Effect on Soluble Cu Cation Release and Passivity of High-Purity Cu-Sn Bronze in Artificial Perspiration

Abstract

The antimicrobial function of Cu surfaces can be linked to soluble Cu release from corrosion. However, direct replacement of high-touch surfaces with Cu-based alloys is limited by knowledge gaps regarding how alloying directly relates to corrosion. A systematic approach to determine the role of Sn as a solute element and the minimum alloy content for passivation has been lacking. High-purity arc-melted binary alloys of Cu-Sn with specific additions of 0.1, 1, 5, and 10 wt% Sn were compared to pure Cu and Sn. The role and amount of Sn in corrosion products (patina) formed on the alloy surface as a function of alloying was interrogated in artificial perspiration. The fate and identity of the solute (Sn) and solvent (Cu) elements following corrosion, as soluble ions or insoluble corrosion products, was investigated. Alloy patinas became increasingly enriched in Sn corrosion products assigned as SnO_2 with increasing Sn content in the alloy. The critical alloy content for complete layer coverage were theoretically quantified through a model based on interfacial surface energy. The predicted minimum solute content for a complete conformal inner layer of SnO_2 was 1 wt% Sn whereas experimentally complete coverage was achieved only at 10 wt% Sn. Differences between theory and experiment are discussed.

3.1 Background

3.1.1 Cu-Sn Alloys as Antimicrobial Surfaces

Copper and its alloys have received revived attention from corrosion and antimicrobial scientific communities due to recent works which demonstrate ability to kill/inactivate drug-resistant pathogenic bacteria [1,6,21,119,153]. Most importantly, these include many antibiotic-resistant strains such as *Mycobacterium tuberculosis* (TB), *Escherichia coli* (E. coli), and epidemic methicillin-resistant *Staphylococcus aureus* (E-MRSA) [6,21]. Novel infection control methods are not simply an attractive alternative to antibiotics, they are critical to the future of world health. Deaths worldwide from antibacterial-resistant infections are projected to surpass those caused by cancer as early as 2050 [7]. Soluble Cu, as either Cu(I) or Cu(II), is the source of copper's antimicrobial function [21,24,26], and its release is directly linked to corrosion of the particular alloy and regulated by its oxide. Little is understood regarding optimization of Cu alloys through alloying, especially concerning critical alloying contents for passivity, which is not desirable in this application as active corrosion is needed to facilitate antimicrobial function. Greater than 65 wt% Cu in the alloy generally confers antimicrobial function in laboratory testing. While much is known about how alloying elements affect corrosion of Cu alloys in seawater and various potable waters [134], little is known in sweat.

Bronze (Cu-Sn), perhaps surprisingly due to its ancient origins, is of particular interest to study in this context due to its enhanced soluble Cu release despite a lower Cu content in the alloy [17,154]. Most Cu alloys rapidly tarnish (form oxides) upon hand contact, but those which remain tarnish-free (e.g., passive alloys) are typically not efficacious against bacteria likely due to their very low corrosion rates and subsequently low soluble Cu release rates. A desirable alloy surface would have to remain aesthetically tarnish-resistant yet permit enough Cu release through corrosion to maintain a constant supply of soluble Cu for continuous passive antimicrobial function. However, ‘drop-in’ replacement of bacteria-transmission sites (e.g., high-touch surfaces) with commercial bronze alloys is currently impractical due to current knowledge gaps between materials and electrochemical (i.e. corrosion) sciences, specifically, how minor alloying affects corrosion and tarnishing, and critical alloying contents needed for passivation.

Resurgent appreciation of Cu’s antimicrobial capabilities merits a second look at these alloys for antimicrobial function. As the soluble Cu cation is responsible for this antimicrobial effect, an investigation into the corrosion of bronze alloys, specifically the role of Sn without the complicating effects of secondary intermetallic phases or ternary alloying, in high-touch environment such as artificial human perspiration is prudent. Sn has demonstrated the ability to enhance soluble Cu ion release but forms a tarnishing layer. In the aims of forming an alloy surface relatively free of tarnish, the amount and critical thresholds of Sn oxidation are of interest to study. The patina formed is known to change with tin content of the alloy [130], yet a systematic approach to elucidating the specific role of Sn on the corrosion products formed and critical alloying content for passivation is needed. An ideal alloy would remain free of tarnish while maintaining antimicrobial function through release of soluble Cu cations.

3.1.2 Minor Elements in Cu-Sn Bronze and Their Influence on Corrosion

The majority of investigations on the corrosion of bronze are conducted with off-the-shelf commercially available alloys, obfuscating the specific effects of the individual alloying elements. Alloying elements can be either beneficial (e.g., Ni, Al) or detrimental (e.g., Fe, Zn) to the corrosion resistance of Cu-based alloys [5,46]. Tin bronzes are usually produced with additional minor elements for various metallurgical reasons. Cu-Sn bronze is commonly alloyed with Zn as a ternary element, i.e. gunmetal: Cu-Sn-Zn. Additional elements such as P, Fe, Pb, and sometimes

Ni are also minor constituents for deoxidizing and machinability or are simply unintentional impurities. In commercial production, these alloys are designed empirically to serve particular mechanical functions with corrosion of this semi-noble alloy system typically a secondary consideration. However, these minor or impurity elements each can affect corrosion differently and confound these effects in a study of a single alloying element.

Zn is a common alloying addition to Cu-Sn alloys (Cu-Sn-Zn – gunmetals [60]). However, Zn is both anodic to Cu and leads to a preferential incongruent release of Zn relative to its alloy content [36,58,155]. Anodic charge attributed to release of Zn is not nearly as useful as Cu in an antimicrobial Cu context. Additionally, Zn (especially in alloys above 15 wt%) dealloys from Cu [5,36,46,58,155], leaving a Cu-rich phase behind.

Cu-Ni alloys have superb corrosion resistance in seawater [46,60]. Increased Ni decreases corrosion of the alloy, however, alloys with greater Ni have more biofouling[60]. Ni is theorized to change the defect structure of the semiconducting cuprite (Cu2O) layer leading to a more corrosion-resistant film by reducing the number of mobile cation vacancies [85]. Ni2+ substitutes Cu+ in the cation sublattice of Cu2O. Electrostatic interactions between the negatively charged Cu vacancies (V_{Cu}') and the positively charged Ni substitution ($Ni_{Cu}^{\bullet}$) not only decrease the mobility of the cation vacancies but increase the electronic resistance as well leading to a more corrosion resistant layer. Ni, unfortunately, is becoming an increasingly-common metal allergen to humans [9] and therefore, release from Ni-containing alloys is being regulated [48]. Ni release from Cu-Ni-Zn alloys in artificial sweat is higher than Cu (nearly 2x) [30] and exceeds maximum tolerable allergy levels: 0.5 $\mu g\ cm^{-2}\ week^{-1}$ of Ni [48]. Ni therefore, would be undesirable alloying addition for an antimicrobial alloy in a high-touch setting, both due to its superb corrosion resistance, and its propensity to trigger an allergic response.

Alloying elements such as Zn, Ni, and Al are considered beneficial as they endue good mechanical properties. Some alloying additions (e.g., Ni, Al) lower the corrosion rates of bronze alloys, however, others (e.g., Zn) tend to increase the corrosion rates and some (e.g., Ni, Zn) are preferentially released instead of Cu. These minor elements are useful in their respective applications, however, for systematic study of Sn in Cu-Sn, they obfuscate the individual contribution of Sn. Moreover, in an antimicrobial context, biological compatibility must be considered, and elements such as Ni are unsuitable for direct hand contact applications.

3.1.3 The Role of Sn on Bronze Corrosion and Patina Formation

Bronze alloys corrode at similar rates (~0.1 mpy [5]) as copper in the early stages of dissolution. At longer times, a thick (10-250 μm [130]) dark brown or black layer forms on the surface which prevents further corrosion. This layer is referred to as patina and is comprised of stratified layers of Sn oxide and Cu oxides[130,142,148,156]. In most atmospheric environments this patina is stable and can prevent further corrosion from centuries to millennia [120,130,157–162]. Increasing the Sn content of the alloy leads to faster formation of this protective patina layer. However, at greater Sn values (>13 wt%), secondary intermetallic alloy phases may form which have different electrochemical properties [46] further complicating the role of Sn in Cu. In contemporary applications, the Sn content is usually lower (4-6 wt% Sn) and the patina is artificially applied using a chemical treatment of nitric, sulfuric, or hydrochloric acid [163–167]. The long-term stability of these patinas formed is subject to investigation and continuous monitoring [130,147,160,163–165,168–173]. However, excessive amounts of aggressive anions: sulfates (SO_4^{2-}), or chlorides (Cl^-) from a polluted atmosphere near urban, industrial, or marine exposure, may ‘destabilize’ this patina. Thermodynamically stable Cu-Cl or Cu-SO_4 phases compared to Cu_2O form, leading to volume change transformations which cause compressive stresses to develop within the patina which eventually leads to spallation [130].

In contrast to well-documented study of bronze corrosion in atmosphere and seawater, studies in biological environments such as human perspiration, however, remains relatively unexplored. Commercial bronze alloys with increasing Sn content in artificial sweat demonstrate enhanced Cu release with corrosion mitigated at greater Sn alloying contents (>5 wt%) theoretically by a partially blocking inner layer of SnO_2 [17,154]. With regard to a Cu-Sn alloy, the stability of Sn in artificial perspiration is also of interest; tin-coated steel-core guitar strings released significant Sn (~0.8 $\mu g/cm^2$) in artificial sweat [174]. Direct hand contact applied to Cu-Sn alloys caused thinner oxide films (as measured by coulometric reduction) and slightly lower corrosion rates than those measured on commercially pure copper and other alloys [57].

The literature at present does well to characterize patinas types and elemental compositions of corrosion products formed on Cu-Sn alloys [129,130,142,146,148,156,160,169,170,172,175,176], the role of aggressive ions on the stability of these patinas [50,54,165,177–181], and while not emphasized here, barrier coatings and inhibitor performance in industrial and marine atmospheric environments [146,163,168,173,182]. However, the Cu-Sn alloys investigated in the literature range in alloy compositions amongst their various applications, and therefore there remains a lack of systematic investigation on the role of Sn on these patinas. Particularly, there remains lack of knowledge regarding the minimum Sn content needed to passivate the alloy, how Sn affects the compositions, structure, and morphology of these patinas and their subsequent effect on corrosion, tarnish, and soluble element dissolution;

especially so in the case of Cu-Sn alloys in biological environments where an antimicrobial alloy system would be of interest.

Tin corrosion products formed on Cu-Sn alloys increase with Sn alloying content. The surface coverage of Sn corrosion products determines the subsequent electrochemical behavior and passivity of these alloys. Prior work has shown that the soluble release, corrosion rates, and total anodic charge were similar for commercial Cu-Sn-Zn alloys tested after 96 h in artificial perspiration [154]. However, the nature of the corrosion products formed on the surface was different amongst the alloy compositions which affected corrosion at later times (130 h). An open circuit exposure for 96 h was selected to evaluate the effect of alloyed Sn in FCC Cu on the corrosion products formed where similar corrosion rates, total anodic charge, and soluble ion release were observed.

Many drug-resistant pathogenic bacteria, particularly MRSA, can proliferate via high-touch surfaces [119]. However, knowledge gaps persist in corrosion science which would link material composition to electrochemical properties, passivity, and the fate of all alloying elements during corrosion. Open circuit exposures coupled with characterization and electrochemical testing were employed to elucidate the roles of Sn in the corrosion product layers and its subsequent effect on corrosion and cation release. An ideal Cu-based alloy would remain tarnish resistant while maintaining continuous soluble Cu release. However, oxide patinas which block antimicrobial function need to first be understood before they can be controlled in a solid solution Cu alloy. This paper will quantify how the chemistry, morphology, and layering of oxides on Cu-Sn alloys changes with alloyed Sn content and discuss the implications for corrosion, passivity, tarnishing, and Cu cation release for antimicrobial function of Cu-Sn alloys.

3.2 Experimental Procedures

3.2.1 Materials

High-Purity Solid Solution Cu-Sn Alloys without Minor Alloying Elements

Commercially pure Cu (99.95 wt%, UNS C11000) and Sn sheet (99.9 wt%) were investigated as controls. For systematic study of the alloying effect of Sn, high-purity alloys of Cu-0.1Sn, Cu-1Sn, Cu-5Sn, and Cu-10Sn (wt%) were fabricated by inert gas (Ar) arc-melting by the Materials Preparation Center at AMES Laboratories. Alloy constituents (Cu and Sn) were of 99.99% elemental purity by weight. The precise compositions of each commercial alloy were evaluated using ASTM E478 [133] and are given in Table 2-1. Alloys of a single-phase were obtained by solutionizing heat treatments (2 h, 600 °C) followed by water quenching and verified with X-ray diffraction.

Electrolyte Solutions

Naturally aerated (quiescent) artificial perspiration was used to simulate a high-touch surface. The composition of simulated human perspiration solution is given in Table 2-2. This solution is modified from the BS EN 1811:2011 standard solution for evaluating nickel release from jewelry [48], but adjusted to pH 6.50 ±0.05 with NH_4OH instead of NaOH. A boric-borate buffer electrolyte media was prepared from 0.11 M boric acid (H_3BO_3) and 21 mM sodium tetraborate ($Na_2B_4O_7$) for coulometric reductions at a pH (pH 8.40 ±0.05) where the pre-formed Cu oxides are chemically stable [126].

3.2.2 Methods

Artificial Perspiration Exposure Conditions

Arc-melted alloy buttons were polished/ground through 1200 grit (US) with SiC grit papers. Samples were polished under ethanol for the final polishing stage. Samples were then rinsed and stored in ethanol until dried with compressed lab air and placed into 3-electrode electrochemical cells for full-immersion exposure. Sample exposure area was 0.8 cm². All cells were cleaned with 0.1 M HCl prior to each experiment and exposure, thoroughly rinsed with deionized water, and finally rinsed with the testing solution. 300 ± 2.5 mL of artificial perspiration was added to cells for soluble ion concentration analysis. In artificial perspiration, electrochemical potentials were measured using saturated calomel electrodes (SCE) with Luggin capillary tips. Corrosion rates were estimated from mass loss measurements (ASTM G1, [139]). The total anodic charge density from these results were then compared to the sum amount of insoluble corrosion products formed on the surface and soluble ions released, i.e. the fate of alloying elements after 96 h of exposure. All quantities of corrosion products were converted to charge density (Coulombs/cm²). Corrosion products were identified and characterized using grazing incidence X-ray diffraction (GIXRD), Raman spectroscopy, and energy-dispersive X-ray spectroscopy (EDS) of corrosion product cross sections prepared by focused ion beam (FIB) milling.

Evaluation of Corrosion Products

<u>Release of Cu and Sn – Soluble Ions in Solution</u>

A sample of 15 mL of solution was taken from each exposure cell at specific time points and stored in metal-free plastic test tubes. The solution was later directly nebulized into the inductively-coupled plasma. A Thermo Scientific™ iCAP 6000 inductively-coupled plasma optical emission spectrometer (ICP-OES) was employed to measure solution ion concentrations. Acidification did not show any differences in measured concentrations. LOD determined was 15 ppb for Cu, and 40 ppb for Sn. Soluble ion concentration measured via ICP-OES were reported as charge, Q_{ICP}, using a Faradaic conversion with a Cu ion valence state determined from prior work [154] to be cuprous (Cu^+, n=1).

Molecular Identity of Solid Corrosion Products

Crystalline corrosion products on the surface of exposed samples were identified using a grazing incidence method using Cu Kα radiation with a 10-mm width-limiting mask. The optimal signal/noise was found to be at an incident grazing angle of $\omega=0.5°$. For compound identification, diffraction patterns were compared to a powder diffraction database: ICDD® PDF-4+. Detection limit was approximately 5 vol% for crystalline compounds for this setup and methodology.

Raman spectra were acquired using a Renishaw® InVia Raman microscope. Raman spectroscopy measurements used a 514 nm laser with 180° back scattering geometry and a 3000 l/mm diffraction grating. Lower laser intensities were selected with long acquisition times, on the order of several minutes, to avoid thermal conversion of analytes by heating due to laser illumination. Spectra from samples were compared with those acquired on cold-pressed powder pellets of known structure and chemistry.

Morphology of Solid Corrosion Products

Corrosion product morphology was evaluated via focused ion beam (FIB) milling with element identification using energy-dispersive X-ray spectroscopy (EDS) cross sections prepared by Ga^+ ion beam milling. The instrument used was a FEI® Helios 600 Nanolab Dual-Beam FIB. A protective Pt-C film was deposited in two stages: an initial thin layer was deposited with the electron beam at low currents to avoid damage to the surface from ion beam damage during the second, thicker layer deposited with the more aggressive ion beam. Following cross sectional ion milling, samples were investigated with SEM and EDS measurements.

Quantification of Solid Corrosion Products

Many copper corrosion products can be individually reduced and quantified electrochemically by coulometric reduction. A deaerated chloride-free boric-borate buffer (pH 8.4) was used as the electrolyte. The buffer solution was deaerated for one hour by grade-4 pure N_2 gas bubbling prior to each test to avoid reduction of dissolved oxygen. Electrochemical cells were also purged with grade-4 nitrogen gas for 10 min before introduction to the electrolyte with continuous bubbling to maintain deaeration throughout the duration of tests. Samples were removed from exposure cells and repositioned to chloride-free cells wherein constant current of -20 μA was applied to an exposed electrode area of 0.8 cm^2 (-25 $\mu A/cm^2$). Cathodic current was applied using Princeton Applied Research PAR273A potentiostat/galvanostats. Potentials were measured with mercury/mercurous sulfate reference electrodes with Luggin capillary tips. Under constant applied cathodic current, the reduction time is directly related to the total charge (Q_{CR}) of the reduced oxide by the expression given in Equation 3.1:

$$Q_{CR} = i_{app} \times t_{red} \qquad \text{Equation 3.1}$$

Where i_{app} is the applied cathodic current density, and t_{red} is the reduction time evaluated from first-derivative analysis. Intervals of the relative maxima of the first derivate of the chronopotential curve indicate reduction times of individual corrosion products.

3.3 Results

3.3.1 Calculated Chemical Stability Diagrams

Calculated chemical stability diagrams of individual Cu and Sn oxides and the chloride composition of artificial perspiration are presented in Figure 3.1. These chemical stability diagrams provide insight to the thermodynamic equilibrium where cations are supplied by dissolution [127]. The pH-dependent chemical stability between corrosion product phases and soluble cations are plotted along with the anodic dissolution line accounting for by the pH change associated with the conjugate cathodic reactions (ORR/HER). According to Pourbaix [125–127], metal dissolution of Cu and Sn compensated by cathodic charge and subsequent pH change are given by Equation 3.2 and 3.3, respectively.

$$[Cu^{+}] = ([OH^{-}] - 10^{-7}) \qquad \text{Equation 3.2}$$

$$[Sn^{4+}] = \left(\frac{1}{2}[H^{+}] - 10^{-7}\right) \qquad \text{Equation 3.3}$$

Increased metal dissolution i.e. increased [Me^{n+}], is compensated by the cathodic charge from ORR increasing the pH. Metal dissolution i.e. following the metal ion hydrolysis line (Cu: solid black line, Sn: dashed black line in Figure 3.1), is not anticipated to change the pH of the solution before chemical precipitation of the oxide phase is expected for both Cu and Sn. From these calculated results the predominant solid phases we expect during dissolution of copper in sweat are cuprite (Cu_2O), and CuCl. Tin oxides demonstrate remarkable stability in neutral solutions and over a wide range of pH. Tin is expected to oxidize as $Sn(OH)_4$ and SnO_2 (cassiterite) in these conditions with no thermodynamically stable soluble products. At thermodynamic equilibrium, the CuCl/Cu_2O chemical thermodynamic boundaries intersect at lower pH values (pH 4.8), thus we might expect Cu_2O to be the predominant phase at neutral pH values (e.g., 6.5) when Cu cations are produced in sweat. Chemical thermodynamics predicts the solid corrosion products to be Cu_2O and CuCl, and $Sn(OH)_4$/SnO_2.

3.3.2 Open Circuit Exposures: Visual Condition and OCP

The visual condition of Cu-Sn samples following 96 h submersed in artificial perspiration is given in Figure 3.3. Alloys with lower (≤1 wt%) Sn content had similar visual morphology as commercially pure Cu. Some light etching is visible on the surface of Cu-0.1Sn and Cu-1Sn, revealing the grain structure. Greater Sn content alloys showed different behavior: darker corrosion products on Cu-5Sn (Figure 3.3) and a thinner and paler greenish brown color on Cu-10Sn. Poorly-adherent, flakey, and likely secondary corrosion products, blue-gray in color, are visible on Cu-5Sn and Cu-10Sn in the lower left periphery.

Open circuit potentials for Cu and Cu-Sn alloys in artificial perspiration up to 130 h are given in Figure 3.4. Cu and Cu-Sn alloys with 1 wt% Sn or less were observed to have an initial increase in potentials to ~ -60 mV_{SCE} which fall to a more negative value (-100 mV_{SCE}) after 24 h in artificial perspiration. In contrast, Cu-Sn alloys with 5 wt% Sn or greater maintained this more positive OCP (-60 mV_{SCE}) compared to Cu and the low Sn Cu-Sn alloys after 24 hours in artificial perspiration (Figure 3.4). Nernst potentials of selected half-cell reactions of interest are indicated on Figure 3.4. Alloys below 5 wt% Sn rested below the potential for cupric ion production. Sn in Cu does not appreciably affect OCP or post-exposure surface at lower concentrations i.e., 0.1 and 1 wt% Sn. However, at higher Sn content, i.e. Cu-5Sn and Cu-10Sn, Sn in the alloy both elevates the OCP and alters the corrosion products visible on the surface.

3.3.3 Corrosion Rates

Mass loss of Cu-Sn alloys over time following exposure to artificial perspiration are provided in Figure 3.5. As was observed with open circuit potential measurements, a clear demarcation is observed between lower (<5 wt%) and greater (≥5 wt%) Sn alloy contents with respect to mass loss values. Cu-10Sn had the greatest mass loss with lower mass loss with decreasing Sn content. Moreover, (Cu-10Sn) demonstrated parabolic kinetics as shown with a parabolic rate (i.e. $Q=kt^{½}$) fit by the dashed line in Figure 3.5, indicative of protective oxide growth.

3.3.4 Released Soluble Ions in Artificial Perspiration

An antimicrobial Cu alloy must be optimized to release soluble Cu ions into the environment to facilitate antimicrobial function. Released aqueous Cu ions measured via aliquots of artificial perspiration solution exposed to Cu-Sn samples are reported in Figure 3.6. Soluble Cu was released from Cu-Sn alloys with a linear dependence of time for all alloy compositions. Pure Cu (99.95 wt%) showed a slight decrease in Cu release after 96 h. Generally, increasing the Sn content increased the amount of soluble Cu released into solution, which is more evident at 130 h. The measured concentration of Sn is below both a congruent dissolution prediction and instrument detection limits (40 ppb) and we have therefore determined that soluble Sn as either Sn^{2+} or Sn^{4+} was not released during testing. Thermodynamically, Sn is also not expected to be soluble in these near-neutral (pH 6.5) environments as demonstrated with the chemical stability thermodynamics calculated in Figure 3.1. Sn was retained on the surface as a solid oxide phase. Soluble Cu release was linear with time and was not impeded by the presence of Sn in the alloy or its oxide on the surface. Sn also tended to increase the release of soluble Cu relative to pure Cu.

3.3.5 Corrosion Products – Molecular Identity and Quantification

Tarnish, i.e. corrosion products, influenced by Sn alloy content is the principal interest of this study. Multiple techniques were employed to characterize the corrosion products formed in artificial perspiration. GIXRD (e.g., Figure 3.2), Raman spectroscopy (Figure 3.7), coulometric reduction (CR, Figure 3.8), and focused ion beam (FIB) milling with cross-sectional EDS mapping (Figure 3.12) were used to identify multiple crystalline products, molecular structure, and possible stratification. Corrosion products identified were nantokite (CuCl), cuprite (Cu_2O), and a hydrated oxidized tin compound (SnO_x/$Sn(OH)_x$) assumed to be cassiterite (SnO_2). Confirmation of solid solution (via shifted 2Θ of FCC lattice positions) and crystalline compounds of Cu_2O and CuCl were observed with GIXRD (see Figure 3.2). Raman spectroscopy (Figure 3.7) revealed crystalline Cu_2O with an additional vibration peak centered at 535 cm^{-1} likely due to OH^- defects present at O^{2-} sites as identified in literature [148]. Understandably therefore, this peak is not present on the prepared powder reference. Raman spectroscopy did not reveal any major differences in spectral 'fingerprints' between Cu and Cu-Sn alloys which confers conclusive evidence that the additional peak at 535 cm^{-1} is not caused or intensified by any influence of Sn. Furthermore, SnO and SnO_2 are nearly impossible to distinguish when cuprite is present due to the shared characteristic Raman bands at ~210 and ~640 cm^{-1}, respectively. This overlap is illustrated with powder references of SnO and SnO_2 in Figure 3.7.

Coulometric reduction curves following Cu-Sn sample exposure to artificial perspiration are represented by Figure 3.8. Several reduction waves were observed on all samples indicative of multiple corrosion products followed by a final plateau of electrolyte reduction (i.e., hydrogen evolution reaction – HER, $E_{red} \sim 1.15\ V_{MMSE}$). Termination times of reduction waves generally increase with increasing exposure times, a feature exemplified by Cu-5Sn in Figure 3.8. Reduction times were delineated by peaks in the first derivative change in potential with time, representing the rate of maximum change due to a switch in electrochemical reduction reaction. The identity and separation of corrosion products was inferred from the reduction plateau potential. The plateau potential was defined as the potential at the midpoint between reduction times. Measured reduction potentials as a function of Sn content following 96 hours exposed to artificial perspiration are given in Figure 3.9. This figure illustrates the ability of the coulometric reduction technique to both quantify and infer identity of individual corrosion products on copper. The corrosion products were defined from their reduction potentials and from previously described characterization as such: Oxide 1 was defined by reduction potentials above -0.8 V_{MMSE} and ascribed to a secondary (i.e.

precipitated) corrosion product CuCl (nantokite), the Nernst potential for direct reduction is (E_r = -0.42 V_{MMSE})[5]. Oxide 2 was defined as having a reduction potential between -0.8 V_{MMSE} and -1.1 V_{MMSE} and is assigned to Cu_2O (cuprite) where its Nernst potential is (-0.68 V_{MMSE}). Oxide 3 was defined as having a reduction potential more negative than -1.1 V_{MMSE} and was determined to be Sn oxide (assumed SnO_2, Nernst potential: -1.25 V_{MMSE})[6] from its increasing amount with increasing Sn content in the alloy. This assumption was validated in prior work with a reduction of pure Sn [154].

Using reduction times derived from peak intervals of the first-derivative of the chronopotential curve, the total corrosion product charge of all alloys following 96 h in artificial perspiration is presented in Figure 3.10. For clarity, the secondary corrosion product, CuCl, reductions were omitted in this figure. This product is chemically precipitated rather than directly formed on the surface. The total charge of corrosion products increased with increasing Sn contents. Furthermore, the type of oxide/hydroxide which covered the surface changed from Cu_2O-rich to SnO_2/$Sn(OH)_4$-rich with increasing Sn content (Figure 3.10). The most significant difference between Sn contents of Cu-Sn alloys is the nature of the corrosion products on the surface. Sn oxide was enriched on the surface with a transition to a Sn-rich (by charge) surface at alloy contents > 5 wt% Sn.

3.3.6 Corrosion Product Morphology: Focused Ion Beam Milling and EDS Cross Sections

The morphology of corrosion products formed in open circuit exposure to artificial perspiration were evaluated using SEM and EDS of FIB-milled cross sections. Secondary electron

---

[5] The reduction potentials are expected to be more negative than their Nernst reactions due to the overvoltage required to drive the reaction at the fixed rate imposed by the galvanostat.

[6] Despite the more negative Nernst potential of SnO_2 compared to electrolyte reduction (HER), SnO_2 was reducible under these conditions because the overvoltage needed to drive this reaction is lower than that required for hydrogen evolution.

micrographs of corrosion product cross-sections prepared by focused ion beam milling and is reported in Figure 3.11. Cu-1Sn, Cu-5Sn, and Cu-10Sn samples for FIB analysis were polished to a 1-µm diamond finish and exposed to artificial perspiration for 96 h at open circuit. Cu and Sn oxide layers were stratified, and delamination was observed at the interface between corrosion products and the base alloy metal on Cu-1Sn (Figure 3.11a) and Cu-5Sn (Figure 3.11b). However, a uniform continuous Sn-rich layer (assigned SnO_2) was found on the Cu-10Sn alloy (Figure 3.11c) which was intact at the oxide/alloy interface. Some platinum and gallium contamination (Figure 3.11b) from the deposited protective layer and ion beam, respectively, are visible as bright contrast in the broken metal/oxide interface of the Cu-5Sn alloy. This Pt/Ga interface contamination was confirmed by EDS.

Corrosion product assignments were determined from EDS analysis of the cross sections. EDS mapping, presented in Figure 3.12, of the Cu-5Sn sample was selected to highlight the different chemical and spatial segregation of corrosion products. The Cu-rich corrosion product phase was porous but continuous across the alloy surface. In contrast, these cross sections reveal the discontinuous nature of the underlying Sn oxide film. Cl^- was found to be evenly distributed throughout the copper oxide film (assigned as Cu_2O) but was not accumulated in the tin-rich corrosion product. This Sn-rich product was retained as an inner product at the metal/oxide interface and was porous and discontinuous across the alloy surface for this alloy (Cu-5Sn) restricted to oxide islands, but at greater Sn contents became continuous (Cu-10Sn). Cu and Sn corrosion products were not evenly distributed through the film thickness but stratified into layers. The nature of the oxide film changes significantly at 5 wt% Sn in the alloy; wherein FIB results revealed stratified oxide layers restricted to islands which were more porous with broken interfaces due to either dehydration or growth stresses. Sn oxide was retained as an inner layer which became thinner and more conformal at a Sn alloying content of 10 wt%.

3.3.7 Total Anodic Charge: Fate of the Elements

The aim of this work is to determine the role of alloyed Sn on the corrosion patinas formed on the surface of solid solution Cu-Sn alloys in artificial perspiration. This required complete information on soluble release, corrosion product identity, and total anodic charge: i.e. the fate of the elements. It should be mentioned that a 96-h exposure to artificial perspiration was selected to compare changes in corrosion products and morphology with systematic additions of Sn in the Cu-Sn alloy system. Subsequent corrosion of the alloy is strongly influenced by the patina morphology, which is in turn affected by the Sn content in the alloy [130]. The fate of the elements during corrosion of Cu-Sn alloys in artificial perspiration based on anodic charge assessments are calculated and reported in Table 2-5. The sum of the charge from soluble Cu (soluble Sn was not detected, LOD_{Sn} = 40 ppb) and corrosion products are given representing an independent measure of the total anodic charge. GIXRD did not reveal any evidence of a pure Cu FCC phase which would be indicative of dealloying. All Cu FCC peaks matched those of the base alloy measured using bulk XRD and were consistent with the displaced 2Θ values for a Cu-Sn solid solution. Therefore, mass loss calculations were performed with a congruent dissolution assumption i.e. dealloying is not taking place and the ratio of total oxidized Cu/Al is identical to the alloying composition. These results (Table 2-5) suggest there were either electrically disconnected or unreduced oxides (e.g., CuCl) in the coulometric reduction procedure or alternatively, overestimation of corrosion rates by the mass loss measurement. As anticipated, the anodic charge related to corrosion products increased with increasing Sn content in the alloy (Figure 3.10) while the soluble release (Figure 3.6) and corrosion rates (Figure 3.5) were maintained approximately constant across Sn alloy contents.

The fraction of soluble Cu cations released in solution, $X_{Cu,Release}$, defined by Equation 3.4, is presented in Figure 3.13a. The Cu release fraction remained constant at about 70% of the total anodic charge despite a decrease in the amount of Cu in the alloy.

$$X_{Cu,Release} = \left[\frac{\frac{Q_{Cu,ICP}}{n_{Cu}}}{\frac{Q_{Cu,ICP}}{n_{Cu}} + \frac{Q_{Cu,CR}}{n_{Cu}} + \frac{Q_{Sn,CR}}{n_{Sn}}}\right] \qquad \text{Equation 3.4}$$

However, while the total fraction of Cu released remained relatively constant with alloying Sn content, the fraction of all of the oxidized Cu which was released as soluble cation, $X_{Cu,Soluble}$, defined by Equation 3.5), increased with increased Sn content of the alloy as demonstrated with Figure 3.13b.

$$X_{Cu,Soluble} = \left[\frac{\frac{Q_{Cu,ICP}}{n_{Cu}}}{\frac{Q_{Cu,ICP}}{n_{Cu}} + \frac{Q_{Cu,CR}}{n_{Cu}}}\right] \qquad \text{Equation 3.5}$$

The slightly increased soluble fraction of Cu with increased Sn content may be explained by Sn oxidation preferentially sequestering oxygen at the patina surface disrupting the chemical stability of the cuprous oxide leading to more soluble Cu. Alternatively or in concert, the diminished metal-metal bond strength of the Cu-Sn bond compared to the Sn-Sn bond may increase the propensity of cuprous cation ejection [154].

3.4 Discussion

3.4.1 Patina Enrichment of SnO_2

Thermodynamically, Sn is expected to be oxidized and enriched in the oxide layer as SnO_2 has effectively no solubility in aqueous environments from pH 0 to 10 (Figure 3.1) while Cu_2O has considerable solubility in aqueous solutions. Assuming that both alloying elements oxidize, the binary alloy oxide enriches in the solute element oxide usually due to greater solubility of the solvent (e.g., Cu) in the electrolyte; this enrichment can be chemically dependent e.g., pH. The amount of Sn oxide present in the corrosion product increases with increasing alloying content (Figure 3.10). Cu-Sn bronze alloys are known to form protective patinas of SnO_2. However, the critical value of Sn in the alloy at which Sn forms a continuous oxide film has not previously been systematically evaluated in literature. Both Cu and Sn oxidized at open circuit in artificial perspiration, and indeed Sn was retained as an inner corrosion product film (Figure 3.12) as expected from prior literature [53–55,129,130,132,142,144,146,148,149,154]. Sn oxide enrichment in the patina was verified by: the lack of soluble Sn release (Figure 3.6b), measurements of Sn oxide reduction from coulometric reductions (Figure 3.8), and FIB EDS cross sectional mapping (Figure 3.12). Increasing Sn content in the alloy leads to the surface becoming predominantly Sn-rich as shown with multiple methods (Figure 3.10 and Figure 3.11). This effect is dominant at just a few atomic percent (5-6 at%) of Sn in the alloy. The most apparent evidence to increased SnO_2 on the surface with increasing Sn content of the alloy is demonstrated by CR-determined corrosion product amounts in Figure 3.10.

Both SnO_2 and $Sn(OH)_4$ have remarkable stability over a wide range of pH (Figure 3.1) [126,183,184]. The OCP values (Figure 3.4) are far above the Nernst potential for Sn oxidation (-0.75 V_{SCE}). Many studies acknowledge that Sn oxide is formed by a three step mechanism [183–185]. Sn is first oxidized to $Sn(OH)_2$.

$$Sn(s) + 2H_2O \rightarrow Sn(OH)_2(s) + 2H^+ + 2e^- \qquad \text{Equation 3.6}$$

Sn further oxidizes to the more stable $Sn(OH)_4$.

$$Sn(OH)_2(s) + 2H_2O \rightarrow Sn(OH)_4(s) + 2H^+ + 2e^- \qquad \text{Equation 3.7}$$

And finally, through either greater anodic polarization, time, or sample extraction, dehydrates to the more stable phase, SnO_2.

$$Sn(OH)_4(s) \rightarrow SnO_2(s) + 2H_2O \qquad \text{Equation 3.8}$$

Following the Sn^{4+} dissolution trajectory (dashed line, Equation 3.2) in the chemical stability diagram calculated in Figure 3.1, the pH at the surface is not affected by cathodic charge before chemical precipitation of both $Sn(OH)_4$ and SnO_2. Interesting to note that the thermodynamic reaction sequence conflicts with the published literature. These Sn oxide and hydroxide products are typically difficult to detect due to their amorphous nature [183], indeed the present work also failed to identify any oxidized Sn using thin-film crystal diffraction (Figure 3.2) or Raman spectroscopy (Figure 3.7). SnO_x compounds in the literature have been identified using stoichiometry, charge balance, and indirect electrochemical methods [183]. Yet, there is a paucity of evidence on the existence of the $Sn(OH)_4$ on the surface [185]. While the SnO_2 was protective (i.e. parabolic kinetics, see Figure 3.5b) this layer allowed release of soluble Cu to the environment (Figure 3.14 and Figure 3.13).

The soluble Cu ion concentration in solution remained roughly the same (Figure 3.6, Figure 3.13a) with a slight trend towards increased Cu release with increased Sn content. At greater Sn contents (10 wt%) the SnO_2 layer becomes more continuous across the surface, in contrast with the islands of particles found on the Cu-5Sn alloy patina (Figure 3.11). Yet despite the continuous layer, Cu-10Sn did not show reduction of Cu cation release potentially available for antimicrobial function, (Figure 3.13a).

The enrichment of Sn in the oxide film can be calculated from the oxide reduction data via the relation given by Equation 3.9).

$$X_{Sn,film} = \left[\frac{\frac{Q_{Sn,CR}}{n_{Sn}}}{\frac{Q_{Cu,CR}}{n_{Cu}} + \frac{Q_{Sn,CR}}{n_{Sn}}} \right] \qquad \text{Equation 3.9}$$

The enrichment of Sn in the oxide film is plotted versus the Sn content of the alloy in Figure 3.14. The values obtained from this study are consistent with the cation fractions measured from archaeological artifacts found in atmospheric, aqueous, and edaphic solutions shown by the trend line presented in work reviewed in ref [130]. The plot line of solute enrichment is described by the theory first presented by Seo and Sato [79] and expanded by Kirchheim et al. [65] and is reproduced in Equation 3.10.

$$X_{Sn,film} = \frac{\beta x_{Sn,alloy}}{1 - X_{Sn,alloy} + \beta X_{Sn,alloy}} \qquad \text{Equation 3.10}$$

Where the fractions of Sn in the film ($X_{Sn,film}$) are dependent on the element enrichment ratio (β) and the alloy content ($X_{Sn,alloy}$). The enrichment line is plotted with an enrichment factor of β = 16.5, which gave a good fit between experimental data and matched with archaeological observations.[130] Seo and Sato described this enrichment factor in terms of the relative dissolution rate constants, i.e. $\beta = i_A/i_B$ [79] for an arbitrary AB binary alloy. However, Kirchheim et al. proposed that transport through the oxide film was limiting and that the relative field-assisted diffusion coefficients of the elements (A and B in an arbitrary AB alloy) described the element enrichment factor, i.e., $\beta = D_A/D_B$ [65]. Presumed in this framework is that passivity occurs when the amount of the passive element in the oxide film reaches a critical threshold often associated with a high surface coverage.

3.4.2 Minimum Sn Content for Passivation

Full details pertaining to the derivation of the following are given in Chapter 4. The minimum fraction of Sn in the oxide needed to form a complete inner layer can be found with a few assumptions. In order to minimize the excess interfacial energy [186], a passivating oxide phase at the alloy/oxide interface may be assumed to take the shape of a spherical cap. Thus, the volume fraction of SnO_2 in the patina up to some critical value may be estimated using Equation 3.11.

$$V_{SnO_2} = \frac{\pi}{24}\left(\frac{D}{R}\right)^3 \left[\frac{2 - 3\cos\Theta + \cos^3\Theta}{\sin^3\Theta}\right] \qquad \text{Equation 3.11}$$

Where D is the diameter of the circular base of the SnO_2 oxide island (apparent area at the oxide/alloy interface) and R is the average interparticle spacing between the centers of particles. The contact angle Θ of the SnO_2 particle is shown schematically at the triple point in Figure 3.15, and determined by the relative interphase boundary surface energies, defined by the Young-Laplace equation[186], and given in Equation 3.12.

$$\cos\Theta = \frac{\gamma_{Cu_2O/alloy} - \gamma_{SnO_2/alloy}}{\gamma_{SnO_2/Cu_2O}} \qquad \text{Equation 3.12}$$

Where γ are the interphase boundary surface energies with their respective subscripts. The area fraction of SnO_2 islands which cover the alloy surface is given by Equation 3.13.

$$A_{SnO_2} = \frac{\pi}{4}\left(\frac{D}{R}\right)^2 \qquad \text{Equation 3.13}$$

Assuming that these particles are evenly distributed across the surface, the value of the critical volume fraction at which the oxide islands coalesce can be calculated by substitutions of Equation 3.13 into Equation 3.11 and setting the area fraction to unity (i.e. complete SnO_2 surface coverage), we arrive at a thermodynamically-based expression of the minimum volume fraction of these individual oxide islands which could yield a complete covering layer of oxide.

$$V_{SnO_2,crit} = \frac{1}{3\sqrt{\pi}}\left[\frac{2 - 3\cos\Theta + \cos^3\Theta}{\sin^3\Theta}\right] \qquad \text{Equation 3.14}$$

Equation 3.14) is only dependent on the volume fraction and the contact angle (or 'wettability') of the particle. The contact angle is thermodynamically fixed for a given binary alloy system. The minimum volume fraction thermodynamically required to form a complete layer as a function of the particle contact angle is plotted in Figure 3.16.

Given the surface energies of the interphase boundaries of the oxide/alloy system and the solute oxide volume fraction enrichment factor (e.g., *ß*) the critical alloying content for complete solute oxide coverage can be described. If the second oxide (alloy solute oxide) in question is passivating, this expression (Equation 3.14) together with a volume fraction enrichment function (e.g., similar to Equation 3.10) describes the critical alloying content of an element needed for passivation by its oxide. The predicted threshold values are quite low as is observed with many alloys with passivating oxides (e.g., Cu-7Al, Cu-3Si, Cu-2Be [187]). The volume fraction of SnO_2 was calculated from coulometric reduction data (see Equation 3.9) adjusted with the same oxide density assumptions used to generate the oxide thickness estimations in Figure 3.10. The contact angle was roughly estimated from the measured angle of the SnO_2 particle contact angle in Figure

3.11b and compensated for the observation tilt angle (52°). The value of the contact angle of SnO_2 atop the Cu-Sn alloy surface within Cu_2O was estimated to be about 30°. At this rough value and using only the solute volume fraction enrichment factor of 16.5 (Figure 3.14), the minimum Sn alloying content thermodynamically needed to form a complete layer is only 1 wt% Sn. Thermodynamic interphase surface energy data would improve this prediction significantly. Literature values of bronze artifacts have observed complete inner layers of Sn in alloys as little as 4 wt% Sn [130]. Given greater exposure time the Cu-5Sn may form a conformal SnO_2 layer as predicted by the proposed threshold and observed in archeological artifacts [130]. A 96-h exposure may not be sufficient time to alloy the oxides to form thermodynamically favored interfacial morphologies. Consequently, the approximation of contact angle from these FIB-prepared cross sections is perhaps not sufficient to accurately describe the interphase surface energies. However, these results qualitatively agree well with the proposed theory, as one would expect to observe a sharp increase of solute oxide volume fraction for alloys beyond the critical threshold value. Complete coverage of an inner layer would inhibit growth of an outer layer as was observed on the Cu-10Sn alloy in Figure 3.11c.

3.5 Conclusions

- Open circuit exposures in artificial perspiration for 96h revealed elevated potentials, and greater tarnishing for Cu-Sn alloys with Sn contents $\geq$ 5 wt%.

- Coulometric reductions revealed a change in primary corrosion products with increasing Sn content in the alloy from Cu_2O-dominant to SnO_2-dominant, with this transition taking place at a Sn alloy content of 5 wt%.

- Sn oxides on alloys with moderate Sn contents (Cu-5Sn) were restricted into oxide islands, phase-separated, porous, and discontinuous at the alloy/patina surface as revealed by FIB and EDS.

- The minimum amount of Sn in the alloy needed to passivate was revealed to be 1 wt% Sn when considering the combined effects of thermodynamic surface energetics and SnO_2 patina enrichment.

- Chloride was observed throughout the porous outer cuprite (Cu_2O) layer via EDS of FIB-prepared corrosion product cross sections but was not observed to incorporate into the inner Sn oxide layer/islands.

- At greater amounts of Sn in the Cu-Sn system (10 wt%), the corrosion product film become predominantly Sn oxide which was more conformal to the alloy surface but was not shown to inhibit soluble Cu release. The fraction of soluble Cu release to Cu corrosion products was increased with increasing Sn.

Tables

Table 3-1. Commercial copper, tin and copper-tin alloy compositions (wt%). Alloy composition testing performed *via* ICP analysis according to ASTM E478 [133]. Pure elements tested using glow-discharge mass spectroscopy (GDMS). Unreported elements < 0.01 wt%.

Alloy	Cu	Sn	Other
Cu	99.997	--	--
Cu-0.1Sn	99.90	0.10	--
Cu-1Sn	98.98	1.02	--
Cu-5Sn	95.01	4.99	--
Cu-10Sn	89.6	10.4	--
Sn	0.04	99.83	0.08 Sb, 0.04 Pb, 0.01 In

Table 3-2. Artificial perspiration solution composition. Based on [48].

Chemical Name	g/L	Molarity (mM)
NaCl – Sodium Chloride	5.00	85.6
CH_4N_2O - Urea	1.00	16.7
$C_3H_6O_3$ - L(+) Lactic Acid (90%)	1.00	11.1
NH_4OH – Ammonium Hydroxide	pH Adjuster	~11

Table 3-3. Anodic charge density (Coul/cm²) of individual corrosion products following 96 h at open circuit in artificial perspiration. Insoluble corrosion product amounts were determined via coulometric reduction (CR) and soluble Cu via ICP-OES. Total anodic charge is the sum of insoluble and soluble products determined at standard error is reported.

Alloy (wt%)	**Sn (at%)**	**CuCl**	**Cu_2O**	**SnO_2**	**Cu^+**	**Total**	**Mass Loss**
		Coulomb cm^{-2}					(Cu^+, Sn^{4+})
Cu	<0.01	< 0.01	0.31	--	0.75	1.1 ±0.1	1.9 ±0.1
Cu-0.1Sn	0.05	< 0.01	0.19	0.13	0.77	1.1 ±0.1	2.7 ±0.5
Cu-1Sn	0.54	< 0.01	0.25	0.07	0.66	1.0 ±0.2	2.4 ±0.4
Cu-5Sn	2.74	0.14	0.21	0.20	0.91	1.5 ±0.3	1.9 ±0.2
Cu-10Sn	5.61	0.02	0.14	0.97	0.79	1.9 ±0.2	2.7 ±0.3
Sn	>99.9	--	--	0.02	--	0.02 ±0.002	0.8 ±0.1

Figures

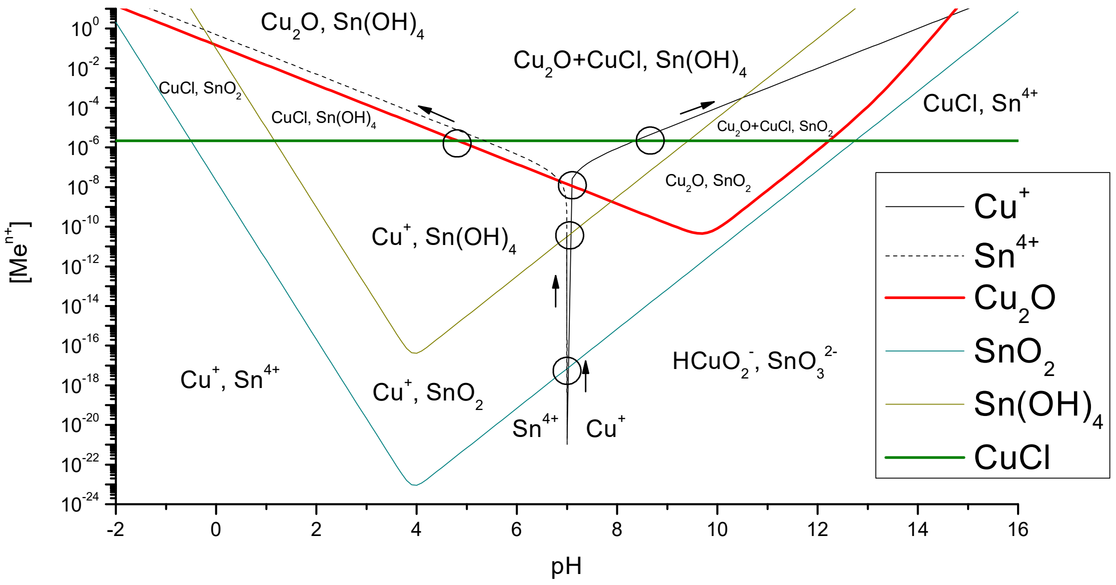

Figure 3.1. Chemical stability diagrams (superimposed) of copper and tin oxides in artificial perspiration solution as a function of pH values. Metal dissolution trajectory see Equation 3.2, indicated by arrows alongside the plot of pH compensation by metal dissolution. Equilibrium values plotted for 0 V_{SCE}. Intersection points highlight the pH and metal ion concentration satisfying chemical equilibrium of species of interest (see text).

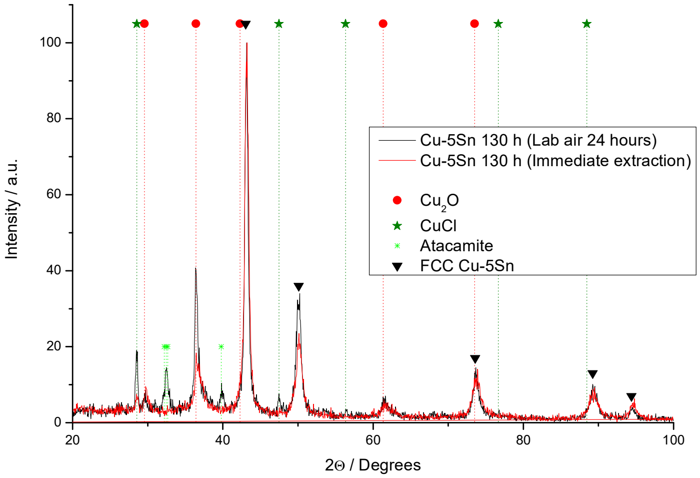

Figure 3.2. GIXRD measurements of Cu-5Sn following 130 h in artificial perspiration measured immediately after extraction and after 24h exposed in lab air.

Cu Cu-0.1Sn Cu-1Sn Cu-5Sn Cu-10Sn

Figure 3.3. Visual condition of Cu and Cu-Sn samples post-exposure following open circuit in artificial perspiration solution after 96 hours. Ø = 1 cm.

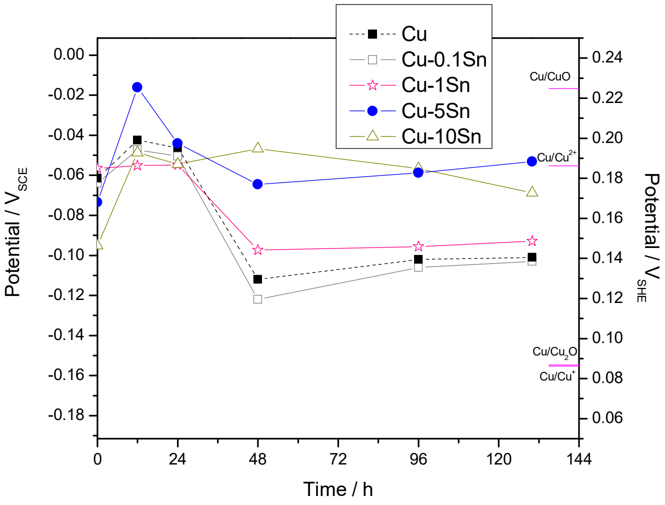

Figure 3.4. Open circuit potential of commercially pure Cu and Sn compared to high-purity model Cu-Sn alloys fully immersed in naturally-aerated artificial perspiration solution (pH 6.5) up to 130 hours. Selected relevant Nernst potentials for half-cell reactions (non-complexed) are overlaid on graph. (E_r: $Sn/SnO_2 \rightarrow -0.75\ V_{SCE}$, off scale and not shown). Pure Sn OCP ≈ $^{-}$0.45 V_{SCE} (not visible on this scale).

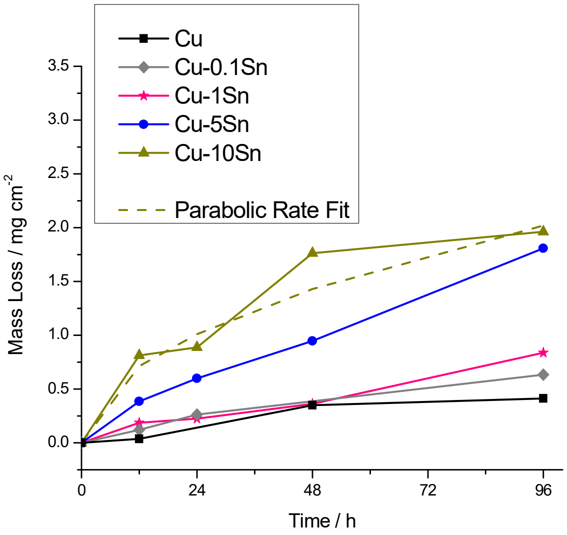

Figure 3.5. Gravimetric mass loss of Cu, and Cu-Sn alloys in artificial perspiration at specified time points up to 96h. Corrosion product removal for mass loss facilitated by 2-3 min exposure to 6M HCl. Dashed line is a numerical fit to the parabolic expression $m=kt^{½}$.

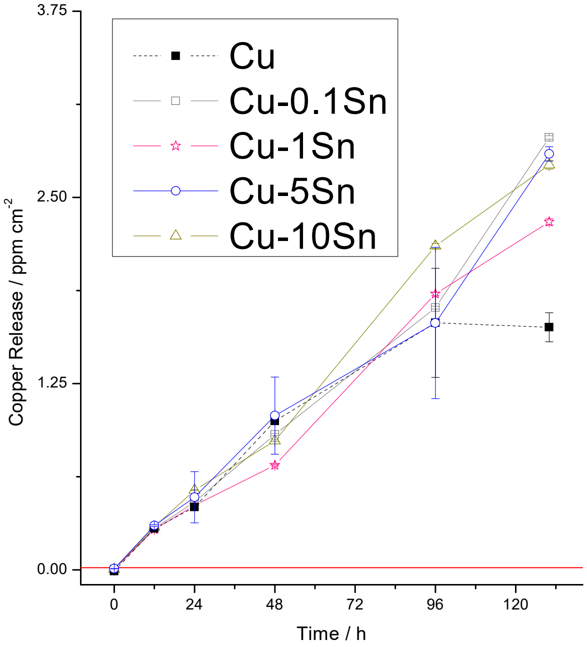

Figure 3.6. Copper release available for antimicrobial function measured via ICP-OES (red line: Cu LOD). Tin release was below LOD of ~40 ppb. Soluble ion concentration in artificial perspiration solution was measured from aliquots of solution taken from open circuit corrosion cells at specified time points. Exposed area 0.8 cm², solution volume 300 mL. Error bars are standard error of three measurements of the aliquot.

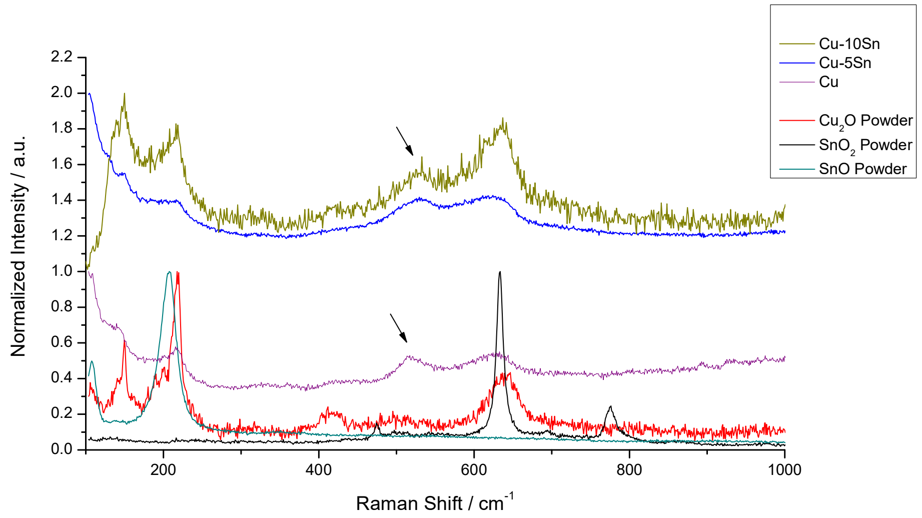

Figure 3.7. Raman spectroscopy on surfaces of Cu-Sn samples (Cu-0.1Sn and Cu-1Sn excluded for clarity) following 130 h in artificial perspiration compared with prepared standard powder pellet references of Cu_2O and SnO_2.

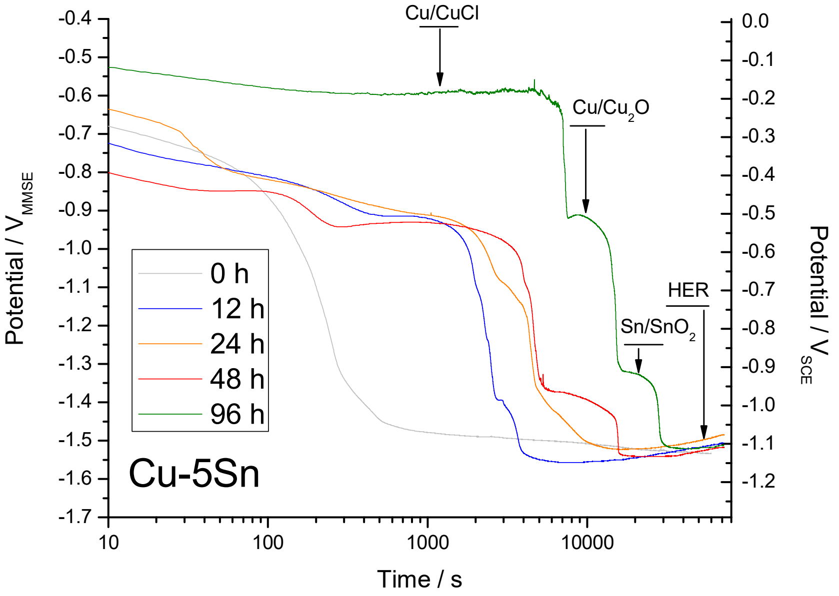

Figure 3.8. Example coulometric cathodic reduction in deaerated borate buffer (pH 8.4) of Cu-Sn alloys following exposures in artificial perspiration solution at open circuit up to 96 hours. Applied cathodic current density of -25 μA/cm².

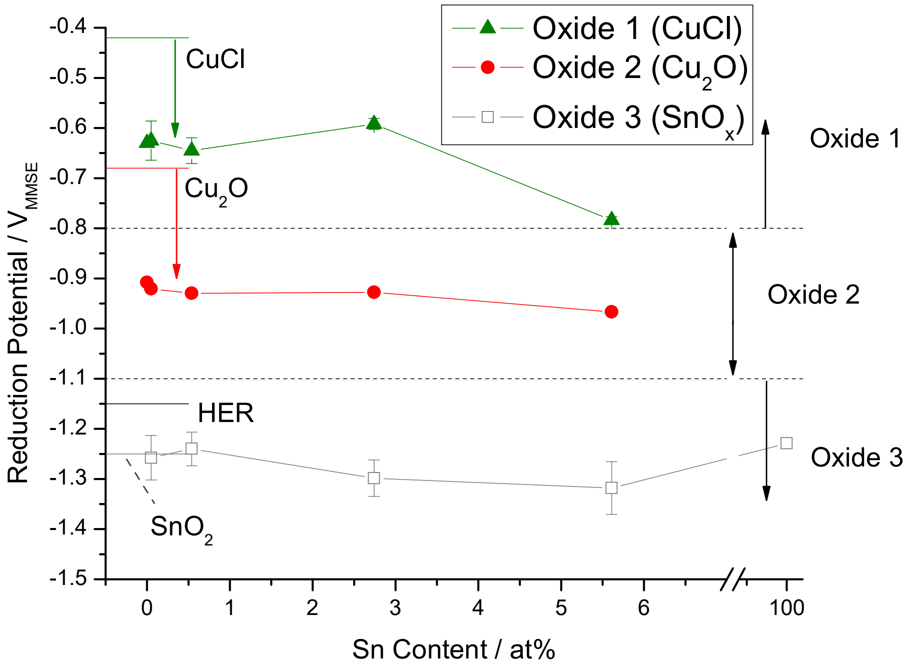

Figure 3.9. Reduction potentials of corrosion products formed on Cu-Sn alloys following 96h in artificial perspiration. A reduction potential was defined at the midpoint between reduction plateaus determined from a first-derivative analysis (see text). Reversible Nernst potentials for reductions of interest are indicate on graph. Oxide definitions are based on reduction potential ranges: Oxide 1: $E > -0.8\ V_{MMSE}$, Oxide 2: $-1.1\ V_{MMSE} \leq E \leq -0.8\ V_{MMSE}$, Oxide 3: $E < -1.1\ V_{MMSE}$. Standard error bars from three replicate samples for Oxide 2 reduction are not visible on this scale.

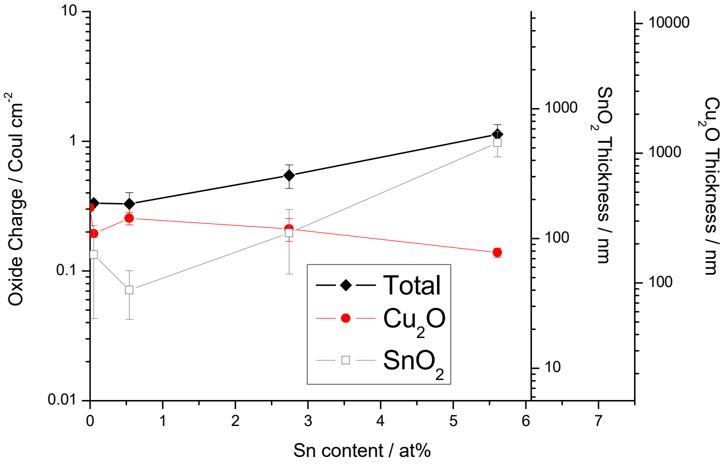

Figure 3.10. Change of primary oxide coverage with increasing Sn content. Corrosion product charge (Equation 3.1) on high-purity model Cu-Sn alloys following 96 h of artificial perspiration. CuCl excluded for clarity (see text). Oxide definitions are based on reduction potential plateaus in set potential ranges; Cu_2O: $-1.1\ V_{MMSE} \leq E \leq -0.8\ V_{MMSE}$, SnO_2: $E < -1.1\ V_{MMSE}$ (see Figure 3.9). Faradaic conversions of charge to approximate thickness are given on the right axes. Assumed densities of SnO_2 and Cu_2O are 6.95 and 6.00 g/cm³, respectively.

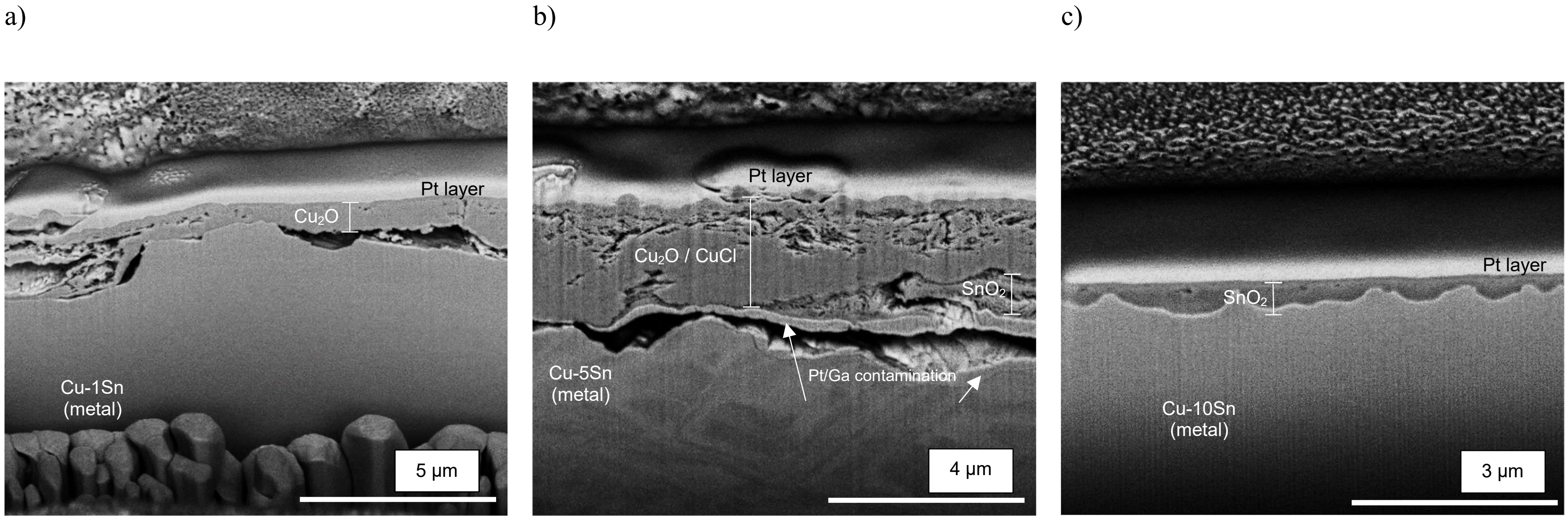

Figure 3.11. Secondary electron images of FIB cross-sections of a) Cu-1Sn, b) Cu-5Sn, and c) Cu-10Sn alloys following 96h in artificial perspiration at open circuit. Areas above the Pt layer are the ion beam damaged surface. Gallium and platinum contamination (determined via EDS) caused during milling is visible on the edges of the metal/oxide interface delamination in b).

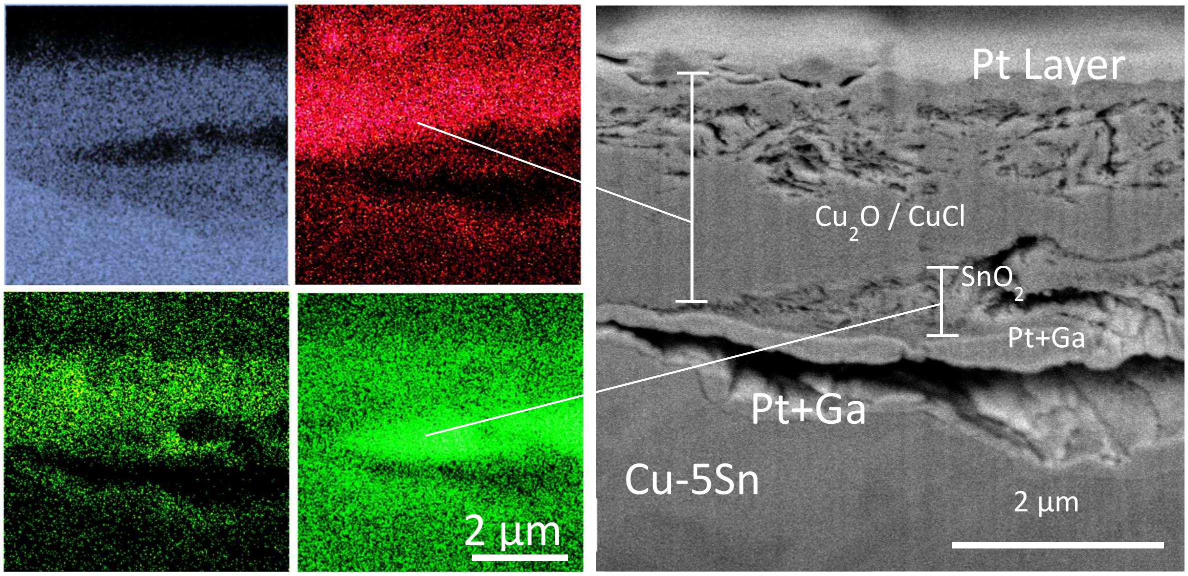

Figure 3.12. Elemental EDS mapping (left) and secondary electron image (right) on FIB-prepared cross-section of corrosion products formed on Cu-5Sn following 96h in artificial perspiration. Pt/Ga indicate Pt and Ga contamination from ion milling (confirmed with EDS).

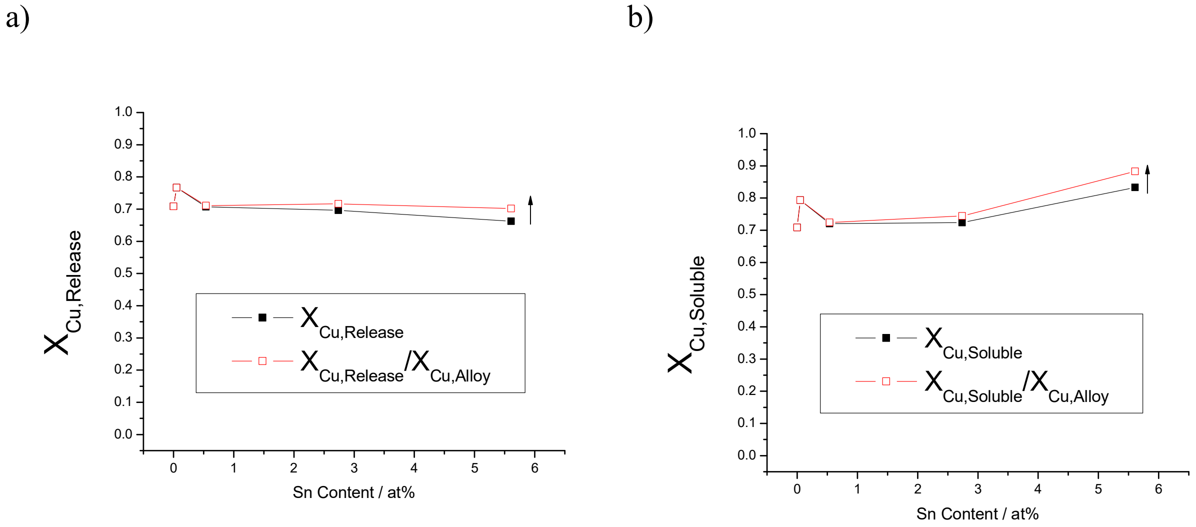

Figure 3.13. Alloying effects of Sn on Cu oxidation products from Cu-Sn alloys exposed to artificial perspiration for 96 h: a) fraction of soluble Cu released from total oxidation products (see Equation 3.4), and b) fraction of soluble Cu from total copper oxidation products (see Equation 3.5).

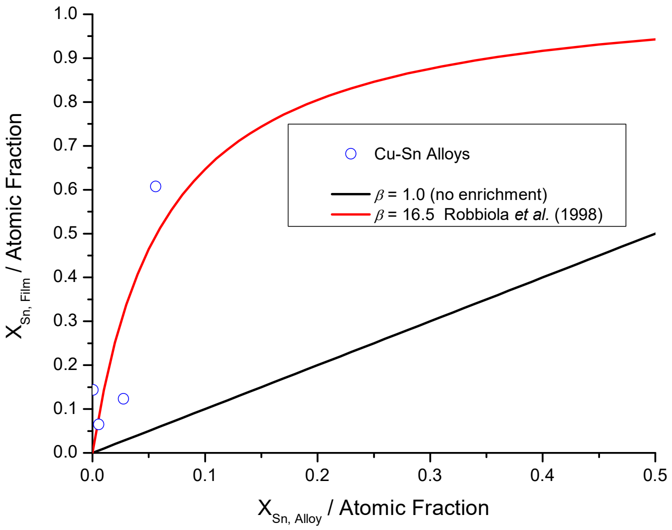

Figure 3.14. Sn enrichment in the corrosion product layer as a function of alloying content. Data points converted using Equation 3.9 in text, enrichment plot calculated using Equation 3.10. Where $\beta = 16.5$ is a good fit to experimental data in agreement with literature observations of archaeological patinas on bronze artifacts [130].

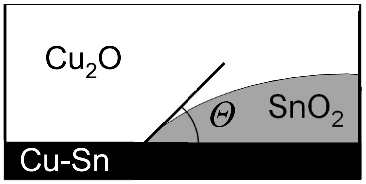

Figure 3.15. Geometry of the Cu_2O/SnO_2/Cu-Sn triple point. The contact angle (Θ) is defined by Equation 3.12.

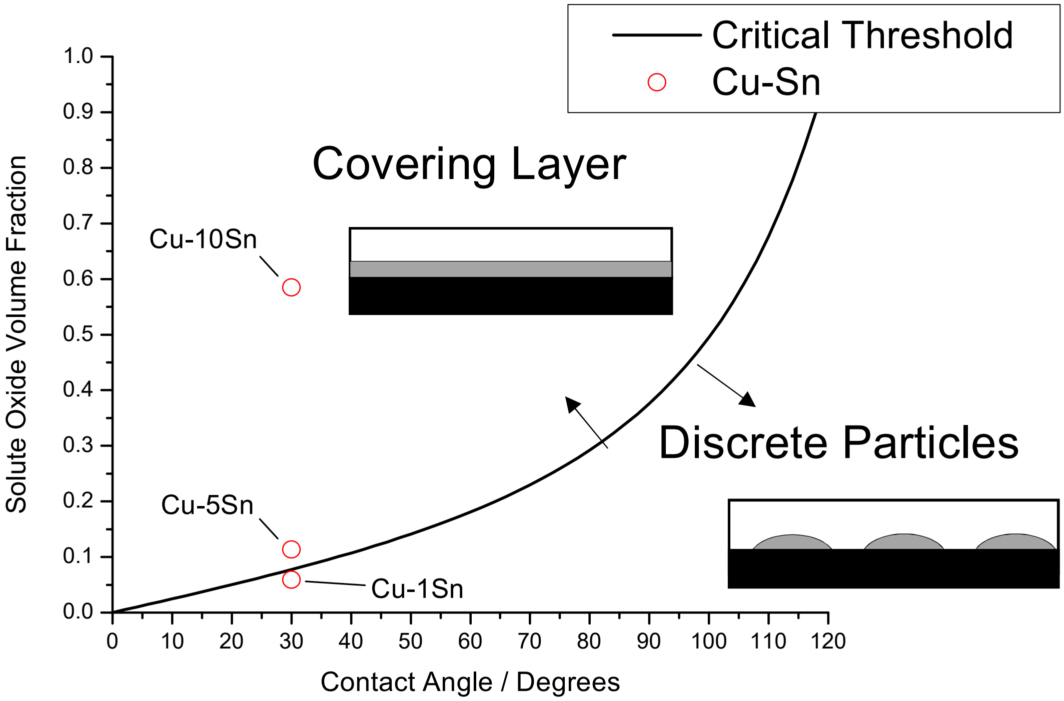

Figure 3.16. Critical solute oxide (e.g., SnO_2) volume fraction in the oxide film to form a complete layer from Equation 3.14. Experimentally found volume fractions calculated from measured anodic charge values with the same density and molecular weight assumptions from Figure 3.10. Contact angle) estimated at 30° from FIB measurements correcting for the 52° observation tilt.

4 Alloying Passivity: Theoretical Predictions and Critical Thresholds

Abstract

Minor concentration of a passivating element such as Cr, Al, or Ti can significantly improve corrosion resistance through passivation of a number of alloys. However, empirical methods are needed to determine the minimum amount of alloying element required to passivate alloys in various environments. Alloying-endued passivity is contingent upon two critical factors: 1) enrichment of the passive element in the surface oxide film, and 2) minimum alloy contents needed to passivate the alloy according to some criterion such as surface coverage e.g., 12 wt% Cr in stainless steel. Experimental values and theoretical predictions regarding solute-enrichment and minimum threshold alloy values have been carried out in the literature however, until now, have not been combined in a single framework. In this chapter, contemporary passivity theories are extended to include solute enrichment for alloys with any number of elements. Enrichment theory is herein combined with a new theory to predict the minimum threshold value for passivation of a binary alloy based on surface coverage enabled by wetting phenomena assuming a protective oxide at the alloy/oxide interface. This minimum threshold is defined by complete surface coverage of immiscible passive oxides whose thermodynamically or kinetically favored geometry is assumed to be determined by interphase surface energetics of the oxides with one another and the alloy. This framework has the potential to predict minimum alloying passivity thresholds based on thermodynamic surface energetics associated with wetting phenomena, and electrochemical kinetics.

4.1 Background

In the case of antimicrobial alloys, passivity needs to be avoided to ensure the continuous release of soluble cytotoxic Cu(I) and Cu(II) cations through active corrosion[26]. Passivation is defined as the situation where a resistive metal oxide forms that is conformal to the metal substrate and controls the anodic dissolution rate [77]. This oxide must be chemically stable and can vary from a few nanometers thick, as in chromium, titanium, and aluminum oxides, to several micrometers thick as in copper and tin oxides [77]. The passive oxide film found on natively passive elements (e.g., Ni, Cr, Al) can also be grown on an alloy. A ubiquitous modern example is Cr in stainless steel, Fe-Cr.

In high-temperature oxidation of multi-element alloys, the relative stability, solid-state cation solubility, and cation diffusivities lead to multiple oxide configurations and element concentration gradients [188]. For simplicity we will consider the cases of a binary AB alloy where both elements oxidize: when oxidized A forms a soluble or non-protective oxide (AO), oxidized B may be soluble in the solid state within the parent AO or B will form a separate protective oxide (BO) in a physical mixture with AO. When solubility of a B cation in the parent AO oxide is exceeded, supersaturation drives chemical precipitation of a new oxide phase of BO [188].

Predicting passivity for elements in the case of an AB alloy where both elements oxidize is contingent upon to two critical factors: (1) predicting the enrichment of the passive element B cation fraction in the surface oxide as a function of alloying content regardless of solubility, and (2) predicting the threshold value of passive element B enrichment in the surface oxide to ensure passivity. Experimentally-derived values of element enrichment and thresholds have been determined for many passive systems [78,189–195] and are a complicated function of solution chemistry, pH, and oxide chemical stability. Some observed minimum alloying thresholds are listed in Table 4-1 however, a theoretical description/prediction of critical values for solute-endued passivity is lacking.

4.2 Solute Element Enrichment in Surface Films

4.2.1 Binary and Ternary Alloys Enrichment

In an attempt to describe the alloy content dependence on passivity, Kericheim *et al.* [65] proposed that the preferential dissolution of non-passivating (solvent, A) elements leads to an enriched cation fraction of passive elements (solute, B) in the remaining surface oxide film at steady-state. An alloy can become passive when enough of the passivating alloying element (B) in the metal has enriched on the surface oxide film. Their model describing this enrichment as a function of alloying content for binary AB alloys where B is the passive element is given by Equation 4.1.

$$x_{B,f} = \frac{\beta x_{B,a}}{1 - x_{B,a} + \beta x_{B,a}} \qquad \text{Equation 4.1}$$

Where $x_{B,f}$ is the cation fraction of B in the film. Beta (β) is defined as the solute enrichment factor and $x_{B,a}$ is the alloy fraction (at%) in the alloy. In the case where AO and BO oxides are soluble in one another in the solid state, dissolution is restricted by cation diffusion through the mixed metal cation oxide film (i.e. Cabrera-Mott condition [196]) then β is determined from the relative cation diffusivities ($\beta = D_A/D_B$) [65]. Whereas in the case of immiscible oxides, the relative dissolution rate constants determine the enrichment factor ($\beta = k_A/k_B$) [65,72,79]. The result of this expression is plotted for several enrichment factors (β) in Figure 4.1. For Fe-Cr alloys, $\beta = 8$ i.e., that Fe is 8x more mobile/soluble than Cr [65].

Extending this idea further, for a ternary Ni-based alloy, Marcus and Grimal [72] also present an enrichment-based description of passivity from variable dissolution from solute enrichment on the alloy surface. However, the assumptions are not violated when considering dissolution through an oxide film. The cation fraction of a passivating element (*B*) in the surface film as a function of the alloying elements in a ternary A-B-C alloy is described by the following expression.

$$x_B^s = \alpha_{A,B}\left(\frac{x_B^b}{x_A^b}\right)\left[1/\left(1+\frac{\alpha_{A,B}x_B^b}{x_A^b}+\frac{\alpha_{A,C}x_C^b}{x_A^b}\right)\right] \qquad \text{Equation 4.2}$$

With $x_B^b \in [0, (1 - x_C^b)]$ when x_C^b is held constant

Where the superscripts *b* denotes bulk (alloy) concentrations *x*, and a superscript *s* denoting a surface concentration. The dissolution rate constant ratios (k_A/k_B) or relative cation diffusivities (D_A/D_B) are encompassed by the parameter $\alpha_{A,B}$ with similar assignment for the other *α* system constants (i.e. $\alpha_{A,C} = k_A/k_C$). The resultant expression gives a theoretical description of the cation fraction of *B* in the surface film which is plotted for several enrichment factors ($\alpha_{A,B}$) in Figure 4.2. Fitting values from angle-resolved XPS measured cation fractions of surface oxides formed on a ternary Ni-21Cr-8Fe lead to values of $\alpha_{Ni,Cr}$ = 11.8 and an assumed $\alpha_{Ni,Fe}$ = 1.0 [72]. Due to the high specific release of Ni and the low Fe content, the assumption of $\alpha_{Ni,Fe}$ =1.0 does not affect the results to a significant extent. The resulting Cr concentration rises sharply up to 15% Cr which fits well with the inference of a passivity threshold on these alloys at these Cr contents.

The critical component to these theories are the enrichment factors: *ß* and *α* which represent the relative dissolution rates, or cation diffusivities at steady-state, for the components in a binary or ternary alloy, respectively. The somewhat vague or indefinite assignments of these parameters do little to detract from the theories' predictive abilities. In fact, originally derived to describe preferential sputtering [72,197], enrichment theory is able describe many phenomena and may be applied to a variety of oxide films which passivate, in both thick and thin oxide films as well as soluble and insoluble oxides [79,130].

4.2.2 N-Element Enrichment Theory

Most alloys contain more than just two or three components, and emerging corrosion-resistant alloys contain up to five or more elements [44]. A desirable extension would be to derive this oxide enrichment expression for an alloy with any 'n'-number of elements.

Under steady-state dissolution, the oxide film is fully-developed chemically. The dissolution rate of element *M*, V_M, at steady state is assumed to be linearly proportional to its surface (or oxide) concentration (C_M^s) through the dissolution rate constant k_M.

$$V_M = k_M C_M^s \qquad \text{Equation 4.3}$$

At steady-state with congruent dissolution (no dealloying is taking place), the film is fully-developed and is neither growing nor shrinking therefore, the ratio of the dissolution rates of the alloy constituent metals is assumed to be reflective of their bulk concentrations (C_M^b).

$$\frac{V_{M1}}{V_{M2}} = \frac{C_{M1}^b}{C_{M2}^b} \qquad \text{Equation 4.4}$$

Thus combining Equation 4.3 with Equation 4.4,

$$\frac{k_{M1} C_{M1}^s}{k_{M2} C_{M2}^s} = \frac{C_{M1}^b}{C_{M2}^b} \qquad \text{Equation 4.5}$$

And solving for C_{M2}^s,

$$C_{M2}^s = \left(\frac{k_{M1}}{k_{M2}}\right)\left(\frac{C_{M2}^b}{C_{M1}^b}\right) C_{M1}^s \qquad \text{Equation 4.6}$$

Similarly, we could express another alloying element (*M3*) with respect to M_1

$$C_{M3}^{s} = \left(\frac{k_{M1}}{k_{M3}}\right)\left(\frac{C_{M3}^{b}}{C_{M1}^{b}}\right)C_{M1}^{s} \qquad \text{Equation 4.7}$$

Note how this separate description does not depend on another alloying element so long as the condition above (Equation 4.4) is met. Up until this point we have followed the derivation of Marcus and Grimal [72]. We may extend this, dropping the notation of individual *M1*, *M2*, *M3*, etc. to the subscript *j*, denoting the alloying element of interest beyond the base element (*M*) in the alloy. The assignment of element base (*M*) is arbitrary but may be mathematically convenient to select one which has the greatest alloy content, or in the case of equiatomic high entropy alloys with five or more elements, the greatest dissolution rate in the corroding media of interest, (e.g., Fe, Cu, Zn).

$$C_{j}^{s} = \left(\frac{k_{M}}{k_{j}}\right)\left(\frac{C_{j}^{b}}{C_{M}^{b}}\right)C_{M}^{s} \qquad \text{Equation 4.8}$$

These assumptions give us one unique expression per alloying element excluding the base alloy element, *M*. This assumes that k is constant and independent of other alloying elements present regardless of composition. We can form a determinate set of expressions by simply imposing the condition of the alloy composition:

$$C_{M}^{b} + \sum_{n} C_{n}^{b} = 1 \qquad \text{Equation 4.9}$$

Where *n* represents the alloying elements beyond the base *M* e.g., Cr and Fe in Ni-Cr-Fe. Combining Equation 4.9 with Equation 4.8 gives the enrichment of any given element *j* from the alloying content and the dissolution rate constants for an alloy with any ‘n’-number of elements.

$$C_j^s = \frac{\frac{k_M}{k_j} C_j^b}{C_M^b + \sum_n \frac{k_M}{k_n} C_n^b}$$

Equation 4.10

$$\text{With } C_j^b \in [0, (1 - \sum_n x_n^b)]$$

This theory assumes that the dissolution rate constants are independent of alloying content or alloy structure, i.e. the dissolution rate constants are not affected by other solutes. The selection of the solvent in this case is arbitrary. Adhering to the same assumptions of Kericheim *et al.* [65], miscible oxides of a single phase can be described by the Cabrera-Mott model [88] then the dissolution rate constants are replaced by the cation diffusivities ($k_M \rightarrow D_M$) [65] though the oxide film. This case is given by the expression in Equation 4.11.

$$C_j^s = \frac{\frac{D_M}{D_j} C_j^b}{C_M^b + \sum_n \frac{D_M}{D_n} C_n^b}$$

Equation 4.11

$$\text{With } C_j^b \in [0, (1 - \sum_n x_n^b)]$$

4.3 Critical Passivating Solute Thresholds in Surface Oxides

Solute-endued passivation requires a minimum amount of the passivating element to protect the alloy from corrosion. Experimentally-observed alloying thresholds for several binary alloy systems are listed in Table 4-1. The critical threshold is not solely dependent on the solute or the solvent element as demonstrated by the various critical Cr values in multiple systems listed in Table 4-1. Several theories have been proposed to predict or explain the threshold solute values for solute-endued passivity. Passive element enrichment theories such as those presented by Kirchheim et al., Marcus, and others [65,72,78,79] serve to describe the cation fractions in the film and provide predictions of continuous functions of solute enrichment (e.g., Figure 4.1 and Figure 4.2) but lack clear demarcations of passive or active alloy composition ranges observed in real systems [76,191]. An underlying assumption in these theories which remains unaddressed is that there exists a critical cation fraction value of the passive alloy element (e.g., $x_{B,f}$ or $x_B{}^s \geq 0.4$) in the surface oxide at which the alloy becomes passive. The question arises as to the origin of this critical threshold and subsequently, how to predict its value as a function of tractable parameters. There are several theoretical developments in the literature which aim to define the minimum threshold value of a passivating element such as Cr, Al, and Ti in the alloy at which the alloy can become passive.

4.3.1 No Oxide: Percolation Theory

Percolation theory [69,70] predicts that the probability for a continuous and passivating oxide is determined by the degree of connectivity of the passive element atoms in the metal lattice, rather than the oxide lattice. As dissolution progresses, active elements are selectively dissolved, i.e. dealloyed, and passive elements are left behind, protected from dissolution by binding with oxygen. The solute passivating elements (e.g., Cr, Ti, Al) must be close enough together in the metal solution to be linked or bridged by adsorbed oxygen atoms continuously. At some critical amount the passive elements become sufficiently connected in the metal lattice such that the passive elements are linked by bound oxygen, or form a covering surface net, which blocks further dissolution. Sharp alloy solute thresholds are usually observed e.g., 12 wt% Cr in stainless steel [59,191] and this theory predicts that past this percolation threshold the probability of a passive film rises sharply when surfaces become covered and dramatically increases with increasing passivating solute content past this critical value. Using a hard-sphere ionic radii model and a random distribution of Cr atoms, the Fe-Cr passivation threshold is predicted at 10 at% for the

BCC lattice, and for the FCC lattice at 12 at%. At these values, the probability is very high of finding Cr atoms in the metal lattice sufficiently close enough to be bridged by co-bound oxygen at expected Me-O bond lengths, arresting further dissolution via percolation of this lattice structure via selective Fe dissolution. The key advantage of this theory is the prediction of metal crystal structure-dependence of solute-endued passivation [69,70]. However, this theory also depends the assumption of selective dissolution of the non-passivating element from the surface without any incorporation in the oxide. In fact, percolation theory ignores the presence of a 3D oxide structure altogether, assuming an adsorbed layer of oxygen or covering surface net is all that is required for passivity. Also, percolation theory does not include effects of surface diffusion or reconstruction or offer insight to enrichment functions of solutes observed in the surface film.

4.3.2 Miscible Oxides: Graph Theory

McCafferty used mathematical Graph Theory [74–77] to propose that the passivating 3D BO oxide must have a degree of continuousness across metal-oxygen bridges. The crystal structures of the passivating oxide (e.g., Cr_2O_3) are reduced to mathematical abstractions known as 'graphs': networks of nodes and bridges. The solvent oxidized atoms (A) randomly disrupt the metal oxygen 'bridges' of the BO oxide to a degree respective of the relative valences of A and B, reducing the degree of connectivity. The oxide becomes passivating when the decreasing cation fraction of 'disruptive' solvent (A) atoms in the BO oxide film structure does not cause any more relative disruption in the degree of 'connectedness' (via the Randic index [74]). For the Fe-Cr example, a cation fraction of 0.7 Fe^{3+} or lower in a Cr_2O_3 structure does not cause any relative change in the degree of 'connectedness' of the passive oxide Cr cation 'graph' meaning that the film can become passive when the Cr^{3+} cation fraction in the oxide film exceeds 30 at% for randomly situated Cr^{3+}. A problem arises as this theory does not directly predict how alloying content relates to the cation fractions in the film. However, surface chemistry (e.g., XPS) data or an effective solute film-enrichment theory (e.g., Equation 4.10) of these films could be used to define threshold predictions of this application of graph theory to other alloy systems.

4.3.3 Immiscible Oxides: Thermodynamic Threshold for Complete Layer Coverage

Graph theory assumes complete miscibility of the base alloy component in the passivating solute oxide (e.g., Fe^{3+} in Cr_2O_3). However, some systems such as Cu-Sn, one component's cation is not soluble in the parent oxide e.g., Sn^{4+} in Cu_2O or Cu^+ in SnO_2 (see Chapter 3). In this case pure oxide phases or distinct mixed oxide (spinel) phases will form. The following section attempts to address this gap in knowledge regarding the minimum threshold value for immiscible systems or oxides which have exceeded the cation solubility limit of B in AO such that precipitation of BO occurs. This minimum threshold can be defined by complete surface coverage of passive oxides that must adopt a geometry such as a conformal layer or hemispherical islands to minimize surface energy. The surface-to-volume ratio is minimized by taking a spherical particle shape and decreases with increasing spherical radius. Thermodynamically-favored geometry is assumed to be determined by interphase surface energetics of the oxides and alloy but may be controlled by other factors such as kinetics. The following assumes that the shape of the oxide islands is defined by thermodynamic rather than kinetic considerations.

Consider a binary alloy (AB) where A is the alloy solvent metal element (e.g., Cu), and B is the solute alloy element (e.g., Sn). AO is the solvent oxide (e.g., Cu_2O), and BO is the solute oxide (e.g., SnO_2) again, assuming no cation solubility in the primary AO oxide. Assumed here is that the oxides are distinct separate phases and that the solute oxide (BO) is present as randomly distributed islands at the alloy/oxide interface. The extreme cases for low and high-volume fractions of BO in the oxide film are illustrated in Figure 4.3. At low solute (B) contents, the oxide is restricted from forming a conformal layer (Figure 4.3a). At higher alloy solute (B) contents, there is enough BO on the surface to form a complete layer and potentially passivate the alloy (Figure 4.3b). For the purposes of this discussion, we will assume that the islands of BO are randomly precipitated at the alloy/oxide interface. In classic precipitation theory: the heterogeneously precipitated oxide island is assumed to 'wet' the alloy surface in the shape of a hemispherical cap [186] reducing total excess free energy from generating a new interphase surface. The geometry of the triple point of contact is determined by the relative surface energies and is illustrated in Figure 3.15. At the temperature of interest, BO is insoluble in AO. We may assume the contact angle of the BO island from the geometry of the balanced line tension forces at the triple point where BO, AO, and AB surfaces meet. The contact angle, defined by the Young-Laplace equation [186], is given by the relation in Equation 4.12.

$$\cos\Theta = \frac{\gamma_{AO/AB} - \gamma_{BO/AB}}{\gamma_{BO/AO}} \qquad \text{Equation 4.12}$$

Where γ is the surface energy of the respective interphase oxide boundary according to the subscripts as indicated. The critical radius (r) of this island can also be determined from the energy balance between excess surface energy of the oxides interphase boundary, and the free energy reduction from the volume of the island thermodynamically formed [186].

$$r = \frac{2\gamma_{AO/BO}}{\Delta G_{v,BO}} \qquad \text{Equation 4.13}$$

The free energy gain per unit volume ($\Delta G_{v,BO}$) of a BO island formed at the AB interface via an electrochemical reaction [198] is given by Equation 4.14.

$$\Delta G_{v,BO} = \frac{-n_{BO} F \rho_{BO} \Delta E}{MW_{BO}} \qquad \text{Equation 4.14}$$

Where n_{BO} is the valence of BO, F is Faraday's constant, ρ_{BO} is the density of BO, ΔE is the overvoltage versus the equilibrium oxide formation potential, and MW_{BO} is the molecular weight of BO. The values of r and $\Delta G_{v,BO}$ are not strictly necessary for the determination of the critical solute content required for passivation as will be demonstrated later but may be used to independently determine the volume fraction leading up to this value.

The geometry and dimension labels of a hemispherical cap (assumed shape of BO island) are described graphically by Figure 4.5. The base diameter of the hemispherical cap (D), and the apparent diameter at the BO/AB surface, can be determined geometrically from the critical radius (Equation 4.13) and the contact angle (Equation 4.15).

$$D = 2r \sin \Theta \qquad \text{Equation 4.15}$$

It is desirable for later mathematical convenience to describe the volume of the hemispherical cap in terms of the base diameter and the contact angle at the surface. The volume of the BO island can be found using integral calculus and is given by Equation 4.16.

$$v_{cap} = \frac{\pi}{24} D^3 \left[\frac{2 - 3\cos\Theta + \cos^3\Theta}{\sin^3\Theta} \right] \qquad \text{Equation 4.16}$$

It is assumed that passivity of the oxide is achieved when the solute oxide islands become sufficiently large and/or numerous to completely block the surface or achieve a very high surface coverage. The apparent area fraction of the BO islands needs to be scaled to the average island spacing (R) a free-floating parameter constrained by other parameters (e.g., the relative BO volume fraction and oxide island geometry) which is schematically described in Figure 4.6. As the dimension of the island's apparent diameter increases relatively with respect the average inter-island center-to-center spacing (R), the fractional area coverage of the BO islands increases according to Equation 4.17.[7]

$$A_{BO} = \frac{\pi}{4}\left(\frac{D}{R}\right)^2 \qquad \text{Equation 4.17}$$

We now have all the necessary factors to form a relationship between the relative volume fraction of the oxides, regardless of thickness, and the fractional area coverage of the island as a function of BO island contact angle. The contact angle is dependent for each system based on the relative surface energies of the island/oxide/alloy interfaces (see Equation 4.12) where BO is buried beneath an AO oxide. However, we still need to constrain the island dimensions with the volume fraction. Recall that an assumption to the theory is that the passivating oxide is restricted to the oxide/alloy interface with no free particles embedded in the parent oxide film to reduce excess surface energy. The thickness of the film is assumed to be on the order of R. The volume fraction of BO is given by the volume of the individual island (Equation 4.16) with the volume density, also expressed in terms of the inter-island density (R^{-3}) given by Equation 4.18.

$$V_{BO} = \frac{\pi}{24}\left(\frac{D}{R}\right)^3 \left[\frac{2 - 3\cos\Theta + \cos^3\Theta}{\sin^3\Theta}\right] \qquad \text{Equation 4.18}$$

Substituting Equation 4.17 into Equation 4.18:

$$V_{BO} = \frac{A_{BO}^{\frac{3}{2}}}{3\sqrt{\pi}} \left[\frac{2 - 3\cos\Theta + \cos^3\Theta}{\sin^3\Theta}\right] \qquad \text{Equation 4.19}$$

---

[7] As D→R, islands begin to coalesce, and this introduces a maximum error to the estimated area fraction of <13%. Refinement of this theory should include the BO grain boundary energy as well. An overestimation by setting D=R•√2 (where the oxide islands 'overlap') leads to a volume fraction of 1.97•$V_{BO,crit}$

As an assumed condition for passivity, we are interested in the critical threshold value at which the volume fraction and contact angle are such to cause complete surface coverage of the system. Therefore, the limit at which $A_{BO} \rightarrow 1$ will yield a relation between the contact angle, determined by the surface energies of the interphase boundaries, and the volume fraction at which the alloy solute covers the surface ($A_{BO} = 1$).

$$V_{BO,crit} = \frac{1}{3\sqrt{\pi}}\left[\frac{2 - 3\cos\Theta + \cos^3\Theta}{\sin^3\Theta}\right] \qquad \text{Equation 4.20}$$

Recall that Θ is defined only by the relative values of the interphase boundary surface energies and described by Equation 4.12. The critical volume fraction of V_{BO} such that BO may form a complete layer between AO and AB is illustrated in Figure 4.7. Note that this expression (Equation 4.20) does not depend on the free energy change to form the volume of the BO island, the island spacing, total oxide thickness, or the critical radius of the island. This function may therefore be scalable from nm to mm thick oxides provided that the assumptions previously mentioned are still held. However, if we wished to define exact fractional area coverages without the use of an empirically-derived or theoretically modeled volume fraction (e.g., Equation 4.10), Equation 4.13 and Equation 4.14 can determine the area coverage and volume fraction independently up to this critical value. This theory predicts the volume fraction of alloying element oxide needed to block the surface given the passive oxide is restricted to the alloy/oxide interface. Thus, the alloying amount in the metal phase needed to form this volume fraction may be found using solute enrichment discussed previously (Equation 4.10).

4.4 Predicting Minimum Alloying Content for Passivity

A combination of solute-enrichment theory with the critical volume fraction may be able to predict the minimum alloying content of a passive element needed for solute-endued passivation.

The volume fraction of the solute oxide (V_{BO}) can be predicted as a function of alloying content from solute enrichment theory calculations. Solute enrichment as described mathematically by Seo and Sato [79] and theoretically expanded by Kirchheim et al. [65] is redefined in terms of volume fraction[8], V_{BO}, in Equation 4.21.

$$V_{BO} = \frac{\beta_v X_B}{1 - X_B + \beta X_B}$$

Equation 4.21

Where β_v is the volume enrichment factor and X_B is the atomic fraction of B in the AB alloy. The volume enrichment factor is dependent on the electrode potential (i.e. dissolution driving force) and electrolyte chemistry, pH, relative valences, molecular weights, and densities of the oxides. Investigations of bronze alloys with physically distinct oxide phases (Cu_2O and SnO_2) have been demonstrated to follow this enrichment relation (see Chapter 3) [130]. In the case where both oxides have no solubility of the other's cation (metastable or otherwise) the cation fraction can be found using Equation 4.22.

$$x_{B,f} = \frac{\beta_v X_B}{1 - X_B + \beta X_B} V_{ox} \left(\frac{\rho_{BO} n}{MW_{BO}} \right)$$

Equation 4.22

Where V_{ox}, is the total volume of the oxide, ρ_{BO} is the mass density of the *BO* oxide, MW_{BO} is the molecular weight of the *BO* oxide and *n* is the number of *B* atoms per mole of *BO* (e.g., n=2, for Cr_2O_3).

Setting Equation 4.21 equal to Equation 4.20 gives the critical solute content presented as a series of plots in Figure 4.8 as a function of both β_v, redefined here for convenience as the volume (rather than cation) enrichment factor, and Θ. Figure 4.8 describes the minimum fraction of B in

---

[8] We have elected to use volume fraction enrichment due to the potential for partial solubility of the cation in the parent oxide. Under the condition of zero cation solubility of B in AO, the volume fraction can then be converted to cation fraction using Equation 4.22.

an AB alloy as a function of the thermodynamic relative surface energies of the interphase boundaries (Θ, Equation 4.12), and the kinetic volume fraction enrichment ratio (β_v, Equation 4.21). The passive element needs to be insoluble in the electrolyte, preferentially retained in the alloy oxide, retained at the inner oxide/alloy interface, and generally have a lower free energy (more negative ΔG_f) than the solvent oxide. In the absence of enrichment (1:1 relative alloy dissolution with respect to alloying content) Figure 4.8 predicts that if the oxide will wet at the interface ($\Theta \leq 90°$) then a solute content of < 40 at% is needed which agrees well with most observations of passivity thresholds (Table 4-1). Experimental results compared with predictions from this theoretical framework are presented and discussed in Chapter 3.

4.4.1 Assumptions

The minimum threshold prediction presented requires several assumptions to remain valid and applicable. The major assumptions are presented below:

- The corroding AB alloy is under steady-state dissolution conditions such that the oxide is constant and does not change in composition, morphology, or thickness with time.
- Only two oxides are considered to form on the surface of the alloy: BO and AO.
- The surface energies of the oxide/alloy interface are independent of composition e.g., $\gamma_{BO/AB}$ is the same for A-5B, and A-50B. This assumption may no longer be valid when the alloy contains a secondary intermetallic phase of distinctly different structure and chemistry.
- All or the majority of BO oxides are immiscible in AO or B cations have exceeded their solubility in AO and restricted to islands precipitated heterogeneously at the alloy/oxide interface to minimize surface energy of the interphase boundary.
- The limit of A→1 is not affected by the coalescence of islands or solute-depleted zones (see footnote 7)

- BO islands in AO assume a hemispherical cap shape to minimize surface energy. Crystalline structure contributions are not considered and Wulff [199] equilibrium particle shapes and epitaxial relationships should be considered to improve this theory at the nanoscale.
- The alloy may become passive when area fraction of BO is sufficiently large to block the surface satisfying the condition that A_{BO} is near or equal to 1 (threshold value).

Tables

Table 4-1. List of experimental observations of critical alloying contents (at%) in various binary alloy systems required for passivity. Data from [76,77].

Alloy System	**Critical Alloy Composition**
Fe-Cr	13 at% Cr
Ni-Cr	8-10 at% Cr
Cu-Ni	30-40 at% Ni
Cu-Sn	6 at% Sn
Cu-Al	13 at% Al
Fe-Si	26-30 at% Si
Co-Cr	9-11 at% Cr
Al-Cr	40-50 at% Cr
Cr-Mo	20 at% Mo
Cr-Zr	10 at% Zr
Mo-Ti	60 at% Ti

Figures

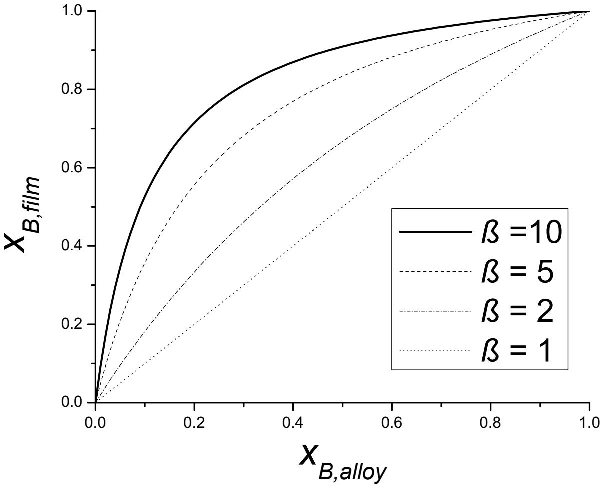

Figure 4.1. Solute enrichment of element B in the surface corrosion product film in a binary A-B alloy where *B* is the passivating element. *ß* is the relative cation diffusivities of A / B (see text). Calculated from expression in Equation 4.1.

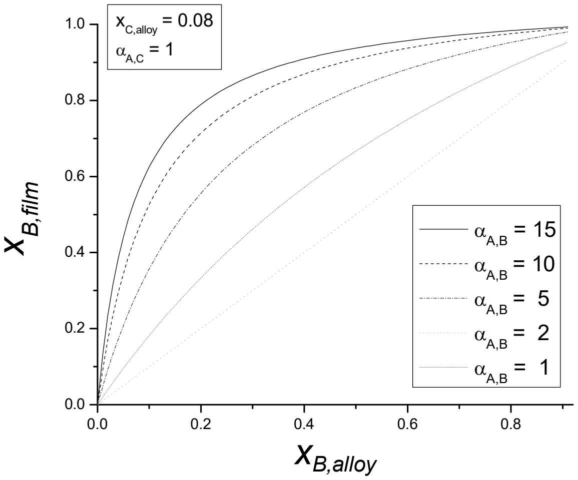

Figure 4.2. Solute enrichment of element B in the surface corrosion product film of a ternary A-B-C alloy where B is the passivating element for $X_{C,alloy} = 0.08$ and $\alpha_{A,C} = 1$. α values are the relative dissolution rate constants (see text). Calculated from expression in Equation 4.2.

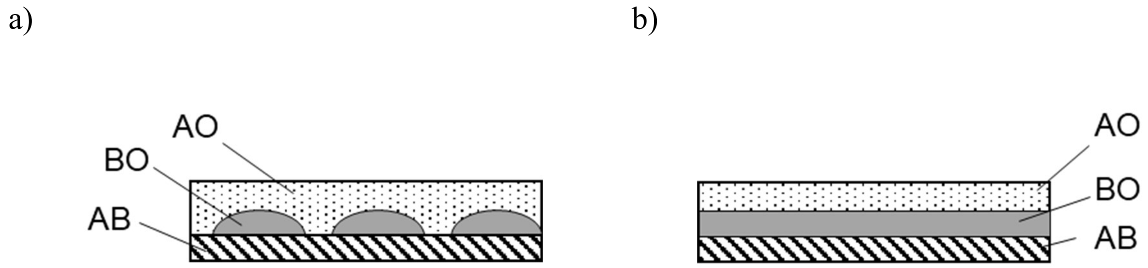

Figure 4.3. Distribution of BO oxide at the metal/oxide interface a) as discrete islands where an insufficient amount of BO is present to create a complete layer and b) where the amount of BO is sufficient to completely cover the surface.

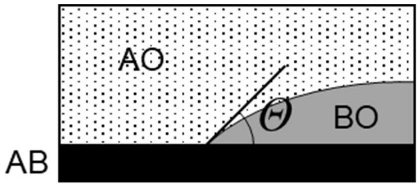

Figure 4.4. Geometry of the AO/BO/AB triple point. The contact angle (Θ) is defined by Equation 4.12.

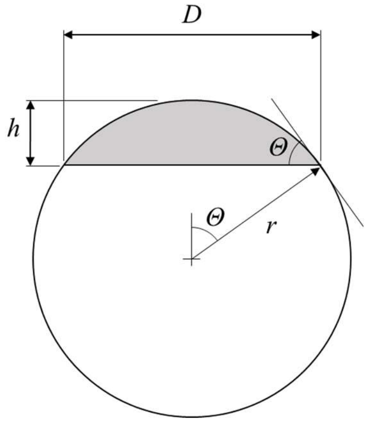

Figure 4.5. Geometry and labels of the spherical cap dimensions. The height of the hemispherical cap is h, Θ is the contact angle of the island (Equation 4.12), D is the diameter of the spherical cap base (Equation 4.15), and r is the radius of the sphere also the critical radius of the precipitate (Equation 4.13).

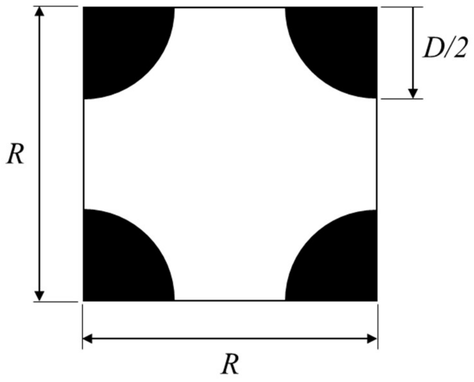

Figure 4.6. Graphical illustration of the apparent fractional area coverage of spherical cap islands at the oxide/alloy interface.

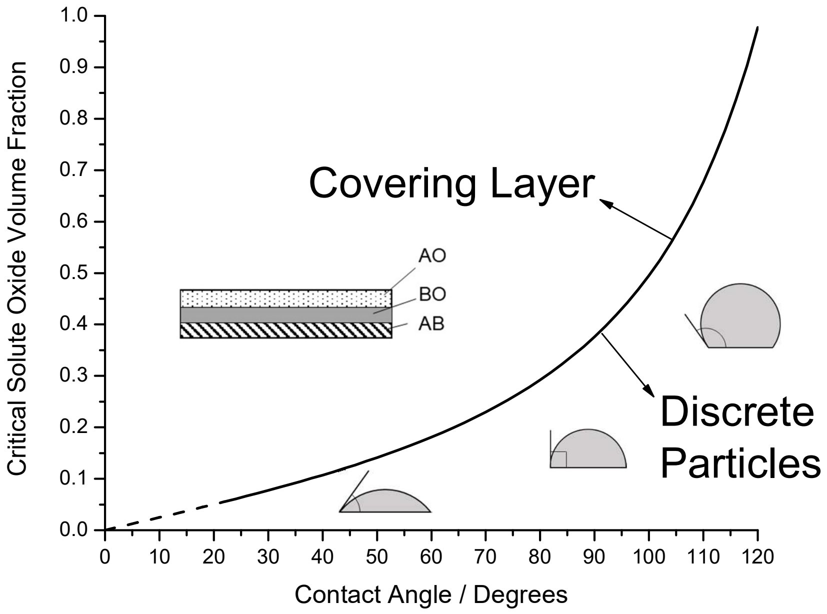

Figure 4.7. Critical solute oxide (BO) volume fraction ($V_{BO,crit}$) for phase-separated oxides as a function of contact angle (Θ) given by Equation 4.20. The contact angle is dependent on the relative surface energies of the solvent oxide, the metal, and the solute oxide given by Equation 4.12.

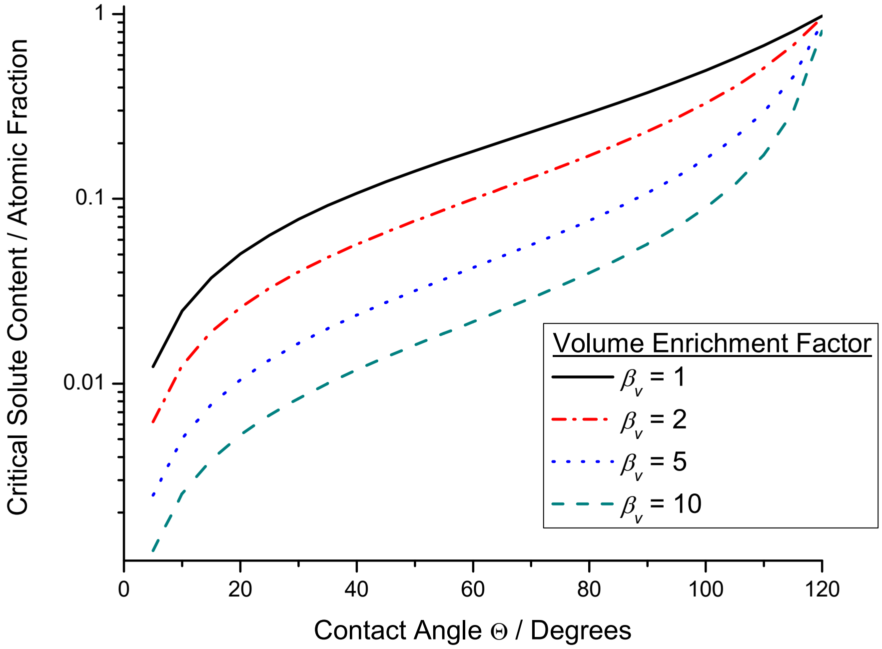

Figure 4.8. Critical solute content for complete coverage by a wetting BO oxide at the alloy/oxide interface as a function of various contact angles (see Equation 4.12), and volume enrichment factor values (see Equation 4.20 and Equation 4.21). Alloy contents below this minimum content are restricted from forming a conformal oxide layer.

5 Solute Capture and Doping of Al in Cu_2O: Corrosion, Tarnish, and Cation Release of High-Purity Cu-Al Alloys in Artificial Perspiration

Abstract

Frequently-touched surfaces are a common transmission vector for hospital and community acquired infections. Cu alloys have shown promise as antimicrobial surfaces, able to kill even antibiotic-resistant bacteria within minutes. However, the most efficacious alloy systems readily tarnish making them unsuitable for hospital applications and tarnish-resistant (e.g., passive) systems do not maintain sufficient Cu ion release to maintain antimicrobial function. An ideal alloy would have optimal corrosion, tarnishing, and Cu release tuned through alloying elements. Cu-Al alloys are tarnish-resistant, yet the precise role of Al remains unclear. High-purity binary alloys of Cu-Al were fully immersed in artificial perspiration at open circuit to evaluate soluble cation release, quantity and identity of corrosion products, as well as interrogate the role of Al on the chemical, structural, and electronic defect structure of oxides formed. Al became captured in Cu_2O as a substitutional cation defect which in turn caused structural, and electronic modifications. This doped film did not inhibit soluble Cu cation release for antimicrobial function even after 144 h. Al-doped cuprous oxide had fewer electronic charge carriers (holes) due to Al-doping and subsequent increased electronic resistance. These results are hopeful regarding the aim of generating a tunable tarnish-resistant layer for an antimicrobial Cu-based alloy.

5.1 Background

5.1.1 Motivation

Cu and some of its alloys have demonstrated the ability to kill antibiotic-resistant so-called 'superbugs' on contact within minutes [119,153,200]. Hospital-acquired patient infections are becoming an increasingly difficult battle worldwide: a battle which we humans are losing [3,7,8,201]. In response, many pharmaceutical companies have significantly reduced future development of antibiotics to combat these multi-drug resistant pathogens due to increased pandrug-resistance [201]. Novel infection control methods are needed to prevent the spread of infection and subsequent deaths of those individuals infected. Cu and its alloys show promise in this regard as antimicrobial high-touch surfaces; targeting the most common transmission vector (hand contact) with a functional antimicrobial alloy [1,3,200]. However, Cu and its alloys tend to tarnish, and this tarnishing layer (patina) can be unaesthetic as a commonly touched surface. Thin passive oxide layers inhibit the corrosion needed to provide soluble Cu ions which are needed for this antimicrobial function [23]. A representative electrolyte solution is needed to appropriately simulate a high-touch surface, such as artificial perspiration. An ideal alloy would be tarnish-resistant but not completely passive, for both aesthetic and functional reasons, yet permit enough soluble Cu to be released through corrosion to facilitate continuous antimicrobial function. In this aim, a solid solution alloy of Cu with Al is a good candidate for a tarnish-resistant antimicrobial alloy.

Tuning of the corrosion layer electronic properties has been demonstrated with Ni in cupro-nickel alloys. Ni in solid solution Cu-Ni and Cu-Al-Ni enhances alloy corrosion resistance by incorporation of Ni^{2+} into Cu_2O replacing the Cu^+ cation vacancies with an ion of greater valence, doping the oxide and decreasing the number of mobile electronic charge carriers (holes) and thus the conductivity of the oxide [86]. This effect increases with increasing Ni content up to 30% Ni.

[64,202]. However, Ni is a common metal allergen [9] and would therefore be unsuitable for an antimicrobial high-touch alloy. Altering the properties of the cuprous oxide layer may also be possible using Al, provided the alloying content is below the passive threshold. An exotic opportunity may exist to generate a tunable alloy by doping the cuprous oxide with an aliovalent solute such as Ni^{2+} or Al^{3+}, modifying the ionic and electronic properties of the cuprous oxide layer in the aims of mitigating corrosion of the alloy. Cu-Al alloys show remarkable corrosion resistance [203,204] with excellent mechanical performance [60,205,206], making this alloy system an attractive material in pumps, impellers and valves exposed to seawater [5,64,207] and dental alloys [204,208]. Alternatively, surface coverage of a corrosion-limiting film may be tunable by controlling the alloy content of Al in solid solution to prevent passivity but permit an allowable amount of soluble Cu release through corrosion. Unlike NiO however, Al_2O_3 is not thermodynamically soluble in Cu_2O and may oxidize in a separate oxide form.

5.1.2 Al-Bronze Metallurgy

The maximum solubility of Al in FCC Cu α-phase is 9.4 wt% at 565 °C [209]. Typically, commercial α-bronze alloys contain between 4 and 7 wt% Al [60]. Under normal commercial alloy production conditions some ß-phase can precipitate at just 7.5 wt% [209]. Therefore, the single-phase alloys of α-Cu-Al bronze are typically less than 8 wt% [60]. At 9 wt% Al or greater, a brittle secondary phase (ß) forms [60], creating a duplex α+ß microstructure which has significant mechanical advantages [210]. The ß phase is BCC and transforms eutectiodally at 565°C to α (FCC) and γ_2 (cubic) [209]. However, if the alloy is quenched, γ_2 can be replaced with a martensitic phase [209]. Secondary phases are intentionally formed for their improvements to mechanical performance however, they obfuscate the systematic study of the effect of Al in solid solution on corrosion and cation release. The difference in chemistry and structure drive local galvanic cells, promoting preferential attack of one phase [211]. In commercial alloys, Tin is usually added to increase fluidity of casting [212]. P and Mn have deoxidizing action and is helpful for improving mechanical and corrosion resistance [208]. When added to Cu-Zn (brass), Al has about the same effect on microstructure and mechanical properties as Zn but is 6x as potent per weight [60]. Elements such as arsenic are added to brass (Cu-Al-Zn) to reduce dealloying/dezincification [213]. Ce may be an alternative to carcinogenic As [213]. Boron in Al-brass helps to refine grains and fills vacancies, inhibiting diffusion of Zn through these vacancies [213]. Fe and Ni are crucial additions to Cu-Al to induce precipitation-hardening and promote martensitic phases that improve mechanical properties of the alloy [208]. However, martensitic phases (i.e. phases formed via massive transformations) and secondary phases are susceptible to dealloying (or dealuminification) [211]. The propensity of dealloying is related to the metallurgical structure; laser surface melting, which homogenizes the surface, was shown to decrease dealloying of a Cu-6Al-4Fe alloy [214]. Therefore, secondary intermetallic phases must be avoided to determine the role alloying Al has on the corrosion behavior of α-Cu alloys. The parting limit of Al, i.e. the amount above which the alloy is susceptible to dealloying, is between 11 and 16 at% [215]. The possibility of incongruent dissolution, i.e. dealloying, necessitates a complete fate of the elements study to determine the effect of Al. For example: Al is more electrochemically active than Cu and therefore an actively dealloying Cu-Al alloy releases Al, not Cu! This important detail is not captured by corrosion rate measurements alone and is certainly unfavorable for antimicrobial function enabled through soluble Cu release.

5.1.3 Possible Fates of Al Following Corrosion

Following corrosion of the Cu-Al alloy, Al may terminate in one of many ‘fates’: release as a soluble aqueous ion, as a separate or mixed stoichiometric oxide phases, or incorporated in a copper corrosion product. Table 5-1 lists the thermodynamic free energies of the solid compounds predicted to form from a Cu-Al alloy in aqueous environment; they are ranked in order of increasing stability (more negative free energy). The role of Al on the corrosion of Cu-Al alloys is dependent on where the Al resides following oxidation, i.e. its ‘fate’. A few probable scenarios as to the fate of the alloy are discussed.

Phase-Segregated Stoichiometric Oxides

Cu-Al alloys are argued to be protected from corrosion by a thin alumina (Al_2O_3) layer [60]. Some research purports [60,216–218] that a duplex layer of Cu_2O and Al_2O_3 coexist on the surface, and that the alumina phase is responsible for the corrosion protection of the alloy [60,216,217]. The increased corrosion protection with increasing Al content is purportedly due to increased surface coverage (site blocking) of transport of Cu^+ at the interface of this oxide.

Cu-Al Mixed Oxide Phases

Another potential fate of Al is in the form of a distinct mixed oxide with copper. Copper, aluminum, and oxygen together may form thermodynamically stable copper aluminate phases. Sanderson and Scully observed copper aluminate phases in high temperature corrosion studies of Al-bronze alloys [187] however, there is a paucity of evidence regarding these phases in aqueous environments. Electrochemical thermodynamics predicts these mixed phases are the most stable (Table 5-1) and predominant phases in neutral aqueous solutions [121]. The corrosion product formed on the surface of corroded Cu-Al in artificial perspiration may form a $CuAlO_2$ or a $CuAl_2O_4$ spinel phase.

Solute Capture of Al^{3+} in Cu_2O

A third possibility exists, that the solute elements may become captured in the growing oxide layer to form a metastable phase containing Al^{3+} in a solid solution with Cu_2O [219,220]. Should the interface velocity of the oxidation front exceed the velocity of the solute diffusional transport perpendicular to the interface then a separate segregated oxide is restricted from forming and solutes such as Al^{3+} are captured in the growing Cu_2O oxide [219]. This metastable oxide then becomes doped with an aliovalent ion and would have significant effects on the electronic properties of the oxide film with subsequent effects on the corrosion of the alloy [77].

Aluminum as a solid solution addition may afford corrosion protection to Cu-Al alloys by one of several mechanisms: Al may oxidize as a separate Al_2O_3 phase, a mixed oxide such as $CuAlO_2$ or a $CuAl_2O_4$, or as a dopant substitutional cation in Cu_2O. In this aim, high-purity single phase FCC model binary alloy buttons of various Al content were fabricated for study. Corrosion rates, electrochemical behavior, oxide identity and quantity, and soluble Cu release were measured in artificial perspiration to simulate the high-touch environment. Specifically, the chemical and structural nature of the tarnish-resistant oxides formed on the surface of Cu-Al alloys was determined with surface analytical techniques and X-ray diffraction. Furthermore, an estimate of the charge carrier density of the semiconducting oxide was determined to measure the effect of doping (if any). The objective of this work is to determine the role of Al on the tarnish-resistance of Cu-Al alloys in the aim of generating a tarnish-resistant oxide which does not inhibit Cu ion release in order to enable antimicrobial function.

5.2 Experimental Procedures

5.2.1 Materials

Alloy Preparation

High-purity binary alloys of Cu-Al were prepared by inert-gas (argon) arc-melting in the Materials Preparation Center at AMES Laboratories. Al concentrations of 0.2, 2, and 11 at% (0.1, 1, and 5 wt%) were prepared from a minimum 99.99 wt% pure Cu and Al materials. Alloy contents are reported in at% unless otherwise indicated. The alloy buttons were melted and flipped three times to homogenize. The actual chemical compositions are given in Table 5-2 as tested by ASTM E478. Alloy buttons were heated to 600 °C for 2 h to solutionize and quenched in water. Solid solution was confirmed with X-ray diffraction by a single Cu FCC diffraction pattern with shifted peaks due to Al in solid solution. Prior to electrolyte solution exposure or electrochemical experiments, alloy samples were ground with SiC polishing paper up to 1200 grit, the final polishing stage was lubricated with ethanol. After polishing, samples were rinsed with and then immersed in ethanol until dried and transferred to sample cells for electrochemical testing or exposure. For visual inspection and photoelectron studies, samples were polished through 1-μm diamond suspension and rinsed with ethanol.

Electrolyte Solutions

Artificial Perspiration

Artificial perspiration was used to represent a high-touch surface [23,26,154,221] and prepared according to BS EN 1811:2011 [48]. The chemical composition of artificial perspiration is given in Table 5-3. The pH was adjusted with ammonium hydroxide (NH_4OH). The pH of the artificial perspiration drifted from 6.5 to 5.8 over the course of 10 days therefore, the artificial perspiration was prepared and pH-adjusted within 6 h before sample exposure.

Borate Buffer

Galvanostatic cathodic coulometric reductions (CR) to assess Cu oxides were performed in a deaerated borate buffer solution (pH 8.4). This buffer to fix pH was prepared from 0.11 M boric acid (H_3BO_3) and 0.02 M sodium tetraborate ($Na_2B_4O_7$). Deaeration of the solution was accomplished by bubbling N_2 gas through a glass fritted bubbler for a minimum of 1 h and hydraulically transferred to a N_2-purged cell to prevent electrolyte exposure to lab air in identical fashion as has been described in detail elsewhere [23,26,154].

5.2.2 Characterization of Corrosion Products Formed on Cu-Al at Open Circuit in Artificial Perspiration

Open circuit exposures were conducted in 300 mL 3-electrode cells. Exposed sample area through a rubber O-ring was 0.8 cm^2. Cell bodies were cleaned using 0.1 M HCl solution prior to each exposure, rinsed with distilled water and rinsed with the respective electrolyte solution. Potentials were measured with a saturated calomel electrode with a Luggin probe tip. Optical photographs were measured with a flatbed digital document scanner with a grey-card color reference background at a resolution of 300 DPI.

An InVia Renishaw® Raman spectrometer acquired Raman spectra generated from the green emission line of an Argon laser (514 nm) with a 3000 l/mm diffraction grating with a Peltier-cooled CCD detector. Raman spectroscopy was measured on samples exposed to artificial perspiration for 96 h. Burning of the sample surface was avoided by using longer exposure times (~minutes) with lower laser powers.

Crystal diffraction patterns from the corrosion product films were measured using a grazing-incidence method. The incident angle gave optimal signal-to-noise at a value of $\omega = 0.5°$. Full penetration through the corrosion product film to the alloy substrate was achieved as evidenced by FCC peaks of the substrate matching those measured from solid solution confirmation results via bulk crystal X-ray diffraction.

The elemental composition, chemical state, and variations through the thickness of the oxide film was evaluated with X-ray photoelectron spectroscopy (XPS). A Thermoscientific K-Alpha XPS instrument used a monochromatic Al K_α X-ray source (1486.6 eV). Photoelectron (PE) spectra were obtained on samples exposed to artificial perspiration for 96 h. PE spectra were acquired on the as-introduced samples as well as sputtered by Ar^+ ions lightly, and at several sputtered depths to the metal substrate. An Ar^+ ion beam energy of 3 KeV was used which corresponded to a sputter rate of 0.3 nm/s using a SiO_2 sample of known thickness. Spectral fits were accomplished using standard fit constraints [222]. The Al 2p peak was resolved by fitting a third peak after constraining the software peak fit of the Cu 3p spit-obit energy split (Δ=2.0 eV) and the relative peak ratios (1:2). For the X-ray generated Auger transition, the main line was determined from spectra fits using the least number of components peaks which gave reasonable agreement with the data (STD < 2).

The concentration of a given element from the integrated element peak area was calculated using standard methodologies [222]. The concentration (C_x) of a given element from the PE spectra is given by Equation 5.1.

$$C_x = \frac{\frac{I_x}{S_x}}{\sum_i \frac{I_i}{S_i}} \qquad \text{Equation 5.1}$$

Where I_x is the integrated peak intensity of element *x*, and the atomic sensitivity factors (*S*) used were 5.321 for Cu, 0.234 for Al, 0.711 for O, and 0.891 for Cl, taken from ref [222].

The charge carrier density of the cuprous oxide (cuprite, Cu_2O) is possibly responsible for the change in electrochemical behavior of these alloys. To determine the electronic/ionic defect density of the oxide, Mott-Schottky experiments were performed in solutions of deaerated borate buffer (pH 8.4) with 0.7 mM of $K_3[Fe(CN)_6]$ as a redox mediator [223]. Oxide films were grown in quiescently-aerated artificial perspiration with an anodic galvanostatic hold at 0.1 mA for 12500 s over an exposed electrode are of 0.8 cm^2. Following sample transfer to deaerated cells, a cathodic sweep was applied to samples starting at 0 V_{MMSE} at a rate of 5 mV/s with an applied AC voltage of 5 mV RMS at a frequency of 10 Hz. Electrode potentials were measured using a mercury/mercurous sulfate electrode (MMSE). The charge carrier density can be approximated with the Mott-Schottky equation reproduced in Equation 5.2.

$$\frac{1}{C^2} = \frac{2}{\varepsilon\varepsilon_0 A^2 e N_d}\left(E - E_{fb}\right) \qquad \text{Equation 5.2}$$

Where C is the measured differential capacitance, ε_0 is the permittivity of free space (8.85 x10^{-14} F/cm), ε is the dielectric constant of the oxide (7.6 [224]), A is the electrode area (0.8 cm^2), e is the elementary charge (1.6 x10^{-19} C), and N_d is the defect density. E and E_{fb} are the electrode potential and the flat band potential of the semiconducting oxide, respectively. The defect density can thus be estimated from the slope of the $1/C^2$ vs. potential plot. The use of a redox mediator ensures that the majority of the Faradaic charge is consumed by the mediator rather than oxidation or reduction of the oxide. While electrochemically-grown oxides violate the assumptions of the ideal conditions of which the Mott-Schottky equation is derived[9] [225], the precise concentration of charge carriers cannot be obtained however, it is nonetheless instructive to compare the approximate relative defect density values between oxides formed on Cu-Al alloys with differing Al contents.

5.2.3 Anodic Charge of Corrosion Products

Insoluble Corrosion Products – Coulometric Reduction

The reversible Nernst potentials for copper corrosion products usually lie within the electrochemical stability window of water (-0.5 to 0.7 V_{SHE} at pH 8.4), in the absence of dissolved oxygen, these compounds can be galvanostatically reduced in aqueous electrolytes. A constant

---

[9] Electrochemically grown oxides are highly defective and contain localized states in the band gap with a wide range of energies. These localized states have various time constants leading to a frequency dependence of the space charge capacity [225]. In the present work we only use Mott-Schottky to compare the relative difference between alloy systems without conferring absolute values to the charge carrier densities.

cathodic current of -20 μA was applied (A=0.8 cm^2, -25 μA/cm^2) to pre-exposed samples in a deaerated aforementioned borate buffer solution (pH 8.4). Deaerated solution was hydraulically transferred to reduction cells. Reduction cells (~400 mL total volume) were N_2-purged for 10 min prior to direct electrolyte transfer from the deaeration flask. Continuous bubbling of reduction cells ensured deaeration throughout the reduction. Reduction potentials were measured using a mercury/mercurous sulfate electrode (MMSE) fitted with Luggin tips. The charge of the oxide can be determined from the chronopotential curve via the following relation (Equation 5.3).

$$Q_{CR} = i_{app} \times t_{red} \qquad \text{Equation 5.3}$$

Where i_{app} is the applied current density (-25 μA/cm^2) and t_{red} is the reduction time, determined as time between local maximum potential changes, i.e. distance (time) between maxima in the first derivative plots of chronopotential curves according to procedures outlined in detail in previous work [17,26,154]. The thickness of the oxide can be roughly estimated through the calculation in Equation 5.4.

$$d = \frac{Q_{CR}(MW)}{nF\rho} \qquad \text{Equation 5.4}$$

Where d is the corrosion product thickness in cm, Q_{CR} is the charge density associated with a reduction wave (Coul/cm^2), MW is the molecular weight of the oxide (g/mole), n is the number of moles of e^- per mole of oxide molecule (e.g., Cu_2O = 2), F is Faraday's constant, and ρ is the oxide density in g/cm^2. Cu_2O density was assumed to be 6.0 g/cm^3.

Soluble Corrosion Products – ICP-OES

Soluble metal ion concentration was measured using inductively-coupled plasma ($T \geq 6000$ K) – optical emission spectroscopy. A Thermoscientific iCap 6000 spectrophotometer was used to collect photoemission spectra from aliquots (15 mL) obtained from cells with 300 mL (± 2.5 mL) of artificial perspiration solution (not acidified). Emission intensities were compared with calibrated standards of known concentrations. LOD were found to be 17 and 198 ppb for Cu and Al, respectively. The measured concentration can be converted to an equivalent charge through the following expression.

$$Q_{ICP} = \sum \frac{CVnF}{AW} \qquad \text{Equation 5.5}$$

Where C is the measured concentration (mg/L), V is the solution volume (L), n is the assumed valence state of the soluble ion, F is Faraday's constant (Coul/mole e^-), and AW is the atomic weight of the element of interest (mg/mole).

5.2.4 Total Anodic Charge – Corrosion Rates in Artificial Perspiration

Gravimetric Mass Loss

Gravimetric mass loss (ASTM-G1 [139]) was used to determine the total corrosion loss from Cu-Al alloy samples exposed to artificial perspiration up to 96 h. Triplicate measurements of samples before (M_1), and after (M_2) exposures were compared with the measured values of samples cleaned of corrosion products using a 6 M HCl solution in one cycle lasting 1-2 minutes (M_3). A 0 h sample with no other exposure was included to show the mass loss from the acid cleaning step alone. The total mass loss was the difference between M_1 and M_3. The mass loss was estimated using a Faradaic relation with the assumed equivalent weights of 63.6, 63.2, 59.9, 48.8, 41.1, and 9.0 g/ equivalent for Cu, Cu-0.2Al, Cu-2Al, Cu-11Al, and Al, respectively.

Electrochemical Interface – EIS

Electrochemical impedance spectroscopy was measured on samples at set interval time points up to 96 h. A 30-min open circuit measurement was taken prior to obtaining EIS spectra. The frequencies applied ranged from 100 kHz to 1 mHz with 8 points per decade. The voltage perturbation applied was 10 mHz RMS. A DC equivalent circuit of two constant phase elements each in parallel with resistors both in series with a solution resistance was used to mathematically approximate the impedance-response of samples and determine the polarization resistance (R_p) value, defined as the impedance at the DC-limit (freq. → 0) under AC conditions. Gamry® software was employed to calculate circuit values using a non-linear regression analysis. The integrated B/Rp (~ i_{corr}) values gave an indication of the total anodic charge Q_{EIS} for corrosion analogous to the charge estimated from mass loss. The total anodic charge integrated from impedance-derived polarization was calculated according to Equation 5.6.

$$Q_{EIS} = \int_0^t \frac{B}{R_p} dt \qquad \text{Equation 5.6}$$

Where B is the Stern-Geary constant ($B = 0.025$ V [23,26,154]) ($b_a b_b/(b_a+b_b)$), R_p is the polarization resistance of the system ($R_{ox}+R_{ct}$), and t is time duration of the sample in artificial perspiration. Integrating the R_p values fit from impedance spectra over the time intervals measured gives an approximate value of the total anodic charge from corrosion over time. The total anodic charge is analogous to the cumulative material loss measured via mass loss and agrees well with the trend where Cu-2Al demonstrated the greatest total anodic charge.

5.2.5 Potentiodynamic Polarizations

Potentiodynamic polarization scans from -1.5 V_{SCE} to 0.5 V_{SCE} were conducted on freshly polished Cu-Al samples in ambiently-aerated artificial perspiration and 1 M HCl at an upward scan rate of +0.1667 mV/s. Prior to polarization scans samples were held at -1.5 V_{SCE} for 10 minutes to remove any air-formed oxides on the surface.

5.3 Results

5.3.1 Characterization of Corrosion Products Formed on Cu-Al in Artificial Perspiration

Open circuit potentials of Cu, Cu-Al, and Al in artificial perspiration were monitored over time and presented in Figure 5.1. A clear delineation between alloys with 2 at% Al or greater is shown at 96 h. Potentials remain high (-40 mV_{SCE}) for 2 at% Al or greater alloys, but the potential falls to a lower value (-100 mV_{SCE}) after 24 h for pure Cu and 48 h for Cu-0.2Al in artificial perspiration solution. The Cu-11Al alloy rises slowly, suggestive of an increasingly resistive or thickening film, but reaches a similar OCP value to Cu-2Al at 96 h. The surface of Cu-Al samples became tarnished with corrosion products as shown in Figure 5.2. Cu-Al samples at 2 at% or lower showed oxide tarnish similar in nature to pure Cu. However, Cu-11Al showed far less tarnishing oxide and some light etching of the grain boundaries.

Ex situ Raman spectroscopy, presented in Figure 5.3, identified cuprite (Cu_2O) as a corrosion product formed on all Cu-Al alloys tested following exposure to artificial perspiration. Raman spectra acquired on a pure Al sample, also exposed in artificial perspiration for 96 h, showed distinctly different Raman peaks, particularly its main broad peak centered at 785 cm^{-1}, which were not observed in the Raman spectra on the Cu-Al samples or on the corundum (Al_2O_3) reference spectra [226]. Notably, an additional Raman band not on the cuprite standard but found on all Cu-based corroded samples at 525 cm^{-1} which has been ascribed to Cu-OH vibrations which would indicate a defective cuprite (Cu_2O) structure[148]. In summary, Raman spectroscopy only revealed defective Cu_2O but did not reveal any independent phase of oxidized aluminum (Al_2O_3) or mixed metal oxide phases (e.g., $CuAlO_2$) on Cu-Al alloys.

Crystalline corrosion products on the surface were characterized using grazing-incidence X-ray diffraction (GIXRD) and diffraction patterns with corrosion product assignments are presented in Figure 5.4. Cuprite (Cu_2O) was found with evidence (one peak) of CuCl. The assignment of cuprite with this singular peak has been previously identified as CuCl in prior work [154]. All diffraction peaks were identified and were also indicated from evidence from other methods (Raman: Figure 5.3, CR: Figure 5.9, XPS: Figure 5.6). Complete penetration to the substrate was achieved, evidenced by the Cu FCC peaks albeit shifted for each alloy due to Al in solid solution (Figure 5.4). Dealloying may be indicated with GIXRD by a shift or separation of Cu FCC lattice peaks which would be present with pure Cu FCC peaks (or possibly shoulder peaks) neither of which were observed here. For the Cu-11Al sample, the cuprite (111) peak was slightly shifted to higher 2Θ values (Figure 5.4). The full width at half maximum (FWHM) of this diffraction peak increases, indicating less structural uniformity of this corrosion product [227]. A decrease in the peak height of cuprite is also observed with increasing Al content in the alloy shown in Figure 5.4. Not only does the thickness of the oxide decrease with increasing Al content, the cuprous oxide on the alloy surface attains a slightly different lattice parameter, evidenced by the shift in the (111) reflection according to Bragg's law demonstrated in Figure 5.5.

High-resolution photoelectron spectra for selected elements measured from corroded Cu-11Al are given in Figure 5.6. A summary of the photoelectron peak fit values and computed areas are given in Table 5-4. Al 2p photoelectron energy overlaps with Cu 3p energies. However, by imposing typical fitting constraints on Cu 3p peaks, the Al 2p signal was resolved from the spectra in the case of the Cu-11Al (Figure 5.6a) and Cu-2Al alloys. The Al 2p energy (73.17 eV) was consistent with an oxidized state, but did not agree with values expected for Al_2O_3 or $Al(OH)_3$ (73.9 and 74.0 eV, respectively [222]). O 1s spectra show two clearly resolved peaks (Figure 5.6b). The first peak (530.27 eV) matches clearly with the expected value for Cu_2O (530.3 eV), while the second (531.11 eV) is more closely related to Al-O bonding in Al_2O_3 (531.0 eV). However, the binding energy was also close to that of $Cu(OH)_2$ (531.2 eV). Al was oxidized as inferred from its 2p spectra and the O 1s peak. This assignment is not entirely conclusive on its own due to the reasons previously mentioned and the confirmed presence of OH from the Raman spectra. The Cu 2p energy does not shift appreciably from Cu(I) to Cu(0), therefore, the Auger Cu_{LMM} transition energy shown in Figure 5.6c was used to delineate the oxide Cu_2O: (Cu(I): 916.7 eV) / alloy (Cu(0): (918.6 eV) boundary. The chlorine peak energy ($2p_{3/2}$ = 198.64 eV, Figure 5.6d) was consistent with well-established energy ranges for chlorine binding in CuCl (198.4-199.5 eV [222]). The cation fractions of Al in the film are discussed in a later section. In summary, the primary corrosion products identified were oxidized Al (though not definitively Al_2O_3 or $Al(OH)_3$), Cu_2O with Cl^- embedded in the cuprite, and possibly also as a separate phase of CuCl on the surface.

Cuprous and cupric oxides are both p-type semiconductors, whereas aluminum oxides are n-type. Mott-Schottky measurements (Figure 5.7a-d) made on galvanostatically-grown oxide films indicate p-type semiconducting properties (Figure 5.7c). The impedance spectra of Cu-Al alloys with pre-grown films in artificial perspiration solution are given in Figure 5.7a and b. The estimated values of electronic defect densities of oxides formed on Cu-Al alloys in sweat are presented in Figure 5.7d. Estimated defect densities revealed relatively decreased electronic charge carriers, i.e. electron holes, in the cuprous oxide formed on Cu-11Al samples compared with the defect density values measured for Cu, Cu-0.2Al and Cu-2Al.

5.3.2 Anodic Charge of Corrosion Products

Insoluble Corrosion Products – Coulometric Reduction

The coulometric methodology utilized and corrosion product assignment procedure has been discussed in detail in a prior publication [154]. The electrochemical nature and amounts of the corrosion products formed were quite different as a function of Al content as shown in Figure 5.8 based on reduction on Cu-Al samples following exposure in artificial perspiration at open circuit. Coulometric reductions show a markedly decreased charge associated with cuprous oxide with increasing Al alloying content. Al is not reducible with this technique; its reduction potential is far below that of HER. Greater amounts of CuCl are found on Cu-2Al compared to Cu-0.2Al and Cu-11Al (Figure 5.9). A general trend of decreased cuprite (Cu_2O) thickness with increasing Al content in the alloy is shown with triplicate measurements in Figure 5.9.

Figure 5.9 illustrates the progression of data processing from the coulometric reduction method. Separate replicate samples showed good reproducibility in coulometric reduction following full immersion for 96 h in artificial perspiration at open circuit demonstrated by their chronopotential plots in Figure 5.9a. Only two corrosion products were identified (via reduction potential) with this method, indicated by the outlined areas in Figure 5.9b. CuCl and Cu_2O were electrochemically reduced from Cu-0.2Al and Cu-2Al samples, but only Cu_2O was electrochemically reduced on Cu-11Al (Figure 5.9b and d). The reduction potential for cuprite (Figure 5.9b) was found to decrease by 100 mV from Cu to Cu-11Al, meaning the cuprous oxide formed on Cu-11Al was more difficult to reduce than the Cu_2O formed on the solute-lean compositions. The modified reduction potential and lattice structure (Figure 5.4 and Figure 5.9b) are unlikely to simply be an effect of the thin oxide itself. The air-formed oxide on the surface reduces at a higher potential, inferring the thin oxide is easier to reduce rather than more difficult. Secondly, the reduction potential for the oxide changes with alloy content (Figure 5.9b) to a far greater degree than over exposure time or oxide thickness. Reducible copper corrosion products significantly decreased in thickness (reducible amounts measured as charge) and increased in electronic resistance with increasing Al content in the alloy (Figure 5.9b).

Soluble Corrosion Products – ICP-OES

Soluble release of Cu and Al at selected time-points following open circuit full-immersion exposure to artificial perspiration are shown in Figure 5.10a and b, respectively. Triplicate measurements using separate samples of soluble Cu release at 96, 130, and 144 h are shown in Figure 5.11. Soluble copper release (Figure 5.10a) from Cu-Al was nearly linear with time for ≥ 2 at% Al Cu-Al alloys. However, Cu release rates (slope) diminished after 96 h for Cu-0.2Al and Cu. Al was not detected as a soluble species from Cu-Al above the limit of detection (0.2 ppm) consistent with prior work[17,23,26], but was significantly released from a pure Al sample (0.84 ±0.06 ppm, Figure 5.11) subjected to the same exposure conditions.

5.3.3 Total Anodic Charge – Corrosion Rates in Artificial Perspiration

Gravimetric mass loss measurements and impedance measurements of Cu-Al alloys following exposure to artificial perspiration are presented as anodic charge and inverse polarization resistance as a function of alloying content at 96 h in Figure 5.12a. Mass loss (mg/cm^2) over time is compared with a corresponding integrated anodic charge from EIS in Figure 5.12b. Cu-2Al had the greatest mass loss of all elements (Cu and Al) and alloys (Cu-Al). A cuprous (n=1) assumption provided the best match between mass loss and derived anodic charge obtained independently from EIS measurements and corroborated by prior work[58,134,154,228]. Electrochemical impedance measurements on Cu-Al samples exposed to artificial perspiration also revealed Cu-2Al had the greatest corrosion rate ($1/R_p \alpha i_{corr}$, Figure 5.12a). Cu and the other Cu-Al alloys had similar mass loss at 96 h.

5.3.4 Potentiodynamic Polarizations and Galvanostatic Anodic Holds

Potentiodynamic polarizations shown in Figure 5.13 illustrate that Al does not passivate Cu-Al alloys in artificial perspiration or HCl. The potential window near the open circuit potential of

Cu-Al alloys from -0.50 V_{SCE} to +0.25 V_{SCE} is shown in Figure 5.13. Al in the alloy does not appreciably affect anodic kinetics. Notably however, Cu-Al alloys had increased cathodic reaction (ORR) rates on the bare metal surface in both artificial perspiration and hydrochloric acid compared to commercially pure Cu. Pure aluminum pits at its open circuit potential in both artificial perspiration and HCl and did not passivate in either solution revealing only ohmic controlled anodic dissolution. The surfaces of Al samples post-experiment were highly pitted with a significant amount (grams) of visible material loss. The native oxide on Al did not protect the surface in either artificial perspiration or 1 M HCl.

Galvanostatic anodic holds of Cu-Al alloys in artificial perspiration are given in Figure 5.14. Anodic dissolution was made easier by the addition of Al to Cu-Al indicated by the reduced anodic potential for the same imposed current. The increased corrosion rates and cation Cu release of Cu-2Al may be ascribed to easier anodic dissolution due to Al as shown by these plots (Figure 5.14) in the absence of a protective film due to insufficient Al.

5.4 Discussion

Aluminum as a solute in FCC solid solution with copper oxidizes and is located in one of three probable states: (1) Al may oxidize to form its own oxide (Al_2O_3) in a physical mixture or stratified layers with copper oxidation products (Cu_2O), (2) Al and Cu may combine to form a mixed oxide or spinel phase (e.g., $CuAlO_2$, or $CuAl_2O_4$) which are more thermodynamically stable than the individual oxides (Table 5-1) but may be kinetically limited at room temperatures and short duration (days), or (3), Al may become captured within the primary Cu (or solvent) oxide phase. Al_2O_3 does not have any thermodynamic solubility in Cu_2O [220]. These individual fates would have consequences on both the compositional and structural nature of the corrosion products formed on the alloy phase, and hence, may strongly influence corrosion properties of the alloy. By interrogating several alloy compositions, we can not only determine the fate of the solute element, Al, but also its role on corrosion of aluminum copper alloys.

From the evidence presented here from GIXRD, CR, XPS, and MS, Al becomes a substitutional cation defect in the cuprite layer. Solute-enrichment is the fate of Al because there is evidence of quantifiable physical, chemical, and electrochemical modifications to cuprite. GIXRD did not show peaks which would correspond to $CuAlO_2$ (PDF 00-035-1401) or $CuAl_2O_4$ (PDF 00-033-0448) and no individual phase of oxidized Al (e.g., Al_2O_3) was observed, which is consistent with other findings in the literature at even longer exposure times (880 h, [211]). Pure Al does not form a stable passive layer and pits at open circuit in artificial perspiration (Figure 5.13a), suggesting that the protective mechanism (Figure 5.9c) is not from an oxide layer of only Al such as Al_2O_3. In addition, CuCl and modified cuprite were the only corrosion product phases observed despite using multiple methodologies including crystal diffraction (Figure 5.4), Raman spectroscopy (Figure 5.3), electrochemical (Figure 5.8) and XPS characterization (Figure 5.6).

5.4.1 Kinetic Conditions Required for Solute-Capture of Al in Cu_2O

The conditions for solute capture may be conceptualized by considering the conditions required to reach chemical equilibrium (or quasi-equilibrium). Figure 5.15 visually illustrates the conditions required for solute capture for a growing cuprous oxide in an electrochemical system. Within this theoretical framework, if the velocity of the growing oxide/metal (n-type) or oxide/fluid (p-type) interface, which can be related to some fraction corrosion current (i_{corr}), is faster than the ability of the solute to diffuse to a neighboring solute to form a separate oxide phase represented by the diffusion coefficient (D) and a required jump distance (a) then the solute becomes captured by the growing interface [229]. In Figure 5.15, several jump distances are considered in calculations. In the range of these experiments the oxide growth current densities from CR results (highlighted in Figure 5.8) are on the order of 10^{-6} to 10^{-7} A/cm². A reasonable assumption for the diffusion of Al in the solid state cuprous oxide is in the range of 10^{-20} to 10^{-30} cm²/s which are similar values for oxide systems such as Cr in NiO (also p-type) [219,230]. For a Cu-Al system, the theoretical requirements for solute capture are indeed met (Figure 5.15). It is therefore possible that Al^{3+} becomes a cation defect in the growing Cu_2O layer during open circuit corrosion artificial perspiration. Indirectly, more negative reduction potentials during CR suggest more thermodynamically stable $(Cu,Al)_2O$ rather than Cu_2O.

Concerning the other potential fates, a physical mixture of Al_2O_3 and Cu_2O would require greater free energy due to the additional interfaces (excess interfacial energy of an interface). While alumina (Al_2O_3) and $CuAlO_2$ and $CuAl_2O_4$ may be more thermodynamically favorable (Table 5-1), these phases were not detected with Raman spectroscopy (Figure 5.3), GIXRD (PDF 00-035-1401 and 00-033-0448, Figure 5.4), or suggested from electrochemical measurements (Figure 5.7, Figure 5.8). The kinetic barriers or stoichiometric constraints (Cu, Al, O chemical fractions available) during dissolution may not be favorable to form these compounds either directly via solid state or indirectly via chemical precipitation from aqueous phase on the actively corroding Cu-Al surface. Solute capture (i.e. doping) of Al cations in cuprite would have consequences on the electrical and structural properties of the oxide layer formed on Cu-Al alloy, which would then affect the tarnish and corrosion behavior of the alloy.

5.4.2 The Fate of Al Following Corrosion in Artificial Perspiration: Solute Capture

The evidence of physical, chemical, and electronic modifications of the cuprite layer all suggest that an aluminum-enriched or doped Cu_2O is formed via solute capture following open circuit corrosion of Cu-Al in artificial perspiration.

Physical Modifications of Cu_2O

Cuprite Lattice Shrinkage

Cuprous oxide is a cubic structure with Cu cations located on an FCC sublattice and oxygen anions on a BCC sublattice translated one-quarter body diagonal. The most compact lattice plane is (111) also having the greatest diffraction multiplicity. GIXRD revealed that the 2Θ peak position relating to the lattice reflection of the (111) plane of cuprite was shifted to greater values (Figure 5.4). A Bragg's law calculation reveals a slightly more compact lattice indicated by a shorter distance ($\Delta d = 0.01$ Angstroms) between (111) lattice planes of this cubic crystal. The full width at half max of the cuprite (111) peak is greater on Cu-11Al (Figure 5.4), indicating that this lattice spacing is more distributed by the presence of Al possibly due to lattice distortions. The lattice is less uniform with possibly bounded lattice strain at the oxide/metal interface indicated by the broader peak with more Al in the cuprite lattice. These results concerning the structure of the cuprous oxide are suggestive of cation substitution of Al in place of some Cu atoms. The degree of enrichment of Al in the cuprite layer can be investigated with quantitative chemical analysis of photoelectron measurements.

Al-Enrichment

X-ray generated PE spectra (Table 5-4, Figure 5.6) were quantified to determine the relative cation fractions of Cu and Al in the films formed in artificial perspiration. The cation fraction of Al in the oxide on Cu-Al alloys tested in this study were compared with the Al content (at%) in the alloy (Figure 5.16). This figure shows the average cation fraction of Al in the film through its thickness from several sputter depths (Table 5-4). The position of the metal phase was determined from the Cu_{LMM} Auger excitation (when KE = 918.6 eV). The results were fit to a model presented by Kirchheim et al. [65] to quantify the enrichment of Cr in Fe-oxide films undergoing steady-state dissolution. Equation 5.7 describes the degree of enrichment of Al in the surface film for a Cu-Al alloy.

$$x_{Al,f} = \frac{\beta x_{Al,a}}{1 - x_{Al,a} + \beta x_{Al,a}} \qquad \text{Equation 5.7}$$

Where β is the ratio of the ion-specific dissolution rates (i_{Cu}/i_{Al}) under steady-state conditions. If the rate-determining step is cation diffusion through a conformal film, then under the assumptions of the Cabrera-Mott model [196], β may be described by the relative cation diffusivities through the film (D_{Cu}/D_{Al}) [65]. The subscripts *f* and *a* denote assignment to the element in the corrosion product film or alloy, respectively. The enrichment factor β was fit using Equation 5.7 from the sum of least squares regression using XPS cation fractions and alloy data values. The fit value of β obtained was 1.9, meaning that Cu was roughly half as likely to remain in the oxide film compared to Al. Chemical stability diagrams show (Figure 5.17) that in near neutral pH solutions that Cu_2O will precipitate first during anodic dissolution, followed by the possibility of hydrated Al_2O_3 compounds. It is therefore unlikely in minor amounts of Al (≤12 at%) that Al_2O_3 will be able to form if a metastable phase of Al-doped Cu_2O is a possible alternative.

Electronic Modifications of Cu_2O with Al^{3+} Solute-Capture

Increase in Reduction Overpotential

Not only does the thickness of the cuprite layer decrease with increasing Al content in the α-phase (Figure 5.9c), but the reduction potential also decreased (Figure 5.9b). An increase in electronic resistance of the oxide would manifest as an increased overvoltage, lowering the potential at which the oxide is galvanostatically reduced. Cathodic reduction indeed revealed that oxide films became more difficult to reduce with increasing Al content (Figure 5.9c). This result implies that the electronic defect structure of the semiconducting oxide, i.e. the charge carriers, are influenced by Al content.

Decrease in Charge Carrier Density

Cuprite (Cu_2O) is a metal-deficient p-type semiconducting oxide [77]. Positively-charge electron holes (p) carry electronic charge while negatively charged cation vacancies (V_{Cu}') are the dominant ionic defect [77]. The Mott-Schottky method can be used to estimate the density of charge carriers in a semiconductor [223]. While the exact defect density cannot be accurately measured from electrochemically grown films on metal substrates [225], relative changes in the defect nature of this semiconducting cuprous oxide were evaluated with a Mott-Schottky analysis (Figure 5.7). A decreased number of charge carriers, i.e. holes, were measured from Cu_2O films grown on the Cu-Al alloys. These results also support that Al^{3+} is likely present in the cuprous oxide cation sublattice either substitutionally in the place of Cu^+ cations or replacing Cu^+ cation vacancies which in turn affect the electronic structure of this oxide. The presence of substitutional Al cations in the oxide have consequences to the electronic structure as measured using the Mott-Schottky method. The defect chemistry of the cuprous oxide is modified by solute capture, i.e. doping, of Al^{3+} which has subsequent effects on corrosion products formed on the alloy.

5.4.3 Consequences of Solute Capture

Defect Chemistry and Aliovalent Solute Effects in Cuprous Oxide

The change in defect chemistry of cuprite due to Al substitution in the cuprous oxide cation sublattice is illustrated in Figure 5.18. The metal-deficient vacancy formation reaction is given by Equation 5.8. The equilibrium defect concentrations follow the thermodynamic relation in Equation 5.9 for a cuprous oxide with dominant cation vacancies.

$$\frac{1}{2}Cu_2O + V'_{Cu} + h^+ = \frac{1}{4}O_2 \qquad \text{Equation 5.8}$$

$$[V'_{Cu}][h^+] = \frac{pO_2^{1/4}}{K_{Cu_2O}} \qquad \text{Equation 5.9}$$

Where $[V'_{Cu}]$ is the concentration of Cu^+ vacancies, $[h^+]$ is the hole concentration, pO_2 is the partial pressure of oxygen, and K_{Cu2O} is the equilibrium constant of the reaction. Increasing the doping of trivalent Al as a substitutional cation in the Cu_2O lattice leads to an increase in Cu cation vacancies (V'_{Cu}) to maintain charge neutrality (Figure 5.18). For a given volume of Cu_2O, the amount of total oxidized Cu as soluble ions increases (Figure 5.10a) as these cation vacancies are created. Consequently, to maintain equilibrium via the law of mass action, and with a constant partial pressure (activity) of oxygen the number of holes (h^+, charge carrier) decreases. Al doping results in an increase in cation vacancies and a decrease in charge carrier density thereby decreasing electronic conduction [77,211]. However, the mobility of these extra cation vacancies is reduced through electrostatic interactions with Al^{3+}. Density-functional calculations have shown that substitutional Al cations (Al^{2+}_{Cu}) strongly binds with two copper cation vacancies with a binding energy of 3.3 eV, thus greatly reducing vacancy mobility [231]. Inhibited electronic and ionic mobility reduces the thickness of the Cu_2O corrosion product (Figure 5.9c). Mott-Schottky analysis corroborates this effect (Figure 5.7). The nature of the fate of the elements is indeed affected by Al; the thinner Al-modified cuprite films promote tarnish-resistance with simultaneous favoring soluble Cu release over oxide formation.

Tarnish Resistance through Thinning of the Cuprite Layer

Decreased thickness of cuprite layers with increasing Al content in α-Cu phase was also observed by Süry and Oswald [211]. They speculated that Al^{3+} cation substitutions in Cu_2O was responsible for the increased electronic resistance of the oxide [211] however until now, physical evidence to this claim has not been presented. The increased electronic resistance of the oxide is confirmed in the present work by CR and MS results given in Figure 5.9 and 6, respectively. Concerning the concept of generating a tarnish-resistant antimicrobial alloy by restricting growth of the oxide layer to undesirable levels, solid solution alloying of copper with oxide doping of aliovalent elements such as Al through solute capture is extremely promising in this regard.

Soluble Copper and Potential Antimicrobial Function

While the increased resistance of the oxide film (Figure 5.9b) contributed to thinner Cu_2O which became more difficult to form, Cu ions continued to be released through this layer (Figure 5.11). An antimicrobial surface must maintain a sustained corrosion rate in order to be continuously functional. The thinner oxide and decreased steady-state thickness at similar corrosion rates drove the corroding system to produce more soluble Cu ions relative to oxide formation with increasing Al content. Greater Al contents would be expected to increase this effect but may be limited by solid-solution alloying limits. In this regard Cu with 11 at% Al effectively formed a ‘leaky’ stable oxide film through which soluble Cu is released, facilitating a tarnish-resistant and continually antimicrobial surface on the Cu-11Al alloy.

5.5 Conclusions

- The fate of Al following corrosion in artificial perspiration is solute captured Al^{3+} cations in the cuprous oxide layer evidenced by (1) structural modifications determined with GIXRD, (2) electrochemical modifications to the oxide layer via coulometric reduction, (3) the presence of Al in the cuprous oxide layer through X-ray photoelectron spectroscopy, and (4) changes in the defect chemistry of the p-type cuprous oxide revealed with Mott-Schottky analysis.

- Al in the cuprite layer decreased the corrosion product thickness consistent with increased electronic and ionic resistivity due to dopant effects of substitutional Al cations on the Cu cation sublattice reducing the amount of electron holes and reducing ionic mobility through binding with metal vacancies. This results in thinner oxides while soluble Cu release remained approximately equal to pure Cu.
- Implantation of Al from the alloy into the cuprous oxide layer formed a more tarnish-resistant surface oxide which was thinner, had greater electronic resistance, and more difficult to electrochemically reduce with increasing Al content.
- Modifying the copper oxide layer with Al solute can alter the corrosion products formed on the surface of a Cu-Al alloy facilitating a tarnish-resistant layer without affecting soluble Cu release for antimicrobial function.

5.6 Tables

Table 5-1. Selected Gibbs Free Energies of Oxidized Cu and Al Compounds [120,121].

Compound Name		**ΔG^0_{298} (kJ/mol)**
$CuCl$	Nantokite	-119.7
CuO	Tenorite	-127.9
Cu_2O	Cuprite	-147.9
$CuCl_2 \cdot 2H_2O$	Eriochalcite	-655.9
$CuAlO_2$	Copper Aluminate	-868.6
$Cu_2(OH)_3Cl$	Botallackite	-1322.6
$Cu_2(OH)_3Cl$	Atacamite	-1339.2
$Cu_2(OH)_3Cl$	Clinoatacamite	-1341.8
Al_2O_3	Alumina	-1581.4
$CuAl_2O_4$	Copper Aluminate	-1695.1

Table 5-2. Elemental composition (wt%) of commercial-grade Cu, Al, and high-purity custom binary Cu-Al alloys as tested according to ASTM E478.

Alloy	**Cu / wt%**	**Al / wt%**	**Other / wt%**
Cu	99.997	--	--
Cu-0.2Al	99.91	0.09	--
Cu-2Al	99.01	0.99	--
Cu-11Al	95.22	4.78	--
Al	00.06	99.38	0.37 Fe , 0.13 Si, 0.02 Ga

Table 5-3. Chemical composition of artificial perspiration solution (pH 6.50 ±0.05) based on B.S. EN1811[48]

Chemical Name	**g/L**	**Molarity (mM)**
NaCl – Sodium Chloride	5.00	85.6
CH_4N_2O - Urea	1.00	16.7
$C_3H_6O_3$ - L(+) Lactic Acid (90%)	1.00	11.1
NH_4OH –Ammonium Hydroxide	pH Adjuster	~11

Table 5-4. Spectra fitted peak values and areas of XPS and X-ray-induced Auger electron data of Cu-Al alloys exposed to artificial perspiration for 96 h at open circuit. Sputtering rate was measured as 0.3 nm/s on a SiO_2 sample.

		Al_{2p}		**O_{1s}**		**Cu_{2p}**		**Cu_{3p}**		**Cu_{LMM}**	**Cl_{2p}**	
	Sputter Time (s)	**Peaks (eV)**	**Area**	**Peaks (eV)**	**Areas**	**Peaks (eV)**	**Areas**	**Peaks (eV)**	**Areas**	**Peaks (eV)**	**Peaks (eV)**	**Areas**
Cu-0.2Al	0	-	-	530.49, 531.05	7883, 8059	932.56, 952.36	145844, 72922	77.56, 75.09	71212, 17700	916.41	198.65, 200.25	1830, 915
	350	-	-	530.39, 530.03	8861, 3377	932.55, 952.35	232191, 116096	77.59, 75.11	8894, 22820	916.71	199.07, 200.67	1123, 562
	700	-	-	530.32, 529.49	1194, 351	932.62, 952.42	2374112, 118706	77.53, 75.06	9344, 23389	918.64	199.31, 200.91	72, 36
	1750	-	-	529.76, 530.43	66, 128	932.62, 952.42	232387, 116193	77.53, 75.06	8919, 22908	918.83	-	-
Cu-2Al	0	71.91	522	530.26, 531.47	13529, 6374	932.34, 952.14	125476, 62738	77.32,74.87	7630, 15597	916.68	198.28, 199.88	1083, 541
	350	-	-	530.34, 531.60	673, 585	932.63, 952.43	339515, 169757	77.46,74.99	13592, 30433	918.68	-	-
	700	-	-	530.39, 531.73	321, 253	932.64, 952.44	340837, 170418	77.46,75.00	13014, 30935	918.66	-	-
	1750	-	-	530.90	653	932.64, 952.44	338932, 169466	77.47,75.01	12767, 31181	918.67	-	-
Cu-11Al	0	73.17	3921	530.27, 531.11	5854, 17096	932.33, 952.13	8428, 42140	77.17,74.82	8791, 9944	916.65	198.64, 200.24	969, 485
	375	71.26	472	531.00, 531.83	22591, 29856	932.84, 952.64	48922, 24461	77.74,74.84	4626, 12347	918.38	198.97, 200.57	586, 2923
	750	72.72	3484	530.96, 531.75	10626, 10590	932.78, 952.58	228817, 114409	77.67,75.07	9411, 18822	918.62	199.03, 200.63	221, 111
	1125	73.00	6718	530.96, 531.88	30153, 427	932.71, 952.51	298279, 149140	77.38,75.03	14643, 17856	918.61	-	
	1500	73.05	7880	530.66, 531.75	362, 1897	932.72, 952.52	326038, 163019	77.35,75.05	16902, 17950	918.61	-	

5.7 Figures

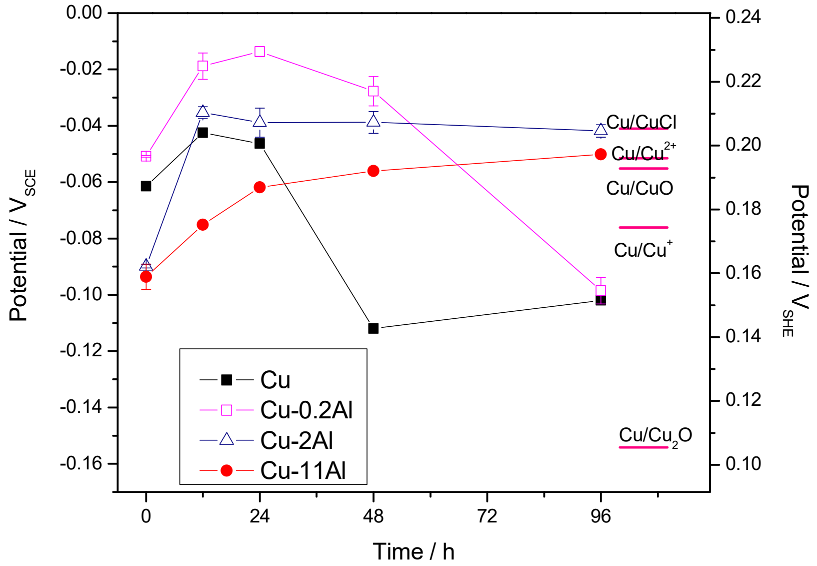

Figure 5.1. Open circuit potential of Cu, Al, and Cu-Al alloys in quiescently-aerated artificial perspiration over time up to 96 hours. Selected Nernst potentials of interest are also shown on plot. Al sample OCP = -0.55 V_{SCE} not visible on this scale. Al→Al_2O_3 E_r = -2.2 V_{SCE}.

Cu Cu-0.2Al Cu-2Al Cu-11Al Al

Figure 5.2. Visual surface condition of Cu-Al alloys following full immersion exposure to artificial perspiration for 96 h. Horizontal dimension is 5 mm.

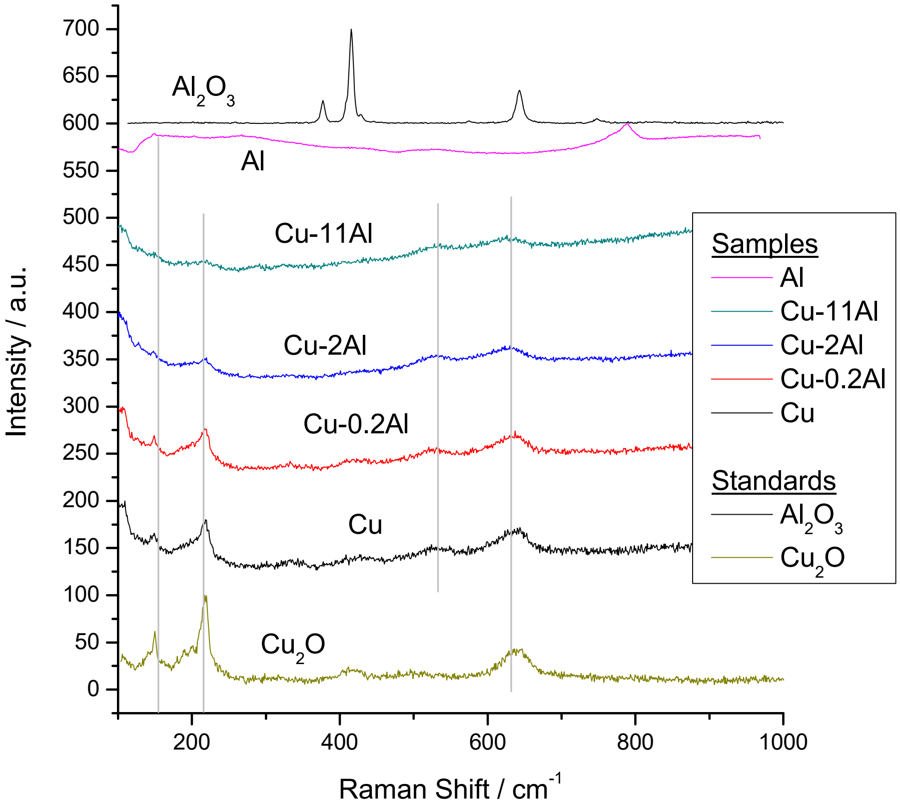

Figure 5.3. Raman spectroscopy of Cu, Al, Cu-Al samples, and standard reference cold-pressed powder pellets of suspected corrosion products Cu_2O and Al_2O_3.

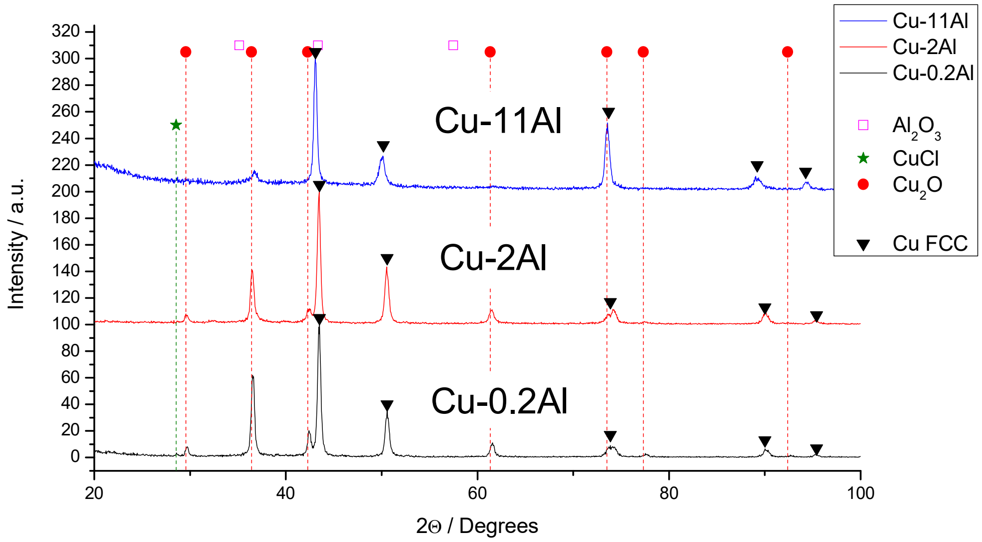

Figure 5.4. Grazing-incidence X-ray diffraction patterns of Cu-Al samples following 96 h at open circuit in artificial perspiration. The incident angle, ω, was set to 0.5° to limit the illumination depth. Alloy substrate assignments account for 2Θ displacement from solid solution alloying.

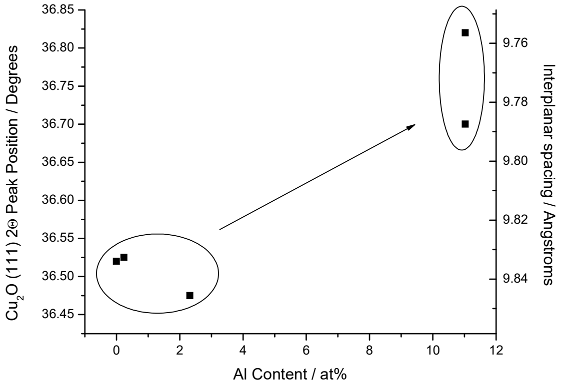

Figure 5.5. Peak position of the (111) Cu_2O lattice and approximate interplanar spacing as a function of Al content.

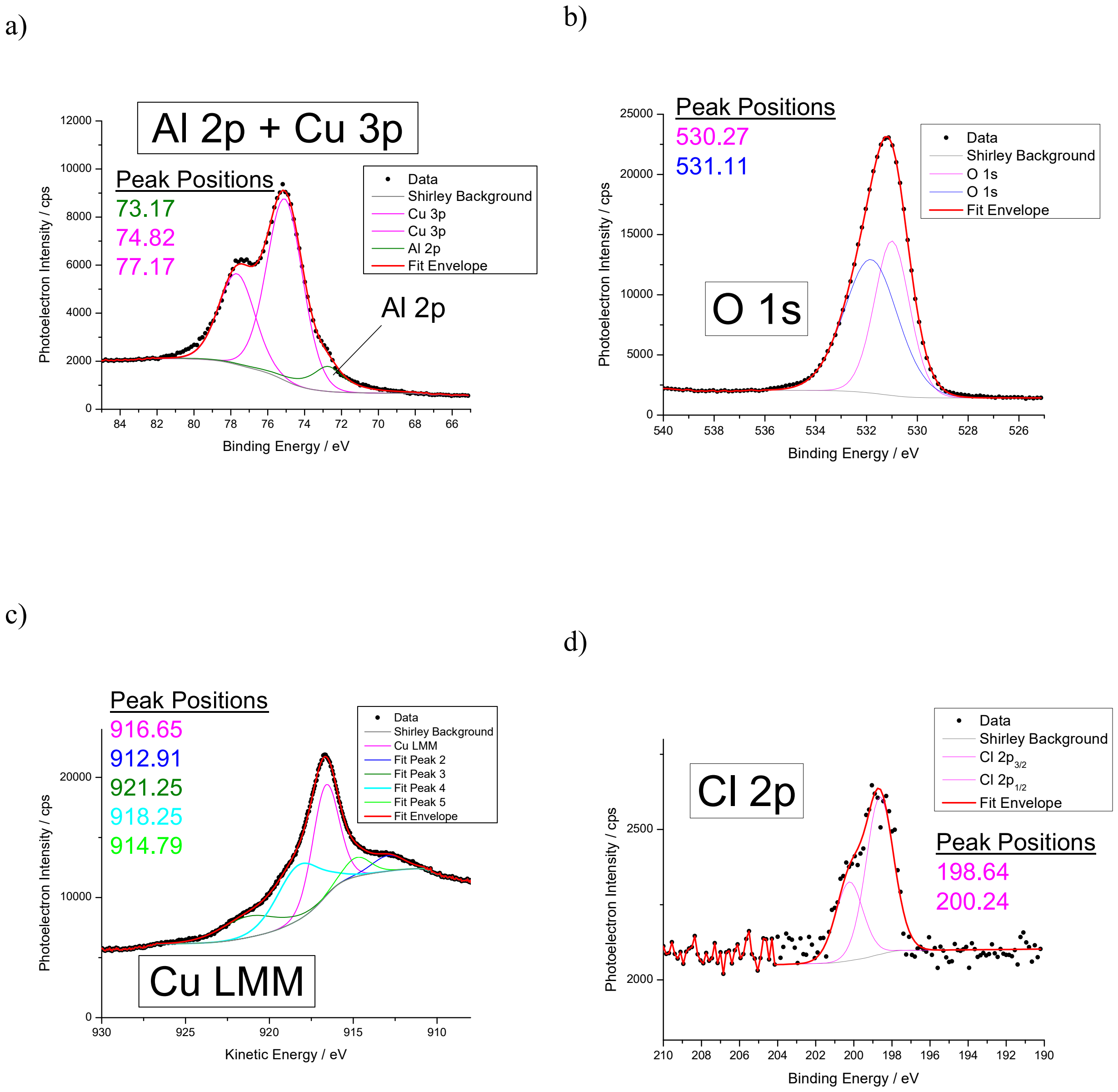

Figure 5.6. High resolution X-Ray photoelectron spectra of the as-introduced sample of Cu-11Al following 96 h of full-immersion exposure to artificial perspiration at open circuit. (a) Aluminum 2p and Copper 3p, (b) Oxygen 1s, (c) Cu LMM Auger transition, and (d) Chloride 2p. Photoelectron energies were calibrated using the Au $4f_{7/2}$ peak set to 84.0 eV.

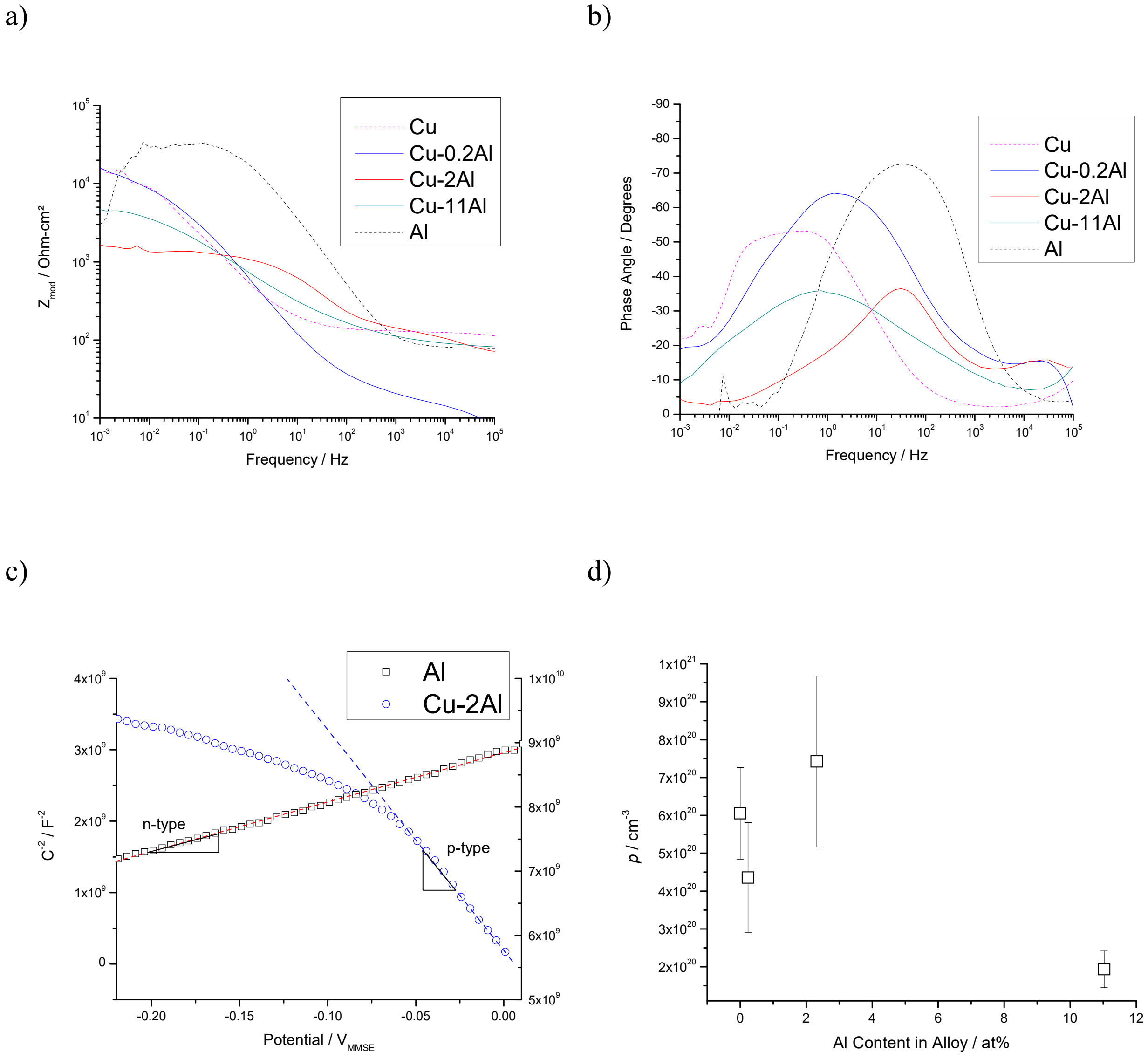

Figure 5.7. Measurements of galvanostatically pre-grown oxide films on Cu-Al alloys using the Mott-Schottky method. Electrochemical impedance spectra Bode magnitude (a) and phase (b) of Cu-Al alloys at open circuit for 96 hours artificial perspiration. Example Mott Schottky plots (c) and approximate defect carrier density (d) of cuprous oxides. Error bars are the standard error of three replicate experiments.

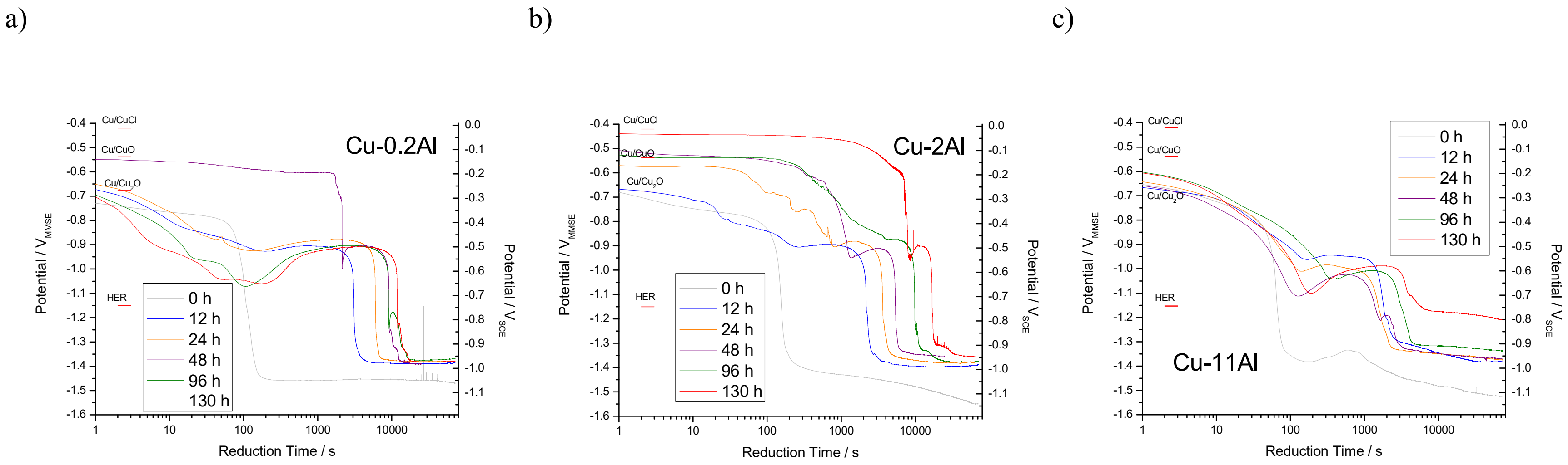

Figure 5.8. Coulometric reduction curves of Cu-Al alloys following open circuit exposure to artificial perspiration at specified durations up to 130 h. a) Cu-0.2Al, b) Cu-2Al, c) Cu-11Al. Reduction media was a deaerated boric/borate buffer at pH 8.4 with an applied cathodic current of 25 µA/cm². Al_2O_3 →Al E_r = -2.6 V_{MMSE}

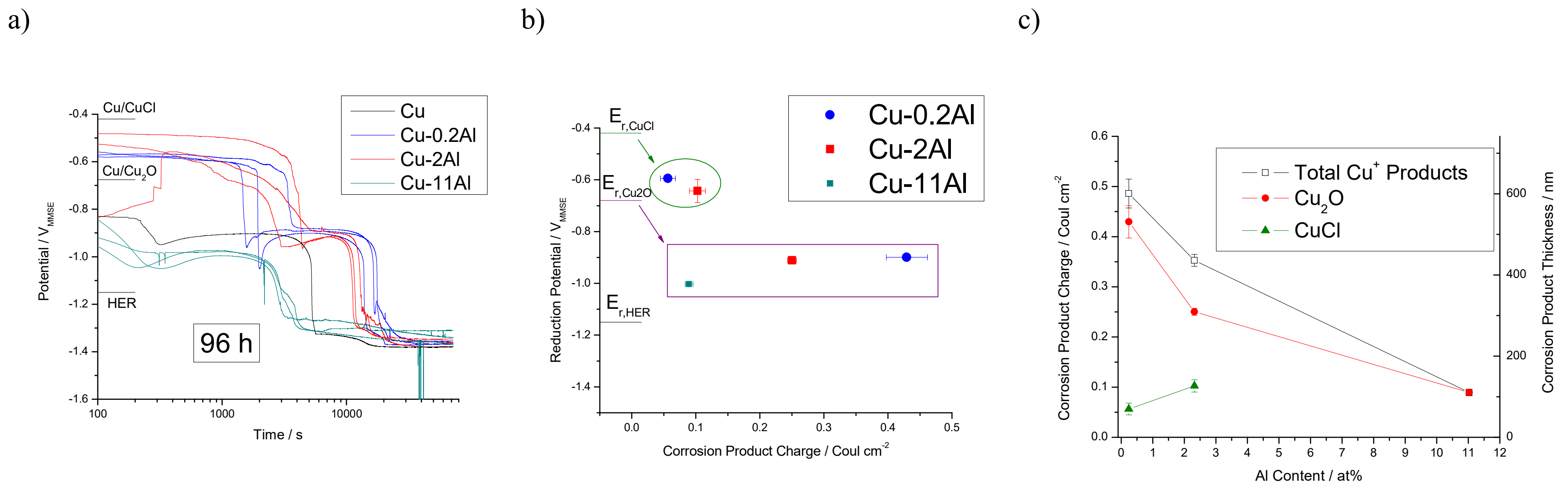

Figure 5.9. Coulometric reduction statistics at 96h in artificial perspiration. a) chronopotential curve, b) Reduction potentials and individual amounts of corrosion products expressed as charge density, and c) Total reducible corrosion product charge as a function of Al content and estimated thickness from Equation 5.4.

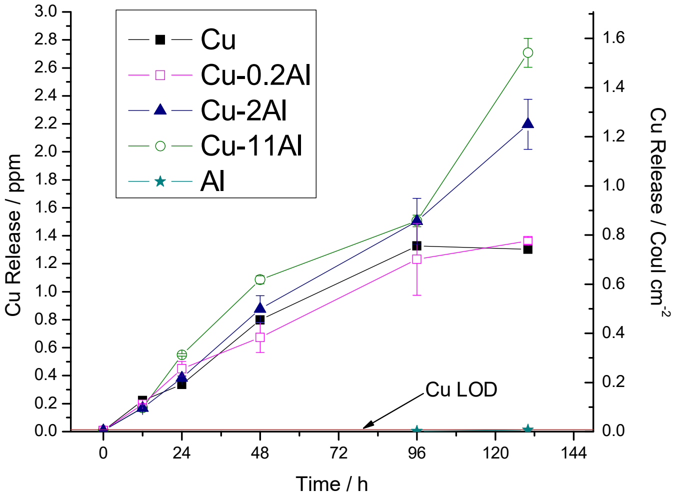

Figure 5.10. Soluble Cu release from Cu, Al, and Cu-Al alloys at set time points in artificial perspiration up to 130 h. Aliquots (15 mL) of separate samples taken at set time intervals and measured using ICP-OES. Error bars are the standard error of three measurements per aliquot. Solid red line is the limit of detection for Cu: 17 ppb.

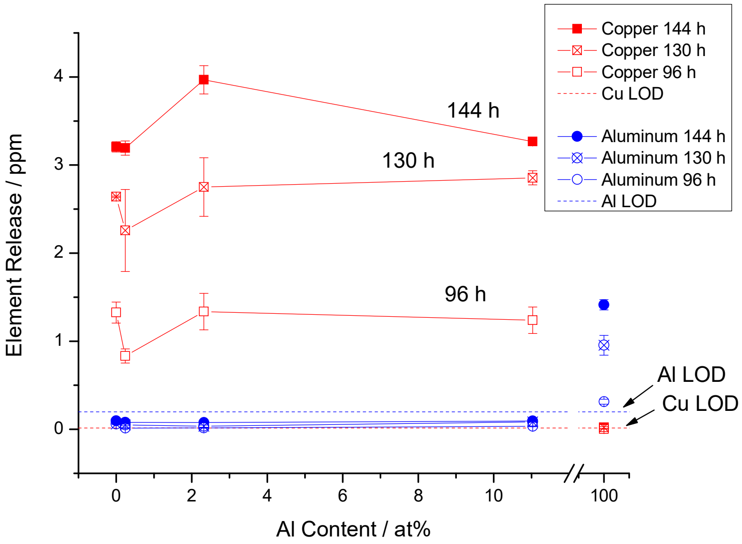

Figure 5.11. Soluble element release via ICP-OES as a function of Al content in the alloy. Error bars are the standard error of three replicate experiments. Cu and Al limits of detection are illustrated by red and blue dashed lines, respectively.

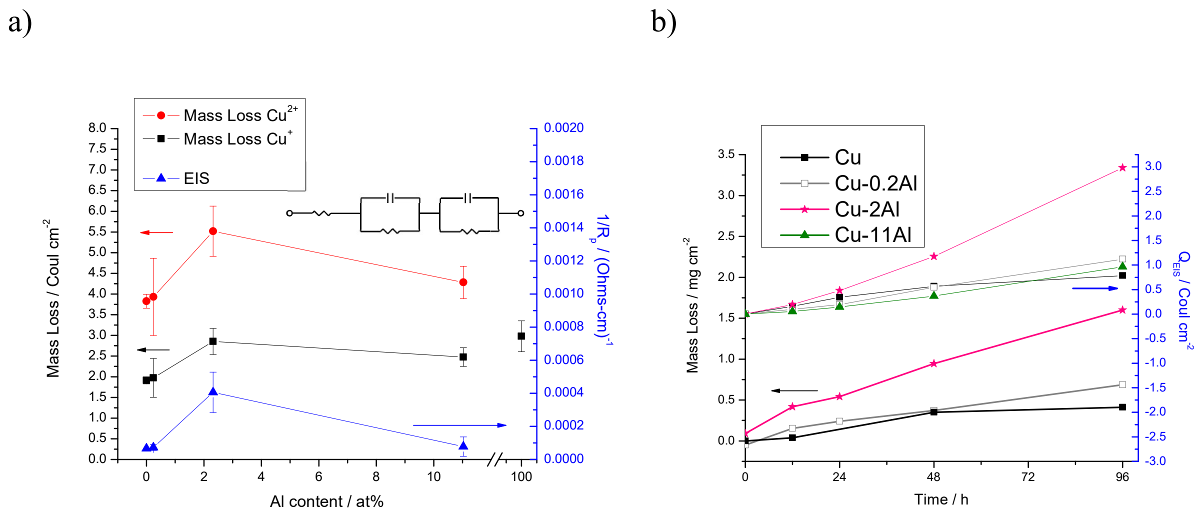

Figure 5.12. Total anodic charge measurements of Cu-Al alloys exposed at open circuit to artificial perspiration a) after 96 h of gravimetric mass loss compared to inverse polarization resistance determined with EIS and b) over time up to 96 h. Inverse polarization resistance (a) and integrated anodic charge (b) were calculated from equivalent circuit fits (circuit shown in inset of a). Error bars are standard error of triplicate measurements. Stern-Geary coefficient, *B*, assumed as 25 mV. Equivalent circuit elements R_s = solution resistance, CPE_{ox} = oxide constant phase element, R_{ox} = oxide resistance, CPE_{dl} = double layer constant phase element. R_{ct} = charge transfer resistance. $R_p = R_{ox} + R_{ct}$.

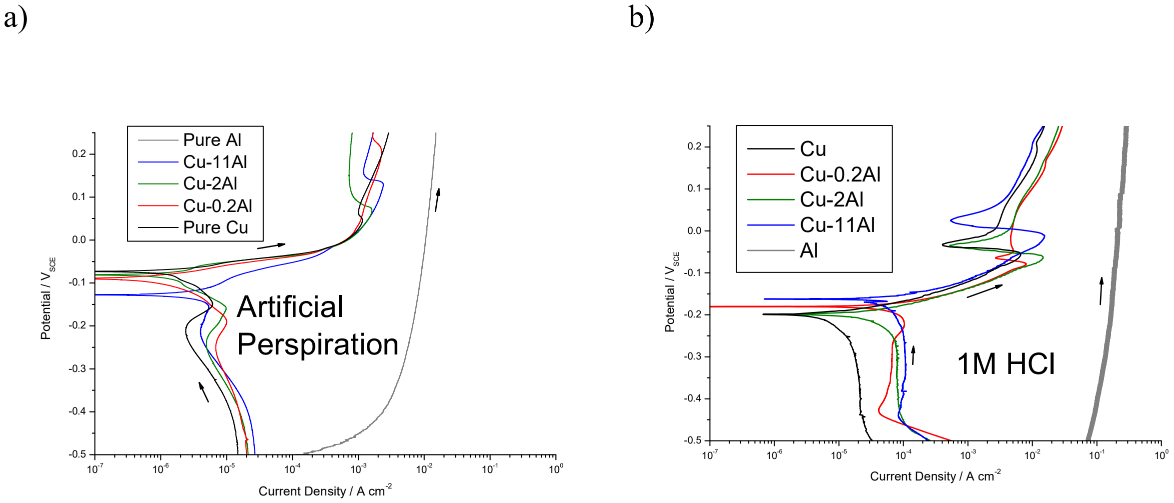

Figure 5.13. Potentiodynamic polarization scans of Cu-Al alloys in a) artificial perspiration, and b) 1M HCl. Scan rate 0.1667 mV/s. Samples were held at -1.5 V_{SCE} for 10 min prior to upward scan.

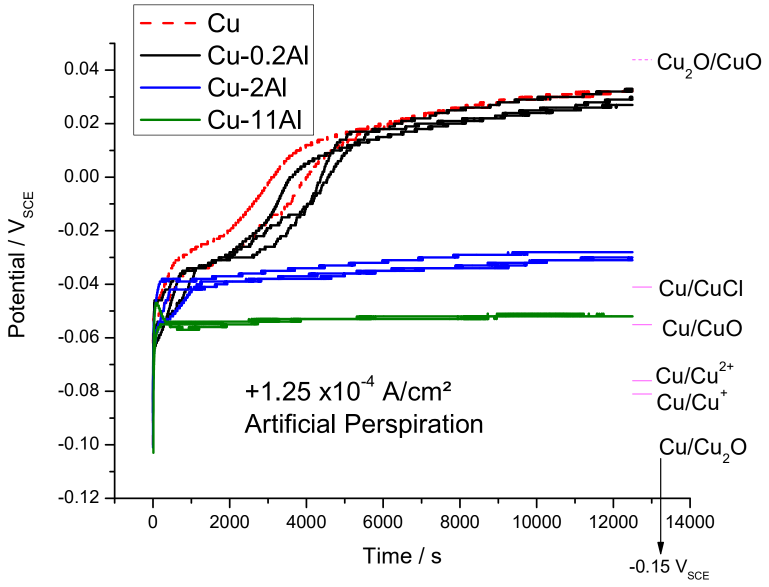

Figure 5.14. Galvanostatic anodic holds of Cu-Al alloys in naturally-aerated artificial perspiration. The anodic current applied was 1.25 x 10^{-4} mA/cm².

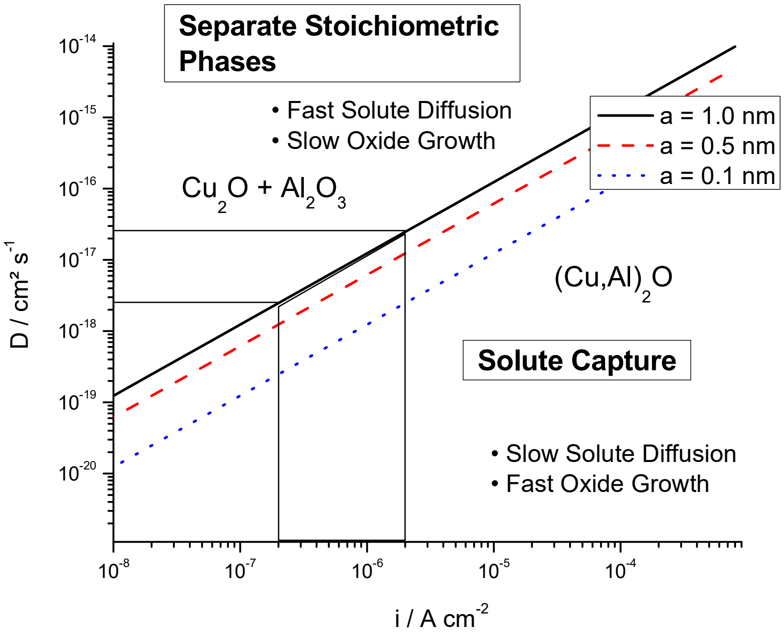

Figure 5.15. Theoretical requirements for solute capture of an element in a growing oxide for various jump distances (a). The diffusion coefficient (D) of the solute in the growing oxide is compared with the current density attributed to the growing oxide interface (*i*). Should the advancement of the oxide front exceed the speed at which the solute can diffuse to form its own oxide, the solute becomes captured as a substitutional defect in the oxide [219].

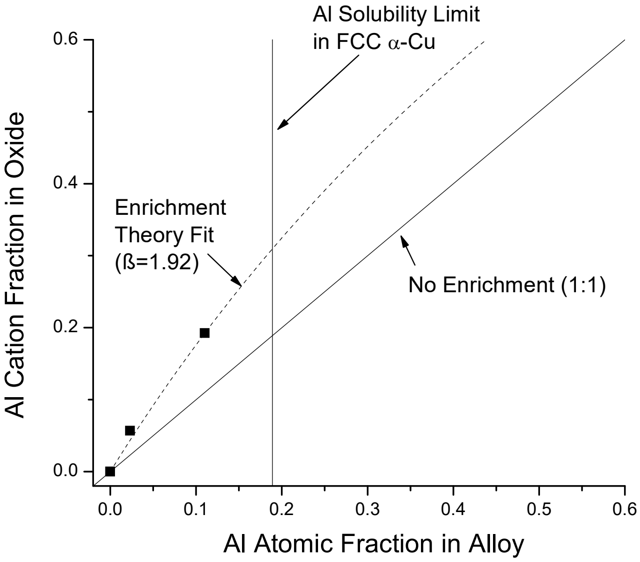

Figure 5.16. Solute enrichment of Al in cuprous oxide. Aluminum cation fractions determined via XPS (Table 5-4) of Al in the cuprite (Cu_2O) layer. Solute enrichment factor was fit using Equation 5.7 [65,79].

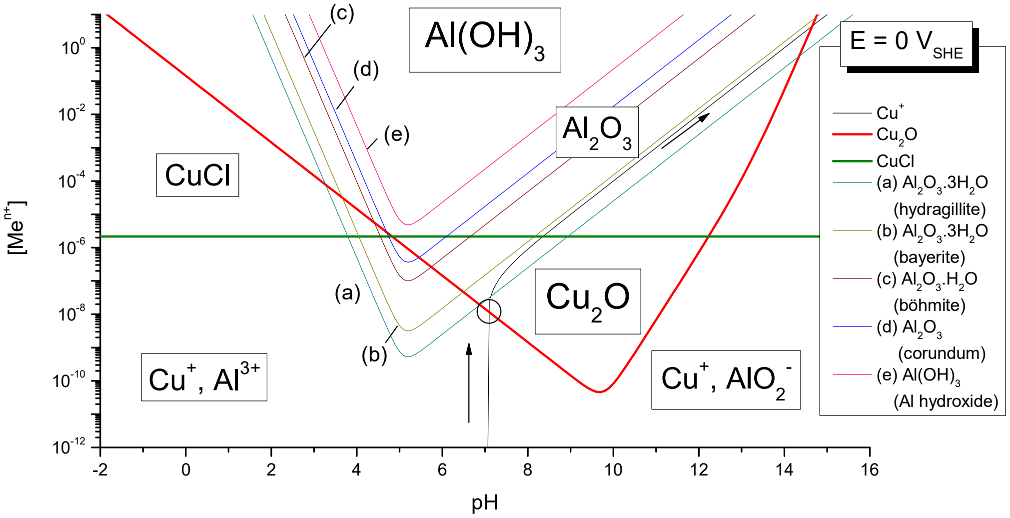

Figure 5.17. Superimposed chemical stability diagrams [126] of Cu and Al oxides as a function of pH with $[Cl^-] = 0.086$ M (artificial perspiration). Metal dissolution trajectory is indicated by arrows. Equilibrium products calculated for a potential of 0 V_{SHE}. The point of first chemical precipitation of an oxide is circled.

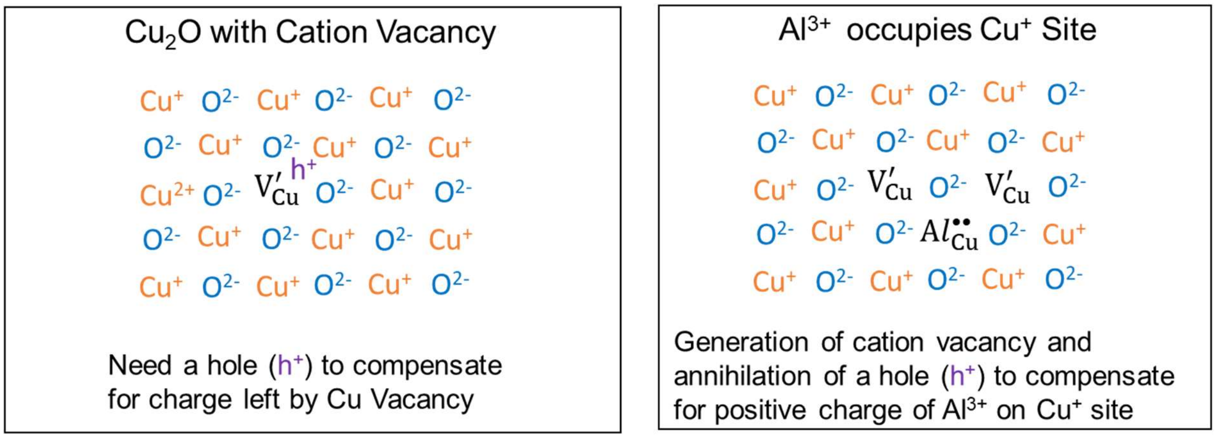

Figure 5.18. Schematic illustration of aluminum doping effects on cuprite electronic properties. Effect of intrinsic defects compared with Al-doped on the equilibrium defect chemistry.

6 Antimicrobial Function, Corrosion Behavior, and Synergistic Effects of Solid Solution Aluminum-Tin-Copper Ternary Alloys in Artificial Perspiration Solution

Abstract

An ideal antimicrobial alloy composition is difficult to predict as element additions to Cu-based alloys demonstrate non-intuitive responses without clear dose-response relationships to corrosion and cation release. A Cu-Al-Sn alloy with strict metallurgical control may remain both antimicrobial and non-tarnishing through regulating enhanced Cu dissolution from Sn and tarnish-resistance through Al. In this chapter, several Cu-Al-Sn alloys were investigated for anti-tarnishing and antimicrobial efficacy. Custom ternary compositions of Cu-Al-Sn with alloying contents corresponding to previously investigated binary alloys were fabricated and studied in artificial perspiration. Ternary Cu-Al-Sn alloys demonstrated that Sn-enhanced Cu dissolution which enhanced Al-enrichment in the oxide. In turn this lead to greater Al-doping of Cu_2O and tarnish-resistance without significantly affecting total Cu release or antimicrobial function. Increased Al-doping led to the formation of a more corrosion-resistant thinner oxide phase which at 5 wt% Sn was not reducible by coulometric reduction inferring that this oxide was not Cu-based. The mechanisms of how the individual effects of Sn and Al function or act cooperatively are discussed. A compositional range of solid solution Cu-Al-Sn alloys were found to be both antimicrobial and tarnish-resistant, able to kill all planktonic *E. Coli* under 24 hours in using a custom disinfection test.

6.1 Background

Tarnish-resistant alloys rely on passive oxides to retard corrosion and maintain a stable aesthetic surface. However, passivity can reduce the corrosion rate that is required to provide sufficient cytotoxic copper ions for antimicrobial function. A number of alloying element additions to Cu do not demonstrate clear dose-response relationships to surface films and/or cation release making an ideal composition for both anti-tarnish and antimicrobial functions difficult to predict. Current tarnish-resistant antimicrobial alloys use Zn or Mn which result in a golden color, or Ni which causes a lustrous white alloy color [232]. However, an antimicrobial alloy should be hypoallergenic while accomplishing these balanced goals uniquely without the use of Ni, an increasingly common metal allergen [9] or Zn or Mn which tend to dealloy [36–42].

Cu-Al-Sn may accomplish these two desired goals, i.e. antimicrobial and non-tarnishing, without the use of Ni, Zn, or Mn which are crucial additions for the function of these other systems [232,233]. Sn when added to Cu-Sn alloys generally increased the cation release of Cu but increased the corrosion rate and formed a tarnishing oxide layer [154]. In contrast, Al when added to Cu-Al decreased the thickness of Cu_2O and visible tarnish formed by doping the oxide with Al^{3+} while still permitting release of soluble Cu (Chapter 5). Too much Al would cause the alloy to passivate and too much Sn or too little Al will cause the alloy to tarnish.

6.1.1 Antimicrobial Cu-Al-Zn-Sn Alloys

Nordic Gold (Cu-5Al-5Zn-1Sn, wt%), a solid solution European coinage metal, is an attractive option for antimicrobial high-touch applications due to its high resistance to tarnishing combined with antimicrobial function [22]. However, this alloy is only antimicrobial in some environments when freshly cleaned or abraded and subsequently demonstrates limited antimicrobial function after just seven days of exposure to ambient laboratory air [26]. Tarnish-resistant alloys form a passivating thin layer which impedes the anodic reaction and subsequent Cu release needed for antimicrobial function. The passive layer on Nordic gold clearly inhibits corrosion (and soluble ion release) to an undesirable degree. However, in artificial perspiration, Cu-5Al-5Zn-1Sn released similar Cu in solution as Cu [17,23,26], likely due to the aggressiveness of the hand-contact simulant [30]. Nordic Gold exemplifies current shortcomings in current evaluative methods for antimicrobial response; Cu(I)/Cu(II) release from corrosion and passive films are dependent on solution chemistry and antimicrobial testing heretofore is not conducted in high-touch representative environments [17,23,26]. Most Al-bronzes are labeled antimicrobial, yet, for example Cu-7Al-7Zn-2Sn (a highly tarnish-resistant alloy) curiously is not [205], conceivably for similar reasons as Cu-5Al-5Zn-1Sn mentioned previously. These alloys possess Zn and Al, which in solid solution with Cu tend to decrease Cu release (see Table 1-3) [5,26,46]. Whereas Sn in solid solution is expected to enhance Cu ion release as discussed previously [154]. Many tarnish-resistant alloys in this system simply may be too rich in passivity-promoting (e.g., Al, Sn) or dissolution-inhibiting (e.g., Zn, Mn) alloying elements to enable sufficient Cu release for antimicrobial function. Moreover, alloys in the Cu-Al-Sn system have demonstrated variable antimicrobial efficacy as a strong function of alloying content [205], alluding to a potentially tunable system through careful metallurgical control of competing elements Al and Sn.

6.1.2 Cu-Al-Sn Corrosion

Effect of Increasing Al

Cu-Al-Sn alloys are more corrosion resistant than Cu and Cu-Al [61]. Several Cu-Al-Sn alloys of various compositions (Sn + Al ≤25 at%, see Figure 6.1) were evaluated for corrosion in various SO_4^{2-} solutions. Increasing the Al content in Cu-Al-Sn decreased the corrosion current densities for all tested pH values (1-12) [62]. Increasing the pH (7→12) also decreased the limiting passive current density [212]. The critical content for Al passivation in this ternary system is 13 at% Al (for 1-3 at% Sn) [61] which agrees well with graph theory, where a cation fraction of 13% Al in the cuprous oxide should be sufficient to passivate the alloy [76]. If the alloy Al content exceeds this value an Al-rich layer rapidly builds on the surface and passivates the alloy [61]. While these corrosion products are known to be protective in various environments, there is ambiguity in the molecular identity and chemical stoichiometry of these compounds.

Molecular Identity of Passive Films

'Al-type' oxides containing Cu and Cu-rich Al oxide phases are reported in the literature [61,62,211] but molecular identity was not determined or confirmed. The passive film could be a thin layer of Al_2O_3, $CuAlO_2$ or $CuAl_2O_4$, or Al-doped Cu_2O (Chapter 5). The primary passive film formed on Cu-Al alloys is cited by many to be Al_2O_3 [64,202,203,216–218]. However, the thermodynamically predicted phases listed in increasing stability are as follows: $Al_2O_3 \rightarrow CuAlO_2 \rightarrow Al_2O_3 + CuAl_2O_4$ [121]. The stability domain of the $CuAlO_2$ compound is significant [121]. Chemical precipitation of solute-stabilized paratacamite ($Cu_3(Me)(OH)_6Cl_2$, atacamite group) and a yet-unidentified compound of Cu, O, and Al is observed on both Cu-Al [211] and Cu-Al-Sn [61,62].

A separate oxide of Al has not been identified in the corrosion literature of Cu-Al-Sn but is labelled an Al-type passive layer [62]. This unidentified phase was enriched in Al and was found in a "poorly crystalline and heavily faulted state" [211]. Indeed, this compound ($CuAlO_2$) may be the unidentified phase highlighted in Cu-Al and Cu-Al-Sn corrosion studies [61,62,211]. Al in the oxide layer increased as time progressed as revealed by Auger Electron Spectroscopy: Al contents in the film on Cu-19Al-3Sn (at %) were 30% after 1 h and 50% after 60 h (via AES) [61].

An Al-doped Cu(I) oxide is speculated in the literature [211] to be responsible for the excellent corrosion resistance of Cu-Al and Cu-Al-Sn through similar mechanism as Ni, discussed previously (Chapter 5), but corrosion studies of Cu-Al-Sn disagree [61], assigning this protective behavior due to the ambiguously assigned 'Al-type' film [62]. Notably, this product afforded protection (either kinetic or thermodynamic) beyond alumina's amphoteric range (pH 4 – 8.5, $[Al^{3+}] = 10^{-6}$ [126]). An extension beyond the chemical stability of Al_2O_3 suggests that either this oxide is modified by Al, Sn, or Cu, or another oxide (e.g., a cuproaluminate) is acting to protect the alloy from dissolution.

Photocurrent measurements on Cu-Al-Sn oxides indicated p-type conduction whereas passive Al_2O_3 is an n-type semiconductor [62]. Initially the band gap is suggestive of a copper oxide layer, yet after longer exposure the bandgap (no values were reported) approaches the value expected for alumina [61]. Passive current densities rise when the pH is <4, which is further evidence that the surface layer is Al-rich as unmodified copper oxides are also not stable at this low pH [61]. The state of the present literature remains a juxtaposition of speculative claims without any clear diagnostic attempts to determine the source of corrosion protection due to thin corrosion product films formed on Cu-Al-Sn. To understand alloy behavior and generate a tunable alloy with antimicrobial function, the specific molecular identity of the passivating oxide species must be known. A passive oxide almost entirely prevents corrosion and subsequent cation release of Cu needed for antimicrobial function.

The Effect of Sn with Al in Cu-Al-Sn Alloys

The addition of Sn further increases the corrosion resistance of Cu-Al. Cu-16Al (at%, above passive alloying threshold) do not show equal corrosion resistance as Cu-Al-Sn alloys of similar Al content [61]. The mechanism of Sn-enhancement has yet to be identified [61]. Sn may act as a dissolution promoter (Figure 1.5), enhancing the effects of Al films. Though, it is improbable that this enhancement is due to a SnO_2 layer as the alloying amount is quite low [61,121]. Sn added to Cu-Al-Sn shows distinctly different behavior based on the amount added. Low amounts of Sn (< 5 at% Sn) had increased corrosion rates compared to higher amounts (> 5 at% Sn) [61]. Leading up to 5 at% Sn, increasing Sn up to this value decreased passive current densities [61], but after this threshold value, the effect reversed: wherein increased passive current densities were observed with increasing Sn [61]. Sn was not enriched on the surface evidenced from Auger electron spectroscopy (AES) measurements [61]. Therefore, Sn must either be functioning within the passive oxide layer [61], trapped at the oxide/alloy interface, or promoting dissolution. Sn lowers E_{corr} by raising the corrosion reaction rate as revealed by potentiodynamic polarizations and cyclic voltammogram (CV) scans (see Appendices). At longer times (~1 year) the enhancement effect of Sn is more pronounced further reducing the corrosion rate [61]. Adding minor Sn amounts (<5 at% Sn) revealed a beneficial effect on the corrosion resistance of 'Al-type' passive films [61]. Furthermore, elucidating effects of alloy chemistry without complications from microstructure constrains the present study to solid solution compositions of Cu-Al-Sn. Therefore, compositions in the solid solution are desired.

6.1.3 Cu-Al-Sn Metallurgical Phase Stability

The Cu-rich corner of the Cu-Al-Sn ternary phase diagram [234] is given in Figure 6.1. Data points of alloy phases [234] from metallurgical literature experiments as well as alloy compositions from corrosion experiments [61,62] are overlaid on thermodynamic alloy phase predictions. Compositions of alloys tested in previous chapters are also shown for comparison. To avoid electrochemical complications (e.g., microgalvanic coupling) from secondary intermetallic phases, compositions were restricted as indicated to solid solution alloy compositions as outlined in the lower left FCC phase domain.

6.2 Critical Unresolved Issues

An abundance of literature exists on corrosion of Cu alloys, and an increasing amount of literature emerging regarding the antimicrobial properties, effectiveness, and mechanisms of the antimicrobial properties of Cu and Cu alloy. Cu-Al-Sn are less well-studied, and therefore suffer from incomplete assessments and characterization of anodic films, critical passivity thresholds, and alloying effects, cooperative interactions and synergisms. The individual roles of Sn and Al have been investigated in Chapters 2 - 5, however, how the mechanisms of Sn and Al combine and interact remains unknown. This system may be ideal for the study of a hypoallergenic (no Ni), tarnish-resistant, and antimicrobial alloy for high-touch surfaces, yet there remain several outstanding issues which need to be addressed before an optimal alloy system could be made.

- With exception to Nordic Gold (Cu-5Al-5Zn-1Sn), few studies have been conducted in representative biological solutions of this system (Cu-Al-Sn) such as artificial perspiration.
- Secondary intermetallic phases in the Cu-Al-Sn system obfuscate the individual effects of Sn and Al in solid solution with FCC Cu. To investigate the effects of these individual elements, a restriction to the solid solution α-Cu (FCC) phase domain must be imposed. Other impurity elements must also be removed; a requirement unattainable with off-the-shelf commercial alloy systems.
- Sn in this ternary system may affect either dissolution kinetics or passive film stability. It remains unclear if Sn still behaves as a Cu dissolution promoter in Cu-Al-Sn as in Cu-Sn. Furthermore, tin’s enhancement of cuprous dissolution may also promote preferential Cu

dissolution leading to the observed enhancement of the protection afforded by Al of these Cu-Al-Sn alloys.

- The specific role of Sn on the Al-type layer has demonstrated to be critical to the corrosion and passivation behavior of these alloys yet remains unexplored in the literature. Systematic control of Al and Sn content should be employed to elucidate the individual roles of these elements on corrosion, film stability, and Cu cation release.
- A mixed Al-Cu-type passive layer has been observed in several works [61,62,121,211]. Yet, a lack of confirmation of the precise identity of this oxide species (potentially Al_2O_3, Al-doped Cu_2O, or $CuAlO_2$) persists in the literature. To understand alloy behavior and generate a tunable alloy, the specific molecular identity of the species must be known. Specifically, the impact and role of this surface film on Cu cation release for antimicrobial function as well as corrosion rate.

An ideal antimicrobial Cu-Al-Sn alloy would be tuned through solid solution alloying of Al and Sn to possess both sufficient antimicrobial function (Sn-catalyzed cation release) and moderate resistance to corrosion while remaining relatively tarnish-free (Al-doped cuprous oxide) and color-stable as facilitated by this Al/Cu-type surface film.

6.3 Objective

The individual effects of Sn and Al from their Cu binary systems may combine in a Cu-Al-Sn ternary alloy to form an alloy system with enhanced soluble Cu ion release in artificial perspiration due to the weaker Cu-Sn bond (Sn effect of enhancing dissolution) while retarding tarnishing through Al-doping of the Cu_2O corrosion product film via solute capture. The present chapter aims to identify the ideal composition of Al and Sn within solid solubility limits and determine how the individual effects of Al and Sn work in combination within a ternary system with Cu. This will be accomplished through a comprehensive analysis ‘fate of the elements’ survey and mechanistic analysis using a series of Cu-Al-Sn alloys in solid solution.

6.4 Experimental Procedures

6.4.1 Alloy Fabrication

Cu-Al-Sn high-purity model ternary alloys were fabricated and evaluated using fate of the elements techniques and methodologies described in detail in prior chapters. Ternary alloys from made from Cu, Al, and Sn elements or 99.99 % pure (or greater) element purity. Alloys were arc-melted in an inert gas atmosphere (argon), flipped three times, remelted, and then drop cast into a chilled cylindrical copper mold. Alloys were then heated to 600° C for 2 hours and then water quenched to solutionize. Single-phase solid solution alloy crystal structures were verified with X-ray diffraction confirming the absence of secondary metallic phases (Figure 6.2).

6.4.2 Electrolyte Solutions

Artificial perspiration was made according to BS EN1811:2011 [48] and titrated to pH 6.5 using NH_4OH. The composition of the artificial perspiration was 0.5 wt% NaCl, 0.1 wt% Urea (CH_4N_2O), and 0.1 wt% 90% lactic acid ($C_3H_6O_3$) in an aqueous solution.

6.4.3 Disinfection Studies

The relative antimicrobial efficacy of Cu-Al-Sn alloys was determined with *Escherichia Coli* (E. Coli, HCB1) survivability via the most probable number (MPN) of colony-forming units (CFU) enumeration method using Quanti-Tray 2000 and Colilert (IDEXX®) indicator. Alloy samples were cast in epoxy with a set exposed area of 1.1 cm² and ground to 1200 grit under ethanol. Samples were placed in 200 mL of gently stirred artificial perspiration and inoculated with ~10^6 colony-forming units of HCB1 *E. Coli* bacteria. Aliquot samples of solution (1 mL) were measured at indicated time intervals up to 48 hours. Aliquots were added to phosphate buffer solution (1 mL

PBS, pH 7.4) to chemically inactivate (precipitate) any free Cu^+/Cu^{2+} in solution to prevent further cell death during indicator incubation. Serial dilutions of this solution were mixed with Colilert indicator and incubated in IDEXX 2000 counting trays for 24 hours at 35±0.5 °C. A control test was conducted in artificial perspiration with no metal contact and bacteria natural die-off was measured at set time intervals up to 96 hours [26].

6.4.4 Cyclic Voltammetry and Potentiodynamic Polarization

Cyclic voltammetry was conducted in deaerated borate buffer (pH 8.4) at a sweep rate of 1 mV/s in identical fashion as described in prior work [154]. Potentiodynamic polarizations of alloy samples were conducted in artificial perspiration, and 1 M HCl. Both solutions were naturally aerated. Freshly-polished samples were cathodically polarized to -1.5 V_{SCE} for 10 min to reduce any air-formed oxide films and then scanned upwards at a rate of +0.1667 mV/s to +0.5 V_{SCE}.

6.4.5 Open Circuit Exposures in Artificial Perspiration

Cu-Al-Sn alloy samples were cast in epoxy and ground to 1200 US grit under ethanol. Samples were rinsed in ethanol and placed in naturally aerated artificial perspiration for up to 96 hours with an exposed area of 0.8 cm^2. Exposure cells were cleaned with 0.1 M HCl between exposures and rinsed with DI water prior to introduction of artificial perspiration.

6.4.6 Visual Appearance

Visual appearance was evaluated after open circuit exposure for 96 h to artificial perspiration with a flat-bed document scanner at a resolution of 300 dpi and color-corrected using a standard grey-card background.

6.4.7 Corrosion Product Characterization

Soluble Corrosion Products

Soluble ion concentration of released Cu, Al, and Sn were measured with inductively-coupled plasma – optical emission spectroscopy with identical procedures as previous chapters. Concentrations were determined from calibration with serial-diluted standards of known concentration. Limits of detection were defined as the value of a blank sample plus three times the standard deviation added to this value. LOD for Cu, Al, and Sn were 17, 198, and 40 ppb, respectively. Neither Al nor Sn were detected as soluble ions in solution within detection limits.

Insoluble Corrosion Products

The reversible Nernst potentials for copper corrosion products formation by oxidation are within the electrochemical stability window of water (0 - 1.23 V_{SHE}), in the absence of dissolved oxygen, therefore these compounds can be galvanostatically reduced by cathodic polarization below Nernst potentials in aqueous electrolytes [235]. A constant cathodic current of -20 µA was applied ($A = 0.8\ cm^2$, $-25\ \mu A/cm^2$) to pre-exposed samples in a deaerated borate buffer solution (pH 8.4). The deaerated solution was hydraulically transferred to reduction cells. Reduction cells (~400 mL total volume) were N_2-purged for 10 min prior to direct electrolyte transfer from the deaeration flask. Continuous bubbling of reduction cells ensured deaeration throughout the reduction. Reduction potentials were measured using a mercury/mercurous sulfate electrode (MMSE) fitted with Luggin tips. The charge of the oxide can be determined according to procedures outlined in detail elsewhere [26,154].

The electronic defect density of the oxide was estimated from Mott-Schottky experiments that were performed in solutions of deaerated borate buffer (pH 8.4) with 0.7 mM of $K_3[Fe(CN)_6]$ as a redox mediator [223]. Oxide films were grown in quiescently-aerated artificial perspiration with an anodic galvanostatic hold at 0.1 mA for 12500 s over an exposed electrode are of 0.8 cm^2. Mott-Schottky measurements were made in identical fashion as detailed in Chapter 5.

Grazing Incidence X-Ray diffraction was measured on samples following open circuit exposure for 96 h in artificial perspiration. The X-Ray diffractometer employed was a PANalytical Emperyean XRD instrument using monochromatic Kα_1 radiation. The incidence angle was set to ω=0.5°.

6.4.8 Impedance Spectra and Corrosion Rates

Impedance of Cu-Al-Sn alloys were measured in artificial perspiration with saturated calomel electrodes (SCE) at set time points up to 96 h. Electrochemical Impedance Spectroscopy was carried out with Gamry REF600 and PCI4-G300 Potentiostats. An AC Amplitude of 10 mV RMS was applied from 100 kHz to 1 mHz at 8 points per decade. Equivalent circuit fits to estimate the polarization resistance were performed in the same manner as Cu-Al alloys given in Chapter 5. Mass loss from samples following exposure was measured using standard methods according to ASTM G1 [139]. The cleaning stage was carried out using 6 M HCl in a single stage lasting 1-2 min.

6.5 Results

6.5.1 Alloy Metallurgy

All alloys showed solid solution compositions without the presence of a second phase as demonstrated in Figure 6.2a. Lattice parameter fits from diffraction data was accomplished using a sum of least squares regression algorithm and are given in Figure 6.2b. The lattice parameter (Figure 6.2b) shifted to greater values as expected from solid solution alloying with increasing amounts of Al and Sn.

6.5.2 Antimicrobial Function

All Cu-Al-Sn alloys were antimicrobial as demonstrated by the *E. Coli* survivability study in Figure 6.3. In the control study without any metal content or contact *E. Coli* were observed to survive in solution for up to 96 h. Planktonic E. Coli was completely killed by all Cu-Al-Sn alloys with non-recoverable rapid cell death within 24 hours. Cu and Cu-1Al-Sn were able to kill *E. Coli* within shorter times: 2 and 8 hours, respectively.

6.5.3 Electrochemical Diagnostics: Cyclic Voltammetry, Potentiodynamic Polarization, and Galvanostatic Anodic Holds

Cyclic voltammograms for Cu-Al-Sn alloys in deaerated borate buffer (pH 8.4) are given in Figure 6.4. Alloys with 1 wt% Sn showed greater anodic peak values at -0.50 V_{MMSE} and -0.33 V_{MMSE} corresponding to cuprous and cupric ion dissolution, respectively [154]. The anodic dissolution slope was decreased to a lower value for alloys with 5 wt% Sn. The potential independent anodic current above -0.25 V_{MMSE} is related to the growth of a layer of Cu_2O and possibly CuO as well [154]. Cathodic reduction integrated peak areas matched well with integrated anodic charge from upward scans, meaning that any Al or Sn oxides are not electrochemically active by the third sweep.

The electrochemical behavior of Cu-Al-Sn alloys in artificial perspiration and 1M HCl are given by potentiodynamic polarizations given in Figure 6.5 and Figure 6.6. Importantly, in the freshly polished condition, none of the alloys tested showed passive behavior in either solution.

Chronopotential plots from anodic holds of Cu-Al-Sn alloys are shown in Figure 6.7a and final potentials following 12500 s are plotted in Figure 6.7b versus Al content for Cu-Al and Cu-Al-Sn alloys. Potentials increased over time indicative of a thickening oxide layer. The final galvanostatic potential generally decreased in with increasing alloying elements of Al indicating that alloys with greater Al content had thinner oxide films. The addition of Al to the alloy rendered

Cu dissolution easier, requiring a lower overpotential to achieve the same imposed current. The addition of Sn only slightly counteracted this effect to a minor degree.

6.5.4 Visual Tarnish Assessment and Open Circuit Potentials

The visual condition (tarnish) of Cu-Al-Sn alloys following 96 hours at open circuit in artificial perspiration is displayed in Figure 6.8. Alloys with lower alloying content showed greater tarnish and darkening due to corrosion products with the Cu-1Al-5Sn alloy showing the dullest visual appearance. Cu-Al-Sn alloys with 5 wt% Al showed significantly decreased tarnish from oxides. Cu-5Al-5Sn had slightly darker corrosion products than Cu-5Al-1Sn.

Open circuit potentials of Cu-Al-Sn alloys exposed to artificial perspiration up to 96 hours are given in Figure 6.9. An initial rise in potential was observed for all alloys for the first 12 h. Generally, alloys with greater Al and Sn showed stable increasing potentials which stabilized to relatively constant values over time, indicative of protective oxide formation. Cu and Cu-5Al-5Sn showed a decrease in potential of 60 and 80 mV after 48 hours in solution, respectively. Open circuit potentials of Cu-Al-Sn alloys are shown alongside results from their respective binary alloys and are given in Figure 6.10a versus Al alloy content and Figure 6.10b versus Sn content.

6.5.5 Soluble Cation Release for Antimicrobial Function

Soluble Cu cations released from the alloys during corrosion were measured with aliquot samples which were then quantified with ICP-OES. The amount of soluble Cu cations in artificial perspiration following 96 hours in artificial perspiration are given as a function of Al content in Figure 6.11a and as a function of Sn content in Figure 6.11b. All alloys with exception to Cu-5Al-5Sn showed similar ion release in artificial perspiration. There was no clear systematic effect on total Cu ion release as a function of Sn or Al. However, the combination of these elements in Cu-5Al-5Sn showed diminished Cu ion release in artificial perspiration.

6.5.6 Surface Corrosion Products

Molecular Identity and Structure

Grazing incidence X-ray diffraction patterns from Cu-Al-Sn alloys following 96 h in artificial perspiration are given in Figure 6.12. GIXRD revealed only cuprite (Cu_2O) on Cu-1Al-1Sn and Cu-1Al-5Sn. However, Cu-5Al-5Sn did not show any corrosion products detectable with this technique aside from one unassigned peak which could either be a reconstructed Cu layer due to Al dealloying, or the third most intense peak from Al_2O_3. Corrosion products were not observable with GIXRD on Cu-5Al-1Sn, revealing only solid solution FCC diffraction peaks for the Cu-Al-Sn alloy substrate.

Total and Individual Quantities of Reducible Corrosion Products

Chronoamperometric curves from reduction of oxides formed on Cu-Al-Sn alloys following 96 hours in artificial perspiration are given in Figure 6.13a. Four reduction plateaus were observed: assigned to three oxides and the reduction of water (HER). CuCl (identified in [154]), Cu_2O, and a third reduction potential which was not below the Nernst potential of SnO_2 and was defined as solute captured (SC) Al-doped Cu_2O as identified in prior work (Chapter 5) and is discussed later. The total and individual amounts of oxides calculated from CR are given by the stacked bar plots in Figure 6.13b. Total corrosion products on the decreased significantly from 200 mC/cm^2 to 30 mC/cm^2 with just an increase of 4 wt% of Al (Cu-1Al-1Sn→Cu-5Al-1Sn), which corresponds to a change in approximate Cu_2O thickness of 250 nm to 40 nm. Oxide amounts were further decreased by a 4 wt% addition of Sn (Cu-5Al-1Sn→Cu-5Al-5Sn). In addition to a decrease in total reducible corrosion products, a second reduction potential was identified on Cu-1Al-5Sn in agreement with the reduction potential from Cu-5Al-1Sn. The second oxide was determined from the previous chapter to be due to solute-capture of Al in Cu_2O.

The total amount of reducible corrosion products from CR on Cu-Al-Sn alloys are shown alongside results from their respective binary alloys and are given in Figure 6.10a versus Al alloy content and Figure 6.10b versus Sn content. Both Figure 6.13b and Figure 6.14 (a and b) demonstrate the Al had a strong effect, particularly at 5 wt%, on the total amount of reducible (cuprous) corrosion products. Figure 6.14a shows that the addition of Sn to Cu-Al alloys further decreased the amount of reducible corrosion products as measured by CR. Cu-Sn alloys with increasing Sn showed increased amounts of total reducible corrosion products (Figure 6.14b). However, the addition of Al was shown to decease this amount to a strong degree sometimes by orders of magnitude as indicated for Cu-5Al-5Sn.

Electronic Properties of Cu_2O: Reduction Potential and Electronic Charge Carrier Density

The reduction potential of Cu_2O measured during CR on Cu-Al-Sn alloys are shown alongside results from their respective binary alloys and are given in Figure 6.15a versus Al content, and in Figure 6.15b versus Sn content. A doped oxide film with greater electronic resistance would manifest an increase in the reduction overvoltage (Chapter 5). Increased amounts of Sn did not appreciably decrease the value of the reduction potential independent of Al (Figure 6.15b) indicative of separate oxide phases (e.g., Cu_2O and SnO_2) with no dopant effects. However, Sn in Cu-Al-Sn enhanced the doping effect of Al and caused decreased Cu_2O reduction potentials compared to binary Cu-Al alloys (Figure 6.15a).

Approximate charge carrier (holes) densities of Cu_2O from Mott-Schottky tests shown in Figure 6.16 revealed fewer charge carriers measured on Cu-5Al-1Sn than other alloys, including Cu-5Al-5Sn. Cu-Al-Sn alloys with 1 wt% Sn added to Cu-1Al showed an increased the number of electron holes, yet when 1 wt% Sn was added to Cu-5Al, there was a measured decrease in the total number of electron hole charge carriers. When 5 wt% Sn was added to Cu-Al-Sn alloys, there was no effect on the measured charge carrier density.

6.5.7 Electrochemical Impedance and Mass Loss

The electrochemical impedance of Cu-Al-Sn alloys in artificial perspiration at selected time points up to 96 h are presented in Bode form for both magnitude and phase in Figure 6.17 and 6, respectively. Low-frequency electrochemical impedance magnitude, inversely related to the corrosion rate, generally increased with increasing alloying contents for both Sn and Al with Al having a slightly greater influence (by wt%) over Sn for comparable values. The greatest corrosion resistance via impedance is found for Cu-5Al-5Sn alloys. The impedance phase angle spectra, presented in Figure 6.18, show quite different RC time constant behavior for Cu-5Al-5Sn alloys compared to lower alloying contents of Al and Sn. Cu-5Al-5Sn switched from similar RC time constant values which had a characteristic frequency similar to the other alloys (~10-20 Hz) but then switched to lower values (~1 Hz) than other alloys with greater phase angle values (-65°) than other alloys (-40°). Other alloys showed very similar impedance behavior which was quickly stabilized after 12 hours in artificial perspiration. Figure 6.19 shows the Bode magnitude (Figure 6.19a) and phase angle (Figure 6.19b) of Cu-Al-Sn alloys alongside Cu, Sn, and Al following 96 hours in artificial perspiration highlighting the differences of the fully-developed films and the differences thereof. The inverse polarization resistance of Cu-Al-Sn alloys compared with their binary counterparts are given in Figure 6.20a against Al content, and again in Figure 6.20b plotted against Sn content. Highlighted in Figure 6.20b, Al had a much stronger effect on the inverse polarization resistance (proportional to corrosion rates) than Sn.

Mass loss of Cu-Al-Sn alloys following open circuit exposure to artificial perspiration are presented in Figure 6.21. Alloys with 5 wt% Al had significantly decreased mass loss compared to alloys with 1 wt% Al. The increased amount of Sn from Cu-1Al-1Sn to Cu-1Al-5Sn increased total mass loss, whereas the same increase of Sn from Cu-5Al-1Sn to Cu-5Al-5Sn decreased the total mass loss from corrosion.

6.6 Discussion

6.6.1 Alloying Effects on Tarnish and Antimicrobial Efficacy

All ternary Cu-Al-Sn alloys were antimicrobial (Figure 6.3), able to kill >2 x10^6 CFU of *E. Coli* bacteria within 24 h in a stirred beaker (200 mL) of artificial perspiration. Greater alloying contents showed a decrease in antimicrobial kinetics with Al having the strongest effect at reducing the killing rates. However, while all alloys were antimicrobial, the tarnishing behavior (Figure 6.8) and surface oxides (Figure 6.13b) were significantly different between minor alloying elements and their amounts (±4 wt%).

6.6.2 The Combination of Effects of Sn and Al on Cu Alloy Corrosion

A clear enhancement effect of Sn with the alloying effect of Al is shown by the unique combination of these alloying elements as demonstrated by the differences in corrosion (Figure 6.20), ion release (Figure 6.11), and oxide formation (Figure 6.14) compared with their respective binary compositions of identical alloying content. The primary effect of Sn was to enhance Cu dissolution in Cu-Al-Sn which served to strengthen the effect of Al alloying due to Al enrichment upon Cu dissolution. Sn increased the enrichment of Al in the Cu_2O film as evidenced by the reduction potential (Figure 6.15), decreased charge carrier density (Figure 6.16), and increase in tarnish-resistance (Figure 6.8 and Figure 6.14) without significantly affecting the electrochemical nature of the oxide film (Figure 6.19).

Tarnish-Resistant Corrosion Product Films Improved by Sn

The tarnishing behavior (Figure 6.8) of these alloys was significantly different despite a change in alloy composition of just a few percent (±4 wt%) and strongly dependent on the minor alloying chemistry (Al vs Sn). The trend for Sn in Cu-Sn was to increase the total corrosion products (Figure 6.14a) however, the addition of tin in the Cu-Al-Sn system enhanced the effect of Al by reducing the total amount of corrosion products compared with binary Cu-Al alloys without Sn (Figure 6.14b). All Cu-Al-Sn alloys systems showed very similar oxide RC time-constants with Al and Sn alloying content (Figure 6.19). However, quite different characteristic frequency for the RC component was observed for the Cu-5Al-5Sn alloy which is suggestive of a film of different character either by a decrease in oxide resistance, increase of area coverage of a protective oxide, or by an increase in dielectric properties (e.g., $\varepsilon_{Al2O3} \sim 10$, $\varepsilon_{Cu2O} \sim 7$) [236]. Strong indications of protective films on Cu-5Al-5Sn is apparent from the high slope in Bode magnitude plots coupled with greater low-frequency impedance (Figure 6.17b), and the lowered time-constant characteristic frequency with greater phase angles found at lower frequencies (Figure 6.18 b).

Sn enhances the Al-effect of modifying the cuprous oxide corrosion product. Both the number of Cu_2O charge carrier densities (Figure 6.16) and the cuprous reduction potential was further decreased by minor amounts of Sn (Figure 6.15). Prior work (Cu-Al, Chapter 5) highlighted that Al likely had two effects at low (1 wt%) and high (5 wt%) amounts, and Sn synergizes with both effects evidenced by increasing the number of charge carriers in the case of 1 wt% Sn added to 1 wt% Al, but having the opposite effect of decreasing the number of charge carrier by enhancing Al-doping and tarnish resistance at 5 wt% with an addition of only 1 wt% Sn (Figure 6.16).

The Effect of Sn on Cu Dissolution

The addition of Al to the alloy made Cu dissolution easier, but with less Cu_2O, requiring a lower overpotential to achieve the same imposed current (Figure 6.7b). Facile dissolution was also observed in potentiodynamic polarizations (Figure 6.5b), where Al and Sn permitted Cu dissolution at a greater rate (anodic current) for a given anodic potential. Adding 5 wt% Sn to Cu-1Al mitigated the deleterious effects of 1 wt% Al on the corrosion rates ($1/R_p$) observed (Figure 6.20a). This observation stands in opposition to the effect of Sn alone which increases the corrosion rate (Figure 6.20b). Sn also slightly decreased the corrosion rate of Cu-1Al when 5 wt% Sn was added.

The addition of Sn had a markedly different effect on the Cu-5Al-5Sn alloy which may be explained through the enrichment and Al-doping models presented in Chapters 4 and 5, respectively: Sn enhances the dissolution rate of Cu as experimentally verified in Chapter 2 and theoretically described through *ab initio* DFT-modeling found in the appendices. This raises the relative dissolution rate constant ratio, $ß=k_{Cu}/k_{Al}$ (Equation 5.7), where $ß$ increases as k_{Cu} is increased by the enhancement of Cu dissolution due to Sn. The increased solute enrichment factor ($ß$) form enhanced Cu dissolution causes greater Al surface enrichment. This leads to increased Al-doping (measured on Cu-5Al-1Sn via MS, see Figure 6.16) of the Cu_2O film with respect to the original Al enrichment. However, in the case of Cu-5Al-5Sn, supersaturation of Al^{3+} beyond its metastable solubility limit in Cu_2O between 12 and 24 hours in artificial perspiration lead to precipitation of either Al_2O_3 [64,202,203,216–218] or a Cu-aluminate film [61,62,121,211] as suggested by literature. A separate non-Cu-based oxide phase was indicated by multiple methods including OCP (Figure 6.9), EIS (Figure 6.17b and Figure 6.18b), the lack of reducible oxides in CR (Figure 6.13), evidence of Al_2O_3 from GIXRD (Figure 6.12), saturation of the doping effect in

Mott-Schottky (Figure 6.16), and decreased corrosion rates due to this protective film (Figure 6.20 and Figure 6.21). However, future work is needed to confirm and quantify the increased amount of Al in the Cu_2O films formed on Cu-Al-Sn alloys compared with Cu-Al, determine the structural and chemical nature of the films formed on Cu-5Al-5Sn, and ascertain the location of either oxidized or retained Sn.

The total mass loss for Cu-Al-Sn samples are compared against their respective Cu ion release and reducible oxide amounts in Figure 6.22. This figure presents the relative preference of a given alloy towards either ion release or tarnish for a given mass loss. The combination of Al and Sn at 5 wt% Al and 1 wt% yielded a tarnish-resistant alloy with preferential ion release over oxide formation with lower corrosion rates as illustrated in Figure 6.22. Tarnish-resistant oxide films due to Sn-enhanced Al-doped Cu_2O films did not impede Cu release in Cu-Al-Sn alloys up to 5 wt% Sn. From this work the ideal compositional range of Al and Sn for antimicrobial Cu-based alloys which are tarnish-resistant is between Cu-5Al-1Sn and Cu-5Al-5Sn.

6.7 Conclusions

- Ternary Cu-Al-Sn alloys (1.1 cm^2) were all antimicrobial, able to kill 2 $x10^6$ CFU *E. Coli* bacteria within 24 h in a stirring beaker (200 mL) or artificial perspiration.
- Despite similar antimicrobial performance, the tarnishing behavior and surface oxides were significantly different between minor alloying elements and their amounts (e.g., ±4 wt%).
- Sn enhanced Cu dissolution on Cu-Al-Sn which led to a synergy with the Al-effect where decreased amounts of total corrosion product thickness and increased Al-doping of Cu_2O were observed with minor Sn amounts, whereas at greater amounts (5 wt% Sn and 5 wt% Al) were found to induce an impedance magnitude and phase change in the surface oxide.

Future work is planned to characterize these films. This composition served as an upper bound for potential tarnish-resistant antimicrobial alloys

- An alloy compositional range of Cu-Al-Sn was identified which functions to support both high antimicrobial efficacy and tarnish-resistant without strong passivation or significantly retarding cuprous ion release for antimicrobial function.

Tables

Table 6-1. Elemental composition (wt%) of pure Cu, Al, and fabricated Cu-Al-Sn alloys tested using ASTM E478.

Alloy	**Cu / wt%**	**Al / wt%**	**Sn / wt%**	**Other / wt%**
Cu	99.997	--	--	--
Cu-0.1Al-0.1Sn	99.83	0.07	0.1	--
Cu-1Al-1Sn	98.09	0.92	0.99	--
Cu-1Al-5Sn	93.75	0.99	5.26	--
Cu-5Al-1Sn	94.00	4.98	1.02	--
Cu-5Al-5Sn	89.99	4.85	5.16	--
Al	00.06	99.38	--	0.37 Fe , 0.13 Si, 0.02 Ga
Sn	0.04	--	99.83	0.08 Sb, 0.04 Pb, 0.01 In

Figures

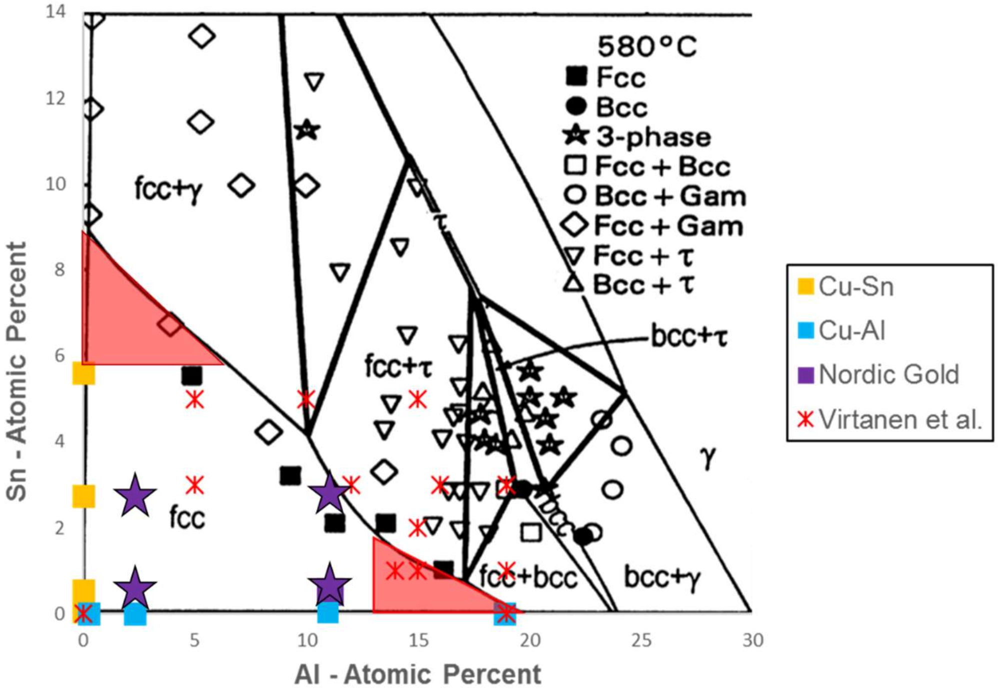

Figure 6.1. Cu-rich corner of Cu-Al-Sn ternary phase diagram. Thermodynamic phase data from [234], T = 580 °C. Cu-Al-Sn compositions evaluated are indicated by purple star symbols. Square symbols represent data points of tested alloy compositions from literature. Colored squares are compositions of Cu-Sn and Cu-Al from previous Chapters 3 and 5, respectively and Nordic Gold [23,26]. Shaded red triangle is the compositional domain for passive α-Cu-Al and α-Cu-Sn from literature values [61]. Red data points from [61,62] as referenced in text.

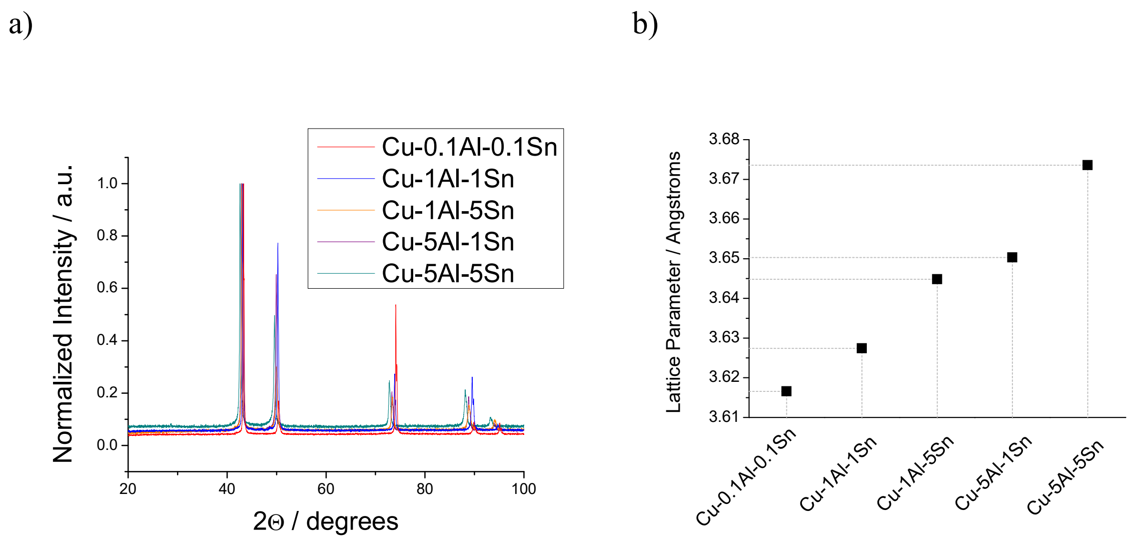

Figure 6.2. X-ray diffraction patterns (a) of heat-treated custom solid solution Cu-Al-Sn alloys fabricated for study. Lattice parameter fits (b) of solid-solution alloys using a sum of least squares regression from diffraction peak locations with Cu $K_{\alpha 1}$ radiation at 1.5406 Å.

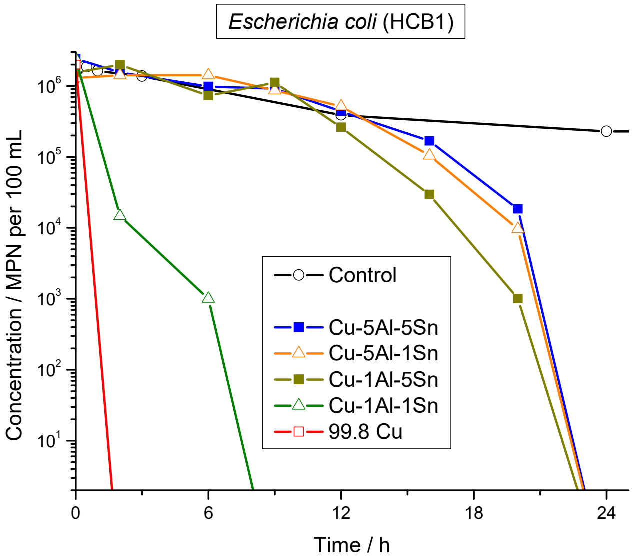

Figure 6.3. Survivability of planktonic E. Coli bacteria exposed to Cu-Al-Sn alloys (1.1 cm²) in 200 mL of gently-stirred naturally-aerated artificial perspiration. Sample aliquots were taken at indicated time intervals and quantified with Colilert indicator and IDEXX 2000 trays using the most-probable number (MPN) method. Control study was conducted in gently-stirred artificial perspiration with no metal contact.

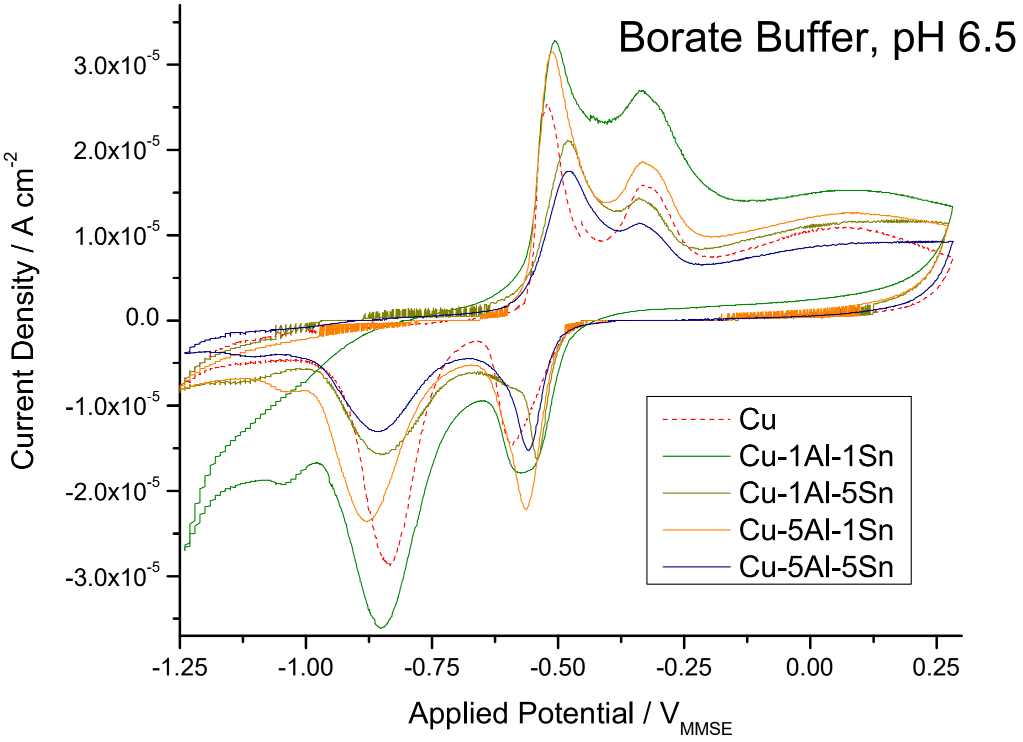

Figure 6.4. Cyclic voltammetry of freshly polished Cu-Al-Sn Alloys in deaerated borate buffer (pH 8.4). Third sweep shown. Scan rate: 1 mV/s.

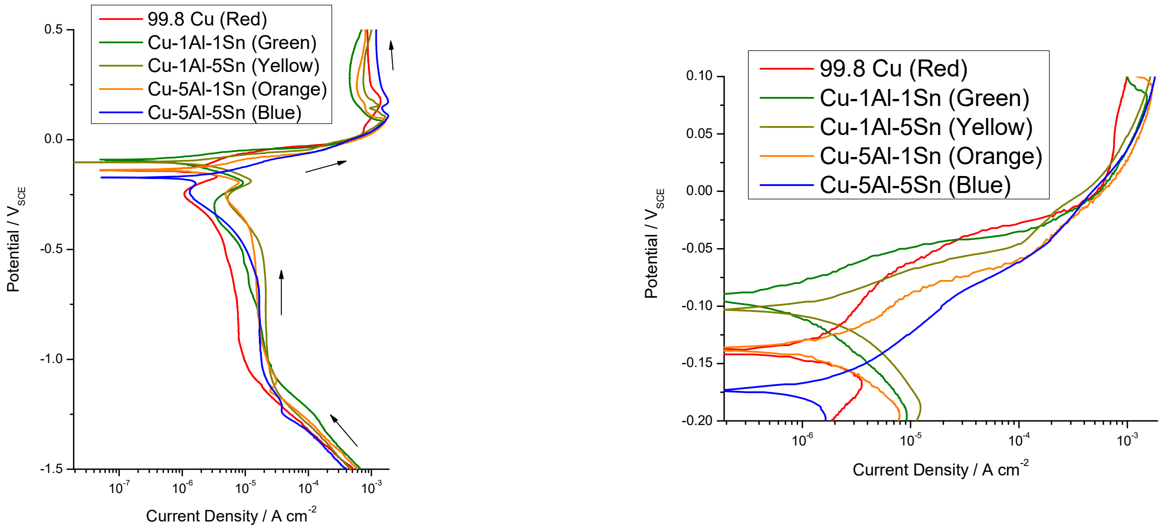

Figure 6.5. Potentiodynamic polarizations of Cu-Al-Sn in artificial perspiration from -1.5 V_{SCE} to +0.5 V_{SCE} following a 10-min cathodic cleaning stage prior to upward sweep. Full sweep (a) and expanded section (b) shown.

a)

b)

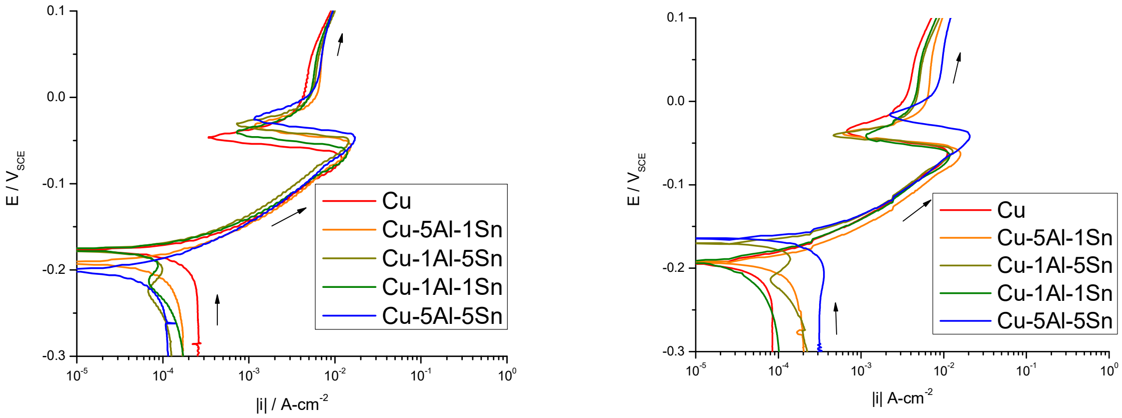

Figure 6.6. Potentiodynamic polarizations of Cu-Al-Sn in ambient-aerated 1 M HCl from -1.5 V_{SCE} to +0.5 V_{SCE} following a 10-min cathodic cleaning stage prior to upward sweep. Anodic section (a) with replicate study (b) shown.

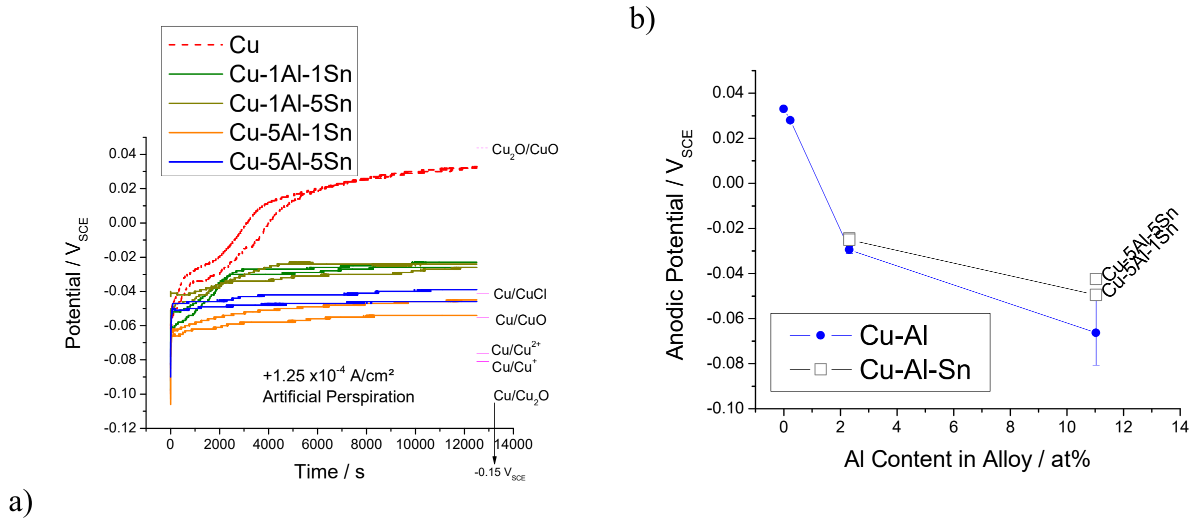

Figure 6.7. Anodic potentials of Cu-Al-Sn alloys held at $+1.25 \times 10^{-4}$ A/cm² in artificial perspiration. (a) Anodic potential of all alloys over time and (b) final potentials (at 12500 s) compared to comparable Cu-Al alloys as a function of Al content.

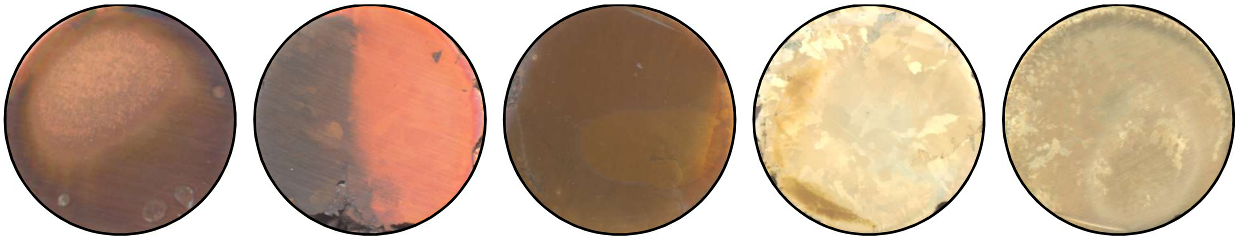

Cu Cu-1Al-1Sn Cu-1Al-5Sn Cu-5Al-1Sn Cu-5Al-5Sn

Figure 6.8. Visual condition of Cu-Al-Sn alloys following 96 h at open circuit in naturally-aerated artificial perspiration solution. Ø = 1 cm.

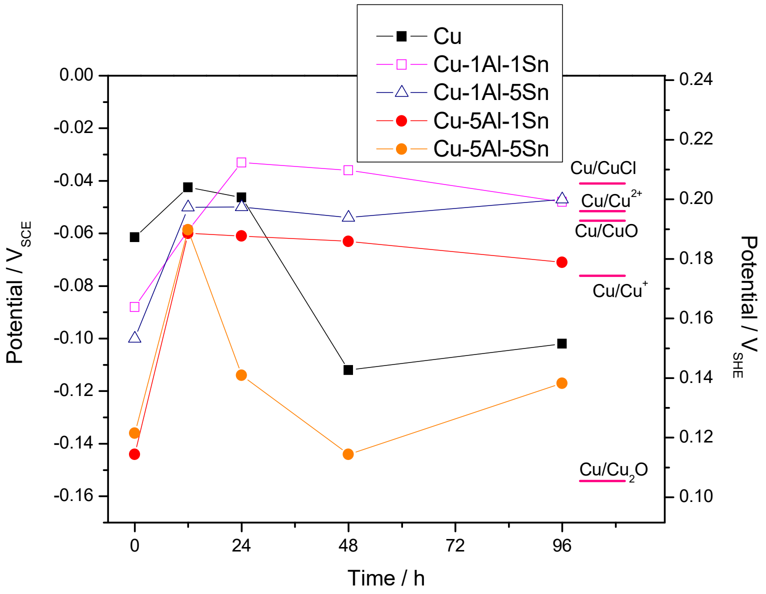

Figure 6.9. Open circuit potential of Cu-Al-Sn alloys in naturally-aerated artificial perspiration solution (pH 6.5).

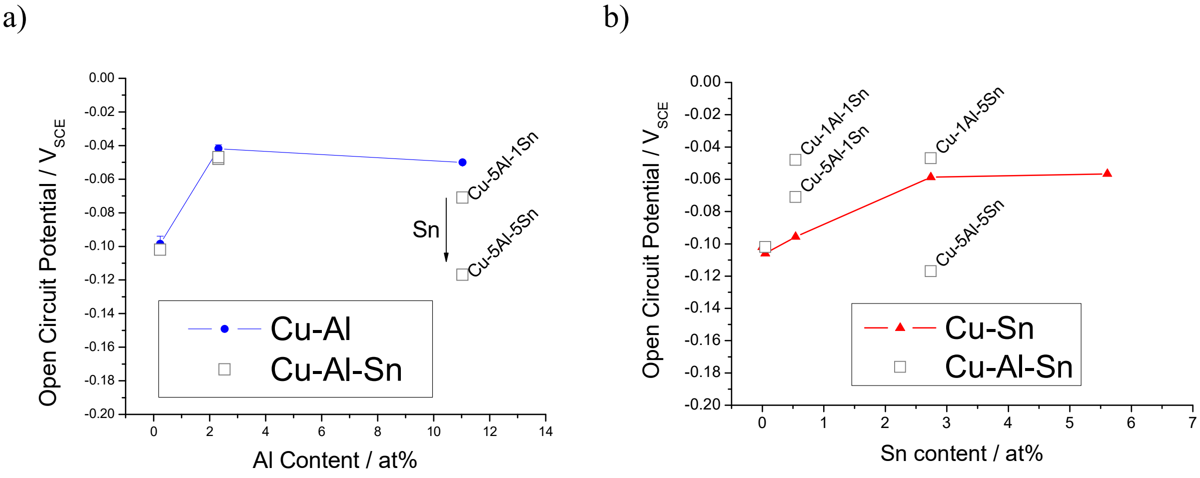

Figure 6.10. Open circuit potential of Cu-Al-Sn alloys compared with respective binary alloys versus (a) Al content and (b) Sn content after 96 hours in naturally-aerated artificial perspiration solution.

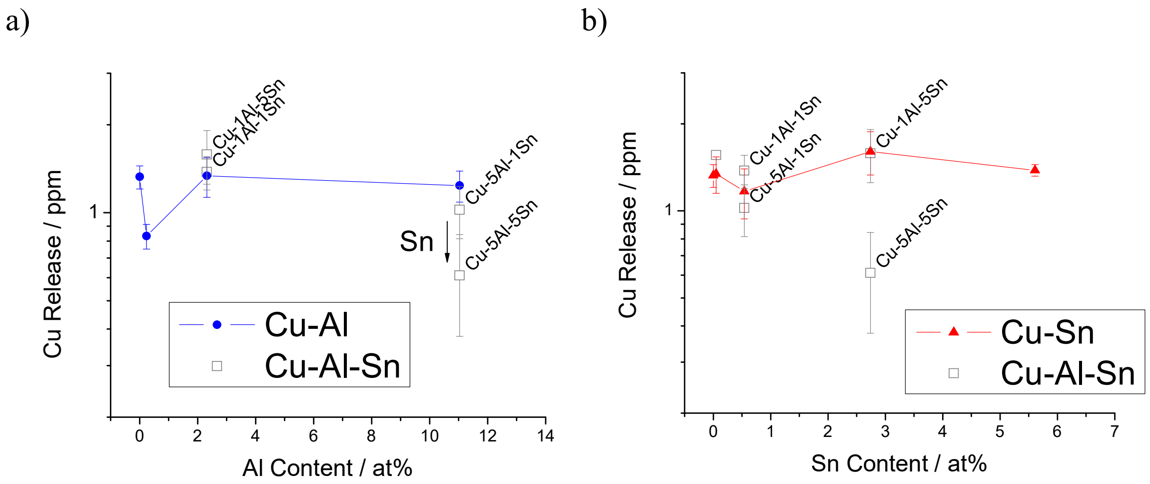

Figure 6.11. Soluble Cu released from Cu-Al-Sn alloys following open circuit corrosion in naturally-aerated artificial perspiration for 96 hours.

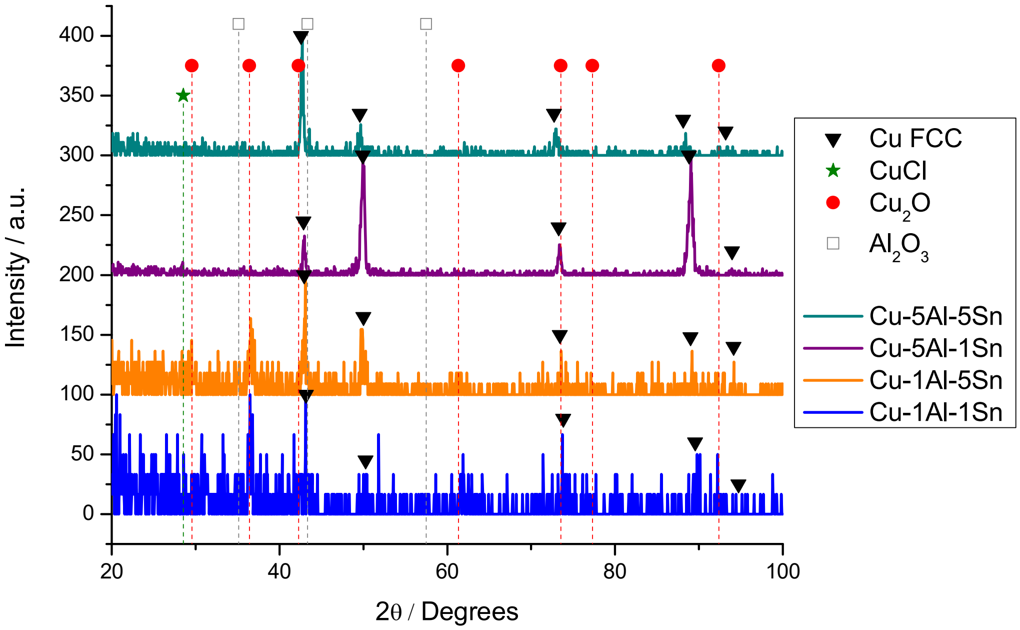

Figure 6.12. Grazing incidence X-Ray diffraction from the surface of Cu-Al-Sn samples following 96 h at open circuit in artificial perspiration. Incidence offset angle ω=0.5°. Cu FCC substrate assignments taken best lattice fits of FCC structure from bulk XRD analysis (Figure 6.2).

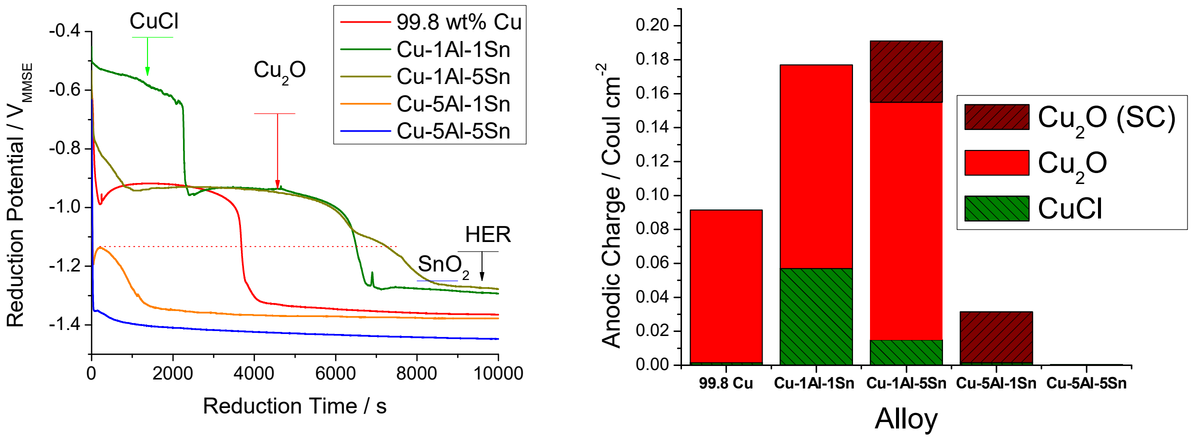

Figure 6.13. Example coulometric reduction of Cu-Al-Sn alloys exposed at open circuit for 96 h to ambiently-aerated artificial perspiration solution. Chronopotential curves (a) with Nernst potentials indicated. Red dashed line indicates the reduction potential of a doped-Cu_2O oxide labeled in bar plots as SC (solute captured, see text). Extracted oxide quantities (b) are expressed as charge density.

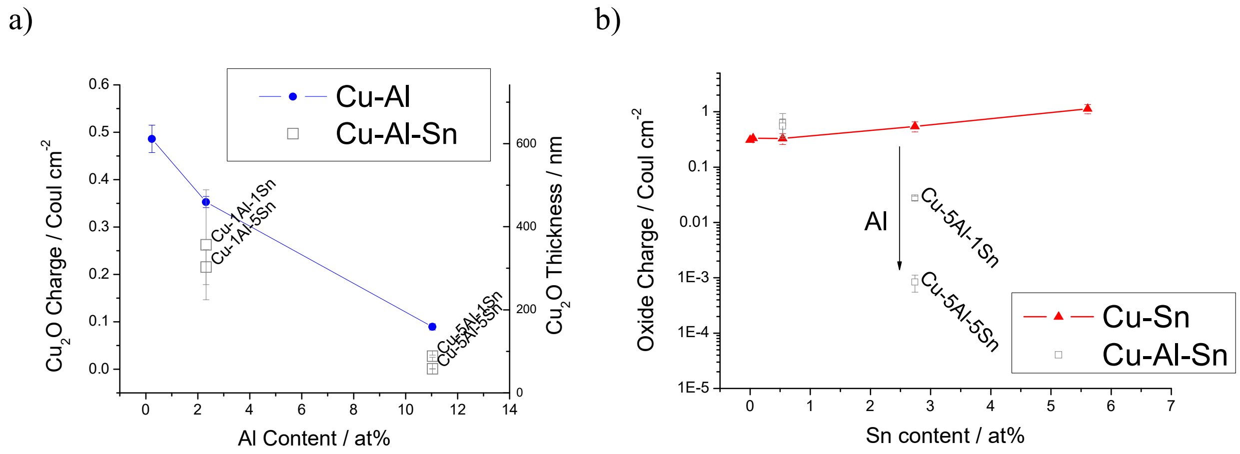

Figure 6.14. Total reducible oxide charge measured from Cu-Al-Sn alloys compared with respective binary alloys versus (a) Al content and (b) Sn content after 96 hours in naturally-aerated artificial perspiration solution.

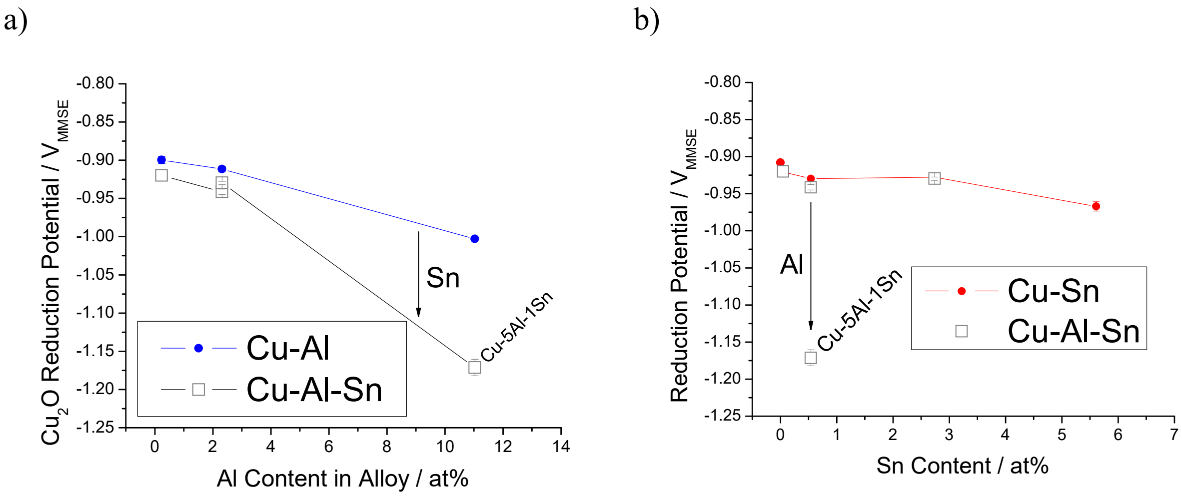

Figure 6.15. Reduction potential of Cu_2O measured from coulometric reductions on Cu-Al-Sn alloys compared with respective binary alloys versus (a) Al content and (b) Sn content after 96 hours in naturally-aerated artificial perspiration solution. Reduction potentials defined as the midpoint potential of reduction plateaus. Cu-5Al-5Sn did not have enough oxide to be characterized in this manner.

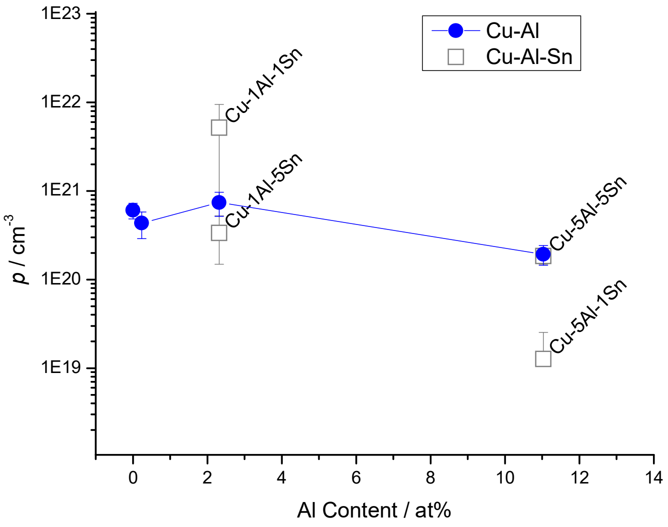

Figure 6.16. Estimate of charge carrier density (e^- holes) compared with Al content of alloys from Mott-Schottky measurements on galvanostatically-grown oxides in artificial perspiration (1.25 C/cm²). Measurements were taken in a deaerated borate buffer with a redox mediator $K_3[Fe(CN)_6]$. Cu-Al alloys are compared with Cu-Al-Sn alloys of similar compositions.

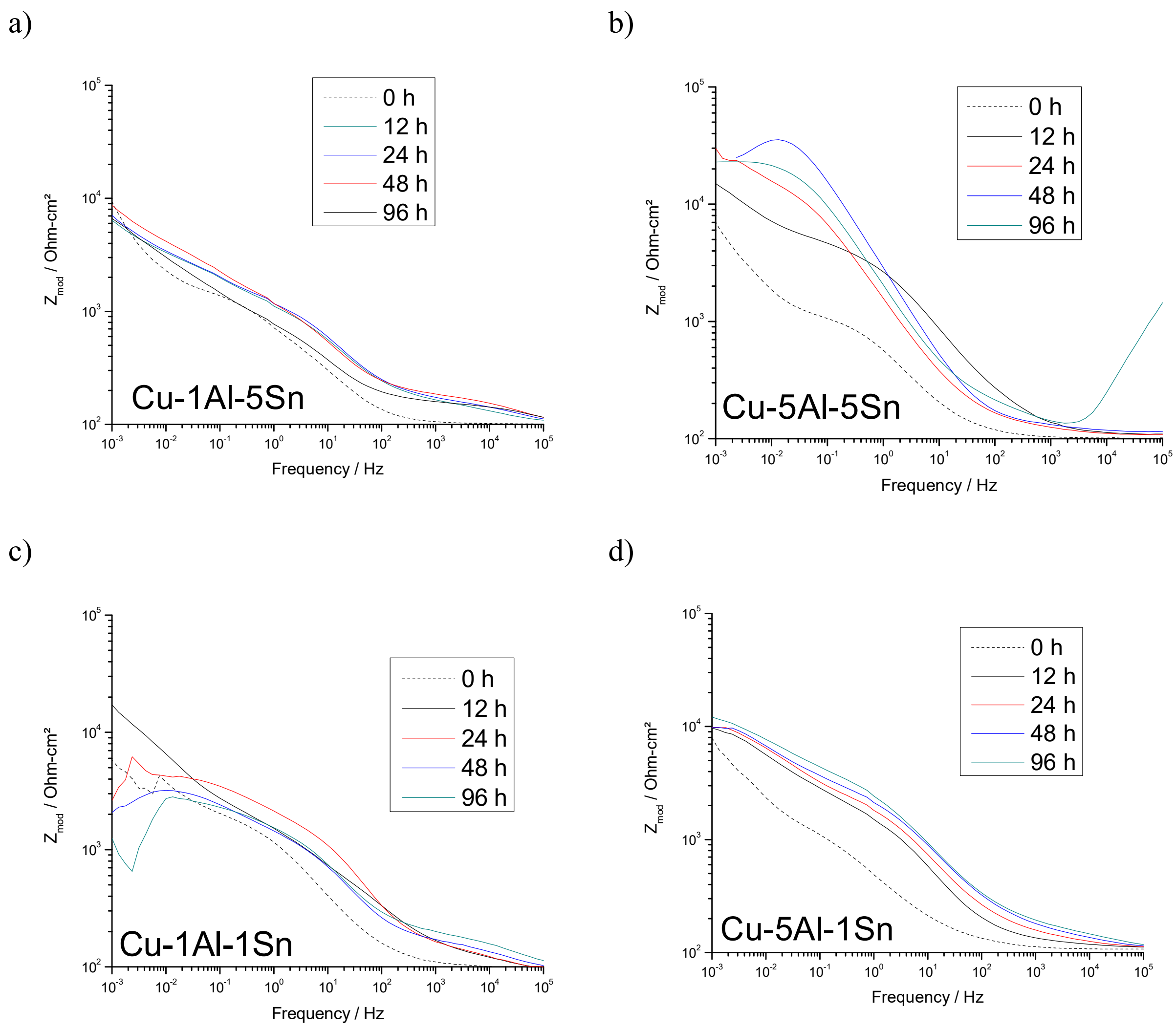

Figure 6.17. Bode magnitude plot of impedance spectra measured at open circuit on Cu-Al-Sn alloys at selected time points up to 96 hours in artificial perspiration.

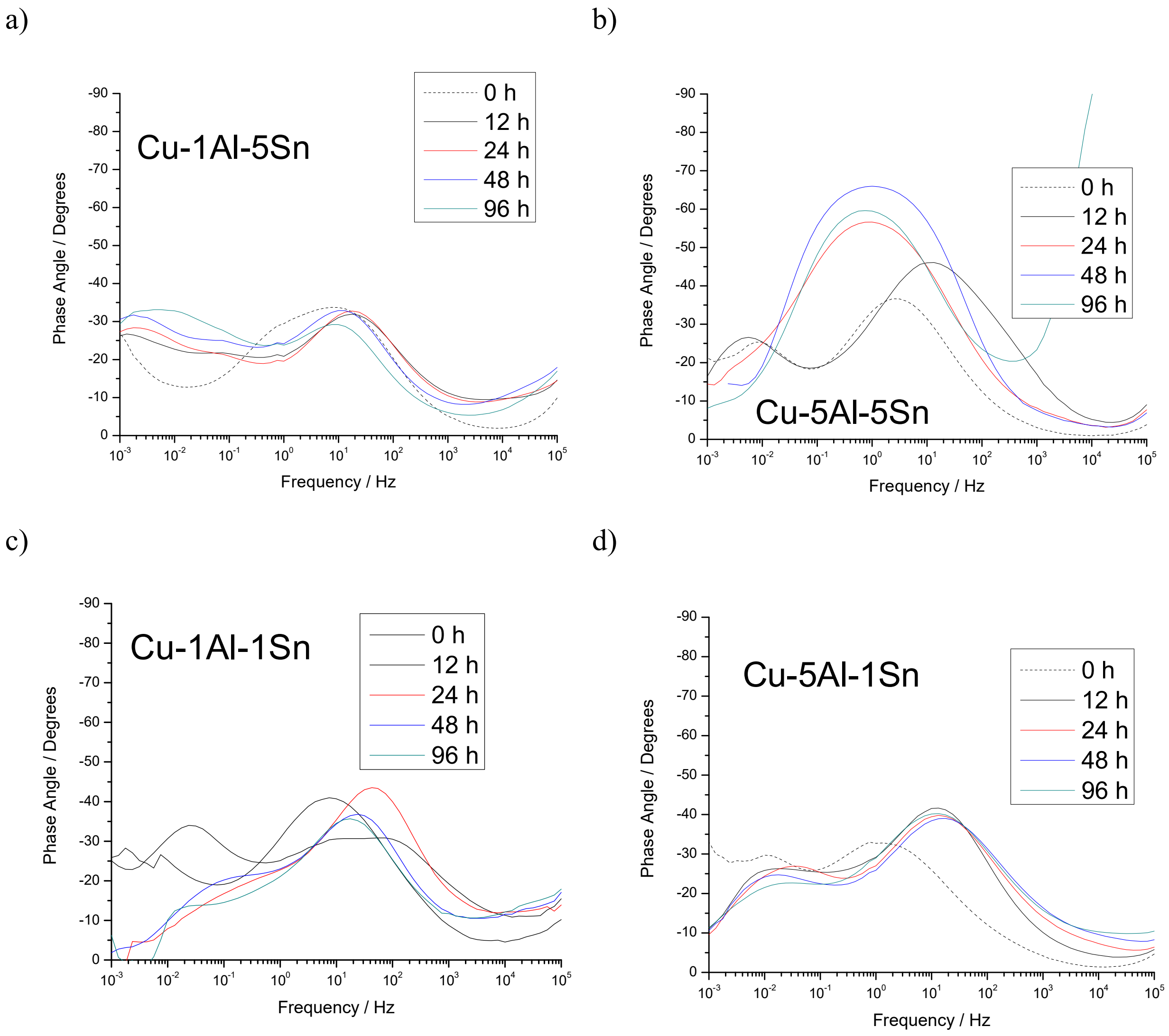

Figure 6.18. Bode phase angle plots of impedance spectra measured at open circuit on Cu-Al-Sn alloys at selected time points up to 96 hours in artificial perspiration.

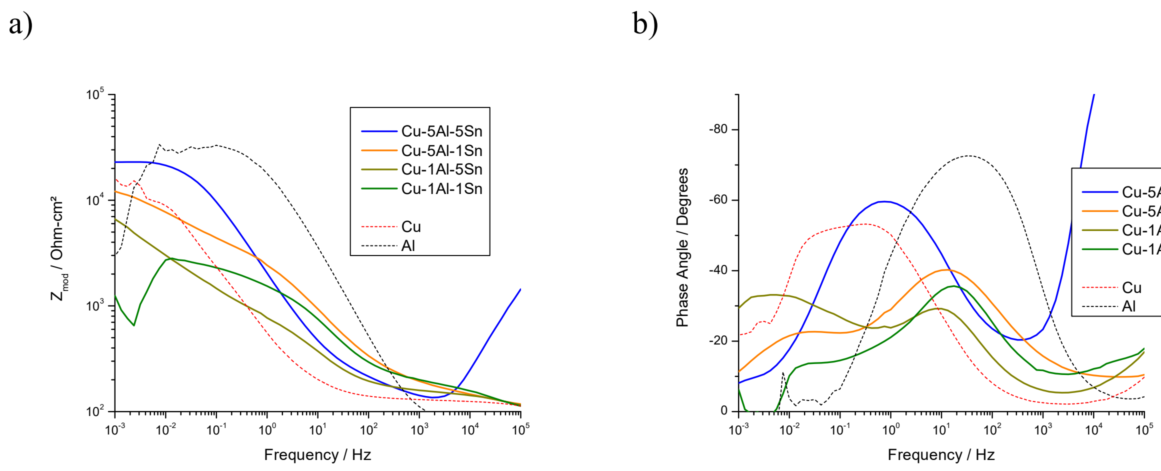

Figure 6.19. Electrochemical impedance spectra measured at open circuit of magnitude (a) and phase angle (b) of Cu-Al-Sn, Cu, and Al alloys following 96 hours in artificial perspiration at open circuit.

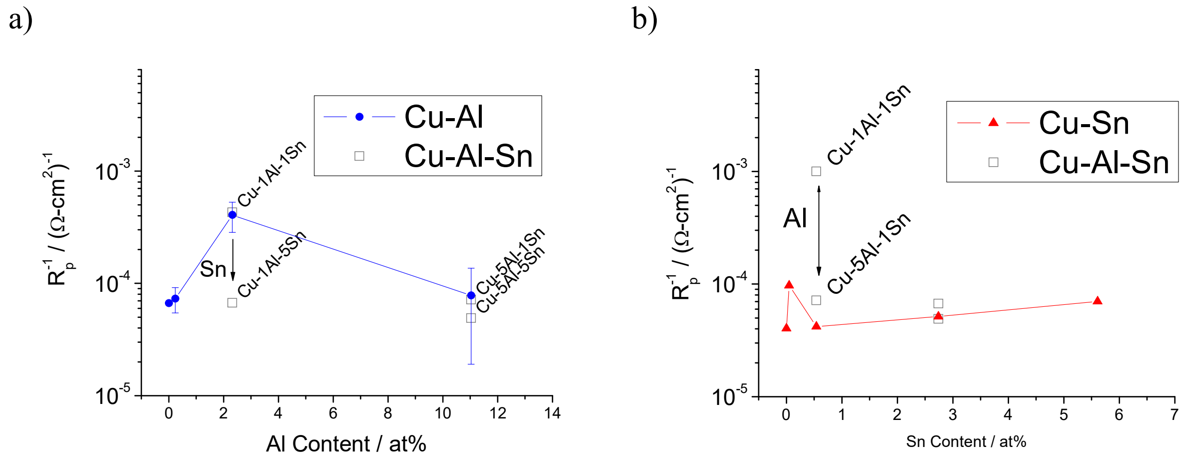

Figure 6.20. Inverse polarization resistance values from impedance fits of Cu-Al-Sn alloys compared with respective binary alloys versus (a) Al content and (b) Sn content after 96 hours in naturally-aerated artificial perspiration solution.

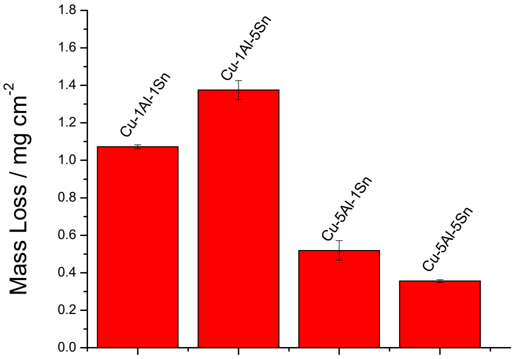

Figure 6.21. Mass loss of Cu-Al-Sn samples following open circuit exposures to naturally aerated artificial perspiration for 96 hours. Error bars represent the standard error of three replicates.

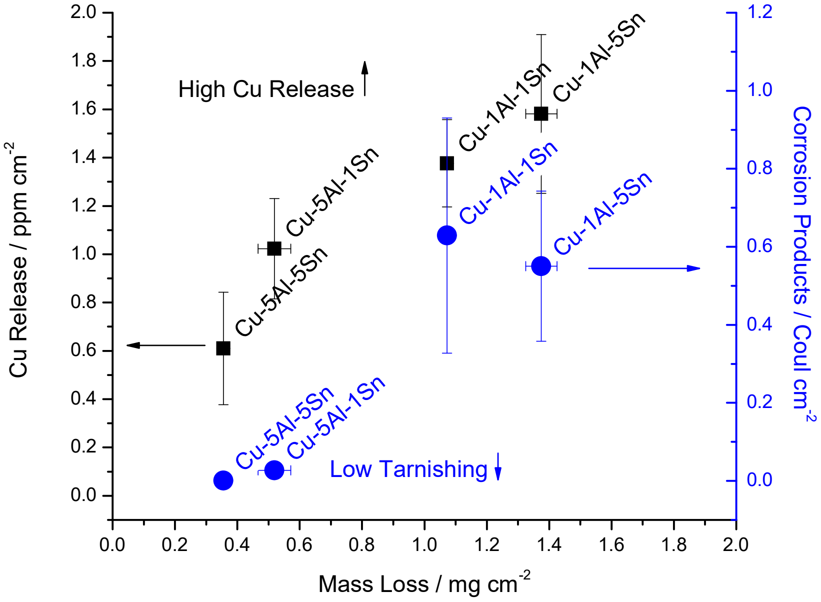

Figure 6.22. Mass loss compared with soluble Cu (black) and reducible corrosion product charge from coulometric reduction (blue) for Cu-Al-Sn alloys following open circuit exposure to artificial perspiration for 96 h.

7 Conclusions and Future Work

7.1 Conclusions

7.1.1 Sn-Enhanced Soluble Cu Release

- In solid solution FCC Cu-Sn, Sn was observed to enhanced Cu release in artificial perspiration due to an elevated corrosion rate. The fraction of soluble Cu release to Cu corrosion products was increased with increasing Sn.

- Greater tarnishing for Cu-Sn alloys was observed with Sn contents ≥ 5 wt%. Oxidized Sn was retained on the surface as SnO_2 due to Sn insolubility with both the electrolyte and within Cu_2O. A change in primary corrosion products with increasing Sn content in the alloy from Cu_2O-dominant to SnO_2-dominant, with this transition taking place at a Sn alloy content of 5 wt%.

- At greater amounts of Sn in the Cu-Sn system (10 wt%), the corrosion product film become predominantly Sn oxide which was more conformal to the alloy surface and was not shown to inhibit soluble Cu release but resulted in greater tarnishing.

7.1.2 Alloying Thresholds for Passivity

- Contemporary solute-enrichment theories were extended to include solute enrichment for alloys with any number of elements.

- Solute enrichment theory was combined with a new model to predict the minimum threshold value for passivation of a binary alloy based on surface coverage enabled by wetting phenomena assuming a protective oxide at the alloy/oxide interface. This minimum threshold is defined by complete surface coverage of immiscible passive oxides whose thermodynamically-favored geometry is assumed to be determined by interphase surface energetics of the oxides with one another and the alloy.

- The minimum amount of Sn in the alloy needed to passivate was revealed to be 1 wt% Sn when considering the combined effects of thermodynamic surface energetics and SnO_2 patina enrichment. The theoretical thermodynamic predictions matched well with qualitative experimental observations measured even at short times.

7.1.3 Tarnish-Resistant Al-Doped Cuprous Oxide Corrosion Products

- The fate of Al following corrosion in artificial perspiration is solute captured Al^{3+} cations in the cuprous oxide layer evidenced by structural and electrochemical modifications, the presence of Al, and changes in the defect chemistry of the p-type oxide.

- Al in the cuprite layer decreased the corrosion product thickness consistent with increased electronic and ionic resistivity due to dopant effects of substitutional Al^{3+} cations on the Cu cation sublattice reducing the amount of electron holes and reducing ionic mobility through binding with metal vacancies.

- Modifying the copper oxide layer with Al solute can alter the corrosion products formed on the surface of a Cu-Al alloy facilitating a tarnish-resistant layer without affecting soluble Cu release for antimicrobial function.

7.1.4 Antimicrobial and Tarnish-Resistant Tunable Cu-Al-Sn Alloys

- Ternary Cu-Al-Sn alloys in solid solution were all antimicrobial, able to kill 2×10^6 CFU *E. Coli* bacteria within 24 h in a stirring beaker (200 mL) or artificial perspiration.

- Despite similar antimicrobial performance, the tarnishing behavior and surface oxides were significantly different between minor alloying elements and their amounts (e.g., ±4 wt%).

- Sn-enhanced Cu dissolution on Cu-Al-Sn led to a synergy with the Al-effect where decreased amounts of total corrosion product thickness and increased Al-doping of Cu_2O were observed with minor (1 wt%) Sn amounts. Future work is planned to characterize these films and determine amount of Al in the film.

- An alloy compositional range of Cu-Al-Sn was identified which functions to support both high antimicrobial efficacy and tarnish-resistant without strong passivation or significantly retarding cuprous ion release for antimicrobial function.

7.2 Future Work

7.2.1 Corrosion Engineering of Cu-Al-Sn Alloys

- Long term corrosion tests in real-world environments should be carried out with selected Cu-Al-Sn. The long-term impact of exposures on the tarnishing of these alloys should be correlated with visual appearance (colorimetric white-light reflectometry), surface morphology and roughness (optical and electron microscopy), as well as composition and structure of thin corrosion product films (transmission electron microscopy).

- Cu-Al-Sn new alloys with potential applications in commercial, residential, and public environments. For these applications, mechanical properties should be investigated to assess formability, ductility, tensile strength, and hardness.

- The continuous/residual antimicrobial efficacy of Cu-Al-Sn alloys with fully-developed oxide films remains unexplored. Disinfection testing of Cu-Al-Sn alloys with electrochemically or pre-grown oxides should be conducted to evaluate the continual antimicrobial efficacy of these alloys and ability to continuously kill bacteria after corrosion products have fully-developed.

- Antimicrobial testing of Cu-Al-Sn surfaces with more resilient strains of pathogenic bacteria such as MRSA, E-MRSA, and HAI-MRSA (Hospital-Acquired) should be interrogated to compare against the efficacy of other alloys available in the literature (see Table 1-2).

- The mechanistic information gathered in this dissertation could be used to generate a multi-element regression model to predict the effects of Al and Sn at any element composition in solid solution. More Cu-Al-Sn alloy compositions tested in standardized protocols (e.g., oxide CR, ion release, corrosion rates) are needed for additional model input data.

7.2.2 Potential Scientific Advancements Using Cu-Based Alloys

Experimental

- Focused-ion beam (FIB) prepared oxide cross sections should be made from corroded Cu-Al and Cu-Al-Sn samples for transmission electron microscopy (TEM) study. Selected-area diffraction (SAD) patterns can reveal the crystal structure (or lack thereof) of the oxide film formed and Energy-Dispersive X-ray spectroscopy (EDS) line scans down the oxide growth direction can reveal the chemical nature of these grown films. High-temperature studies [188] as well as Wagner models [237] predict that the differences in cation diffusion rates should yield at steady-state a cation concentration gradient across the film. Cu-based alloys usually form thicker films (~10^{-7} m) than Cr-based passive films (~10^{-8} m) and thus the Cu system may be more amenable to study this detail of oxidation theory in aqueous environments contrasted with high-temperature environments.

- 3-D atom probe tomography of electrochemically grown oxide layers on Cu-Al and Cu-Al-Sn alloys may provide direct evidence of Al-doping. If the solute-capture model is operative in this case, electrochemically-imposed fast oxide growth versus slow oxide growth may substantiate this theoretical framework and in concert with *ab initio* density-functional theory (DFT) and molecular dynamics (MD) simulations provide insight to the diffusion of atoms in oxide films at the nanoscale which has far-reaching applications towards predictive models of kinetic corrosion protection via passivity.

- The influence of tertiary elements on dissolution rates in the context of solute enrichment have not been previously explored (Chapter 4). X-ray photoelectron spectroscopy (XPS) of air-formed oxide films and grown oxide films at open circuit should be performed to measure Al cation fractions in the cuprous oxide film form Cu-Al-Sn alloys to test if enrichment factors are indeed increased by Sn as suggested from results in Chapter 6.

- Semiconductor characterization studies (e.g., conductivity vs. temperature, Mott-Schottky) of Cu_2O films doped with Al and/or Sn grown separately (not electrochemically) or with *in vacuo* methods will drastically improve our understanding of the roles of dopants to p-type semiconductors which can be grown via electrochemical methods. This knowledge may be useful not only for corrosion but solar cell technology as well.

- Careful thin-film X-Ray or electron diffraction studies should be conducted to track the crystal structure of Cu_2O structure with dopant concentration either formed electrochemically, or through other independent methods.

Modeling

- Dissolution kinetic investigations using Cu-Sn *ab initio* density-functional theory simulations could be combined with experimental studies of high-purity single crystal studies of Sn-implanted Cu surfaces. The combination of *ab initio* methods with experiment may be useful towards bridging the gap between atomistic physics simulations and experimental materials sciences.

- The effect of doping for a wide variety of elements may be explored using DFT simulations of Cu_2O crystals with various doping elements. The relative stability of crystals, relaxation structures, and electronic structure of the bandgap with various dopants could be used as a reasonably high-throughput method to determine potential solute-capturable oxide dopants. These investigations may also be useful in the manufacture of electrochemically-grown (from alloys) doped p-type oxides for tunable dopants solar cell technology.

- Molecular dynamics studies of surface diffusion of Sn and Al on Cu and Cu-Al may elucidate the potential, or lack thereof, for solute-capture of these elements in the cuprous oxide. Critical dealloying phenomena may also be investigated using MD simulations with Cu-based alloys such as the effect of Sn in arresting dealloying of Cu-Zn-Sn alloys.

References

[1] H.T. Michels, C.A. Michels, Copper alloys-The new 'old'weapon in the fight against infectious disease, Microbiology. 10 (2016).

[2] A. Ala, A.P. Walker, K. Ashkan, J.S. Dooley, M.L. Schilsky, Wilson's disease, The Lancet. 369 (2007) 397–408. doi:10.1016/S0140-6736(07)60196-2.

[3] P.J. Kuhn, Doorknobs: a source of nosocomial infection, Diagn. Med. 6 (1983) 62–63.

[4] J.M. Bingeman, J.P. Bethell, P. Goodwin, A.T. Mack, Copper and other sheathing in the Royal Navy, Int. J. Naut. Archaeol. 29 (2000) 218–229. doi:10.1111/j.1095-9270.2000.tb01453.x.

[5] M. Schumacher, Seawater corrosion handbook, (1979). http://books.google.com/books?id=HNRRAAAAMAAJ.

[6] G. Grass, C. Rensing, M. Solioz, Metallic Copper as an Antimicrobial Surface, Appl. Environ. Microbiol. 77 (2011) 1541–1547. doi:10.1128/aem.02766-10.

[7] J. O'Neill, Antimicrobial Resistance: Tackling a crisis for the health and wealth of nations, HM Government, Wellcome Trust, 2014.

[8] S.S. Magill, J.R. Edwards, W. Bamberg, Z.G. Beldavs, G. Dumyati, M.A. Kainer, R. Lynfield, M. Maloney, L. McAllister-Hollod, J. Nadle, S.M. Ray, D.L. Thompson, L.E. Wilson, S.K. Fridkin, Multistate Point-Prevalence Survey of Health Care–Associated Infections, N. Engl. J. Med. 370 (2014) 1198–1208. doi:10.1056/NEJMoa1306801.

[9] V.M. Villapún, L.G. Dover, A. Cross, S. González, Antibacterial Metallic Touch Surfaces, Materials. 9 (2016) 736. doi:10.3390/ma9090736.

[10] S.L. Warnes, C.J. Highmore, C.W. Keevil, Horizontal transfer of antibiotic resistance genes on abiotic touch surfaces: implications for public health, MBio. 3 (2012) e00489-12.

[11] S.L. Warnes, Z.R. Little, C.W. Keevil, Human coronavirus 229E remains infectious on common touch surface materials, MBio. 6 (2015) e01697-15.

[12] P. Airey, J. Verran, Potential use of copper as a hygienic surface; problems associated with cumulative soiling and cleaning, J. Hosp. Infect. 67 (2007) 271–277. doi:10.1016/j.jhin.2007.09.002.

[13] M.G. Schmidt, J.J. John, K.D. Freeman, P.A. Sharpe, A.A. Estelle, H.T. Michels, Perspectives from the field in response to "It is time to revise our approach to registering antimicrobial agents for health care settings," Am. J. Infect. Control. 44 (2016) 1187–1189.

[14] M.G. Schmidt, H.H. Attaway, P.A. Sharpe, J. John, K.A. Sepkowitz, A. Morgan, S.E. Fairey, S. Singh, L.L. Steed, J.R. Cantey, K.D. Freeman, H.T. Michels, C.D. Salgado, Sustained Reduction of Microbial Burden on Common Hospital Surfaces through Introduction of Copper, J. Clin. Microbiol. 50 (2012) 2217–2223. doi:10.1128/JCM.01032-12.

[15] H.T. Michels, C.W. Keevil, C.D. Salgado, M.G. Schmidt, From laboratory research to a clinical trial: copper alloy surfaces kill bacteria and reduce hospital-acquired infections, HERD Health Environ. Res. Des. J. 9 (2015) 64–79.

[16] A.L. Casey, D. Adams, T.J. Karpanen, P.A. Lambert, B.D. Cookson, P. Nightingale, L. Miruszenko, R. Shillam, P. Christian, T.S.J. Elliott, Role of copper in reducing hospital environment contamination, J. Hosp. Infect. 74 (2010) 72–77. doi:10.1016/j.jhin.2009.08.018.

[17] D.J. Horton, H. Ha, L.L. Foster, H.J. Bindig, J.R. Scully, Tarnishing and Cu Ion release in Selected Copper-Base Alloys: Implications towards Antimicrobial Functionality, Electrochimica Acta. 169 (2015) 351–366. doi:10.1016/j.electacta.2015.04.001.

[18] L. Weaver, H.T. Michels, C.W. Keevil, Survival of Clostridium difficile on copper and steel: futuristic options for hospital hygiene, J. Hosp. Infect. 68 (2008) 145–151. doi:10.1016/j.jhin.2007.11.011.

[19] H.T. Michels, J.O. Noyce, C.W. Keevil, Effects of temperature and humidity on the efficacy of methicillin-resistant Staphylococcus aureus challenged antimicrobial materials containing silver and copper, Lett. Appl. Microbiol. 49 (2009) 191–195. doi:10.1111/j.1472-765X.2009.02637.x.

[20] J.O. Noyce, H. Michels, C.W. Keevil, Potential use of copper surfaces to reduce survival of epidemic meticillin-resistant Staphylococcus aureus in the healthcare environment, J. Hosp. Infect. 63 (2006) 289–297. doi:10.1016/j.jhin.2005.12.008.

[21] C.E. Santo, E.W. Lam, C.G. Elowsky, D. Quaranta, D.W. Domaille, C.J. Chang, G. Grass, Bacterial Killing by Dry Metallic Copper Surfaces, Appl Env. Microbiol. 77 (2011) 794–802. doi:10.1128/aem.01599-10.

[22] D. Quaranta, T. Krans, C.E. Santo, C.G. Elowsky, D.W. Domaille, C.J. Chang, G. Grass, Mechanisms of Contact-Mediated Killing of Yeast Cells on Dry Metallic Copper Surfaces, Appl. Environ. Microbiol. 77 (2011) 416–426. doi:10.1128/aem.01704-10.

[23] L.L. Foster, J.R. Scully, Corrosion of Cu-5Zn-5Al-1Sn (89% Cu, 5% Zn, 5% Al, 1% Sn) Compared to Copper in Synthetic Perspiration During Cyclic Wetting and Drying: The Fate of Copper, Corrosion. 72 (2016) 1095–1106. doi:10.5006/2063.

[24] Y.-S.E. Lin, R.D. Vidic, J.E. Stout, V.L. Yu, Individual and combined effects of copper and silver ions on inactivation of Legionella pneumophila, Water Res. 30 (1996) 1905–1913. doi:10.1016/0043-1354(96)00077-2.

[25] C. Molteni, H.K. Abicht, M. Solioz, Killing of bacteria by copper surfaces involves dissolved copper, Appl. Environ. Microbiol. 76 (2010) 4099–4101.

[26] L.L. Foster, M. Hutchison, J.R. Scully, The Fate of Copper During Corrosion of Cu-5Zn-5Al-1Sn (89% Cu, 5% Zn, 5% Al, 1% Sn) Compared to Copper in Synthetic Perspiration Solution, Corrosion. 72 (2016) 51–65. doi:10.5006/1885.

[27] J. Sandberg, I.O. Wallinder, C. Leygraf, N. Le Bozec, Corrosion-induced copper runoff from naturally and pre-patinated copper in a marine environment, Corros. Sci. 48 (2006) 4316–4338. doi:10.1016/j.corsci.2006.04.004.

[28] S. Djokić, Antimicrobial Activity of Electrochemically Oxidized Silver and Copper, ECS Trans. 25 (2010) 7–15. doi:10.1149/1.3298945.

[29] C. Zhang, N. Xu, B. Yang, The corrosion behaviour of copper in simulated uterine fluid, Corros. Sci. 38 (1996) 635–641. doi:10.1016/0010-938X(95)00154-C.

[30] I. Milošev, T. Kosec, Metal ion release and surface composition of the Cu–18Ni–20Zn nickel–silver during 30 days immersion in artificial sweat, Appl. Surf. Sci. 254 (2007) 644–652. doi:10.1016/j.apsusc.2007.06.049.

[31] S.S. Djokic, Deposition of Silver Oxysalts and Their Antimicrobial Properties, J. Electrochem. Soc. 151 (2004) C359–C364.

[32] J. Erlebacher, M.J. Aziz, A. Karma, N. Dimitrov, K. Sieradzki, Evolution of nanoporosity in dealloying, Nature. 410 (2001) 450–453. doi:10.1038/35068529.

[33] H. Abe, K. Sato, H. Nishikawa, T. Takemoto, M. Fukuhara, A. Inoue, Dealloying of Cu-Zr-Ti bulk metallic glass in hydrofluoric acid solution, Mater. Trans. 50 (2009) 1255.

[34] L. Burzyńska, Comparison of the spontaneous and anodic processes during dissolution of brass, Corros. Sci. 43 (2001) 1053–1069. doi:10.1016/S0010-938X(00)00130-X.

[35] Z. Dan, Refinement of Nanoporous Copper by Dealloying MgCuY Amorphous Alloys in Sulfuric Acids Containing Polyvinylpyrrolidone, J. Electrochem. Soc. 161 (2014) C120–C125. doi:10.1149/2.076403jes.

[36] R.H. Heidersbach, E.D. Verink, The Dezincification of Alpha and Beta Brasses, Corrosion. 28 (1972) 397–418. doi:10.5006/0010-9312-28.11.397.

[37] T. Aburada, J.M. Fitz-Gerald, J.R. Scully, Synthesis of nanoporous copper by dealloying of Al-Cu-Mg amorphous alloys in acidic solution: The effect of nickel, Corros. Sci. 53 (2011) 1627–1632. doi:10.1016/j.corsci.2011.01.033.

[38] L.-Y. Chen, J.-S. Yu, T. Fujita, M.-W. Chen, Nanoporous Copper with Tunable Nanoporosity for SERS Applications, Adv. Funct. Mater. 19 (2009) 1221–1226. doi:10.1002/adfm.200801239.

[39] D.S. Keir, The Dealloying of Copper-Manganese Alloys, J. Electrochem. Soc. 127 (1980) 2138. doi:10.1149/1.2129360.

[40] M. Li, Y. Zhou, H. Geng, Fabrication of nanoporous copper ribbons by dealloying of Al-Cu alloys, J. Porous Mater. 19 (2012) 791–796. doi:10.1007/s10934-011-9532-3.

[41] Y. Tang, Y. Liu, L. Lian, X. Zhou, L. He, Formation of nanoporous copper through dealloying of dual-phase Cu–Mn–Al alloy: The evolution of microstructure and composition, J. Mater. Res. 27 (2012) 2771–2778. doi:10.1557/jmr.2012.307.

[42] T. Song, M. Yan, Z. Shi, A. Atrens, M. Qian, Creation of bimodal porous copper materials by an annealing-electrochemical dealloying approach, Electrochimica Acta. 164 (2015) 288–296. doi:10.1016/j.electacta.2015.02.217.

[43] G. Shiflet, The more elements, the merrier, Science. 300 (2003) 443–444. doi:10.1126/science.1083759.

[44] C.D. Taylor, P. Lu, J. Saal, G.S. Frankel, J.R. Scully, Integrated computational materials engineering of corrosion resistant alloys, Npj Mater. Degrad. 2 (2018) 6.

[45] P. Marcus, On some fundamental factors in the effect of alloying elements on passivation of alloys, Corros. Sci. 36 (1994) 2155–2158. doi:10.1016/0010-938X(94)90013-2.

[46] A.S.M.I.H.C. ASM Handbook Committee, Metals handbook, American Society for Metals, Metals Park, Ohio, 1978.

[47] A. Drach, I. Tsukrov, J. DeCew, J. Aufrecht, A. Grohbauer, U. Hofmann, Field studies of corrosion behaviour of copper alloys in natural seawater, Corros. Sci. 76 (2013) 453–464. doi:10.1016/j.corsci.2013.07.019.

[48] British Standards Institute, BS EN 1811: Reference test method for release of nickel from all post assemblies which are inserted into pierced parts of the human body and articles intended to come into direct and prolonged contact with the skin, 2008.

[49] I.O. Wallinder, C. Leygraf, A study of copper runoff in an urban atmosphere, Corros. Sci. 39 (1997) 2039–2052.

[50] I.O. Wallinder, C. Leygraf, Seasonal variations in corrosion rate and runoff rate of copper roofs in an urban and a rural atmospheric environment, Corros. Sci. 43 (2001) 2379–2396.

[51] I.O. Wallinder, B. Bahar, C. Leygraf, J. Tidblad, Modelling and mapping of copper runoff for Europe, J. Environ. Monit. 9 (2007) 66–73. doi:10.1039/B61241e.

[52] L.G. Sillén, A.E. Martell, J. Bjerrum, Stability constants of metal-ion complexes, Chemical Society, London, 1964.

[53] C. Alonso, E. Casero, E. Román, S.F.P. Campos, M.F.L. de Mele, Effective inhibition of the early copper ion burst release by purine adsorption in simulated uterine fluids, Electrochimica Acta. 189 (2016) 54–63. doi:10.1016/j.electacta.2015.12.093.

[54] I. Wallinder Odnevall, X. Zhang, S. Goidanich, N. Le Bozec, G. Herting, C. Leygraf, Corrosion and runoff rates of Cu and three Cu-alloys in marine environments with increasing chloride deposition rate, Sci. Total Environ. 472 (2014) 681–694. doi:10.1016/j.scitotenv.2013.11.080.
[55] S. Goidanich, I. Odnevall Wallinder, G. Herting, C. Leygraf, Corrosion induced metal release from copper based alloys compared to their pure elements, Corros. Eng. Sci. Technol. 43 (2008) 134–141. doi:10.1179/174327808x286383.
[56] G. Herting, S. Goidanich, I.O. Wallinder, C. Leygraf, Corrosion-induced release of Cu and Zn into rainwater from brass, bronze and their pure metals. A 2-year field study, Environ. Monit. Assess. 144 (2008) 455–461. doi:10.1007/s10661-007-0008-5.
[57] N. Fredj, J.S. Kolar, D.M. Prichard, T.D. Burleigh, Study of relative color stability and corrosion resistance of commercial copper alloys exposed to hand contact and synthetic hand sweat, Corros. Sci. 76 (2013) 415–423. doi:10.1016/j.corsci.2013.07.015.
[58] P. Zhou, M.J. Hutchison, J.W. Erning, J.R. Scully, K. Ogle, An in situ kinetic study of brass dezincification and corrosion, Electrochimica Acta. 229 (2017) 141–154. doi:10.1016/j.electacta.2017.01.078.
[59] M.G. Fontana, Corrosion Engineering, 2nd ed., McGraw-Hill, New York, 1986.
[60] Copper Development Association, Copper and its Alloys Engineering and Technology, 2nd ed., 1949.
[61] H. Wojtas, S. Virtanen, H. Böhni, Electrochemical characterization of new stainless Cu-Al-Sn alloys, Corros. Sci. 37 (1995) 793–799. doi:10.1016/0010-938X(95)80009-3.
[62] S. Virtanen, H. Wojtas, P. Schmuki, H. Böhni, Passivity of High Corrosion Resistant Cu-Al-Sn Alloys, J. Electrochem. Soc. 140 (1993) 2786–2790. doi:10.1149/1.2220911.
[63] M.J. Pryor, K.K. Giam, The Effect of Arsenic on the Dealloying of Alpha-Brass, J. Electrochem. Soc. 129 (1982) 2157–2163.
[64] W.A. Badawy, M.M. El-Rabiei, H. Nady, Synergistic effects of alloying elements in Cu-ternary alloys in chloride solutions, Electrochimica Acta. 120 (2014) 39–45. doi:10.1016/j.electacta.2013.12.043.
[65] R. Kirchheim, B. Heine, H. Fischmeister, S. Hofmann, H. Knote, U. Stolz, The passivity of iron-chromium alloys, Corros. Sci. 29 (1989) 899–917. doi:10.1016/0010-938X(89)90060-7.
[66] C. Wagner, Passivity and inhibition during the oxidation of metals at elevated temperatures, Corros. Sci. 5 (1965) 751–764. doi:10.1016/S0010-938X(65)80003-8.
[67] R. Babic, M. Metikos-Hukovic, A. Jukic, A Study of Copper Passivity by Electrochemical Impedance Spectroscopy, J. Electrochem. Soc. 148 (2001) B146–B151.
[68] H.-H. Strehblow, Passivity of Metals, 1st ed., John Wiley & Sons Inc, 2003.
[69] K. Sieradzki, R.C. Newman, A Percolation Model for Passivation in Stainless Steels, J. Electrochem. Soc. 133 (1986) 1979–1980. doi:10.1149/1.2109065.
[70] D. Williams, R. Newman, Q. Song, R. Kelly, Passivity breakdown and pitting corrosion of binary alloys, Nature. 350 (1991) 216–219.
[71] J. Kunze, V. Maurice, L.H. Klein, H.H. Strehblow, P. Marcus, In situ STM study of the duplex passive films formed on Cu(111) and Cu(001) in 0.1 M NaOH, Corros. Sci. 46 (2004) 245–264.
[72] P. Marcus, J.M. Grimal, The anodic dissolution and passivation of NiCrFe alloys studied by ESCA, Corros. Sci. 33 (1992) 805–814. doi:10.1016/0010-938X(92)90113-H.

[73] C.A.C. Sequeira, Some considerations on the background of passivity, Corros. E Prot. Mater. 29 (2010) 126–137.
[74] E. McCafferty, Oxide networks, graph theory, and the passivity of binary alloys, Corros. Sci. 44 (2002) 1393–1409. doi:10.1016/S0010-938X(01)00172-X.
[75] E. McCafferty, Graph Theory and the Passivity of Iron-Chromium Binary Alloys, Electrochem. Solid-State Lett. 3 (2000) 28–30. doi:10.1149/1.1390948.
[76] E. McCafferty, Graph Theory and the Passivity of Binary Alloys: More Examples, J. Electrochem. Soc. 151 (2004) B82–B89. doi:10.1149/1.1637899.
[77] E. McCafferty, Introduction to Corrosion Science, Springer New York, 2010. https://books.google.com/books?id=g9oXcE-gQKUC.
[78] J.E. Castle, K. Asami, A more general method for ranking the enrichment of alloying elements in passivation films, Surf. Interface Anal. 36 (2004) 220–224. doi:10.1002/sia.1676.
[79] M. Seo, N. Sato, Theoretical approach to corrosion resistivity of alloys, Langmuir. 3 (1987) 917–921.
[80] F.M. Al-Kharafi, Y.A. El-Tantawy, Passivation of copper: Role of some anions in the mechanism of film formation and breakdown, Corros. Sci. 22 (1982) 1–12. doi:10.1016/0010-938X(82)90126-3.
[81] I. Hugh S, The localized breakdown and repair of passive surfaces during pitting, Corros. Sci. 29 (1989) 313–323. doi:10.1016/0010-938x(89)90038-3.
[82] S.A. Kaluzhina, I.V. Sieber, Copper passivity and its breakdown in sodium bicarbonate solutions: A scanning electron microscopy and X-ray photoelectron and Auger spectroscopy study, Russ. J. Electrochem. 42 (2006) 1352–1357.
[83] P. Marcus, V. Maurice, H.H. Strehblow, Localized corrosion (pitting): A model of passivity breakdown including the role of the oxide layer nanostructure, Corros. Sci. 50 (2008) 2698–2704. doi:10.1016/j.corsci.2008.06.047.
[84] H. Bohni, Breakdown of Passivity and Localized Corrosion Processes, Langmuir. 3 (1987) 924–930.
[85] I. Milošev, M. Metikoš-Huković, The behaviour of Cu-xNi (x = 10 to 40 wt%) alloys in alkaline solutions containing chloride ions, Electrochimica Acta. 42 (1997) 1537–1548. doi:10.1016/S0013-4686(96)00315-5.
[86] R.F. North, M.J. Pryor, The influence of corrosion product structure on the corrosion rate of Cu-Ni alloys, Corros. Sci. 10 (1970) 297–311. doi:10.1016/S0010-938X(70)80022-1.
[87] L. Foster, Tarnishing of a Cu-Al-Zn-Sn Alloy Compared to Commercially Pure Copper: Implications Toward Antimicrobial Function, University of Virginia, 2014. http://libra.virginia.edu/catalog/libra-oa:7745.
[88] G.T. Burstein, A.J. Davenport, The Current-Time Relationship during Anodic Oxide Film Growth under High Electric Field, J. Electrochem. Soc. 136 (1989) 936–941. doi:10.1149/1.2096890.
[89] A.J. Davenport, G.T. Burstein, Concerning the distribution of the overpotential during anodic oxide film growth, J. Electrochem. Soc. 137 (1990) 1496–1501.
[90] C.Y. Chao, L.F. Lin, D.D. Macdonald, A Point Defect Model for Anodic Passive Films: I . Film Growth Kinetics, J. Electrochem. Soc. 128 (1981) 1187–1194. doi:10.1149/1.2127591.
[91] D.D. Macdonald, The history of the Point Defect Model for the passive state: A brief review of film growth aspects, Adv. Corros. Sci. LIFETIME Predict. Sustain. Pap. 8th ISE Spring

Meet.-5 May 2010 Columb. OH USA. 56 (2011) 1761–1772. doi:10.1016/j.electacta.2010.11.005.

[92] S. Mehtar, I. Wiid, S.D. Todorov, The antimicrobial activity of copper and copper alloys against nosocomial pathogens and Mycobacterium tuberculosis isolated from healthcare facilities in the Western Cape: an in-vitro study, J. Hosp. Infect. 68 (2008) 45–51. doi:10.1016/j.jhin.2007.10.009.

[93] M. Souli, I. Galani, D. Plachouras, T. Panagea, A. Armaganidis, G. Petrikkos, H. Giamarellou, Antimicrobial activity of copper surfaces against carbapenemase-producing contemporary Gram-negative clinical isolates, J. Antimicrob. Chemother. 68 (2012) 852–857.

[94] O.K. Eser, A. Ergin, G. Hascelik, Antimicrobial activity of copper alloys against invasive multidrug-resistant nosocomial pathogens, Curr. Microbiol. 71 (2015) 291–295.

[95] C. Espirito Santo, P.V. Morais, G. Grass, Isolation and Characterization of Bacteria Resistant to Metallic Copper Surfaces, Appl Env. Microbiol. 76 (2010) 1341–1348. doi:10.1128/aem.01952-09.

[96] K. San, J. Long, C.A. Michels, N. Gadura, Antimicrobial copper alloy surfaces are effective against vegetative but not sporulated cells of gram-positive Bacillus subtilis, MicrobiologyOpen. 4 (2015) 753–763.

[97] P. Bleichert, C. Espírito Santo, M. Hanczaruk, H. Meyer, G. Grass, Inactivation of bacterial and viral biothreat agents on metallic copper surfaces, BioMetals. 27 (2014) 1179–1189. doi:10.1007/s10534-014-9781-0.

[98] Z. Cui, M. Ibrahim, C. Yang, Y. Fang, H. Annam, B. Li, Y. Wang, G.-L. Xie, G. Sun, Susceptibility of opportunistic Burkholderia glumae to copper surfaces following wet or dry surface contact, Molecules. 19 (2014) 9975–9985.

[99] M. Ibrahim, F. Wang, M. Lou, G. Xie, B. Li, Z. Bo, G. Zhang, H. Liu, A. Wareth, Copper as an antibacterial agent for human pathogenic multidrug resistant Burkholderia cepacia complex bacteria, J. Biosci. Bioeng. 112 (2011) 570–576.

[100] G. Faúndez, M. Troncoso, P. Navarrete, G. Figueroa, Antimicrobial activity of copper surfaces against suspensions of Salmonella enterica and Campylobacter jejuni, BMC Microbiol. 4 (2004) 19.

[101] L. Wheeldon, T. Worthington, P.A. Lambert, A. Hilton, C. Lowden, T.S. Elliott, Antimicrobial efficacy of copper surfaces against spores and vegetative cells of Clostridium difficile: the germination theory, J. Antimicrob. Chemother. 62 (2008) 522–525.

[102] S.W. Gould, M.D. Fielder, A.F. Kelly, M. Morgan, J. Kenny, D.P. Naughton, The antimicrobial properties of copper surfaces against a range of important nosocomial pathogens, Ann. Microbiol. 59 (2009) 151–156.

[103] S. Warnes, S. Green, H. Michels, C. Keevil, Biocidal efficacy of copper alloys against pathogenic enterococci involves degradation of genomic and plasmid DNAs, Appl. Environ. Microbiol. 76 (2010) 5390–5401.

[104] S. Warnes, C. Keevil, Mechanism of copper surface toxicity in vancomycin-resistant enterococci following wet or dry surface contact, Appl. Environ. Microbiol. 77 (2011) 6049–6059.

[105] J. Elguindi, J. Wagner, C. Rensing, Genes involved in copper resistance influence survival of Pseudomonas aeruginosa on copper surfaces, J. Appl. Microbiol. 106 (2009) 1448–1455.

[106] S. Wilks, H. Michels, C. Keevil, The survival of Escherichia coli O157 on a range of metal surfaces, Int. J. Food Microbiol. 105 (2005) 445–454.

[107] R. Hong, T.Y. Kang, C.A. Michels, N. Gadura, Membrane lipid peroxidation in copper alloy-mediated contact killing of Escherichia coli, Appl. Environ. Microbiol. 78 (2012) 1776–1784.
[108] C.E. Santo, N. Taudte, D.H. Nies, G. Grass, Contribution of copper ion resistance to survival of Escherichia coli on metallic copper surfaces, Appl. Environ. Microbiol. 74 (2008) 977–986.
[109] L. Weaver, H. Michels, C. Keevil, Potential for preventing spread of fungi in air-conditioning systems constructed using copper instead of aluminium, Lett. Appl. Microbiol. 50 (2010) 18–23.
[110] J. Rogers, A. Dowsett, P. Dennis, J. Lee, C. Keevil, Influence of plumbing materials on biofilm formation and growth of Legionella pneumophila in potable water systems, Appl. Environ. Microbiol. 60 (1994) 1842–1851.
[111] S.A. Wilks, H.T. Michels, C.W. Keevil, Survival of Listeria monocytogenes Scott A on metal surfaces: Implications for cross-contamination, Int. J. Food Microbiol. 111 (2006) 93–98. doi:10.1016/j.ijfoodmicro.2006.04.037.
[112] L. Zhu, J. Elguindi, C. Rensing, S. Ravishankar, Antimicrobial activity of different copper alloy surfaces against copper resistant and sensitive Salmonella enterica, Food Microbiol. 30 (2012) 303–310.
[113] C.E. Santo, D. Quaranta, G. Grass, Antimicrobial metallic copper surfaces kill Staphylococcus haemolyticus via membrane damage, Microbiologyopen. 1 (2012) 46–52.
[114] J. Noyce, H. Michels, C. Keevil, Inactivation of influenza A virus on copper versus stainless steel surfaces, Appl. Environ. Microbiol. 73 (2007) 2748–2750.
[115] S.L. Warnes, C.W. Keevil, Inactivation of norovirus on dry copper alloy surfaces, PloS One. 8 (2013) e75017.
[116] S.L. Warnes, E.N. Summersgill, C.W. Keevil, Inactivation of murine norovirus on a range of copper alloy surfaces is accompanied by loss of capsid integrity, Appl. Environ. Microbiol. 81 (2015) 1085–1091.
[117] C. Manuel, M. Moore, L. Jaykus, Destruction of the capsid and genome of GII. 4 human norovirus occurs during exposure to metal alloys containing copper, Appl. Environ. Microbiol. 81 (2015) 4940–4946.
[118] J. Li, J.J. Dennehy, Differential bacteriophage mortality on exposure to copper, Appl. Environ. Microbiol. 77 (2011) 6878–6883.
[119] H.T. Michels, W. Moran, J. Michel, Antimicrobial Properties of Copper Alloy Surfaces, with a Focus on Hospital-Acquired Infections, Int. J. Met. (2008) 47–56.
[120] R.L. Frost, Raman spectroscopy of selected copper minerals of significance in corrosion, Spectrochim. Acta. A. Mol. Biomol. Spectrosc. 59 (2003) 1195–1204. doi:10.1016/S1386-1425(02)00315-3.
[121] A.G. Tyurin, Thermodynamics of chemical and electrochemical stability of aluminum, silicon, and tin bronzes, Prot. Met. 44 (2008) 292–300. doi:10.1134/S0033173208030132.
[122] P. Barton, P.M. Bethke, Thermodynamic properties of some synthetic zinc and copper minerals, Am. J. Sci. A. 258 (1960) 21–34.
[123] B. Vink, Stability relations of malachite and azurite, Mineral. Mag. 50 (1986) 41–47.
[124] J.G. Speight, Lange's Handbook of Chemistry: Bond Dissociation Energies, n.d.
[125] M. Pourbaix, Some Applications of Potential-Ph Diagrams to Study of Localized Corrosion, J. Electrochem. Soc. 123 (1976) C25–C36.

[126] P. Marcel, Atlas of Electrochemical Equilibria in Aqueous Solutions, Second English Edition, National Association of Corrosion Engineers, Houston, TX, 1974.

[127] R.J. Santucci, M.E. McMahon, J.R. Scully, Utilization of chemical stability diagrams for improved understanding of electrochemical systems: evolution of solution chemistry towards equilibrium, Npj Mater. Degrad. 2 (2018). doi:10.1038/s41529-017-0021-2.

[128] C. Leygraf, T. Graedel, Atmospheric Corrosion, John Wiley & Sons, INC., 2000.

[129] L. Robbiola, K. Rahmouni, C. Chiavari, C. Martini, D. Prandstraller, A. Texier, H. Takenouti, P. Vermaut, New insight into the nature and properties of pale green surfaces of outdoor bronze monuments, Appl. Phys. A. 92 (2008) 161–169. doi:10.1007/s00339-008-4468-4.

[130] L. Robbiola, J.M. Blengino, C. Fiaud, Morphology and mechanisms of formation of natural patinas on archaeological Cu–Sn alloys, Corros. Sci. 40 (1998) 2083–2111. doi:10.1016/S0010-938X(98)00096-1.

[131] I. Mabille, A. Bertrand, E.M.M. Sutter, C. Fiaud, Mechanism of dissolution of a Cu–13Sn alloy in low aggressive conditions, Corros. Sci. 45 (2003) 855–866. doi:10.1016/S0010-938X(02)00207-X.

[132] X. Zhang, I. Odnevall Wallinder, C. Leygraf, Mechanistic studies of corrosion product flaking on copper and copper-based alloys in marine environments, Corros. Sci. 85 (2014) 15–25. doi:10.1016/j.corsci.2014.03.028.

[133] ASTM, Standard Test Methods for Chemical Analysis of Copper Alloys, ASTM International, West Conshohocken, PA, 2005. www.astm.org.

[134] P. Zhou, M.J. Hutchison, J.R. Scully, K. Ogle, The anodic dissolution of copper alloys: Pure copper in synthetic tap water, Electrochimica Acta. 191 (2016) 548–557. doi:10.1016/j.electacta.2016.01.093.

[135] K. Ogle, J. Baeyens, J. Swiatowska, P. Volovitch, Atomic emission spectroelectrochemistry applied to dealloying phenomena: I. The formation and dissolution of residual copper films on stainless steel, Electrochimica Acta. 54 (2009) 5163–5170. doi:10.1016/j.electacta.2009.01.037.

[136] K. Ogle, M. Serdechnova, M. Mokaddem, P. Volovitch, The cathodic dissolution of Al, Al2Cu, and Al alloys, Electrochimica Acta. 56 (2011) 1711–1718. doi:10.1016/j.electacta.2010.09.058.

[137] K. Ogle, A. Tomandl, N. Meddahi, M. Wolpers, The alkaline stability of phosphate coatings I: ICP atomic emission spectroelectrochemistry, Corros. Sci. 46 (2004) 979–995. doi:10.1016/S0010-938X(03)00182-3.

[138] K. Ogle, S. Weber, Anodic Dissolution of 304 Stainless Steel Using Atomic Emission Spectroelectrochemistry, J. Electrochem. Soc. 147 (2000) 1770–1780. doi:10.1149/1.1393433.

[139] ASTM G1-03(2011) Standard Practice for Preparing, Cleaning, and Evaluating Corrosion Test Specimens, ASTM International, 2011.

[140] C. Gabrielli, M. Keddam, H. Takenouti, V. Quang Kinh, F. Bourelier, The relationship between the impedance of corroding electrode and its polarization resistance determined by a linear voltage sweep technique, Electrochimica Acta. 24 (1979) 61–65. doi:10.1016/0013-4686(79)80042-0.

[141] S. Colin, E. Beche, R. Berjoan, H. Jolibois, A. Chambaudet, An XPS and AES study of the free corrosion of Cu-, Ni- and Zn-based alloys in synthetic sweat, Corros. Sci. 41 (1999) 1051–1065. doi:10.1016/S0010-938X(98)00141-3.

[142] M.C. Squarcialupi, G.P. Bernardini, V. Faso, A. Atrei, G. Rovida, Characterisation by XPS of the corrosion patina formed on bronze surfaces, J. Cult. Herit. 3 (2002) 199–204. doi:10.1016/S1296-2074(02)01179-2.

[143] G. Masi, C. Chiavari, J. Avila, J. Esvan, S. Raffo, M.C. Bignozzi, M.C. Asensio, L. Robbiola, C. Martini, Corrosion investigation of fire-gilded bronze involving high surface resolution spectroscopic imaging, Appl. Surf. Sci. 366 (2016) 317–327. doi:10.1016/j.apsusc.2016.01.101.

[144] C. Debiemme-Chouvy, F. Ammeloot, E.M.M. Sutter, X-ray photoemission investigation of the corrosion film formed on a polished Cu–13Sn alloy in aerated NaCl solution, Appl. Surf. Sci. 174 (2001) 55–61. doi:10.1016/S0169-4332(01)00023-X.

[145] R. Walker, Aqueous Corrosion of Tin-Bronze and Inhibition by Benzotriazole, Corrosion. 56 (2000) 1211–1219. doi:10.5006/1.3280509.

[146] F. Ammeloot, C. Fiaud, E.M.M. Sutter, Characterization of the oxide layers on a Cu□13Sn alloy in a NaCl aqueous solution without and with 0.1 M benzotriazole. Electrochemical and photoelectrochemical contributions, Electrochimica Acta. 44 (1999) 2549–2558. doi:10.1016/S0013-4686(98)00391-0.

[147] V. Hayez, V. Costa, J. Guillaume, H. Terryn, A. Hubin, Micro Raman spectroscopy used for the study of corrosion products on copper alloys: study of the chemical composition of artificial patinas used for restoration purposes, Analyst. 130 (2005) 550–556. doi:10.1039/b419080g.

[148] F. Ospitali, C. Chiavari, C. Martini, E. Bernardi, F. Passarini, L. Robbiola, The characterization of Sn-based corrosion products in ancient bronzes: a Raman approach, J. Raman Spectrosc. 43 (2012) 1596–1603. doi:10.1002/jrs.4037.

[149] C. Chiavari, E. Bernardi, A. Balbo, C. Monticelli, S. Raffo, M.C. Bignozzi, C. Martini, Atmospheric corrosion of fire-gilded bronze: corrosion and corrosion protection during accelerated ageing tests, Corros. Sci. 100 (2015) 435–447. doi:10.1016/j.corsci.2015.08.013.

[150] L. Robbiola, T.T.M. Tran, P. Dubot, O. Majerus, K. Rahmouni, Characterisation of anodic layers on Cu–10Sn bronze (RDE) in aerated NaCl solution, Corros. Sci. 50 (2008) 2205–2215. doi:10.1016/j.corsci.2008.06.003.

[151] R. Parsons, Handbook of electrochemical constants, Academic Press, New York, 1959.

[152] B. Malki, S. Saedlou, I. Guillotte, B. Baroux, Ab Initio Monte Carlo Simulations of the Acidic Dissolution of Stainless Steels: Influence of the Alloying Elements, J. Electrochem. Soc. 163 (2016) C807–C814.

[153] H.T. Michels, Anti-Microbial Characteristics of Copper, ASTM Stand. News. 34 (2006) 28–31.

[154] M.J. Hutchison, P. Zhou, K. Ogle, J.R. Scully, Enhanced Electrochemical Cu Release from Commercial Cu-Sn Alloys: Fate of the Alloying Elements in Artificial Perspiration, Electrochimica Acta. (2017). doi:10.1016/j.electacta.2017.04.092.

[155] H. Sugawara, H. Ebiko, Dezincification of brass, Corros. Sci. 7 (1967) 513–523. doi:10.1016/S0010-938X(67)80090-8.

[156] C. Chiavari, K. Rahmouni, H. Takenouti, S. Joiret, P. Vermaut, L. Robbiola, Composition and electrochemical properties of natural patinas of outdoor bronze monuments, Electrochimica Acta. 52 (2007) 7760–7769. doi:10.1016/j.electacta.2006.12.053.

[157] G.M. Ingo, E. Angelini, T. De Caro, G. Bultrini, A. Mezzi, Combined use of XPS and SEM + EDS for the study of surface microchemical structure of archaeological bronze Roman mirrors, Surf. Interface Anal. 36 (2004) 871–875. doi:10.1002/sia.1789.

[158] G. Bertolotti, D. Bersani, P. Lottici, M. Alesiani, T. Malcherek, J. Schlüter, Micro-Raman study of copper hydroxychlorides and other corrosion products of bronze samples mimicking archaeological coins, Anal. Bioanal. Chem. 402 (2012) 1451–1457. doi:10.1007/s00216-011-5268-9.

[159] R.L. Frost, W. Martens, J.T. Kloprogge, P.A. Williams, Raman spectroscopy of the basic copper chloride minerals atacamite and paratacamite: implications for the study of copper, brass and bronze objects of archaeological significance, J. Raman Spectrosc. 33 (2002) 801–806. doi:10.1002/jrs.921.

[160] M. Serghini-Idrissi, M.C. Bernard, F.Z. Harrif, S. Joiret, K. Rahmouni, A. Srhiri, H. Takenouti, V. Vivier, M. Ziani, Electrochemical and spectroscopic characterizations of patinas formed on an archaeological bronze coin, Electrochimica Acta. 50 (2005) 4699–4709. doi:10.1016/j.electacta.2005.01.050.

[161] G.D. Smith, R.J.H. Clark, Raman microscopy in archaeological science, J. Archaeol. Sci. 31 (2004) 1137–1160. doi:10.1016/j.jas.2004.02.008.

[162] J. Wang, C. Xu, G. Lv, Formation processes of CuCl and regenerated Cu crystals on bronze surfaces in neutral and acidic media, Appl. Surf. Sci. 252 (2006) 6294–6303. doi:10.1016/j.apsusc.2005.08.041.

[163] T. Kosec, H.O. Ćurković, A. Legat, Investigation of the corrosion protection of chemically and electrochemically formed patinas on recent bronze, Electrochimica Acta. 56 (2010) 722–731. doi:10.1016/j.electacta.2010.09.093.

[164] H. Otmačić Ćurković, T. Kosec, K. Marušić, A. Legat, An electrochemical impedance study of the corrosion protection of artificially formed patinas on recent bronze, Electrochimica Acta. 83 (2012) 28–39. doi:10.1016/j.electacta.2012.07.094.

[165] S. Bertling, I.O. Wallinder, D.B. Kleja, C. Leygraf, Long-term corrosion-induced copper runoff from natural and artificial patina and its environmental impact, Environ. Toxicol. Chem. 25 (2006) 891–898.

[166] P. Ropret, T. Kosec, Raman investigation of artificial patinas on recent bronze – Part I: climatic chamber exposure, J. Raman Spectrosc. 43 (2012) 1578–1586. doi:10.1002/jrs.4068.

[167] T. Kosec, P. Ropret, A. Legat, Raman investigation of artificial patinas on recent bronze–part II: urban rain exposure, J. Raman Spectrosc. 43 (2012) 1587–1595. doi:10.1002/jrs.4124.

[168] S. Goidanich, L. Toniolo, S. Jafarzadeh, I.O. Wallinder, Effects of wax-based anti-graffiti on copper patina composition and dissolution during four years of outdoor urban exposure, J. Cult. Herit. 11 (2010) 288–296. doi:10.1016/j.culher.2010.02.001.

[169] T. Chang, I. Odnevall Wallinder, D. de la Fuente, B. Chico, M. Morcillo, J.-M. Welter, C. Leygraf, Analysis of Historic Copper Patinas. Influence of Inclusions on Patina Uniformity, Materials. 10 (2017). doi:10.3390/ma10030298.

[170] F.J.R. de Oliveira, D.C.B. Lago, L.F. Senna, L.R.M. de Miranda, E. D'Elia, Study of patina formation on bronze specimens, Mater. Chem. Phys. 115 (2009) 761–770. doi:10.1016/j.matchemphys.2009.02.035.

[171] R. del P.B. Hernández, I.V. Aoki, B. Tribollet, H.G. de Melo, Electrochemical impedance spectroscopy investigation of the electrochemical behaviour of copper coated with artificial

patina layers and submitted to wet and dry cycles, Electrochimica Acta. 56 (2011) 2801–2814. doi:10.1016/j.electacta.2010.12.059.

[172] A. Kratschmer, I.O. Wallinder, C. Leygraf, The evolution of outdoor copper patina, Corros. Sci. 44 (2002) 425–450.

[173] K. Marušić, H. Otmačić-Ćurković, Š. Horvat-Kurbegović, H. Takenouti, E. Stupnišek-Lisac, Comparative studies of chemical and electrochemical preparation of artificial bronze patinas and their protection by corrosion inhibitor, Electrochimica Acta. 54 (2009) 7106–7113. doi:10.1016/j.electacta.2009.07.014.

[174] I. Rezić, L. Ćurković, M. Ujević, Metal ion release from electric guitar strings in artificial sweat, Corros. Sci. 51 (2009) 1985–1989. doi:10.1016/j.corsci.2009.05.018.

[175] A.J. Muller, C. McCrory-Joy, Chromatographic analysis of copper patinas formed in the atmosphere, Corros. Sci. 27 (1987) 695–701. doi:10.1016/0010-938X(87)90051-5.

[176] L. Guadagnini, C. Chiavari, C. Martini, E. Bernardi, L. Morselli, D. Tonelli, The use of scanning electrochemical microscopy for the characterisation of patinas on copper alloys, Electrochimica Acta. 56 (2011) 6598–6606. doi:10.1016/j.electacta.2011.04.080.

[177] Z.Y. Chen, S. Zakipour, D. Persson, C. Leygraf, Effect of sodium chloride particles on the atmospheric corrosion of pure copper, Corrosion. 60 (2004) 479–491.

[178] Z.Y. Chen, D. Persson, F. Samie, S. Zakipour, C. Leygraf, Effect of carbon dioxide on sodium chloride-induced atmospheric corrosion of copper, J. Electrochem. Soc. 152 (2005) B502–B511. doi:10.1149/1.2098327.

[179] Z.Y. Chen, S. Zakipour, D. Persson, C. Leygraf, Combined effects of gaseous pollutants and sodium chloride particles on the atmospheric corrosion of copper, Corrosion. 61 (2005) 1022–1034.

[180] I.O. Wallinder, S. Bertling, X.Y. Zhang, C. Leygraf, Predictive models of copper runoff from external structures, J. Environ. Monit. 6 (2004) 704–712. doi:10.1039/B402223h.

[181] M. Drogowska, L. Brossard, H. Menard, Influence of anions on the passivity behavior of copper in alkaline solutions, Surf. Coat. Technol. 34 (1988) 383–400.

[182] R. Babić, M. Metikoš-Huković, M. Lončar, Impedance and photoelectrochemical study of surface layers on Cu and Cu–10Ni in acetate solution containing benzotriazole, Electrochimica Acta. 44 (1999) 2413–2421. doi:10.1016/S0013-4686(98)00367-3.

[183] I.A. Ammar, S. Darwish, M.W. Khalil, S. El-Taher, A review on the electrochemistry of tin, Mater. Chem. Phys. 21 (1989) 1–47. doi:10.1016/0254-0584(89)90100-4.

[184] M.S. ABDELAAL, I.M. ISSA, M.M. SELEEM, Electrochemical Behavior of 80% Sn-Cu Alloy in Some Carboxylic Acids and Buffer Solutions, CORROSION. 32 (1976) 30–34. doi:10.5006/0010-9312-32.1.30.

[185] P.E. Alvarez, S.B. Ribotta, M.E. Folquer, C.A. Gervasi, J.R. Vilche, Potentiodynamic behaviour of tin in different buffer solutions, Corros. Sci. 44 (2002) 49–65. doi:10.1016/S0010-938X(01)00032-4.

[186] K.E.E. D. A. Porter, Phase Transformations in Metals and Alloys, 2nd ed., CRC Press, 1992.

[187] M.D. Sanderson, J.C. Scully, The high-temperature oxidation of some oxidation-resistant copper-based alloys, Oxid. Met. 3 (1971) 59–90.

[188] B.D. Bastow, G.C. Wood, D.P. Whittle, Morphologies of uniform adherent scales on binary alloys, Oxid. Met. 16 (1981) 1–28. doi:10.1007/BF00603743.

[189] H.H. Uhlig, G.E. Woodside, Anodic Polarization of Passive and Non-passive Chromium–Iron Alloys., J. Phys. Chem. 57 (1953) 280–283.

[190] I. Milošev, M. Metikoš-Hukovic, Passive Films on 90Cu-10Ni Alloy: The Mechanism of Breakdown in Chloride Containing Solutions, J. Electrochem. Soc. 138 (1991) 61–67. doi:10.1149/1.2085579.

[191] S. Fujimoto, R.C. Newman, G.S. Smith, S.P. Kaye, H. Kheyrandish, J.S. Colligon, Passivation thresholds in iron-chromium alloys prepared by ion-beam sputtering, Adv. Corros. Prot. 35 (1993) 51–55. doi:10.1016/0010-938X(93)90132-Z.

[192] A.P. Bond, H. Uhlig, Corrosion Behavior and Passivity of Nickel-Chromium and Cobalt-Chromium Alloys, J. Electrochem. Soc. 107 (1960) 488–493.

[193] P. Druska, H.H. Strehblow, Surface analytical examination of passive layers on Cu-Ni alloys part II. Acidic solutions, Corros. Sci. 38 (1996) 1369–1383. doi:10.1016/0010-938X(96)00026-1.

[194] P. Keller, H.-H. Strehblow, Passivity of Tin and CuSn Alloys in Alkaline Media studied by X-ray Photoelectron Spectroscopy, in: Passiv. Met. Semicond. Prop. Thin Oxide Layers, Elsevier Science, Amsterdam, 2006: pp. 137–142. doi:10.1016/B978-044452224-5/50023-8.

[195] B. Laurent, N. Gruet, B. Gwinner, F. Miserque, K. Rousseau, K. Ogle, Dissolution and Passivation of a Silicon-Rich Austenitic Stainless Steel during Active-Passive Cycles in Sulfuric and Nitric Acid, J. Electrochem. Soc. 164 (2017) C892–C900. doi:10.1149/2.1531713jes.

[196] N Cabrera and N F Mott, Theory of the oxidation of metals, Rep. Prog. Phys. 12 (1949) 163.

[197] H. Shimizu, M. Ono, K. Nakayama, Quantitative auger analysis of copper-nickel alloy surfaces after argon ion bombardment, Surf. Sci. 36 (1973) 817–821. doi:10.1016/0039-6028(73)90428-7.

[198] C.H. Hamann, A. Hamnett, W. Vielstich, Electrochemistry, Wiley, 2007. https://books.google.com/books?id=EXljvgAACAAJ.

[199] W.. Winterbottom, Equilibrium shape of a small particle in contact with a foreign substrate, Acta Metall. 15 (1967) 303–310. doi:10.1016/0001-6160(67)90206-4.

[200] H.T. Michels, S.A. Wilks, J.O. Noyce, C.W. Keevil, Copper alloys for human infectious disease control, Stainl. Steel. 77000 (2005) 27–0.

[201] E. Sukkar, Why are there so few antibiotics in the research and development pipeline, Pharm. J. 13 (2013).

[202] W.A. Badawy, R.M. El-Sherif, H. Shehata, Electrochemical stability of Cu–10Al–5Ni alloy in chloride–sulfate electrolytes, Electrochimica Acta. 54 (2009) 4501–4505. doi:10.1016/j.electacta.2009.03.040.

[203] W.A. Badawy, R.M. El-Sherif, H. Shehata, Electrochemical behavior of aluminum bronze in sulfate-chloride media, J. Appl. Electrochem. 37 (2007) 1099–1106. doi:10.1007/s10800-007-9362-9.

[204] O.F.M. Benatti, W.G. Miranda Jr, A. Muench, In vitro and in vivo corrosion evaluation of nickel-chromium- and copper-aluminum-based alloys, J. Prosthet. Dent. 84 (2000) 360–363. doi:10.1067/mpr.2000.109377.

[205] Copper Development Association, Wrought and Cast Copper Alloys, n.d. https://alloys.copper.org/ (accessed December 16, 2016).

[206] Copper Data, Copper Development Association, 1949.

[207] A.M. Alfantazi, T.M. Ahmed, D. Tromans, Corrosion behavior of copper alloys in chloride media, Mater. Des. 30 (2009) 2425–2430. doi:10.1016/j.matdes.2008.10.015.

[208] G.S. Duffó, S.B. Farina, Corrosion behaviour of a dental alloy in some beverages and drinks, Mater. Chem. Phys. 115 (2009) 235–238. doi:10.1016/j.matchemphys.2008.11.053.

[209] R.J. Raudebaugh, Nonferrous physical metallurgy., Pitman Pub. Corp., New York, 1952. http://search.lib.virginia.edu/catalog/u923733.

[210] M. Tb, O. H, S. PR, Binary Alloy Phase Diagrams, 2nd Edition (3 Volume Set), A S M International (OH), 1990. https://books.google.com/books?id=7UI9mwEACAAJ.

[211] P. Süry, H.R. Oswald, On the corrosion behaviour of individual phases present in aluminium bronzes, Corros. Sci. 12 (1972) 77–90. doi:10.1016/S0010-938X(72)90581-1.

[212] F.H. Assaf, Anodic polarization of Al-Sn alloy in H3PO4 solutions, J. Solid State Electrochem. 3 (1998) 39–47.

[213] J.L. Chen, Z. Li, Y.Y. Zhao, Corrosion characteristic of Ce Al brass in comparison with As Al brass, Mater. Des. 30 (2009) 1743–1747. doi:10.1016/j.matdes.2008.07.041.

[214] C.W. DRAPER, R.E. WOODS, L.S. MEYER, Enhanced Corrosion Resistance of Laser Surface Melted Aluminum Bronze D (CDA-614), CORROSION. 36 (1980) 405–408. doi:10.5006/0010-9312-36.8.405.

[215] K. Sieradzki, J.S. Kim, A.T. Cole, R.C. Newman, The Relationship Between Dealloying and Transgranular Stress-Corrosion Cracking of Cu-Zn and Cu-Al Alloys, J. Electrochem. Soc. 134 (1987) 1635–1639. doi:10.1149/1.2100726.

[216] C. Young-Gab, P. Su-Il, K. Chang-Ha, Effect of aluminium content on the anodic behaviour of copper-aluminium alloys in 3.5 wt% NaCl solution, Mater. Lett. 20 (1994) 265–270. doi:10.1016/0167-577X(94)90027-2.

[217] T. Chang, G. Herting, Y. Jin, C. Leygraf, I. Odnevall Wallinder, The golden alloy Cu5Zn5Al1Sn: Patina evolution in chloride-containing atmospheres, Corros. Sci. (2018). doi:10.1016/j.corsci.2018.01.027.

[218] T. Chang, I.O. Wallinder, Y. Jin, C. Leygraf, The golden alloy Cu-5Zn-5Al-1Sn: A multi-analytical surface characterization, Corros. Sci. 131 (2018) 94–103. doi:10.1016/j.corsci.2017.11.014.

[219] T.K. Andersen, S. Cook, G. Wan, H. Hong, L.D. Marks, D.D. Fong, Layer-by-Layer Epitaxial Growth of Defect-Engineered Strontium Cobaltites, ACS Appl. Mater. Interfaces. 10 (2018) 5949–5958. doi:10.1021/acsami.7b16970.

[220] C.W. Bale, E. Bélisle, P. Chartrand, S.A. Decterov, G. Eriksson, A.E. Gheribi, K. Hack, I.-H. Jung, Y.-B. Kang, J. Melançon, A.D. Pelton, S. Petersen, C. Robelin, J. Sangster, P. Spencer, M.-A. Van Ende, FactSage thermochemical software and databases, 2010–2016, Calphad. 54 (2016) 35–53. doi:10.1016/j.calphad.2016.05.002.

[221] D.J. Horton, J.R. Scully, The Effect of the Amorphous and Crystalline States on Preferential Corrosion of Hf from a Cu75Hf20Dy05 Alloy, Metall. Mater. Trans. -Phys. Metall. Mater. Sci. 43A (2012) 2706–2720. doi:10.1007/s11661-011-1065-5.

[222] J.F. Moulder, J. Chastain, Handbook of X-ray Photoelectron Spectroscopy: A Reference Book of Standard Spectra for Identification and Interpretation of XPS Data, Physical Electronics Division, Perkin-Elmer Corporation, 1992. https://books.google.com/books?id=A_XGQgAACAAJ.

[223] K. Gelderman, L. Lee, S.W. Donne, Flat-band potential of a semiconductor: using the Mott–Schottky equation, J Chem Educ. 84 (2007) 685.

[224] S. Laidoudi, A.Y. Bioud, A. Azizi, G. Schmerber, J. Bartringer, S. Barre, A. Dinia, Growth and characterization of electrodeposited Cu $_2$ O thin films, Semicond. Sci. Technol. 28 (2013) 115005. doi:10.1088/0268-1242/28/11/115005.

[225] W. Schmickler, Interfacial Electrochemistry, Oxford University Press, USA, 1996. https://books.google.com/books?id=iJh1mAEACAAJ.

[226] Database of Raman Spectroscopy, X-ray Diffraction and Chemistry of Minerals, RRUFF Project, n.d. http://rruff.info/ (accessed December 19, 2016).

[227] G.S. Rohrer, Structure and Bonding in Crystalline Materials, Cambridge University Press, 2001. https://books.google.com/books?id=a0jPqKw2Zx8C.

[228] O. Gharbi, N. Birbilis, K. Ogle, In-Situ Monitoring of Alloy Dissolution and Residual Film Formation during the Pretreatment of Al-Alloy AA2024-T3, J. Electrochem. Soc. 163 (2016) C240–C251. doi:10.1149/2.1121605jes.

[229] J.C. Baker, J.W. Cahn, Solute trapping by rapid solidification, Acta Metall. 17 (1969) 575–578.

[230] S. Mrowec, Defects and diffusion in solids: an introduction, Elsevier Scientific Pub. Co., 1980. https://books.google.com/books?id=UQtRAAAAMAAJ.

[231] A.F. Wright, J.S. Nelson, Theory of the copper vacancy in cuprous oxide, J. Appl. Phys. 92 (2002) 5849–5851. doi:10.1063/1.1516620.

[232] M. Murray, M. Sahoo, White antimicrobial copper alloy, 2017.

[233] C.L. Trybus, R.P. Vierod, P.W. Robinson, Antitarnish, antimicrobial copper alloys and surfaces made from such alloys, 2011.

[234] J. Miettinen, Thermodynamic description of the Cu-Al-Sn system in the copper-rich corner, Metall. Mater. Trans. A. 33 (2002) 1639–1648. doi:10.1007/s11661-002-0173-7.

[235] ATSM, B825 - Standard Test Method for Coulometric Reduction of Surface Films on Metallic Test Samples, ASTM Int. (2013). doi:10.1520/B0825.

[236] M.E. Orazem, B. Tribollet, Electrochemical Impedance Spectroscopy, Wiley, 2011. https://books.google.com/books?id=uSO08d-FBh0C.

[237] C. Wagner, The distribution of cations in metal oxide and metal sulphide solid solutions formed during the oxidation of alloys, Corros. Sci. 9 (1969) 91–109. doi:10.1016/S0010-938X(69)80046-6.

[238] H.H. Pham, C.D. Taylor, N.J. Henson, Metal desorption from Fe(1 1 0) and its alloyed surfaces, Chem. Phys. Lett. 585 (2013) 162–166. doi:10.1016/j.cplett.2013.09.011.

Appendices

Transformation of Secondary Corrosion Products: Bronze Disease

Quantifying the total anodic charge, i.e. the fate of the elements, for Cu-Sn alloys required characterization within a limited time window (24 h) following extraction to prevent spontaneous conversion in lab air of cuprous products to cupric compounds as demonstrated by Figure 3.2. The disparity between mass loss values and total anodic charge from soluble Cu and coulometrically reduced oxides may be caused by the precipitation of unquantified secondary corrosion products such as nantokite (CuCl). These products simply may not be adherent enough to survive sample rinsing and transfer to the reduction cell or may be electrically disconnected from the surface. CuCl is formed by chemical precipitation from excess soluble Cu^+ in solution. Following the Cu dissolution trajectory in Figure 3.1 (solid black line), Cu_2O is precipitated first (K_{sp}=2.6 x 10^{-2}), followed by CuCl (K_{sp}=1.87 x 10^{-7}).

The amount of Cu^+ thermodynamically needed to begin precipitation of CuCl is only 2 x 10^{-6} M (~0.1 ppm) in artificial perspiration ($[Cl^-]$ from Table 2-2). The measured concentration of soluble Cu after 96 h in full immersion ranged from 1-2 ppm (Figure 3.6), therefore, CuCl precipitation is indeed a favorable chemical reaction in these conditions. Precipitation of secondary corrosion products are an unavoidable chemical consequence $[Cu^+]$ release from Cu-based alloys in chloride-containing environments. Cupric compounds formed from cuprous products can be detrimental to the stability of bronze patina. The destabilization of bronze patinas due chloride-induced attack is commonly referred to as 'bronze disease' and is a common issue for outdoor architectural and statuary bronze materials exposed to chloride-containing environments [130]. Following sample extraction, nantokite (CuCl) begins to transform in ambient air into atacamite (see Figure 3.2) according to the full cell reaction in Equation (A.1).

$$12CuCl + 6H_2O + 3O_2 \rightarrow 4Cu_2(OH)_3Cl + 4CuCl_2 \qquad \text{(A.1)}$$

In ambient air conditions, O_2 becomes more available pushing this reaction to the right. Energetically, this reaction is spontaneous. The standard Gibbs free energy of CuCl is just -119.7 kJ/mol while the two products formed by the reaction eq. (A.1) are -1339.2 and -655.9 kJ/mol, respectively [120]. Atacamite is known to cause flaking and spallation when formed within Cu patinas due to volumetric stresses caused by crystal structure changes [132]. Thus, the formation of atacamite from a drying event is dangerous to the corrosion protection and aesthetics of a stable bronze patina layer.

However, these secondary cupric compounds are not directly formed at the alloy/oxide interface, are loosely adherent, and may be easily wiped off with frequent abrasion or chemical cleaning of the surface which would be expected on a high-touch antimicrobial surface. The disparity between total (mass loss) and combined (ICP+CR) anodic charge decreases with increasing Sn content suggesting this may be due to the formation of more conformal Sn oxide barrier layer.

Enhancement of Cu Dissolution from Sn-implanted Cu (111) Surfaces: Electrochemical and *Ab Initio* Modeling Studies

Background

Enhanced dissolution of Cu was observed from Cu-Sn alloys in artificial solution [17,154]. The increase in cation release decreased the amount of Cu corrosion products, leading to a greater soluble fraction of Cu (Chapter 3). The origin of this enhancement is expected to be due to an increase in anodic dissolution kinetics due to the decreased Cu-Sn bonding strength compared with Cu-Cu (Figure 1.5). The following attempts to describe the enhanced dissolution of Cu from Cu-Sn surfaces using both experimental and *ab initio* Density-Functional Theory (DFT) modeling approaches.

Experimental Procedures

Cyclic voltammetry sweeps were conducted on high purity Cu-Sn alloys from Chapter 3 in a deaerated boric acid buffer which was adjusted to the same pH as artificial perspiration (6.50 ±0.05) and was prepared by mixing solutions of 0.1 M boric acid (H_3BO_3) and 0.1 M sodium tetraborate ($Na_2B_4O_7$) to the target pH value. Sweep rates were 10 mV/s following a 10 min cathodic polarization at -1.4 V_{MMSE} to reduce any surface oxides. Potentiodynamic polarizations in 1 M HCl were conducted following a 10-min cathodic polarization at -1.5 V_{SCE}. Upward scans were carried out at a rate of +1 mV/s. The aeration of the electrolyte solution was not controlled and was ambiently aerated.

Modeling Setup

Using first principles an FCC Cu (111) slab surface was simulated in a vacuum with a Cu adatom forcibly held at increasing distances above and also translated across the surface. The slab surface was then modified by replacing a surface plane atom with Al or Sn underneath the Cu adatom. The Vienna *ab initio* Simulation Package (VASP) was used to implement Density

Functional Theory (DFT) calculations. The projector augmented wave PBE-generalized gradient approximation (PAW-GGA) exchange-correlation was used, with a plane-wave energy cutoff at 400 eV. A vacuum of 20 angstroms was included above the Cu slab. The Cu slab was 5 atoms by 5 atoms with 3 atomic layers thick and oriented to the (111) planar surface with periodic boundary conditions on all boundary surfaces. Initial and final geometries of the dissolution/desorption simulation setup are given in Figure A.3a and b, respectively. The bottom layer of the slab was held fixed to simulate bulk Cu conditions but was initially allowed to fully relax (geometrically) before introducing the neutral Cu adatom to account for lattice strain caused by the addition of Al or Sn in the crystal. Following local geometry relaxation, the adatom z position, defined here as normal to the (111) surface, is held fixed while allowing all other positions free to relax ($n = 5$ iteration steps), with exception to the bottom slab layer, which was held fixed to approximate an infinite bulk Cu crystal beneath the surface.

Results

Cyclic voltammetry results from high purity Cu-Sn alloys are presented in Figure A.1. These tests are conducted in a deaerated buffered media without the complexing effects of Cl^-, ammonia, or other sweat constituents. This E-I behavior was likely due to direct ion ejection of cuprous and then cupric ions during oxidation since all alloys demonstrate two cathodic reduction peaks at -1.0 V_{MMSE} and -0.5 V_{MMSE}, respectively. This is most apparent in the commercially pure Cu case (black line in Figure A.1a). Anodic current densities were highest for Cu-1Sn for all cycles when compared to the other alloys. Cu-5Sn and Cu-10Sn had less anodic current (Figure A.1a) likely due to blocking of the surface by SnO_2 oxidation which takes place initially in the first sweep and is then electrochemically inert in these potential ranges [154]. From these results Cu-1Sn shows the highest anodic currents. Yet, a lower slope on the anodic curve for Cu-5Sn and higher Sn contents shows a change in dissolution kinetics for alloys possessing 5 wt% and greater Sn contents. Notably, the potential at which the net current is zero (Figure A.1b) is the same for the cathodic sweep direction for all alloys. However, the anodic sweep direction (Figure A.1b) shows decreasing net-zero-current potentials with increasing Sn content, this effect saturating after 5 wt% (2.5 at%).

Potentiodynamic polarizations of Cu-Sn alloys in 1M HCl (pH 0) are given fully in Figure A.2a, and focused on the anodic region in Figure A.2b. The cathodic range is indicative of mass-transport limited oxygen reduction as the primary cathodic reaction and does not appreciably change character between alloys. The anodic polarization behavior (Figure A.2b) of the Cu-Sn alloys however, showed different behavior between the alloys of various Sn contents. The corrosion current density was found to increase with Sn content and matched well to mixed potential theory with an increase in anodic exchange current density. These scans were done in an environment selected to avoid forming solid corrosion products (thermodynamically, Figure 3.1). However, we still observe dynamic thick-film passivity in the Cu-10Sn alloy in the potential window between -0.5 V_{SCE} to -0.2 V_{SCE} thereafter, the film either breaks down, or does not impede further oxidation resuming similar potential-dependent behavior as the other Cu-Sn alloys. However, the presence of this film may partially block the surface and may decrease the total anodic current. This ‘thick film’ is dynamically formed (as opposed to thermodynamically) from the relatively fast scan rate whose dissolution rate outcompetes the diffusive flux of the soluble anodic species away from the surface whereby the dissolution kinetics of this film are limiting. Furthermore, the upper nose of this potentiodynamic plots are precipitation of a CuCl salt film, again an artifact of low diffusion relative to scan rates and the high [Cl^-]. From the excess cuprous/cupric ion release at this scan rate (1 mV/s) near the surface which is not mitigated by the diffusive flux of this species away from the surface, therefore chemically precipitating with 1M Cl^- in the environment to form CuCl or $CuCl_2$.

DFT-Simulated Cu crystals in vacuum show minor surface distortion from FCC positions when the adatom is present on the surface (Figure A.3a); this distortion is resolved to the more familiar (visually) Cu FCC configuration when the adatom is displaced far enough away from the surface (Figure A.3b). The specific energy/force of the adsorption/desorption event is tracked for various implanted solute atoms in the surface layer and hence, trends may indeed be observed between these cases.

Calculated adsorption forces acting on the Cu adatom lifted from the surface are given in Figure A.4. We see little differences in maximum and overall desorption forces as a function of vertical displacement. From these simulated results, desorption (and implicitly, dissolution) of Cu is not affected by either Al or Sn. However, the same exact adatom configuration for the Cu-Sn case could not be obtained while allowing local geometry relaxation, and this a nearby site was chosen to highlight how distance of the adatom to the Sn surface atom is critical, as is reinforced below.

Further investigating the effect of Sn in Cu we shifted from a vertical displacement setup to hovering and then dragging the adatom over this Sn-implanted surface site (as illustrated in Figure A.5) at the vertical position indicated by the grey dashed vertical line in Figure A.4. The z-position of the adatom was fixed, as well as the displacement vector (y-direction), and the bottom layer of the slab was also fixed (after initial geometry relaxation without adatom) to simulate the bulk Cu-Sn crystal. Illustrated in Figure A.5, as we drag the Cu 'adatom' above the surface to the equivalent position (see Figure A.5) as Cu and Cu[Al], there is an observed decrease (~50%) in calculated attractive force acting on the Cu atom. The z-position was selected above the slab in the bond-breaking region [238]. The attractive force in the z direction ($\perp$ to surface) falls rapidly as we move towards the Sn-atom-neighbor site. Then sharply increases again over the neighboring site. Atom geometry positions were allowed to relax to a local energy minimization at each displacement step (5 relaxation iterations).

Discussion

Electrochemical Behavior

SnO_2 has already formed in the first sweep of the CV (Chapter 2). The reduced peak current observed for the Cu-5Sn and Cu-10Sn is likely due to this effect. However, the reduced potential at which the net current is zero for the anodic direction seemingly indicates that Cu dissolution is easier from Cu-Sn surfaces, either by an effect of Sn or the presence of SnO_2. Noteworthy, the corrosion current densities in these environments (pH 0.1M [Cl^-]) are increased for Cu-5Sn and Cu-10Sn. The demarcation observed for other results (e.g., Chapter 2 OCP, EIS, Mass Loss) of these alloys is consistent in this strong acid environment as well. This increase does not seem to be due to significant change in anodic or cathodic Tafel kinetic slopes, nor by a significant alteration of cathodic current exchange density. If we assume that anodic kinetics are altered in the form of exchange current densities of the anodic process (i.e., Cu dissolution/redeposition) we can assert that the Cu-Sn surface is more favorable towards Cu dissolution, and/or less favorable in to Cu redeposition in equilibrium.

DFT-Modeling

Cu dissolution is made easier, and redeposition is made more difficult by the presence of Sn inferred by the decreased attractive force in the bond-breaking region. The anodic exchange kinetics therefore would increase as the force inhibiting desorption/dissolution from the surface is significantly (50%) reduced. We assert a claim that the forward and backward rate constants of the anodic exchange current density are altered by this effect. Adsorption, as other sites (non-Sn) may become more preferable than Cu-Sn surface sites. Furthermore, an adatom dragged from its stacking fault location (1 neighbor displaced) across the surface over this same site as the other cases (Cu and Cu[Al]) showed a significant decrease (50%) of the acting adsorption force (in the z-direction) on the floating adatom, this demonstrates the source of affected surface behavior due to Sn in the surface.

Figures

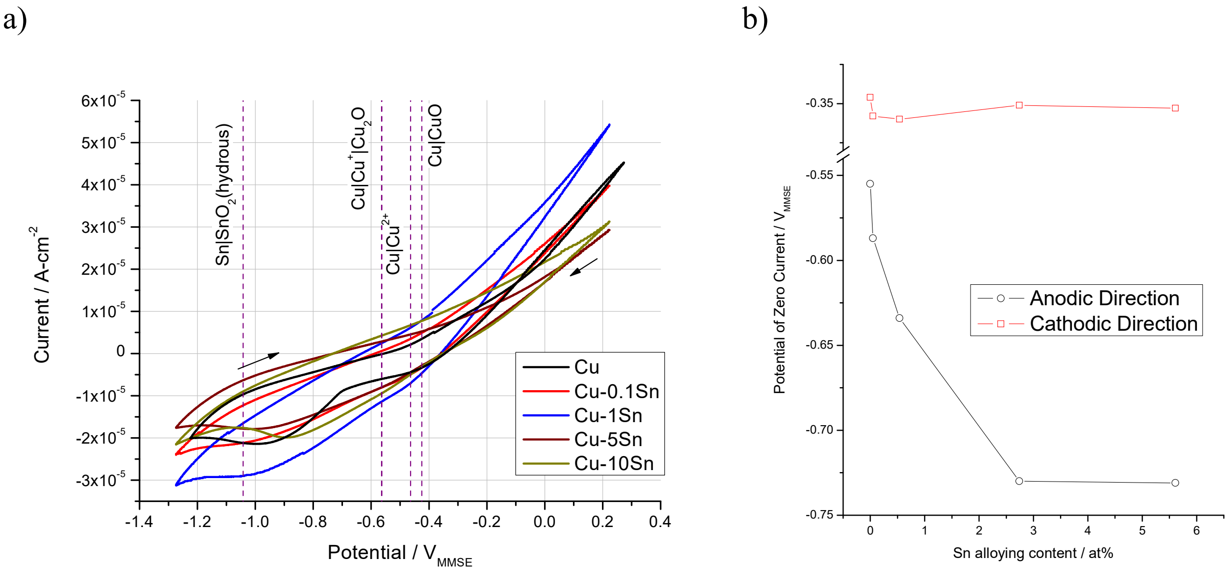

Figure A.1. a) Cyclic voltammograms in borate buffer (pH 6.5). Scan rate 10 mV/s. Third sweep shown. Samples were held at -1.4 V_{MMSE} for 10 min prior to initial scan. Selected Nernst potentials of interest are overlain as dashed lines on plot. b) Potential of zero current of the anodic and cathodic sweep direction compared to Sn alloying content in atomic percent.

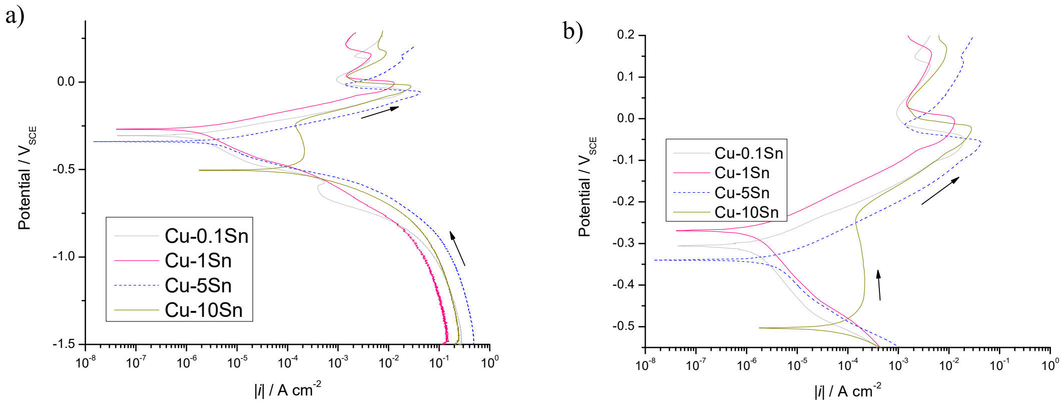

Figure A.2. Potentiodynamic polarizations of Cu-Sn samples in 1M HCl. Scan rate: 1 mV/s. Full scan range (a) and anodic range (b). A 15-minute cathodic reduction of -1.5 V_{SCE} was applied before testing.

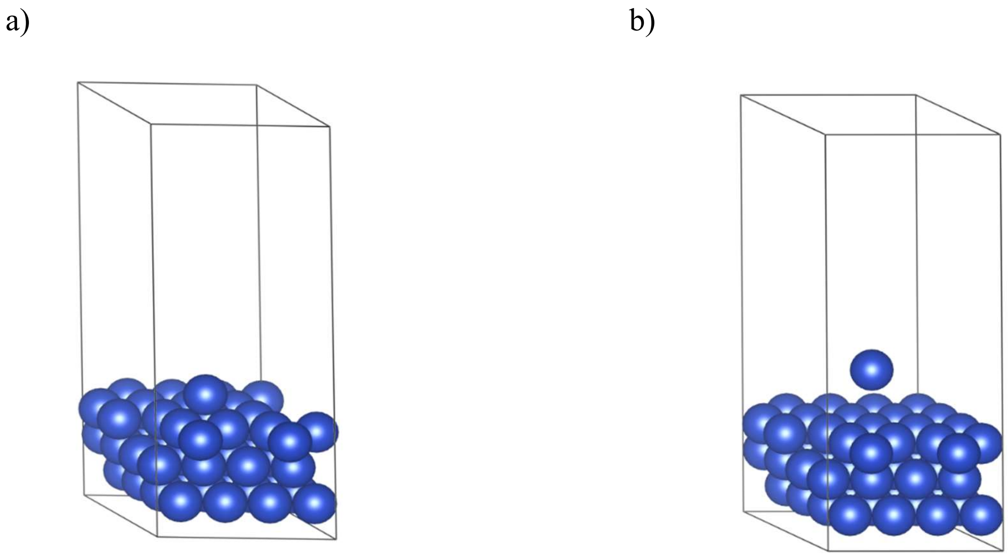

Figure A.3. Initial Cu adatom position (a) and fully displaced Cu adatom position (b) both are in geometrically relaxed conditions with the exception that the adatom z coordinate is held fixed

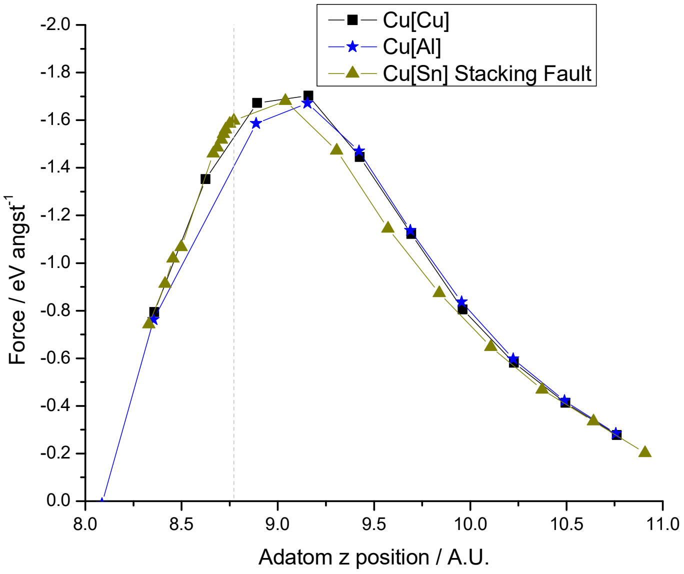

Figure A.4. Calculated adsorption force of a Cu adatom above solute-implanted Cu FCC (111) surface. Adatom positions are defined in the text. Vertical dashed line is in reference to relative z-position for Figure A.5.

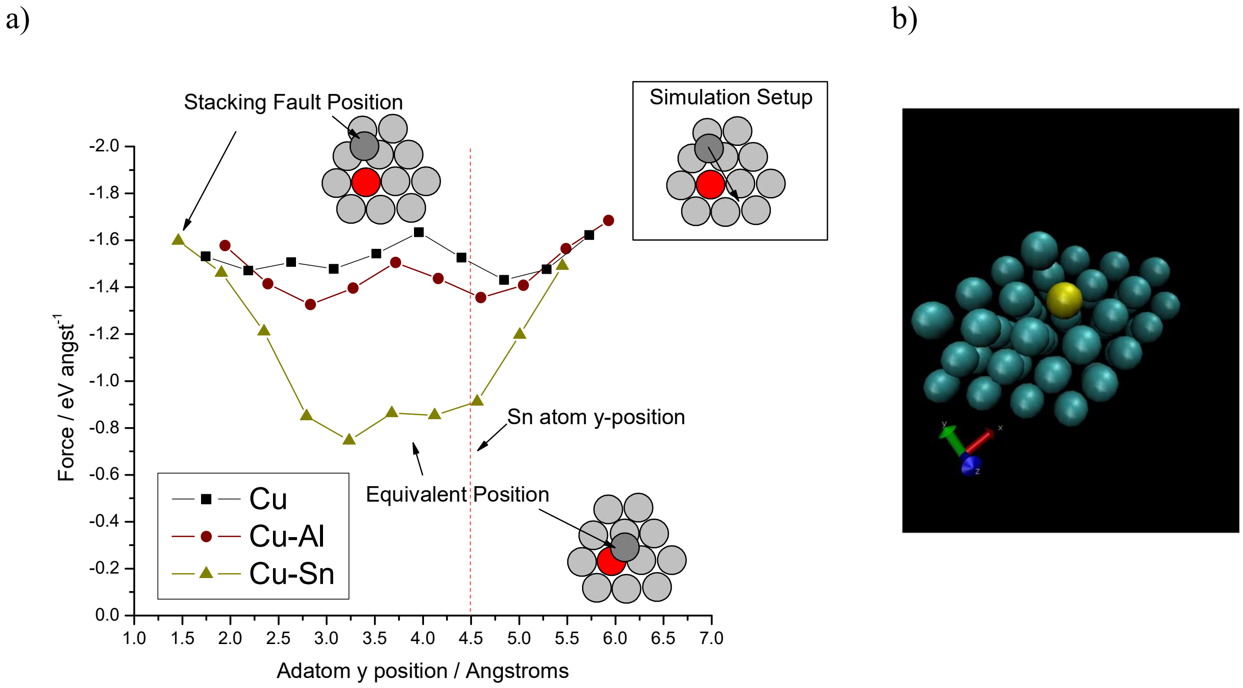

Figure A.5. Calculated force in the z-direction of Cu adatom (a) dragged across surface sites at a fixed z position above a Sn-implanted Cu FCC (111) surface (b). Equivalent position is the site corresponding to Cu and Cu[Al] simulation results as indicated in figure.